Thèse n° 9434

Exploring new avenues for perovskite photovoltaics: Molecular functionalization of layered lead-halide perovskites and defect mitigation in lead-free double perovskites

Présentée le 1^{er} avril 2022

Faculté des sciences de base
Laboratoire d’ingénierie moléculaire des nanomatériaux optoélectroniques
Programme doctoral en chimie et génie chimique

pour l’obtention du grade de Docteur ès Sciences

par

Barbara Alexandra PRIMERA DARWICH

Acceptée sur proposition du jury

Prof. J.-E. Moser, président du jury
Prof. K. Sivula, J. H. Yum, directeurs de thèse
Prof. I. Mora Seró, rapporteur
Prof. T. Bein, rapporteur
Prof. F. Nüesch, rapporteur

École
polytechnique
fédérale
de Lausanne

2022

To my mother,

For her wonderful spirit,

For always dreaming big

And loving and supporting me

Wherever I go.

"Nothing in life is to be feared, it is only to be understood. Now is the time to understand more, so that we may fear less."

Marie Curie

Acknowledgements

I am very much grateful to so many individuals who have helped and supported me throughout the years and also throughout the progress of this doctoral thesis.

First, I would like to thank my thesis supervisors Prof. Kevin Sivula and Dr. Jun-Ho Yum at LIMNO for taking me on board and providing me with the opportunity to pursue this research project at EPFL. Thank you for allowing me to explore various research questions and topics, for being available to discuss scientific findings and for making sure the laboratory environment was well suited to carry out the research work. Kevin, thank you for having always an open door and being always available to promptly solve issues in the laboratory. Junho, thank you for making me feel welcome from the very start of my time at LIMNO and for supporting my development. I have great memories from our ski and hiking days together with our team.

In LIMNO I have had the opportunity to meet some very special individuals and friends, that I hold very close to my heart. I would first and foremost like to give a very special thanks to Dr. Nestor Guijarro, who, with his wonderful spirit, both personally and professionally, has been an immense support in these past years. Thank you for being always there to discuss and provide stimulating insights on experimental procedures, research findings and life and for being always able to bring a smile to the faces of everyone around. Also, your work ethic and way of approaching science has been greatly inspiring as well as your unparalleled scientific illustrations. Certainly, your unique combination of having a kind heart and being a prolific scientist stands out and sets high standards for the environment that surrounds you. Thank you for always encouraging me.

I would also like to thank Dr. Liang Yao, who from the very beginning of my time at LIMNO provided great support. Thank you for setting a great example and for training me on various photovoltaic experimental procedures in the lab as well as calculation methods. I truly appreciate the time and effort you spent on supporting my research work and for always providing great insights. I truly enjoyed our time during the NanoGe conference in Berlin. Also, thank you for sharing with us your delicious Chinese dumplings. For this I also thank Yongpeng, for always sharing delicious meals with us and keeping us up to date on Chinese festivities, thank you for the great times.

Arvindh, you have been my brother in the lab on our doctoral journey. Your company in the lab until late at night was always very reassuring as well as your constant check-ins. Your hard work in the lab was always very motivating as well as your questions that always led to fruitful discussion. I trust a wonderful career future awaits you after your time at LIMNO. Thank you for being a great friend and for all the laughs.

Marina, you have been my sister in the lab, thank you for the great friendship and support during these past years. Our travel and field trip adventures have allowed for a nice work-life balance during the time of the PhD. I am very grateful to have had you around and for always keeping us all safe in the lab with all your efforts.

Dr. Liza Mensi, thank you for providing for such a great atmosphere in the lab, for being a role model and for being a great friend. Your energy and work ethic are admirable. Thank you also to Dr. Mounir Mensi for the great support. Thank you both for your kindness and for the delicious meals that you have shared with us.

Narumi, although your time in the lab was quite short during your summer internship your presence, your kindness and smiles were never forgotten. Thank you for being always so kind and energetic, I very much enjoyed our summer adventures in and around Switzerland.

Thanks to Dr. Han-Hee Cho for being a great office mate and support, both in research and data processing. Furthermore, you always knew how to navigate life in Switzerland smoothly and were always willing to share with the others, thank you for that. Thank you also for sharing delicious Korean meals with us.

I would also like to thank my lab colleague Yeonju for her kindness and support, as well as Connor, for being always up for a chat, and for his efforts in providing a beautiful work environment. Thank you, Dr. Emeline Rideau, for being a great lab-mate and colleague, as well as Lucas, for being a great lab-mate during your time at LIMNO, and for being a great friend. Thanks to Nukorn and Rebekah for being great colleagues. Nukorn, thank for your bringing always joy and Rebekah for making me feel welcome from the very beginning. I will never forget our overnight shifts at the Synchrotron facility in Grenoble where we enjoyed various musical genres together throughout the night to support us. Thanks to Colin and Simon also for being great lab mates. Thanks also to Dr. Haizhou Lu, for his great support and sharing of the LPI equipment with me. Thank you also to Dr. Miskovic and Christine Kupper for being always so kind and willing to chat, thank you both for being great and supportive lab neighbors.

To my two dear Master students, Basile and Benjamin, thank you for being such great colleagues and for being always so motivated to work together. Your efforts have made a wonderful contribution to the research as well as your great company.

I am also very much grateful to various technicians and staff throughout the EPFL facilities. I would like to start by thanking Dr. Farzaneh Fadaei Tirani, at the X-ray diffraction facility, it was always such a joy to head to your lab, thank you for being always so kind, welcoming and enthusiastic. Your smiles could always turn any day better. Thank you to Dr. Laura Piveteau at the NMR facilities for being such a great support during my last few experiments, thank for being always so kind and responsive and for all the encouragement. Thank you to Dr. Pascal Schouwink for being a great support at the EPFL XRD facilities and during our visit to the synchrotron and for always providing wonderful insights. Thanks also to Dr. Victor Boureau for his great support at the transmission electron microscopy laboratories and for being always available. Thanks to our administrator Irina Lopez, for being such a great colleague and for always being so kind, while also keeping us all organized. Sofia, merci pour ta gentillesse, et pour avoir partagé des histoires fascinantes toujours avec nous, pour tes visites et tes cadeaux délicieux ; grâce à toi, notre bureau était toujours impeccable, merci. I would also like to thank the mechanical and electronic workshops, specially Harald for being so kind and helpful. Thank you also to Grégoire, Benjamin, Supardi and Yves for their great support and attention. I would also like to thank Jacques and the rest of the magasin team for being always so welcoming at the chemical shops.

I would also like to personally thank the jury for taking on the task of evaluating this thesis work as well as the Korea Electric Power Corporation (KEPCO) for the funding of my doctorate.

Going back to my time before the beginning of my doctorate, I would like to also thank Dr. Qilei Song, my Master Thesis supervisor at Imperial College London. Your work ethic and training provided immense inspiration and provided a set of tools that equipped me well to embark on the work presented on this thesis.

I would also like to thank my friends, Mihai, Anamika, Cheema and Sourabh for always providing great encouragement. Mihai, thank you for having always encouraged me to pursue research and for setting a great example. Anamika and Sourabh, thank you for always checking in and for all the laughs. Cheema, thank you for always following my progress throughout my doctorate and for being a truly great friend, may you rest in peace.

Finally, I would like to deeply thank my family, my mother, father and sister, for being always present, for their support and kindness throughout my lifetime. Gracias a mi mamá, por apoyarme siempre a perseguir mis sueños, por caminar a mi lado, aún a miles de kilómetros de distancia, por tus bendiciones, amor y apoyo que palabras no pueden describir, a mi papá, por siempre establecer un gran ejemplo de perseverancia, por soñar conmigo y por tus visiones, consejo y apoyo, y a mi hermana, por tener el corazón más noble, por ser un modelo a seguir, por apoyarme y celebrar conmigo siempre. Le agradezco también a mi Tía Flori por siempre apoyarme desde tan lejos y por todo el amor y mi Tío Goyo, Dr. José Gregorio Darwich, por inspirarme a estudiar un doctorado, siguiendo su ejemplo. Gracias a mis tíos y primos por su apoyo igualmente.

Barbara Primera Darwich

Abstract

Halide perovskites have seen, over the past years, a tremendous increase in photovoltaic power conversion efficiencies as device working mechanisms are unveiled. Lead halide perovskites are at the forefront of halide perovskite research given their intriguing optoelectronic properties. However, their short lifespan under thermal and moisture stress and their intrinsic toxicity both still stand as the main hurdle to their daily life application.

Layered perovskites have emerged as a modified version of conventional bulk halide perovskites with the promise of increasing their stability by incorporating bulky organic cations within the structure. These, while serving as moisture ingress blockers, further contribute to tailor the optoelectronic properties of perovskites. Although generally, optoelectronically-innocent organic spacers are used, the first Chapters of this thesis will explore the possibility of incorporating optoelectronically-active functional cations to further tailor the properties of the perovskite. Within this framework, two spacers, namely, naphthalene diimide (NDI) and benzodithiophene (BDT) will be described. While the incorporation of the former into a layered perovskite appeared challenging, BDT could successfully lead to Ruddlesden-Popper-type perovskite structures when the alkyl ammonium side chain was optimized. Following these results, quasi-layered lead halide perovskites were fabricated using BDT. The performance and stability outperformed those obtained using a standard phenylethylammonium (PEA) spacer. The combination of an assortment of techniques revealed that the improved charge transport in the active layer and the passivation of surface iodide vacancies were behind the enhanced photovoltaic response.

Being aware of the toxicity and stability concerns of lead halide perovskites for photovoltaic applications, the emerging double perovskite $Cs_2AgBiBr_6$ was investigated. With a Shockley-Queisser limit standing at 16.4%, but with much lower reported photovoltaic device efficiencies, current research aims at understanding the defects present in these materials as well as at establishing novel routes to optimize the performance. The work set out in this thesis first explores the effect of tuning the stoichiometry of the double perovskite. Since bromide vacancies are known to be present in the structure causing defects, the aim was to patch this issue by incorporating additional bromides using an excess CsBr in the precursor. The

enhanced photovoltaic response with excess CsBr was accounted for by the passivation of surface bromide vacancies, as suggested by solid-state NMR and photoluminescence measurements, as well as the larger crystal grains. To improve on these results, an alternative smaller cation salt, *i.e.* LiBr, was further tested as an additive to the double perovskite. A clear enhancement in device performance was observed, where a LiBr diffusion treatment, as opposed to a precursor solution additive, was deemed optimal. ^{7}Li solid-state NMR measurements revealed a distinct environment, likely of the Li$^+$ ions at interstitial positions accompanying the bromide anions towards vacancy sites while intensity modulated photovoltage spectroscopy yields longer charge recombination lifetimes. These findings pave the way for the exploration and optimization of defect-mitigating treatments in double perovskites.

Résumé

Les pérovskites aux halogénures ont connu, au cours des dernières années, une augmentation considérable des rendements de conversion de l'énergie photovoltaïque à mesure que les mécanismes de fonctionnement des dispositifs sont dévoilés. Les pérovskites aux halogénures de plomb sont à la pointe de la recherche sur les pérovskites aux halogénures compte tenu de leurs propriétés optoélectroniques intrigantes. Cependant, leur courte durée de vie sous stress thermique et hydrique et leur toxicité intrinsèque constituent toujours le principal obstacle à leur application dans la vie quotidienne.

Les pérovskites en couches sont apparues comme une version modifiée des pérovskites halogénures massives conventionnelles avec la promesse d'augmenter leur stabilité en incorporant des cations organiques volumineux dans la structure. Ceux-ci, tout en servant de bloqueurs d'entrée d'humidité, contribuent en outre à adapter les propriétés optoélectroniques des pérovskites. Bien que généralement, des espaceurs organiques optoélectroniquement inoffensifs soient utilisés, les premiers chapitres de cette thèse exploreront la possibilité d'incorporer des cations fonctionnels optoélectroniquement actifs pour mieux adapter les propriétés de la pérovskite. Dans ce cadre, deux espaceurs, à savoir le naphtalène diimide (NDI) et le benzodithiophène (BDT) seront décrits. Alors que l'incorporation du premier dans une pérovskite en couches semblait difficile, le BDT pourrait conduire avec succès à des structures de pérovskite de type Ruddlesden-Popper lorsque la chaîne latérale d'alkylammonium était optimisée. Suite à ces résultats, des pérovskites aux halogénures de plomb quasi-couches ont été fabriquées à l'aide de BDT. Les performances et la stabilité ont surpassé celles obtenues avec un espaceur standard en phényléthylammonium (PEA). La combinaison d'un assortiment de techniques a révélé que le transport de charge amélioré dans la couche active et la passivation des lacunes d'iodure de surface étaient à l'origine de la réponse photovoltaïque améliorée.

Conscients des problèmes de toxicité et de stabilité des pérovskites aux halogénures de plomb pour les applications photovoltaïques, la double pérovskite émergente $Cs_2AgBiBr_6$ a été étudiée. Avec une limite de Shockley-Queisser de 16,4 %, mais avec des efficacités de dispositifs photovoltaïques rapportées beaucoup plus faibles, les recherches actuelles visent à comprendre les défauts présents dans ces matériaux ainsi qu'à établir de nouvelles voies pour optimiser les performances. Le travail présenté dans cette thèse explore d'abord l'effet de réglage de la stœchiométrie de la double pérovskite. Étant donné que les lacunes de bromure sont connues pour être présentes dans la structure provoquant des défauts, l'objectif était de corriger ce problème en incorporant des bromures supplémentaires en utilisant un excès de CsBr dans le précurseur. La réponse photovoltaïque améliorée avec un excès de CsBr a été expliquée par la passivation des lacunes de bromure de surface, comme suggéré par les mesures de RMN à l'état solide et de photoluminescence, ainsi que par les grains des cristaux plus gros. Pour améliorer ces résultats, un autre sel de cation plus petit, c'est-à-dire LiBr, a été testé en tant qu'additif à la double pérovskite. Une nette amélioration des performances du dispositif a été observée, où un traitement de diffusion de LiBr, par opposition à un additif de solution précurseur, a été jugé optimal. Les mesures de RMN à l'état solide du ^{7}Li ont révélé un environnement distinct, probablement correspondant à des ions Li^{+} aux positions interstitielles accompagnant les anions bromure vers les sites vacants, tandis que la spectroscopie de photovoltage modulée en intensité donne des durées de vie de recombinaison de charge plus longues. Ces découvertes ouvrent la voie à l'exploration et à l'optimisation des traitements d'atténuation des défauts dans les doubles pérovskites.

Table of Contents

Chapter 1: An Introduction to Perovskites..34

1.0 General background, renewable energies and photovoltaic technologies..................35

1.1 Definition and properties of 3D, 2D and quasi 2D halide perovskites........................38

1.1.1 Optoelectronically-active cations in layered halide perovskites...............................42

1.2 Photovoltaic device structures with perovskite active layers.......................................45

1.3 Toxicity concerns of lead-based perovskites and lead-free structures.........................46

1.3.1 $Cs_2AgBiBr_6$ Lead-free Double Perovskites..47

1.4 Motivation for the research work...50

1.5 References..54

Chapter 2: Experimental Procedures 60

2.0 Preparatory protocols...61

2.0.1 Lead-based perovskites (Chapters 3 and 4)...61

2.0.2 Lead-free based perovskites (Chapters 5 and 6)..66

2.1 Physical Characterization..67

2.1.1 X-ray diffraction measurements 67

2.2 Microscopy techniques...69

2.2.1 Transmission and Scanning electron Microscopy..69

2.2.2 Conductive- Atomic Force Microscopy 69

2.3 Spectroscopy techniques..70

2.3.1 UV-Visible absorption spectroscopy...70

2.3.2 Steady-state emission spectroscopy (Photoluminescence) 71

2.3.3 Intensity-Modulated Photovoltage Spectroscopy 72

2.3.4 Fourier transformed infrared spectroscopy 73

2.3.5 Solid-state nuclear magnetic resonance...75

2.3.6 Photoemission and X-ray spectroscopy..76

2.4 Solar Cell Characterization..77

2.4.1 *JV* curves...77

2.4.2 Incident photon-to-current efficiency 78

2.4.3 Transient photocurrent measurement...79

Appendix 1: Full synthetic details for NDI-based organic cations 80

Appendix 2: Full synthetic details for BDT-based organic cations 82

Chapter 3: NDI Layered Lead-Halide Perovskites **92**

3.1 Introduction 93

3.2 Results and Discussion 94

3.2.1 The solution-based approach 95

3.2.2 The two-layer method 99

3.2.3 The PbI_2 film dip-coating method 101

3.2.4 The Solvent evaporation and solvent transport/antisolvent diffusion methods ... 103

3.3 Conclusion 107

3.4 References 109

Chapter 4: BDT Layered Lead-Halide Perovskites **111**

4.1 Introduction 112

4.2 Results and Discussion 113

4.2.1 Benzodithiophene incorporation in layered perovskites 113

4.2.2 Quasi-layered photovoltaic devices 119

4.2.3 Origin of the device performance difference 131

4.2.4 Device stability comparison 141

4.3 Conclusions 142

4.4 References 144

Chapter 5: Homogeneous Bromide Treatment on Lead-free $Cs_2AgBiBr_6$ Double Perovskites **148**

5.1 Introduction 149

5.2 Sample preparation and identification 150

5.3 Results and Discussion 150

5.3.1 Material's characterization 150

5.3.2 Optoelectronic properties 153

5.3.3 Photovoltaic devices 155

5.3.4 Further spectroscopic analysis 160

5.4 Conclusions 166

5.5 References 168

Chapter 6: Heterogeneous Bromide Treatments on Lead-free $Cs_2AgBiBr_6$ Double Perovskites **170**

6.1 Introduction 171

6.2 Sample preparation and identification 172
6.3 Results and discussion 173
6.3.1 Material's characterization 173
6.3.2 Photovoltaic device results and characterization 177
6.3.3 Further spectroscopy characterization experiments 192
6.4 Conclusions 198
6.5 References 200
Chapter 7: Overview and Outlook 202
Curriculum Vitae 208

List of Figures

Chapter 1

Figure 1.1. Three-dimensional general halide perovskite structure with the ABX_3 crystal definition 38

Figure 1.2. Two-dimensional, quasi two-dimensional and three-dimensional halide perovskite structures (a) two-dimensional halide perovskite with 1 octahedral layer (n=1), (b) quasi two-dimensional structures with 2 layers (n=2) and (c) three-dimensional bulk halide perovskite structure. 40

Figure 1.3. Reported octahedral layer distortion from organic molecular cation insertion (a) Cation penetration into the octahedral layers, (b) Pb-X-Pb bond angle torsion and (c) in- and out-of-plane distortions 44

Figure 1.4. Common perovskite photovoltaic device configurations, namely n-i-p structures (left) and p-i-n structures (right). 46

Figure 1.5. Schematic of the unit cell of a $Cs_2AgBiBr_6$ double perovskite structure 47

Figure 2.1. Setup of powder synthesis methods tested, namely (a) solvent evaporation and (b) solvent transport/antisolvent diffusion. 64

Figure 2.2. Scheme of the diffraction of X-rays (red lines) by a crystalline lattice of atoms (orange spheres). The difference in the optical path between the two beams reflected by two crystalline planes separated by a distance d is $2d\ sin\theta$. Therefore, constructive interferences between the two beams are obtained when Bragg's law is validated, that is, when $2d\ sin\theta = n\,\lambda$. 68

Figure 2.3. Scheme of the IMVS setup including the detail of the phase shift in between the illumination intensity and the V_{OC} response (a). Example of the IMVS response highlighting the characteristic point ω_{MAX} from which τ_{rec} is calculated (b). 72

Figure 2.4. Block scheme of a FT-IR instrument and of the conversion from the interferogram to the IR spectrum applying Fourier transform 74

Figure A1.1. ^1H NMR of NDI-dibutylammonium, NDI-diethylammonium, NDI-monoammonium 81

Figure A2.1. ^{1}H NMR spectrum of **E1** 83
Figure A2.2. ^{1}H NMR spectrum of E2 (top) and closer view of the area of interest (bottom).84
Figure A2.3. ^{1}H NMR spectrum of **B1** 86
Figure A2.4. ^{1}H NMR spectrum of **B2** 87
Figure A2.5. ^{1}H NMR spectrum of **H1** 88
Figure A2.6. ^{1}H NMR spectrum of **H2** 89

Chapter 3

Figure 3.1. NDI molecular variants: (a) NDI ethyl ammonium iodide (NDI-E), (b) NDI diethyl ammonium iodide (NDI-diE) and (c) NDI dibutyl ammonium iodide (NDI-diB). 94
Figure 3.2. NDI-based chromophore characterization. (a) X-ray diffraction patterns, (b) UV-vis absorption and (c) photoluminescence spectra (375 nm excitation). 95
Figure 3.3. Chromophore molecular cation incorporation methods studied towards 2D halide perovskite synthesis. (a) Solution-based method, (b) two-layer method, (c) PbI_2 film dip-coating into a chromophore solution, (d) solvent evaporation and (e) solvent transport/antisolvent diffusion. 97
Figure 3.4. (a) XRD patterns, (b) UV-vis absorption and (c) photoluminescence spectra (d) including a zoom-in, for PEA_2PbI_4 thin films prepared by the solution-based approach and varying NDI-E contents from 0 to 67 mol% (375 nm excitation). 98
Figure 3.5. GIWAXS data for all prepared films with (PEA and/or NDI-E)$_2$PbI$_4$ 99
Figure 3.6. Solutions prepared with the two-layer method for PEA_2PbI_4 (0% NDI-E) and PEA_2PbI_4 with 3-67 mol% NDI-E in the system. 100
Figure 3.7. NDI-E incorporation into PEA_2PbI_4 for samples with 0-67 mol% NDI-E content with the two-layer method. (a) XRD patterns of NDI-E containing samples in addition to the PEAI precursor, (b) UV-vis absorption spectra, (c) photoluminescence spectra and (d) zoom-in photoluminescence spectra of samples with 8-67% NDI-E (350 nm excitation). 101
Figure 3.8. X-ray diffraction pattern of the film resulting from dip coating PbI_2 into an NDI-E solution in IPA, P1 and P2 represent new phases not ascribed to either precursor and could possibly represent a new 2D halide perovskite phase. 102

Figure 3.9. NDI-E incorporation attempt into Pb-I octahedral layers with the solvent transport/antisolvent diffusion method. (a) UV-visible absorption spectrum, (b) photoluminescence (475 nm excitation), (c) SEM image and (d) X-ray diffraction pattern of the drop cast redissolved powder in DMF, P1 represents a new phase not ascribed to either precursor and could possibly represent a new 2D halide perovskite phase. 103

Figure 3.10. 2D halide perovskite interlayer spacing determination from synchrotron powder X-ray diffraction data for the powder resulting from the solvent transport/antisolvent diffusion method on a solution of NDI-E and PbI_2. (a) Chem3D software simulation of NDI-E molecular length (13.5 Å), (b) synchrotron powder X-ray diffraction data for sample temperatures ramped from 300 to 100 K and back, and interlayer spacing corresponding to the 1.27° (2θ) first diffraction peak. 105

Figure 3.11. NDI-E anchoring at the corners of Pb-I octahedra: front-view and side-view, with the NDI-E groups oriented perpendicular to the inorganic layers (models generated with the VESTA software[18]). 105

Figure 3.12. UV-vis spectra (a,d), PL spectra (b,e) (350 nm excitation) and XRD spectra (c,f) for NDI di-E and NDI-diB incorporation attempts into layered lead halide perovskites, respectively. 107

Chapter 4

Figure 4.1. (a) Benzodithiophene-based ligand chemical structures where m represents the number of carbon atoms in the alkyl chain between the aminium cation and the conjugated BDT core. (b) X-ray diffraction patterns of $(BDT\text{-}Cm)_2PbI_4$ thin films and (c) corresponding UV-vis absorption and photoluminescence (PL) spectra. Note that PL is only observed for $(BDT\text{-}C6)_2PbI_4$. (d) GIWAXS patterns of $(BDT\text{-}Cm)_2PbI_4$ thin films. (e) shows a schematic of a proposed layer arrangement of the $(BDT\text{-}C6)_2PbI_4$ perovskite (drawn with the Vesta software[22]). (f) J-V curve for a $(BDT\text{-}C6)_2PbI_4$ -based photovoltaic device under 1-sun illumination (energy levels of the device in the inset).* For $BDT\text{-}C2_2PbI_4$, the formula denotes the stoichiometry of the fabrication solution and not the final crystal, which is not formed. 114

Figure 4.2. UV-vis absorption spectra of BDT-C2, BDT-C4 and BDT-C6 drop-cast films..... 115

Figure 4.3. UV-vis absorption spectrum and photoluminescence of a thin film of $(PEA)_2PbI_4$ prepared on a glass substrate. 116

Figure 4.4. a) X-ray diffraction patterns for $(BDT\text{-}C4)_2PbI_4$ thin films annealed at 100, 110, 120, 130, 150 and 180°C b) corresponding UV-vis spectra and c) photoluminescence spectra. ... 117

Figure 4.5. Tauc plots for (a) $(BDT\text{-}C6)_2PbI_4$ (simply called BDT_2PbI_4 here) and (b) PEA_2PbI_4 and UPS linear scale plots with a fitting of the VBM for (c) BDT_2PbI_4 and PEA_2PbI_4 (d) UPS linear scale plots with a fitting of the secondary electron cut-off for BDT_2PbI_4 and PEA_2PbI_4 as well as (e) the corresponding energy levels (see the corresponding method of calculation in the experimental section of **Chapter 2**). 118

Figure 4.6. Schematic representation of the quasi-layered perovskite fabrication steps (a) spin-coating of precursor solution, (b) antisolvent dripping, and (c) thermal annealing (see experimental section in **Chapter 2** for further details). 120

Figure 4.7. X-ray diffraction patterns of thin films of the quasi-layered perovskites studied in this work, as prepared on FTO(*) substrates, for the (a) MBDT series and (b) MPEA series. 121

Figure 4.8. Investigating the crystalline distribution of mixed N-number perovskites with high resolution transmission electron microscopy (HRTEM) of (a) N20 MPEA, (b) N100 MPEA, (c) N20 MBDT, and (d) N100 MBDT. The red rectangles represent the n=∞ regions analyzed in the Fourier transform images, whereas the yellow rectangles similarly represent the layered perovskite regions analyzed in the Fourier transform. 121

Figure 4.9. TEM image and the corresponding EDX maps (for the element indicated) of a portion of an N20 MBDT film removed from a substrate. 122

Figure 4.10. Steady-state photoluminescence of (a) N20 & N100 MBDT and (b) N20 & N100 MPEA and the $MAPbI_3$ reference shown in both cases. The excitation wavelength was 450 nm. 122

Figure 4.11. UV-visible absorption spectra of the QLLHPs N20 MBDT, N20 MPEA, N100 MBDT and N100 MPEA prepared on glass substrates. 123

Figure 4.12. QLLHP band gap energy determination via Tauc plot analysis for (a) N20 MBDT, (b) N20 MPEA, (c) N100 MBDT, and (d) N100 MPEA. 123

Figure 4.13. UPS linear scale plots with a fitting of the VBM for (a) the N20 series, (b) the N100 series, and (c) $MAPbI_3$. 124

Figure 4.14. UPS linear scale plots with a fitting of the secondary electron cut-off for (a) the N20 series, (b) the N100 series, and (c) $MAPbI_3$. 125

Figure 4.15. Summary of calculated VBM, work function (W_F) and ionization energy (I_E) values for $MAPbI_3$, the N100 series and the N20 series. 126

Figure 4.16. Quasi-layered devices. (a) Energy level and band gap alignment of the four QLLHP materials tested (inside the dashed box) with respect to the hole-transporting and electron-transporting contacts used. (b) Champion cell J-V curves obtained with a 0.09 cm^2 active area and AM 1.5G illumination. (c) Box plots with results of 20 devices for each QLLHP material and (d) device incident photon-to-current efficiency (IPCE) and integrated currents with respect to illumination wavelength. 127

Figure 4.17. (a) *Jsc*, (b) *Voc* and (c) FF distributions for 20 devices of N20 MBDT, N20 MPEA, N100 MBDT and N100 MPEA devices (reverse curves) 128

Figure 4.18. Forward and reverse J-V curves for the N20 MBDT, N20 MPEA, N100 MBDT and N100 MPEA devices 129

Figure 4.19. (a) Top and (b) cross-sectional SEM images of N20 MBDT and (c) top and (d) cross-sectional SEM images of N20 MPEA layers solution-processed onto FTO substrates. Note cross-sectional images show films capped with an Au overlayer (to facilitate measurement). 131

Figure 4.20. (a) Top and (b) cross-sectional SEM images of N100 MBDT and (c) top and (d) cross-sectional SEM images of N100 MPEA layers solution-processed onto FTO substrates. Note cross-sectional images show films capped with an Au overlayer (to facilitate measurement). 133

Figure 4.21. Normalized device photocurrent as a function of time after a 5 ns pulse (550 nm wavelength) shown in the log scale over the long time frame and a linear scale for the short time regime (inset). 135

Figure 4.22. (Left) Atomic force microscopy (AFM) and (right) conductive atomic force microscopy images of (a) N100MBDT and (b) N100 MPEA 137

Figure 4.23. (a) UV photoelectron spectroscopy measurements of the perovskite thin films deposited on FTO substrates. The inset shows a schematic of hypothesized undercoordinated Pb passivation via vI• – S (thiophene) Lewis adduct formation (b) ATR-FTIR data for a BDT drop cast film, BDT_2PbI_4, N20 MBDT, N100 MBDT and $MAPbI_3$ reference thin films with a highlight of the C-S stretch peak shift, the asterisks represent the peak positions. 138

Figure 4.24. Narrow-scan XPS Pb 4f spectra of the QLLHP samples N20 MPEA, N20 MBDT, N100 MPEA, N100 MBDT. 139

Figure 4.25. QLLHP stability and moisture resistance measurements. (a) Normalized PCE of the N100-based devices (and an $n = \infty$ control) with respect to time in a dry N_2 environment under constant one-sun illumination (open circuit conditions) (b) XRD patterns of bare QLLHP active layers exposed to 75% RH air (25°C) for different times. (c) water contact angle measurements for bare films of N100 MPEA (top) and N100 MBDT (bottom). 141

Figure 4.26. Normalized (a) Jsc (b) Voc and (c) FF performance parameters for constant one-sun illumination stability studies on N100 MPEA, N100 MBDT and $MAPbI_3$ reference devices. 142

Chapter 5

Figure 5.1. (a) X-ray diffraction patterns for the $Cs_2AgBiBr_6$ reference samples and samples with progressive addition of CsBr excess (b) GIWAXS patterns for the $Cs_2AgBiBr_6$ reference and 10% excess CsBr thin films. 151

Figure 5.2. Scanning electron microscopy (SEM) images of $Cs_2AgBiBr_6$ thin films and the films with 5, 7.5, 10, 12.5 and 15% CsBr in excess. 153

Figure 5.3. (a) Spectral absorptance for the $Cs_2AgBiBr_6$ reference sample and films with 5 to 15% CsBr in excess (b) Corresponding steady-state photoluminescence spectra for the $Cs_2AgBiBr_6$ reference film and samples with 5, 10 and 15% CsBr in excess 154

Figure 5.4. (a) Space-charge-limited current (SCLC) curves for electron-only devices with a $Cs_2AgBiBr_6$ reference layer and one with a 5% excess CsBr (b) corresponding SCLC device schematic. with a sample cross-sectional SEM image of the 5% excess CsBr device. The electron-only devices are namely comprised of a fluorine-doped tin oxide (FTO) substrate, a compact TiO_2 ($cTiO_2$) electron transport underlayer, the double perovskite under study, a PCBM electron transport overlayer and a silver electrode. While the trap-filled limit voltages (V_{TFL}) for both the reference and 5% excess CsBr samples are similar, indicating a comparable density of electron traps, the calculated electron mobility in the 5% excess CsBr sample does increase slightly to 1.64 x 10^{-4} cm^2/ Vs compared to 1.40 x 10^{-4} cm^2/ Vs for the $Cs_2AgBiBr_6$ reference sample. We note that while we expect an overall decrease in the density of charge carrier traps, following the results of the PL spectra, one may conclude that the excess CsBr mainly leads to a reduction in hole traps in the material, given the comparable electron trap densities observed on **Figure 5.4a**...154

Figure 5.5. (a) Schematic diagram of the implemented n-i-p photovoltaic device structure and (b) resulting photovoltaic forward and reverse scan curves from the best devices with and without LiTFSI-treated $mpTiO_2$ electron transport layer...156

Figure 5.6. Photovoltaic results (reverse scan) for LiTFSI-treated and untreated (a) $mpTiO_2$ layers under the $Cs_2AgBiBr_6$ active layer (a) Power conversion efficiencies (b) Short-circuit current densities (c) Open circuit voltages and (d) fill factors..157

Figure 5.7. Photovoltaic device box plots depicting (a) power conversion efficiencies (b) short-circuit current densities (c) open circuit voltages and (d) fill factors for the $Cs_2AgBiBr_6$ reference and 5, 10 and 15% CsBr excess devices...158

Figure 5.8. Photovoltaic J-V curves for the best performing $Cs_2AgBiBr_6$ reference device and the 10% CsBr device...159

Figure 5.9. (a) Secondary electron cut-off fittings and (b) valence band maximum fittings for the $Cs_2AgBiBr_6$ double perovskite film as well as the double perovskite with several different CsBr excess amounts 160

Figure 5.10. (a) Indirect bandgap Tauc plot analysis for the $Cs_2AgBiBr_6$ reference sample in addition to different CsBr excess loadings and (b) resulting calculated energy levels..........161

Figure 5.11. ^{133}Cs solid state NMR spectra for CsBr, $Cs_2AgBiBr_6$ and double perovskite samples with a 10% and 17.5% CsBr excess. 162

Figure 5.12. (a) Proposed schematic of the suggested Br vacancy defects on the $Cs_2AgBiBr_6$ reference material based on experimental observations and (b) the CsBr terminated surface on the 10% CsBr excess sample providing a healing treatment for these defects.......................163

Figure 5.13. Angle-dependent X-ray photoelectron spectroscopy (XPS) of (a) $Cs_2AgBiBr_6$ and (b) the double perovskite with 10% CsBr in excess tracking the Cs, Ag, Bi and Br content from the surface to about the first 10 nm of the films. 165

Chapter 6

Figure 6.1. (a) X-ray diffraction patterns of the $Cs_2AgBiBr_6$ reference sample, as well as with 1 to 6% LiBr addition, and a diffraction pattern for a $Cs_2AgBiBr_6$ sample with a LiBr diffusion post-treatment (b) close-up image of the (004) XRD peaks for the aforementioned samples 174

Figure 6.2. Steady-state photoluminescence measurements of the $Cs_2AgBiBr_6$ reference thin film and films with a 1, 3 and 5% LiBr loading. 176

Figure 6.3. SEM images of the reference $Cs_2AgBiBr_6$ thin film and films fabricated with method 1, *i.e.* LiBr additives in the double perovskite precursor solution (1-6%, with respect to CsBr) and lastly a $Cs_2AgBiBr_6$ thin film after an LiBr diffusion post-treatment (Method 2)........ 177

Figure 6.4. (a) Power conversion efficiencies, (b) short-circuit current densities, (c) open-circuit voltages and (d) fill factors for photovoltaic devices made from the reference $Cs_2AgBiBr_6$ perovskite active layer and double perovskites prepared with a 1 to 6% LiBr additive loading (Method 1). 178

Figure 6.5. Current density (J)-voltage (V) curves for the champion $Cs_2AgBiBr_6$ and 3% LiBr photovoltaic devices. 179

Figure 6.6. (a) Power conversion efficiencies, (b) short-circuit current densities, (c) open-circuit voltages and (d) fill factors for photovoltaic devices made from the reference $Cs_2AgBiBr_6$ perovskite active layer and double perovskites immersed for 10 minutes in LiBr solutions of various concentrations (Method 2). 180

Figure 6.7. (a) Power conversion efficiencies, (b) short-circuit current densities, (c) open-circuit voltages and (d) fill factors for photovoltaic devices made from the reference $Cs_2AgBiBr_6$ perovskite active layer and double perovskites immersed for 1, 5 and 10 minutes in LiBr solutions (10 mg/ml in isopropanol) (Method 2). 182

Figure 6.8. Current-density(J)-voltage(V) curves for the champion $Cs_2AgBiBr_6$ and the 5 and 10 minute LiBr diffusion photovoltaic devices. 183

Figure 6.9. Forward and reverse scan current-density(J)-voltage(V) curves for the champion $Cs_2AgBiBr_6$ device, the 3% LiBr device fabricated through Method 1 and the optimized LiBr diffusion device fabricated through Method 2. 184

Figure 6.10. Nyquist plots (real, Re, and imaginary, - Im, components) of intensity-modulated photovoltage spectroscopy measurements on a $Cs_2AgBiBr_6$ reference device and a device prepared with Method 2 (LiBr diffusion). 185

Figure 6.11. (a) Power conversion efficiencies, (b) short-circuit current densities, (c) open-circuit voltages and (d) fill factors for photovoltaic devices made from the reference $Cs_2AgBiBr_6$ perovskite active layer and double perovskites with MABr additive in concentrations ranging from (1-15 % with respect to CsBr content). 187

Figure 6.12. (a) Power conversion efficiencies, (b) short-circuit current densities, (c) open-circuit voltages and (d) fill factors for photovoltaic devices made from the reference $Cs_2AgBiBr_6$ perovskite active layer and double perovskites after MABr diffusion after 1, 5 and 10 minutes. 188

Figure 6.13. (a) Power conversion efficiencies, (b) short-circuit current densities, (c) open-circuit voltages and (d) fill factors for photovoltaic devices made from the reference $Cs_2AgBiBr_6$ perovskite active layer and double perovskites annealed under a bromine vapor environment. 189

Figure 6.14. (a) X-ray diffraction patterns and (b) steady-state photoluminescence spectra for $Cs_2AgBiBr_6$ reference thin films and films treated with LiSCN additives. 190

Figure 6.15. SEM images of the reference $Cs_2AgBiBr_6$ thin film and films fabricated with LiSCN additives in the double perovskite precursor solution (1-10%, with respect to CsBr). 191

Figure 6.16. (a) Power conversion efficiencies, (b) short-circuit current densities, (c) open-circuit voltages and (d) fill factors for photovoltaic devices made from the reference $Cs_2AgBiBr_6$ perovskite active layer and double perovskites treated with a LiSCN additive in molar concentrations of 1-10% with respect to CsBr. 191

Figure 6.17. Linear fits of the (a) secondary electron cut-off and (b) the valence band maxima for the reference $Cs_2AgBiBr_6$ perovskite and the double perovskite with LiBr as an additive in several amounts as well as with an LiBr diffusion treatment (LiBr Dif.) 192

Figure 6.18. (a) Spectral absorptance and corresponding Tauc plots (b) for the $Cs_2AgBiBr_6$ reference thin film and films treated with LiBr via the additive or diffusion method. 193

Figure 6.19. Double perovskite calculated energy levels following various LiBr treatments and corresponding energy band alignments with n-i-p device electron and hole collecting layers. 194

Figure 6.20. Depth-profile X-ray photoelectron spectroscopy of (a) $Cs_2AgBiBr_6$ and the double perovskite with (b) a 3% LiBr additive treatment and (c) an LiBr diffusion treatment, tracking the Cs, Ag, Bi and Br content from the surface to about the first 10 nm of the films. 195

Figure 6.21. ^{7}Li solid state NMR spectra for LiBr, and the $Cs_2AgBiBr_6$ double perovskite samples with a 3% and 7.5% LiBr additives as well as samples submitted to LiBr diffusion treatments 197

Chapter 7

Figure 7.1. (a) Comparison and images of $Cs_2AgBiBr_6$ active layer reference photovoltaic devices with 100 nm and 8 nm Au electrodes (b) optimized device image and transmittance measurements 205

List of Tables

Chapter 1

Table 1.1 Reported $Cs_2AgBiBr_6$ photovoltaic device structures and efficiencies 49

Chapter 3

Table 3.1. Stoichiometries for partial and full NDI-E incorporation attempts into 2D perovskites 96

Chapter 4

Table 4.1. XRD plane and corresponding d-spacing calculation for $(BDT\text{-}C6)_2PbI_4$ 114

Table 4.2. Comparative numerical photovoltaic results for QLLHP-based solar cells (reverse scans) 128

Table 4.3. Comparative numerical photovoltaic results for QLLHP-based solar cells in the reverse (-r) and forward (-f) scans 130

Table 4.4. Domain size for N20 MBDT and MPEA series..132

Table 4.5. Domain size for N100 MBDT and MPEA series..134

Table 4.6. Extracted TPC exponential decay times (τ_c) for QLLHP-based devices (standard errors given in parenthesis)...136

Chapter 5

Table 5.1. X-ray diffraction peak intensities for the (442) (reference), (004) and (002) peaks and the (004) and (002) peak intensity ratios versus the (442) peak intensity for the $Cs_2AgBiBr_6$ and CsBr excess samples..152

Table 5.2. Comparative numerical photovoltaic results for LiTFSI treated and untreated mpTiO$_2$ layers under the $Cs_2AgBiBr_6$ active layer in the forward (f) and reverse (r) scans ..156

Table 5.3. Comparative numerical photovoltaic results (reverse scans) for the reference $Cs_2AgBiBr_6$-based devices and those with 5, 10 and 15% CsBr excess 159

Table 5.4. ^{133}Cs solid state NMR results for the reference $Cs_2AgBiBr_6$-based devices and those with 10 and 17.5% CsBr excess...164

Table 5.5. Angle-dependent XPS Cs atomic concentration results for the $Cs_2AgBiBr_6$ reference sample and the double perovskite sample with 10% CsBr in excess, distributed along the approximately first 10 nm of the sample..166

Chapter 6

Table 6.1. Reported ionic radii and calculated tolerance factors for $Cs_2AgBiBr_6$ and $Li_2AgBiBr_6$ perovskite structures 175

Table 6.2. Comparative numerical photovoltaic results (average and champion) for the reference photovoltaic devices with a $Cs_2AgBiBr_6$ active layer and devices with 1-6% LiBr additive loadings..179

Table 6.3. Comparative numerical photovoltaic results (average and champion) for the reference $Cs_2AgBiBr_6$ devices and devices with an LiBr diffusion post-treatment of the double perovskite with different LiBr solution concentrations...181

Table 6.4. Comparative numerical photovoltaic results (average and champion) for the reference $Cs_2AgBiBr_6$ devices and devices with an LiBr diffusion post-treatment (10 mg/ml) of the double perovskite with different LiBr diffusion times.. 182

Table 6.5. Comparative numerical photovoltaic results (average and champion) for the reference $Cs_2AgBiBr_6$ devices and devices with the double perovskite dipped in isopropanol (IPA) as a control.. 184

Table 6.6. Average recombination lifetime results of $Cs_2AgBiBr_6$ and LiBr-treated photovoltaic cells from intensity modulated photovoltage spectroscopy measurements 185

Table 6.7. Angle-dependent XPS Br 3d/Bi4f atomic percent ratios for the $Cs_2AgBiBr_6$ reference sample and a 3% LiBr additive treatment as well as a sample from the LiBr diffusion treatment distributed along the approximately first 10 nm of the sample 196

Chapter 7

Table 7.1. Semi-transparent solar cell technologies 206

List of Schemes

Chapter 1

Scheme 1.1. Most relevant photovoltaic technologies, properties, cost categories and highest reported power conversion efficiencies (PCE) in 2021. Adapted from:[4,5] 36

Chapter 2

Scheme A1.1. NDI-diB, NDI-diE and NDI-E amino synthesis 80

Scheme A2.1. Synthetic routes for the preparation of **BDT-C2** 82

Scheme A2.2. Synthetic routes for the preparation of **BDT-C4** and **BDT-C6** [2] 82

Chapter 5

Scheme 5.1. $Cs_2AgBiBr_6$ fabrication steps with the solution-processing method with isopropanol (IPA) antisolvent. In addition to the control sample, samples with 5, 7.5, 10, 12.5 and 15 mol% CsBr excess (with respect to the stoichiometric CsBr content) were prepared by adding the corresponding CsBr excess amount to the precursor solution in DMSO solvent. 150

Chapter 6

Scheme 6.1. Preparation method for introducing the LiBr additive into the perovskite precursor solution, following the solution-based approach 172

Scheme 6.2. LiBr diffusion and thermal annealing post-treatment on the $Cs_2AgBiBr_6$ thin film 173

Scheme 6.3. Proposed bromide vacancy healing mechanism via the LiBr diffusion method (Method 2). 198

List of Abbreviations

ATR: attenuated total reflectance

BDT: Benzo[1,2-*b*:4,5-*b′*]dithiophene

BTBT: benzothienobenzothiophene

c-AFM: conductive atomic force microscopy

c-TiO_2: Compact TiO_2

DPK: Double perovskite

EDX: Energy-dispersive X-ray spectroscopy

FF: Fill factor

FTIR: Fourier-transform infrared spectroscopy

FTO: Fluorine-doped tin oxide

FWHM: Full width at half maximum

IMVS: Intensity modulated photovoltage spectroscopy

IPCE: Incident photon-to-current efficiency

J_{sc}: Short-circuit photocurrent (mA/cm^2)

LLHPs: Layered lead halide perovskites

mp-TiO_2: mesoporous TiO_2

NDI: Naphthalene diimide

PCE: Power conversion efficiency

PDI: Perylene diimide

PEAI: Phenylethylammonium iodide

PL: Photoluminescence

PV: Photovoltaic

QLLHPs: Quasi layered lead halide perovskites

SCLC : Space-charge layer current

SEM: Scanning electron microscopy

ssNMR: solid-state Nuclear Magnetic Resonance

TEM: Transmission electron microscopy

TPC: Transient photocurrent

UPS: Ultraviolet photoelectron spectroscopy

VBM: Valence band maximum

V_{TFL}: trap-filled limit voltages

V_{OC}: Open circuit potential (V)

XPS: X-ray photoelectron spectroscopy

XRD: X-ray diffraction

Chapter 1

An Introduction to Perovskites

Toxicity and stability bottlenecks, alternatives and aims

This chapter provides a general introduction to the field of renewable energies, with an emphasis on solar energy harvesting. Different photovoltaic technologies are presented, while the advantages and thus interest in perovskite photovoltaics is explained. The definition and optoelectronic properties of 3D perovskites are established, while the stability bottlenecks and hence motivation for 2D perovskite structures is presented. Moreover, the motivation for and reported works on the incorporation of optoelectronically-active large organic cations is summarized. Different photovoltaic device structures implementing perovskite active layers are discussed, while the toxicity of lead-based perovskites is acknowledged. Therefore, alternative lead-free perovskite structures, *i.e.* double perovskites, are introduced, and compared to other lead-free perovskite structures. Lastly, the benefits, bottlenecks and reported photovoltaic devices of $Cs_2AgBiBr_6$ double perovskite structures in particular are reviewed.

A brief section of this chapter is in part built from the introductory material to the following publication:

''Benzodithiophene-based Spacers for Layered and Quasi-layered Lead Halide Perovskite Solar Cells''

B. Primera Darwich, N. Guijarro, H.-H. Cho, L. Yao, L. Monnier, P. Schouwink, M. Mensi, J.-H. Yum, K. Sivula, *ChemSusChem* **2021**, *14*, 3001.

1.0 General background, renewable energies and photovoltaic technologies

The demand for more efficient and economical energy harvesting methods to accommodate increasing population levels in addition to objectives on reduced greenhouse gas emissions from primarily fossil fuel-based economies have over the recent years motivated research in the fields of renewable energy conversion and storage. All countries worldwide, from undeveloped to developed have a great common necessity brought about by their increasing energy demands. In developing countries, power outages remain a serious burden to daily operations in crucial facilities such as hospitals as well as at homes and markets for day-to-day food and pharmaceuticals refrigeration. In more developed nations, not only these but also financial and industrial facilities require electricity for their fast-paced functioning. Interactions between all these nations for commercial exchange, transport of goods, exchange of knowledge and information and travel in addition to efforts to provide electricity to individuals equally worldwide furthermore require once again a plentiful supply of energy. Nonetheless, as per the European Climate law for instance, by 2050 greenhouse gas emissions should have achieved net zero while they should have been already reduced by 55% with respect to 1990 emissions by the year 2030, following the Fit for 55 package.[1] By the same year, 40% of the European Union's energy should be supplied by renewable energy sources.[2] Such objectives result from the evidently reduced oil and natural gas reserves and increased concerning greenhouse gas emissions, which call for efficient renewable energy harvesting.

The principal renewable energy sources include wind, solar, geothermal, hydropower as well as biomass. Of these, solar energy demonstrates unparalleled potential given its significantly greater availability, 89 000 TW, while the current world energy demand stands at only around 15 TW.[3] A straightforward method to harvest solar energy is to convert it directly into electricity with a photovoltaic device. Photovoltaic technologies range from silicon-based to organic semiconductors, III-V semiconductors, chalcogenides, quantum dots, dye-sensitized solar cells as well as hybrid organic-inorganic or inorganic lead halide perovskites.[4] A summary of the most relevant photovoltaic technologies alongside their properties, cost categories as well as highest-reported photovoltaic efficiencies are provided on **Scheme 1.1** based on reports from Mohammed *et al.* and the National Renewable Energy Laboratory.[4,5]

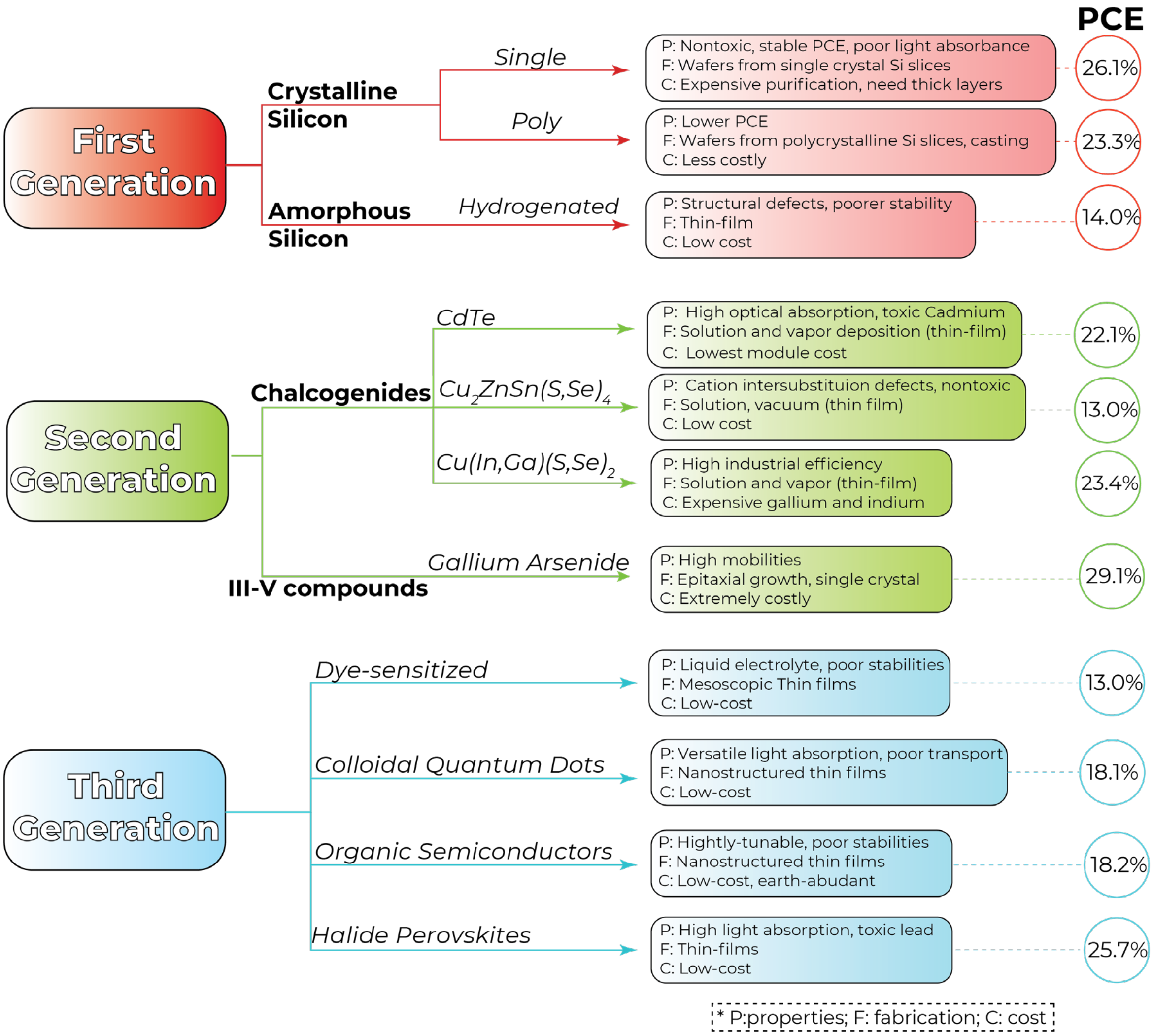
PCE
First Generation
Crystalline Silicon
Single
Poly
Amorphous Silicon
Hydrogenated
P: Nontoxic, stable PCE, poor light absorbance
F: Wafers from single crystal Si slices
C: Expensive purification, need thick layers
26.1%
P: Lower PCE
F: Wafers from polycrystalline Si slices, casting
C: Less costly
23.3%
P: Structural defects, poorer stability
F: Thin-film
C: Low cost
14.0%
Second Generation
Chalcogenides
CdTe
$Cu_2ZnSn(S,Se)_4$
$Cu(In,Ga)(S,Se)_2$
III-V compounds
Gallium Arsenide
P: High optical absorption, toxic Cadmium
F: Solution and vapor deposition (thin-film)
C: Lowest module cost
22.1%
P: Cation intersubstituion defects, nontoxic
F: Solution, vacuum (thin film)
C: Low cost
13.0%
P: High industrial efficiency
F: Solution and vapor (thin-film)
C: Expensive gallium and indium
23.4%
P: High mobilities
F: Epitaxial growth, single crystal
C: Extremely costly
29.1%
Third Generation
Dye-sensitized
Colloidal Quantum Dots
Organic Semiconductors
Halide Perovskites
P: Liquid electrolyte, poor stabilities
F: Mesoscopic Thin films
C: Low-cost
13.0%
P: Versatile light absorption, poor transport
F: Nanostructured thin films
C: Low-cost
18.1%
P: Hightly-tunable, poor stabilities
F: Nanostructured thin films
C: Low-cost, earth-abudant
18.2%
P: High light absorption, toxic lead
F: Thin-films
C: Low-cost
25.7%
* P:properties; F: fabrication; C: cost

Scheme 1.1. Most relevant photovoltaic technologies, properties, cost categories and highest reported power conversion efficiencies (PCE) in 2021. Adapted from:[4,5]

Namely, silicon-based photovoltaic devices are the most commonly used type (first-generation), of which there are crystalline and amorphous variants. The crystalline variants are better-performing, amongst which the single crystalline are better able to transport the photogenerated charge carriers than the polycrystalline silicon-based module variants. Both the single- and polycrystalline silicon module fabrication methods involve the preparation of silicon wafers, from the respective crystal grade precursors. While monocrystalline silicon solar panels are the most efficient of the silicon-based photovoltaic devices, there are expensive purification steps required in their fabrication. Moreover, a low-cost alternative to silicon solar panel fabrication is the use of amorphous hydrogenated silicon thin films, where a plasma-enhanced chemical vapor deposition approach, with mainly H_2 and SiH_4 precursors, is implemented for fabrication.[6] While silicon is very abundant and nontoxic, it does however have poor light-absorbing capabilities, due to its indirect bandgap, and therefore, thick silicon layers are required for enough light absorption of the best-performing configurations.

Second generation photovoltaic materials involve the chalcogenides and III-V compounds. Chalcogenide photoactive materials such as cadmium telluride and copper zinc tin sulfide/selenide (CZTS) would fall in this category, alongside copper indium gallium sulfide/selenide (CIGS). While cadmium telluride offers great optical absorption qualities, the toxicity of cadmium is a concern. Moreover, while CZTS materials are nontoxic and low-cost, they suffer from Cu and Zn cation inter-substitutional defects.[4] Lastly, gallium arsenide is the best-performing single-junction photovoltaic device, however the extremely costly epitaxial growth method from expensive gallium and toxic arsenic very much limit its commercial development.

Lastly, the third generation photovoltaic materials have the greatest prospects for commercial application from a processing and cost (solution-processable) perspective. Of these, dye-sensitized solar cells (DSSC) implement a dye-impregnated titanium dioxide layer encapsulated and topped with a liquid electrolyte and counter electrode.[7] DSSCs have however shown stability issues over the years which have limited their implementation. Colloidal quantum dot solar cells are also solution-processable where films of semiconductor nanocrystals of sizes smaller than 10 nm are fabricated. These types of solar cells can take advantage of the tunability of the quantum dot size to engineer the light-absorbing properties of the active layer. However, poor transport prevails in these devices and interfacial recombination is common.[8] Moreover, organic solar cells are extremely versatile, where light-absorbing donor and acceptor materials are combined to reach power conversion efficiencies as high as 18.2%. Normally, binary or ternary blends of materials are implemented.[9] Challenges in organic solar cells are the complex synthesis routes of donor and acceptor blend components as well as the interfacial recombination and long-term operational stability. Amongst the third generation photovoltaic materials, lead halide perovskites stand out due to their long charge carrier diffusion lengths and higher optical absorption for a given film thickness, meaning smaller travelling distances for charge carriers towards the charge collectors of a photovoltaic device thus hampering nonradiative recombination.[10] Furthermore, halide perovskites are reported to have benign grain boundaries, such that polycrystalline perovskite films with extensive grain boundaries behave like their single crystal equivalents,[10] however adequate film coverage on the surface and packing are essential for a well-functioning device. The solution-processability and low-temperature processing of halide perovskite materials facilitates their synthesis and sets them as interesting options for scale-up. The remainder of this introductory Chapter will focus on lead halide perovskites, their optoelectronic properties and variations.

1.1 Definition and properties of 3D, 2D and quasi 2D halide perovskites

Three-dimensional (3D) halide perovskites (**Figure 1.1**) consist of an A-site cation, a B-site cation, commonly lead or tin, and X-sites occupied by halide anions, such as iodides, chlorides and/or bromides, all assembled together following the general formula ABX_3.[9]

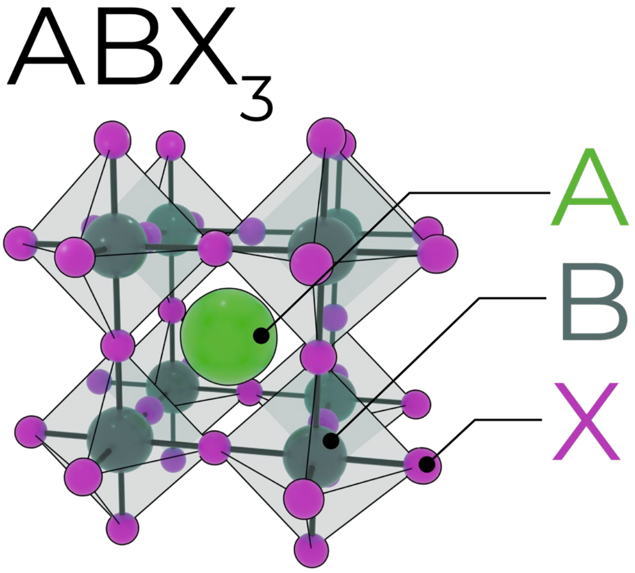

Figure 1.1. Three-dimensional general halide perovskite structure with the ABX_3 crystal definition

Three-dimensional halide perovskites can be further subdivided into two categories, inorganic halide perovskites and hybrid halide perovskites, where for inorganic halide perovskites the A-site cation located at the center of four surrounding octahedra, is an inorganic element such as caesium and in hybrid halide perovskites it is a small organic molecule such as methylammonium or formamidinium.[9]

The nature of the A-site cation is however limited by the Goldschmidt tolerance factor, for a given B-site cation and X anion:[11]

$$t = \frac{r_A + r_X}{\sqrt{2(r_B + r_X)}}$$

where r_A, r_B and r_X are the ionic radii of the A-site cation, B-site cation and X halide anions, respectively. With the tolerance factor, the stability of a given three-dimensional structure may be studied: for tolerance factor values of 1, a perfect cation fit results as well as a stable halide perovskite structure, for tolerance factor values lower than 1, the octahedral structure is distorted from tilting of the octahedra, while for tolerance factor values greater than 1, the A-site cation is too large to fit at the central cavity of corner-sharing octahedra; the general rule states that tolerance factor values greater than or equal to 0.8 and less than or equal to 1 will form a three-dimensional halide perovskite structure.[11]

Regarding the optoelectronic properties of halide perovskite materials and in particular their exciton binding energy, *i.e.* the binding energy of a bound electron-hole pair, the typical room-temperature exciton binding energy of three-dimensional organohalide perovskites has been reported to be approximately 10 meV.[12] This is rather small compared to the values reported, for instance, for organic semiconductors which are greater than 200 meV, hence requiring the formation of heterojunctions to effectively separate charges. This is not the case for three-dimensional (3D) halide perovskite materials as well as for Si, GaAs and CdTe semiconductors, which can effectively separate charges over one single material layer (*i.e.*, small exciton binding energies are a result of large dielectric constants).[12] Halide perovskite materials in general also exhibit photoluminescent properties at room temperature which reflects their defect tolerance, that is, the minimum deleterious impact of structural defects in the optoelectronic properties.[13] Moreover, lead-based halide perovskites have direct bandgaps with *p-p* orbital transitions, which are stronger than the *p-s* transitions observed in other systems; these are possible due to the lone-pair-filled *s* orbitals below the valence band maximum.[10] As a result, lead-based halide perovskites exhibit strong absorption coefficients that guarantee efficient light harvesting.[14]

While 3D halide perovskites are attractive due to their small bandgaps, *i.e.* high light absorption within the visible range, as well as low exciton binding energies, their stability under light and ambient conditions remains a principal concern to their deployment. In this regard, two-dimensional (2D) halide perovskites have become of interest, given their higher resistance to moisture-induced degradation.[15] In essence, the use of a larger organic cation to form the two dimensional halide perovskite structure induces a certain degree of hydrophobicity in the system, protecting it from or at least delaying the humidity-driven degradation process.[15] The reason for 2D halide perovskite formation can be understood with the tolerance factor rule, where cations resulting in t values greater than 1 will no longer fit within the octahedral cavities but would rather anchor at the halides which locate themselves at the shared corners of the octahedra (composed of the B and X components of the 3D halide perovskite analogue) and extend out in space, defining the distance between two octahedral layers (**Figure 1.2a**).

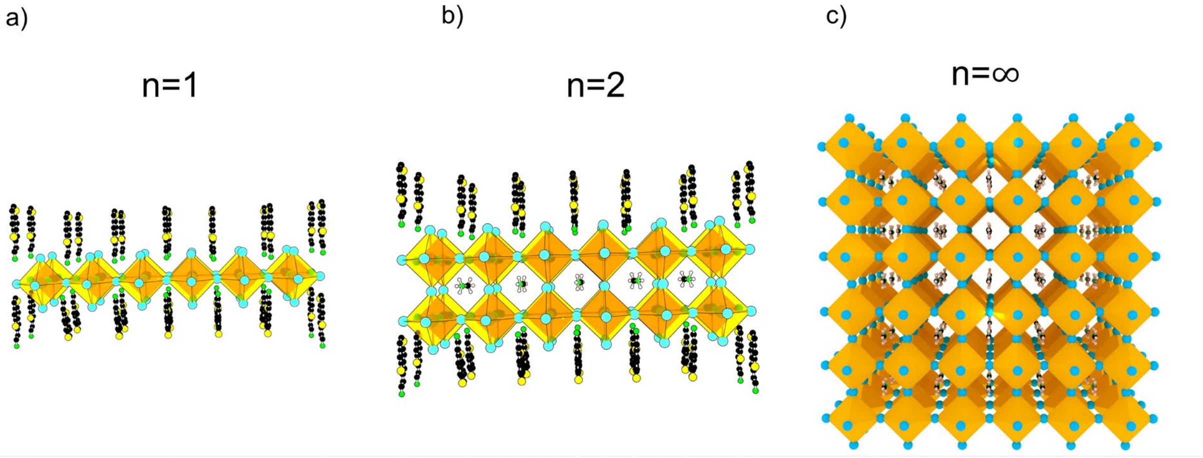

Figure 1.2. Two-dimensional, quasi two-dimensional and three-dimensional halide perovskite structures (a) two-dimensional halide perovskite with 1 octahedral layer (n=1), (b) quasi two-dimensional structures with 2 layers (n=2) and (c) three-dimensional bulk halide perovskite structure.

Nevertheless, a drawback of 2D halide perovskites is their high exciton binding energies, which are a result of the quantum confinement that enhances Coulombic interactions between electrons and holes in the few-nanometers-thick octahedral layers. Broadly speaking, excitons are confined in the inorganic layers due to the organic cation obstructions,[16] this creates an obstacle to photogenerated charge separation in a photovoltaic device. Such tightly bound excitons are defined as Frenkel excitons. Note that in 3D halide perovskites Wannier-Mott excitons are generated instead, these are free excitons whose Coulombic interactions are easily screened by an external electric field, thus easily separated.[16] Pathways towards improving the photovoltaic performance of 2D halide perovskites have nevertheless been suggested, such as proper alignment of the inorganic layers perpendicular to the substrate as well as a bulk-heterojunction-type assembly where the 2D halide perovskites are embedded in a second phase, whereby the interface will allow for efficient photogenerated charge extraction.[16]

In this regard, an optimum structure combining the lower exciton binding energy and higher stability of 3D and 2D halide perovskites, respectively, is highly desired, hence the quasi 2D halide perovskites (**Figure 1.2b**). Quasi 2D halide perovskites consist of adjacent octahedral layers, *i.e.* two layers or greater, separated by the bulkier organic cations that form 2D halide perovskite structures. Quasi 2D or layered hybrid organic-inorganic lead halide perovskites have recently emerged as promising advanced semiconductors to replace the traditional pseudo-cubic "3D" lead halide perovskites in applications such as solar cells, photodetectors, and light emitting diodes, since they offer significantly improved stability and greater tunability of optoelectronic properties.[17–21] Layered lead halide perovskites (LLHPs) formed from typical R cations including butylammonium (BA) and phenylethylammonium (PEA) have been extensively studied in device applications, both in their pure 2D phase form and in quasi-layered structures where the number of inorganic layers (*n*) is increased relative to the organic; the latter increases the light absorption and charge carrier transport since BA and PEA are optically transparent and electrically insulating.[22–27]

Furthermore, organometal trihalide perovskites are reported to suffer from halide migration (due to the low activation energy for migration) through mainly grain boundary pathways, leading to the stark hysteresis observed when implemented in photovoltaic devices, these diminish device stabilities as well as prevent accurate efficiency measurements.[28] In this respect, two-dimensional and quasi two-dimensional structures, given their additional organic molecule components, may be viable candidates to passivate defects and block pathways for halide migration. For instance, the incorporation of phenylethylammonium lead iodide into formamidinium lead iodide was shown to enhance moisture stability while also hampering ion migration, due to the preferential positioning of the two-dimensional halide perovskite at the grain boundaries of the 3D phases.[29]

Layered perovskites can be fabricated in one of two conformations depending on the nature of the spacer cation. The structure of the most-commonly studied layered lead halide perovskites (*i.e.* the Ruddlesden-Popper phase) consists of sheets of corner-sharing PbX_6 octahedra (X = Cl, Br, I) separated by layers of bulky asymmetric monocation-functionalized organic spacers, R, giving a chemical formula of $(R)_2PbX_4$ that can be simply prepared as thin films using solution-based methods. For Ruddlesden-Popper structures, therefore, due to the anchoring of the cation at the inter-octahedral halide position, the inorganic slabs are not stacked on top of each other but rather shifted to accommodate the cation linkages in between the inorganic layers.[30] However, for Dion-Jacobson layered perovskite structures, diammonium cationic salts allow for anchoring of the organic spacer at analogous positions of neighboring octahedral layers, *i.e.,* at the top linkage and at the bottom linkage sites, where inorganic slabs are stacked exactly on top of each other with the respective inter-inorganic slab organic spacers. Recently, Fu *et al.* have reported mixed Ruddlesden-Popper and Dion-Jacobson phase mixtures leading to enhanced perovskite crystal growth and enhanced stabilities.[31]

1.1.1 Optoelectronically-active cations in layered halide perovskites

Organic molecular cations in 2D halide perovskites, such as butylammonium, in general serve as spacers and have no optical activity whatsoever.[32] In this regard, implementing the use of chromophore or large molecular cations that would otherwise enhance the light-absorbing capacities of the resulting halide perovskite material is of great interest. These can be engineered as cations in the 2D halide perovskite structure by utilizing functional groups, for instance NH_3^+ as a side chain of the chromophore units that can anchor at the corners of neighboring halide perovskite octahedra. Computational studies for the incorporation of electron-donating chromophore benzothienobenzothiophene (BTBT) and the electron-withdrawing chromophores perylene diimide (PDI) and naphthalene diimide (NDI) into Pb-I-based octahedral layers have been reported;[32] these demonstrated that for electron-donating systems, the effective mass of conduction band electrons, mainly located at the inorganic layers, is much lower than the effective mass of the valence band holes, since the holes are mostly located at the electron-donating organic groups, thus their transport relies on molecular coupling. On the other hand, for electron-withdrawing systems, the effective mass of valence band holes, mainly located at the inorganic layers, is less than that of the conduction band electrons, which locate themselves around the organic molecules, thus electron transport relies on π- π interactions between adjacent molecules.

Furthermore, as reported, naphthalene, pyrene and perylene chromophores each with an ether linkage as well as several chain lengths (except perylene) were incorporated into Pb-I octahedral layers leading to improved energy level matching with the inorganic layers due to the enhanced conductivity perpendicular to these layers (out-of-plane);[33] this was concluded from the enhanced conductivity of layered halide perovskites synthesized with pyrene and perylene in particular compared to those with simple aliphatic cation systems. The thin films were prepared by direct spin-coating from the precursor solutions (organic salt: PbI_2 in a 2:1 ratio); it is however important to note that the larger chromophore, perylene-, based halide perovskite could not crystallize in thin films using the traditional solution-based method. Additionally, single crystals with the three chromophore systems were synthesized through an antisolvent vapor diffusion method, whereby dichloromethane antisolvent vapor was allowed to diffuse into the chromophore and lead iodide precursor solution in ɣ–butyrolactone solvent.

Additionally, the effect of the alkyl linker chain length on the out-of-plane conductivity was studied and from this it was concluded that for aliphatic and naphthalene-based halide perovskites, the out-of-plane conductivity decreased (although within the same order of magnitude) as the alkyl chain length was increased. However, for the pyrene system, a clear pattern dependent on the alkyl chain length could not be observed, given that the pyrene-o-ethyl and pyrene-o-butyl systems experienced the highest conductivity compared to the pyrene-o-propyl-based system. Hence, the alkyl chain length itself cannot be used as a means of predicting enhanced or worsened conductivity, however, it can induce certain conformational changes that themselves affect conductivity. Following this logic and the crystal structure measurements in this work, it was established that the higher conductivity systems experienced edge-to-face chromophore interactions, whereas the lower-conductivity systems experienced edge-to-edge-type interactions. Therefore, enhanced interactions, either edge-to-face or perhaps face-to-face as suggested in this work, could further ameliorate the out-of-plane conductivity in chromophore systems. However, the perylene-o-ethyl system studied resulted in the highest conductivity despite the edge-to-edge-type interactions, which was attributed to the better band alignment with the inorganic layers. In this work a champion 1.14% efficient device was reported for the (pyrene-O-propyl-NH_3)$_2$$PbI_4$ system.

Du *et al.*. had also previously studied the effect of the molecular cation and alkyl linker chain length (though from smaller molecular cation systems) on octahedral layer distortions.[34] In this work, acene alkylamine 2D halide perovskites (*i.e.*, phenylethylammonium, phenylmethylammonium, napthylmethanammonium and napthylethanammonium-based) were synthesized through a solution-based crystal growth method, some on a two-layer system, where the chromophore amine solution in methanol was placed on top of a PbI_2 solution layer in hydriodic acid (HI) after which crystals formed at the interface and precipitated overnight. In all cases, the powders were spun-coat into thin films from dissolution in DMF. Two types of chromophore penetration-induced distortions in the octahedral layer were introduced (**Figure 1.3a**): a halide perovskite layer distortion of the Pb-I-Pb bond angle (**Figure 1.3b**) as well as octahedral distortion of the I-Pb-I bond angles (**Figure 1.3c**).

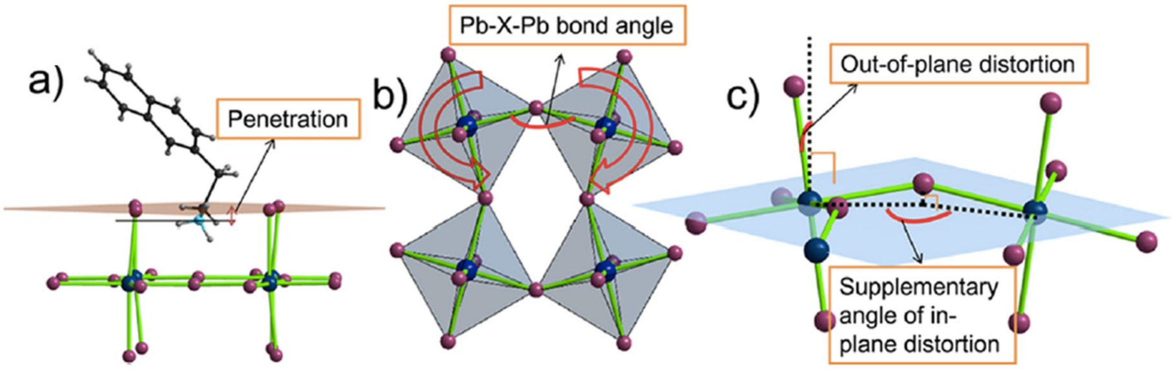

Figure 1.3. Reported octahedral layer distortion from organic molecular cation insertion (modified from Ref. [34] © 2018 American Chemical Society). (a) Cation penetration into the octahedral layers, (b) Pb-X-Pb bond angle torsion and (c) in- and out-of-plane distortions.

The aforementioned distortions were reported to have a direct impact on the exciton absorption and emission properties of the halide perovskite materials, where the perovskite layer distortion led to a widening of the bandgap, *i.e.,* not ideal for photovoltaic applications due to reduced visible light absorption, whereas increased octahedral distortion granted broader photoluminescent emission properties through the reduced energy barrier of some interface defect states. Furthermore, the direct effect of the alkyl NH_3^+ linker chain length from the organic molecular cation on the photoluminescence range was also reported. Additionally, with regards to the inorganic layer's effect on 2D perovskite formation, Denis *et al.* also reported the effect of the halide conformation in the inorganic layers, *i.e.,* iodide, bromide or chloride, in determining the fate of the formation of the reduced dimensionality perovskite (by tuning the octahedral dimensions), where bromide-based inorganic octahedra were observed to prevent the formation of unwanted lower dimensional phases.[35]

Interestingly, Elshanawany *et al.* have recently observed, by means of transient absorption spectroscopy, energy transfer between the lead halide inorganic layers and singlet and triplet states of organic chromophores as large as 1-pyrenemethylammonium in the layered perovskite structures.[36] This, in addition to X-ray diffraction data, confirms the feasibility of incorporation of large cationic components with also effective energy transfer.

1.2 Photovoltaic device structures with perovskite active layers

In order to fabricate photovoltaic devices from perovskite active layers, the latter are normally sandwiched in between charge (*i.e.* electron and hole) collecting layers. In general, two types of photovoltaic device structures are used; these are namely the n-i-p structures and the p-i-n structures.[37] For n-i-p structure devices, the perovskite layer is sandwiched in between a bottom electron transport layer (ETL) and a top hole transport material (HTM) (**Figure 1.4,** left). Common n-type bottom layers are tin oxide (SnO_2) and titanium dioxide (TiO_2). In planar structures, only compact layers of the aforementioned metal oxides are implemented, whereas in mesoporous structures, mesoporous layers of the metal oxides are also deposited on top of their compact layers. Common p-type top layers are hole transport materials such as Spiro-MeOTAD and Poly[bis(4-phenyl)(2,4,6-trimethylphenyl)amine (PTAA). In p-i-n structures (**Figure 1.4**, right), the reverse configuration holds, where the perovskite layer is instead sandwiched between hole transporting bottom layers, normally metal oxides such as nickel oxide, and top electron transport layers, commonly molecules such as [6,6]-phenyl-C_{61}-butyric (PCBM) or C_{60}. Both n-i-p and p-i-n configurations consist of top metal collectors and bottom transparent conductive oxide (TCO) substrates.

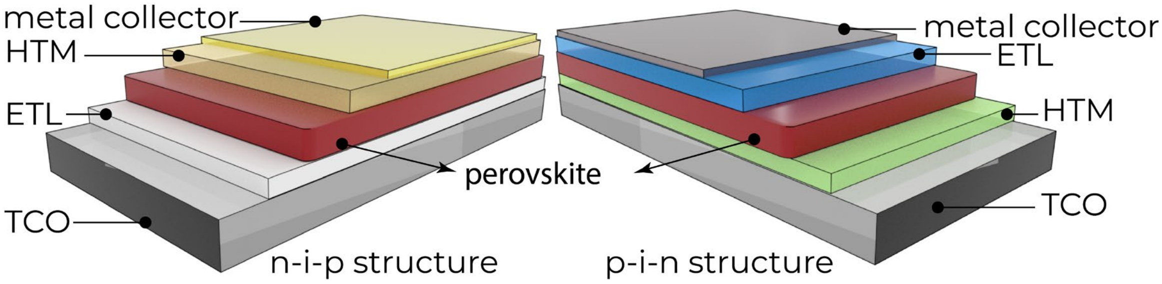

Figure 1.4. Common perovskite photovoltaic device configurations, namely n-i-p structures (left) and p-i-n structures (right).

1.3 Toxicity concerns of lead-based perovskites and lead-free structures

A serious concern for the implementation of lead-based perovskites for photovoltaic applications is their toxicity, given the possibility of lead leaching into the environment and the water solubility of the lead-based precursor.[38] This, in addition to the hazardous lead waste handling both in production facilities and at the end of the photovoltaic device's utilization present further concerns. As a result, lead-free perovskite structures are also widely spread in the literature. Principal lead-free perovskite structures are based on (1) tin or germanium replacements of lead, *i.e.* $ASnX_3$ or $AGeX_3$, or (2) double perovskite structures with the formula $A_2M(I)M'(III)X_6$ where A is a cation and M(I) is a monovalent metal cation, such as Ag^+, Au^+, Cu^+, Rb^+, K^+ or Na^+, and M'(III) is a trivalent metal cation, such as Bi^{3+} or In^{3+};[39,40] in both cases A is the A-site cation and X is the halide anion.[41,42] In the case of tin- and germanium-based perovskites, tin and germanium are able to easily replace lead in the structure given their equal oxidation number (II). In the case of double perovskites however, a pair of metal cations with I and III oxidation states, respectively, are required, where in essence they substitute, two divalent lead cations Pb^{2+}.

Tin-based perovskites are however highly unstable, given the possible tin oxidation states which yield the structure thermodynamically unstable. Moreover, germanium-based perovskite photovoltaic devices are also less-performing and unstable. Therefore, double perovskites remain of high interest. Typical A-site cations for double perovskites include caesium, Cs, or rubidium, Rb.

1.3.1 $Cs_2AgBiBr_6$ Lead-free Double Perovskites

The $Cs_2AgBiBr_6$ structure of double perovskites stands out due to its visible-light absorption, structural stability and nontoxic nature, which renders it as a promising perovskite photovoltaic candidate. The structure of the $Cs_2AgBiBr_6$ double perovskite is depicted on **Figure 1.5**, namely, the cuboctahedral structure is composed of alternating Ag^+ and Bi^{3+} octahedra, each comprised of 6 bonds to bromide anions. The Cs atoms place themselves at the cuboctahedral cavities.

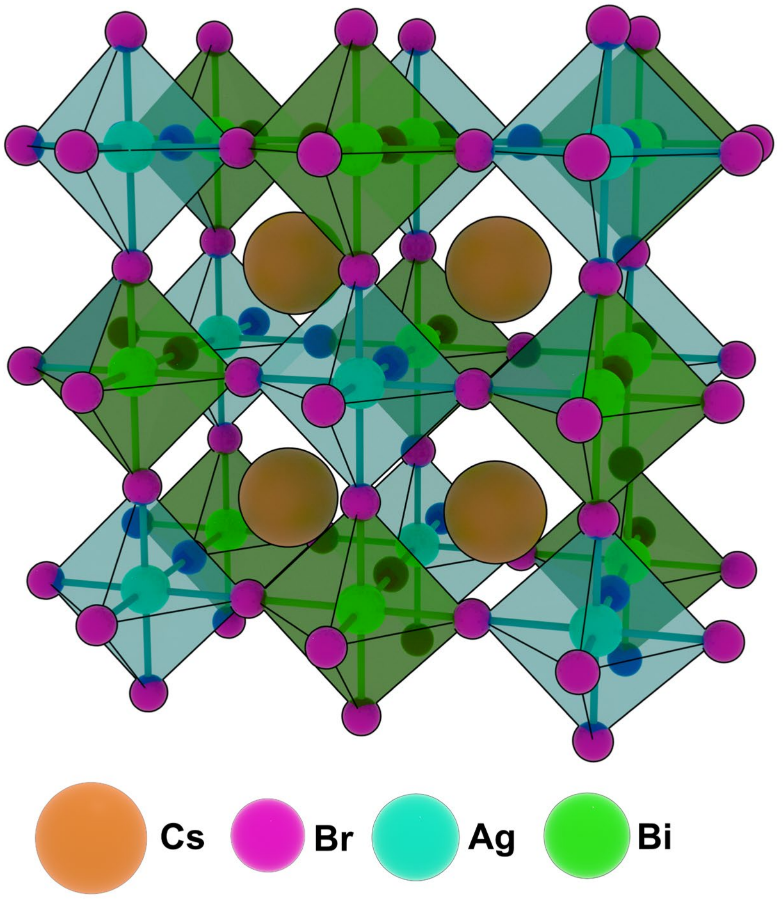

Figure 1.5. Schematic of the unit cell of a $Cs_2AgBiBr_6$ double perovskite structure.

In 2017, Greul *et al.* reported a photovoltaic device with a 2.43% power conversion efficiency, which provided great prospects of the applications of $Cs_2AgBiBr_6$ perovskite active layers in photovoltaic devices.[43] Since then, however, as observed from literature reports, achieving $Cs_2AgBiBr_6$ photovoltaic device power conversion efficiencies higher than 2.5% has been challenging given the defects that still dominate in the structure.

Furthermore, $Cs_2AgBiBr_6$ is an indirect bandgap material, where the conduction band minimum is mainly composed of Bi *6p* orbitals while the valence band maximum is composed of Br *4p* and Ag *4d* antibonding orbitals.[40] In principle, the indirect bandgap of $Cs_2AgBiBr_6$, 1.8-2.2 eV,[39] is a result of the Ag *d* and Bi *s* orbital mismatch and Ag-Bi interactions.[44,45] It is worth noting that while iodide double perovskites remain very interesting due to the expected resulting smaller bandgaps and therefore enhanced visible-light absorbing range, the direct synthesis of a stable double perovskite iodide phase has not been possible; namely, only anion-exchange methods have been successful at synthesizing (unstable) Cs_2AgBiI_6 nanocrystals while computational studies yield it thermodynamically unstable.[46,47]

Nevertheless, despite its indirect bandgap, $Cs_2AgBiBr_6$ remains a promising candidate for photovoltaic applications. Indeed, the Shockley-Queisser model sets a 16.4% power conversion efficiency limit for a $Cs_2AgBiBr_6$ photovoltaic device.[43] Furthermore, Bartesaghi *et al.* have observed that even with a high density of traps in the structure, the measured bulk trap-assisted recombination of charges is slow in $Cs_2AgBiBr_6$.[48] Common defects leading to the high trap density in these double perovskites have been ascribed to Ag or Bi vacancies, Ag-Bi antisites and Br vacancies.[45,49–52] Moreover, Sirtl *et al.* report poor charge collection contact selectivity alongside energy level mismatches which call for further $Cs_2AgBiBr_6$ photovoltaic device optimizations.[53] Longo *et al.* further shed light on the bottlenecks to $Cs_2AgBiBr_6$ photovoltaic device performance, namely concluding that low electron diffusion lengths and a high density of electron traps (determined via external quantum efficiency and photothermal deflection spectroscopy and surface photovoltage measurements, respectively) are mainly responsible.[54]

A summary of reported $Cs_2AgBiBr_6$ perovskite photovoltaic devices are presented on **Table 1.1**.

Table 1.1 Reported $Cs_2AgBiBr_6$ photovoltaic device structures and efficiencies

Device structure	**PCE (%)**	**Reference**
FTO/c-TiO_2/m-TiO_2/$Cs_2AgBiBr_6$/Spiro-OMeTAD/Au	2.43	[43]
FTO/c-TiO_2/$Cs_2AgBiBr_6$/Spiro-OMeTAD/MoO_3/Ag	2.51	[55]
ITO/c-TiO_2/$Cs_2AgBiBr_6$/Spiro-OMeTAD/Au	1.22	[56]
FTO/c-TiO_2/$Cs_2AgBiBr_6$/Spiro-OMeTAD/Ag	0.70	[57]
FTO/c-TiO_2/$Cs_2AgBiBr_6$/P3HT/Au	1.37	[58]
FTO/c-TiO_2/m-TiO_2/$Cs_2AgBiBr_6$/PTAA/Au	1.26	[59]
FTO/SnO_2/$Cs_2AgBiBr_6$/P3HT/Au	1.44	[60]
ITO/Cu-NiO/$Cs_2AgBiBr_6$/C60/BCP/Ag	2.23	[61]
FTO/c-TiO_2/m-TiO_2/GuaSCN*$Cs_2AgBiBr_6$/Spiro-OMeTAD/Au	3.02	[62]
FTO/c-TiO2/m-TiO_2/$Cs_2AgBiBr_6$/ PTB7/Au	2.53	[63]
ITO/SnO_2/hydrogenated $Cs_2AgBiBr_6$/Spiro-OMeTAD/Au	6.27	[64]
ITO/SnO_2/$(Cs_{0.9}Rb_{0.1})_2AgBiBr_6$/Spiro-OMeTAD/Au	1.52	[65]
FTO/c-TiO_2/$Cs_2AgBiBr_{5.8}S_{0.1}$/Spiro-OMeTAD/MoO_3/Ag	1.90	[66]
ITO/SnO_2/$Cs_2AgBiBr_6$/Zn-chlorophyll/Ag	3.11	[67]
FTO/c-TiO_2/m-TiO_2/**indoline-dyes***$Cs_2AgBiBr_6$/Spiro-OMeTAD/Ag	4.23	[68]
FTO/c-TiO_2/m-TiO_2/$Cs_2AgBiBr_6$/N719/spiro-OMeTAD/Ag	2.84	[69]
FTO/c-TiO2/mp-TiO2/Cs2AgBiBr6/(PEA)4AgBiBr8/Spiro-OMeTAD/Au	2.5	[70]

These are arranged in six different categories (from top to bottom), namely (1) n-i-p devices with bare $Cs_2AgBiBr_6$ active layers and Spiro-OMeTAD hole transport materials, with reported efficiencies as high as 2.51%,[55] (2) n-i-p devices with alternative hole transport materials to Spiro-OMeTAD, with a maximum 1.44% efficiency being reported with poly(3-hexylthiophene-2,5-diyl) (P3HT) as a hole transport material,[60] (3) a p-i-n structure device with a Cu-NiO hole transport layer and a C_{60} electron transport overlayer, reaching efficiencies as high as 2.23%,[61] (4) additive engineering of $Cs_2AgBiBr_6$ via intermediates such as guanidium thiocyanate or methylammonium bromide, leading to efficiencies of 3.02% and 2..53%, respectively;[62,63] moreover, dopants such as hydrogen, rubidium and sulfide lead to device efficiencies of 6.27% (black phase), 1.52% and 1.90%,[64–66] (5) dye additives into the perovskite provide an additional source of light absorption, yielding efficiencies as high as 4.23% for an indoline-dye-doped device, though the enhanced light absorption cannot be fully-attributed to the double perovskite,[68] (6) and lastly a recently reported 2D/3D double perovskite combination whereby PEABr is deposited on top of the $Cs_2AgBiBr_6$ yields power conversion efficiencies as high as 2.5%.[70]

All in all, reported double perovskite device efficiencies are encouraging to continue efforts on understanding the bottlenecks to device performance and improving the $Cs_2AgBiBr_6$ photovoltaic device power conversion efficiencies, in an effort to promote a clean nontoxic future for perovskite photovoltaics.

1.4 Motivation for the research work

1.4.1. Layered lead halide perovskite functional cation incorporation

Research on halide perovskite materials continues at a fast pace, with the fastest efficiency increase over the years reported compared to other photovoltaic technologies and with the highest reported lead halide perovskite device efficiency reaching 25.7% in the year 2021 at dedicated laboratory facilities, according to the National Renewable Energy Laboratory (NREL). Nevertheless, there remain drawbacks in the use of halide perovskite materials and further developments to be carried out: improvement of the photovoltaic performance of halide perovskites remains of high interest, with a special focus on ameliorating device stability, photogenerated charge carrier mobility and in general, efficient charge carrier extraction, in efforts to obtain reproducible and high-efficiency devices.

Implementation of low-dimensional halide perovskites and more specifically chromophore/functional molecular cation incorporation into halide perovskite octahedral layers has thus far demonstrated potential in moving the technology of halide perovskites forward in this direction, with vast possibilities for two-dimensional halide perovskite conformations, though the amount of published work in this field still remains discreet.

In this work to follow, particularly the incorporation of naphthalene diimide (NDI) and benzodithiophene (BDT) chromophores into Pb-I-based octahedral layers will be covered, including the challenges of incorporation and resulting optoelectronic properties of the synthesized systems. In **Chapter 3** work on the attempted incorporation of NDI into layered lead halide perovskites is presented. The motivation behind the NDI cation stands on its well-known charge-transporting properties, as evidenced by previous implementations as an electron-transporting material in perovskite photovoltaic devices, reported by Kurdi et al.,[71] Heo *et al.*,[72] Jung *et al.*,[73–75] Nakamura *et al.*,[76] and its wide applications as an electron acceptor in organic solar cells.[77,78] Furthermore, the computational studies presented above confirm the activity of the NDI molecule as an electron-withdrawing group in the 2D halide perovskite structure actively participating in charge transport.[32] Given the bulky nature of the NDI cation, a range of kinetically-fast and slow crystallization methods are screened to explore the various possibilities of experimental incorporation, where it is hypothesized that a slower method could facilitate crystallization with the larger cation.

In **Chapter 4** the incorporation of the BDT cation into layered lead halide perovskites is presented. The motivation behind the choice of the BDT cation is based on the initial observations in Chapter 3. Namely, being aware of the size limitations brought forward by the PbX_6 octahedra, a smaller yet still functional cation is tested with a hypothesized lower degree of π-π stacking than in the case of the NDI. Moreover, the still conjugated nature of the BDT cation is hypothesized to bring about enhanced charge transport compared to a conventional insulating cationic spacer.

Both studies presented in **Chapters 3 and 4** benefit from a harnessing of the well-known 2D perovskite structure with the phenylethylammonium cation. In **Chapter 3**, it is hypothesized that the presence of some phenylethylammonium cation in the layered lead halide perovskite precursor solution, alongside the NDI cation, could eventually establish a scaffold or framework to facilitate the incorporation of the large NDI cation. Whereas, in **Chapter 4**, a comparative study is developed between layered perovskites based on BDT and PEA, to better understand the properties of the former functional versus latter insulating cations on their respective layered perovskite structures. Both studies presented on **Chapters 3 and 4** also explore tuning of the alkyl linker chain lengths where structural conformation effects are hypothesized. In this regard, the underlying hypothesis is that longer alkyl chain lengths or di-alkyl linker functionality (in the case of the NDI work) would facilitate the anchoring capability of the molecular cation into lead-halide octahedral layers.

All in all, the work presented in **Chapters 3 and 4** aims at determining whether visible-light absorbing and optoelectronically-active organic cations can be incorporated into 2D perovskite layers while improving the charge transport and photovoltaic properties of conventional 2D materials; an additional goal of this work is to insert the functional cations as additives in three-dimensional perovskites in order to form quasi layered lead halide perovskite structures (i.e. with reduced dimensionality and thus enhanced stability together with hypothesized improved optoelectronic properties). In summary, **Chapters 3 and 4** will investigate the optoelectronic and photovoltaic properties of this new family of 2D perovskite active layers.

1.4.2. Lead-free, double perovskite defect mitigation

There is a clear motivation to move on to safer, lead-free and nontoxic perovskite structures for photovoltaic applications. The state-of-the art reported photovoltaic efficiencies for the $Cs_2AgBiBr_6$ double perovskite show a clear room for improvement given its reported Shockley-Queisser limit of 16.4%.[43] As presented above, numerous defects innate to the $Cs_2AgBiBr_6$ double perovskite structure have been reported. Therefore, the work presented in **Chapters 5 and 6** will be demonstrating a reverse engineering of the defects in the double perovskite, where in particular several bromide treatments, via stoichiometric tuning and post-treatments to the solution-deposited double perovskite will be presented, to then better understand the nature and magnitude of the innate defects in the solution-processed double perovskite, as well as the comparative efficiency of the treatments.

In **Chapter 5**, the bromide content in the double perovskite will be tuned via a CsBr excess in the double perovskite precursor solution. This is supported by work from Sirtl *et al.*

where clear effects of AgBr and $BiBr_3$ precursor ratios on the crystallinity and optoelectronic properties of the double perovskite have been observed.[79] Moreover, the CsBr allows for a homogeneous treatment, where foreign elements are not added to the double perovskite structure.

Following observations from Chapter 5, in **Chapter 6**, an alternative, now heterogenous method for a bromide treatment of the double perovskite is presented via LiBr incorporation. This is motivated by the desire to implement a smaller “spectator” cation accompanying the bromide, where it is hypothesized that a smaller spectator cation alongside the bromide can allow for a limited disturbance to the double perovskite structure while carrying out bromide incorporation for the hypothesized bromide vacancy defect healing.

For the LiBr incorporation, kinetically- fast and slow incorporation methods are tested. For the fast method, certain amounts of LiBr are added into the double perovskite precursor solution, where the perovskite is then deposited via a solution-based approach. In the kinetically-slow method, the LiBr is allowed to slowly diffuse into a prepared double perovskite thin film. It is hypothesized that a slower method allows enough time for transport and targeting of the defect sites.

All in all, the work presented in **Chapters 5 and 6** aims to bring the field of double perovskite photovoltaics forward, with an enhanced understanding of the magnitude of innate defects. The work also targets the development of viable methods for healing and thus hampering of photogenerated charge carrier recombination during photovoltaic activity for more efficient photovoltaic devices.

1.5 References

[1] European Commission, "2030 Climate Target Plan," can be found under https://ec.europa.eu/clima/eu-action/european-green-deal/2030-climate-target-plan_en, **2021**.

[2] European Parliament, "Revision of the Renewable Energy Directive: Fit for 55 package | Think Tank | European Parliament," can be found under https://www.europarl.europa.eu/thinktank/en/document/EPRS_BRI(2021)698781, **2021**.

[3] G. H. Bauer, in *Photovoltaic Solar Energy Conversion*, Springer Berlin Heidelberg, Berlin, Heidelberg, **2015**, pp. 5–8.

[4] T. Ibn-Mohammed, S. C. L. Koh, I. M. Reaney, A. Acquaye, G. Schileo, K. B. Mustapha, R. Greenough, *Renewable and Sustainable Energy Reviews* **2017**, *80*, 1321.

[5] "Best Research-Cell Efficiency Chart," can be found under https://www.nrel.gov/pv/cell-efficiency.html, **2021**.

[6] M. Stuckelberger, R. Biron, N. Wyrsch, F.-J. Haug, C. Ballif, *Renewable and Sustainable Energy Reviews* **2017**, *76*, 1497.

[7] K. Sharma, V. Sharma, S. S. Sharma, *Nanoscale Research Letters* **2018**, *13*, 381.

[8] H. Lee, H.-J. Song, M. Shim, C. Lee, *Energy Environ. Sci.* **2020**, *13*, 404.

[9] Y. Dang, D. Ju, L. Wang, X. Tao, *CrystEngComm* **2016**, *18*, 4476.

[10] W.-J. Yin, T. Shi, Y. Yan, *Advanced Materials* **2014**, *26*, 4653.

[11] W. Travis, E. N. K. Glover, H. Bronstein, D. O. Scanlon, R. G. Palgrave, *Chem. Sci.* **2016**, *7*, 4548.

[12] Q. Lin, A. Armin, P. L. Burn, P. Meredith, *Acc. Chem. Res.* **2016**, *49*, 545.

[13] Q. A. Akkerman, G. Rainò, M. V. Kovalenko, L. Manna, *Nat. Mater.* **2018**, *17*, 394.

[14] S. De Wolf, J. Holovsky, S.-J. Moon, P. Löper, B. Niesen, M. Ledinsky, F.-J. Haug, J.-H. Yum, C. Ballif, *J. Phys. Chem. Lett.* **2014**, *5*, 1035.

[15] B.-E. Cohen, M. Wierzbowska, L. Etgar, *Sustainable Energy Fuels* **2017**, *1*, 1935.

[16] L. Etgar, *Energy Environ. Sci.* **2018**, *11*, 234.

[17] J.-C. Blancon, J. Even, Costas. C. Stoumpos, Mercouri. G. Kanatzidis, A. D. Mohite, *Nat. Nanotechnol.* **2020**, *15*, 969.

[18] F. Zhang, H. Lu, J. Tong, J. J. Berry, M. C. Beard, K. Zhu, *Energy Environ. Sci.* **2020**, *13*, 1154.

[19] J. Wong, K. Yang, *Sol. RRL* **2021**, *5*, 2000395.

[20] C. Ortiz-Cervantes, P. Carmona-Monroy, D. Solis-Ibarra, *ChemSusChem* **2019**, *12*, 1560.

[21] P. Liu, N. Han, W. Wang, R. Ran, W. Zhou, Z. Shao, *Advanced Materials* **2021**, *33*, 2002582.

[22] D. H. Cao, C. C. Stoumpos, O. K. Farha, J. T. Hupp, M. G. Kanatzidis, *J. Am. Chem. Soc.* **2015**, *137*, 7843.

[23] C. C. Stoumpos, D. H. Cao, D. J. Clark, J. Young, J. M. Rondinelli, J. I. Jang, J. T. Hupp, M. G. Kanatzidis, *Chemistry of Materials* **2016**, *28*, 2852.

[24] B.-E. Cohen, M. Wierzbowska, L. Etgar, *Advanced Functional Materials* **2017**, *27*, 1604733.

[25] J.-W. Lee, Z. Dai, T.-H. Han, C. Choi, S.-Y. Chang, S.-J. Lee, N. D. Marco, H. Zhao, P. Sun, Y. Huang, Y. Yang, *Nature Communications* **2018**, *9*, 3021.

[26] Y. Chen, S. Yu, Y. Sun, Z. Liang, *The Journal of Physical Chemistry Letters* **2018**, *9*, 2627.

[27] J. Yang, S. Xiong, J. Song, H. Wu, Y. Zeng, L. Lu, K. Shen, T. Hao, Z. Ma, F. Liu, C. Duan, M. Fahlman, Q. Bao, *Advanced Energy Materials* **2020**, *10*, 2000687.

[28] Y. Yuan, J. Huang, *Accounts of Chemical Research* **2016**, *49*, 286.

[29] J.-W. Lee, Z. Dai, T.-H. Han, C. Choi, S.-Y. Chang, S.-J. Lee, N. De Marco, H. Zhao, P. Sun, Y. Huang, Y. Yang, *Nature Communications* **2018**, *9, 3021.*

[30] E. S. Vasileiadou, B. Wang, I. Spanopoulos, I. Hadar, A. Navrotsky, M. G. Kanatzidis, *J. Am. Chem. Soc.* **2021**, *143*, 2523.

[31] P. Fu, Y. Liu, S. Yu, H. Yin, B. Yang, S. Ahmad, X. Guo, C. Li, *Nano Energy* **2021**, *88*, 106249.

[32] S. Maheshwari, T. J. Savenije, N. Renaud, F. C. Grozema, *J. Phys. Chem. C* **2018**, *122*, 17118.

[33] J. V. Passarelli, D. J. Fairfield, N. A. Sather, M. P. Hendricks, H. Sai, C. L. Stern, S. I. Stupp, *J. Am. Chem. Soc.* **2018**, *140*, 7313.

[34] K. Du, Q. Tu, X. Zhang, Q. Han, J. Liu, S. Zauscher, D. B. Mitzi, *Inorganic Chemistry* **2017**, *56*, 9291.

[35] P.-H. Denis, M. Mertens, W. T. M. Van Gompel, K. Van Hecke, B. Ruttens, J. D'Haen, L. Lutsen, D. Vanderzande, *Chem. Mater.* **2021**, *33*, 5177.

[36] M. M. Elshanawany, A. Gaetano Ricciardulli, M. Saliba, J. Wachtveitl, M. Braun, *Nanoscale* **2021**, *13*, 15668.

[37] S. S. Mali, C. K. Hong, *Nanoscale* **2016**, *8*, 10528.

[38] M. Ren, X. Qian, Y. Chen, T. Wang, Y. Zhao, *Journal of Hazardous Materials* **2022**, *426*, 127848.

[39] P.-K. Kung, M.-H. Li, P.-Y. Lin, J.-Y. Jhang, M. Pantaler, D. C. Lupascu, G. Grancini, P. Chen, *Solar RRL* **2020**, *4*, 1900306.

[40] X. Yang, W. Wang, R. Ran, W. Zhou, Z. Shao, *Energy Fuels* **2020**, *34*, 10513.

[41] F. De Angelis, *ACS Energy Lett.* **2021**, *6*, 1586.

[42] W. Ke, M. G. Kanatzidis, *Nat Commun* **2019**, *10*, 965.

[43] E. Greul, M. L. Petrus, A. Binek, P. Docampo, T. Bein, *J. Mater. Chem. A* **2017**, *5*, 19972.

[44] E. T. McClure, M. R. Ball, W. Windl, P. M. Woodward, *Chem. Mater.* **2016**, *28*, 1348.

[45] Z. Xiao, W. Meng, J. Wang, Y. Yan, *ChemSusChem* **2016**, *9*, 2628.

[46] S. E. Creutz, E. N. Crites, M. C. De Siena, D. R. Gamelin, *Nano Lett.* **2018**, *18*, 1118.

[47] C. N. Savory, A. Walsh, D. O. Scanlon, *ACS Energy Lett.* **2016**, *1*, 949.

[48] D. Bartesaghi, A. H. Slavney, M. C. Gélvez-Rueda, B. A. Connor, F. C. Grozema, H. I. Karunadasa, T. J. Savenije, *J. Phys. Chem. C* **2018**, *122*, 4809.

[49] B. Yang, W. Pan, H. Wu, G. Niu, J.-H. Yuan, K.-H. Xue, L. Yin, X. Du, X.-S. Miao, X. Yang, Q. Xie, J. Tang, *Nat Commun* **2019**, *10*, 1989.

[50] W. Pan, H. Wu, J. Luo, Z. Deng, C. Ge, C. Chen, X. Jiang, W.-J. Yin, G. Niu, L. Zhu, L. Yin, Y. Zhou, Q. Xie, X. Ke, M. Sui, J. Tang, *Nature Photon* **2017**, *11*, 726.

[51] F. Lv, T. Zhong, Y. Qin, H. Qin, W. Wang, F. Liu, W. Kong, *Nanomaterials* **2021**, *11*, 1361.

[52] T. Li, X. Zhao, D. Yang, M.-H. Du, L. Zhang, *Phys. Rev. Applied* **2018**, *10*, 041001.

[53] M. T. Sirtl, F. Ebadi, B. T. van Gorkom, P. Ganswindt, R. A. J. Janssen, T. Bein, W. Tress, *Advanced Optical Materials* **2021**, *9*, 2100202.

[54] G. Longo, S. Mahesh, L. R. V. Buizza, A. D. Wright, A. J. Ramadan, M. Abdi-Jalebi, P. K. Nayak, L. M. Herz, H. J. Snaith, *ACS Energy Lett.* **2020**, *5*, 2200.

[55] F. Igbari, R. Wang, Z.-K. Wang, X.-J. Ma, Q. Wang, K.-L. Wang, Y. Zhang, L.-S. Liao, Y. Yang, *Nano Lett.* **2019**, *19*, 2066.

[56] W. Ning, F. Wang, B. Wu, J. Lu, Z. Yan, X. Liu, Y. Tao, J.-M. Liu, W. Huang, M. Fahlman, L. Hultman, T. C. Sum, F. Gao, *Advanced Materials* **2018**, *30*, 1706246.

[57] P. Fan, H.-X. Peng, Z.-H. Zheng, Z.-H. Chen, S.-J. Tan, X.-Y. Chen, Y.-D. Luo, Z.-H. Su, J.-T. Luo, G.-X. Liang, *Nanomaterials (Basel)* **2019**, *9*, E1760.

[58] M. Wang, P. Zeng, S. Bai, J. Gu, F. Li, Z. Yang, M. Liu, *Solar RRL* **2018**, *2*, 1800217.

[59] M. Pantaler, K. T. Cho, V. I. E. Queloz, I. García Benito, C. Fettkenhauer, I. Anusca, M. K. Nazeeruddin, D. C. Lupascu, G. Grancini, *ACS Energy Lett.* **2018**, *3*, 1781.

[60] C. Wu, Q. Zhang, Y. Liu, W. Luo, X. Guo, Z. Huang, H. Ting, W. Sun, X. Zhong, S. Wei, S. Wang, Z. Chen, L. Xiao, *Adv Sci (Weinh)* **2017**, *5*, 1700759.

[61] W. Gao, C. Ran, J. Xi, B. Jiao, W. Zhang, M. Wu, X. Hou, Z. Wu, *Chemphyschem* **2018**, *19*, 1696.

[62] X. Yang, A. Xie, H. Xiang, W. Wang, R. Ran, W. Zhou, Z. Shao, *Applied Physics Reviews* **2021**, *8*, 041402.

[63] H. Wu, Y. Wang, A. Liu, J. Wang, B. J. Kim, Y. Liu, Y. Fang, X. Zhang, G. Boschloo, E. M. J. Johansson, *Adv. Funct. Mater.* **2021,** 2109402.

[64] Z. Zhang, Q. Sun, Y. Lu, F. Lu, X. Mu, S.-H. Wei, M. Sui, **2022**, DOI 10.21203/rs.3.rs-587497/v1.

[65] Z. Zhang, C. Wu, D. Wang, G. Liu, Q. Zhang, W. Luo, X. Qi, X. Guo, Y. Zhang, Y. Lao, B. Qu, L. Xiao, Z. Chen, *Organic Electronics* **2019**, *74*, 204.

[66] N. Pai, J. Lu, M. Wang, A. S. R. Chesman, A. Seeber, P. V. Cherepanov, D. C. Senevirathna, T. R. Gengenbach, N. V. Medhekar, P. C. Andrews, U. Bach, A. N. Simonov, *J. Mater. Chem. A* **2020**, *8*, 2008.

[67] B. Wang, N. Li, L. Yang, C. Dall'Agnese, A. K. Jena, S. Sasaki, T. Miyasaka, H. Tamiaki, X.-F. Wang, *J. Am. Chem. Soc.* **2021**, *143*, 2207.

[68] B. Wang, N. Li, L. Yang, C. Dall'Agnese, A. K. Jena, T. Miyasaka, X.-F. Wang, *J. Am. Chem. Soc.* **2021**, *143*, 14877.

[69] X. Yang, Y. Chen, P. Liu, H. Xiang, W. Wang, R. Ran, W. Zhou, Z. Shao, *Adv. Funct. Mater***.** **2020**, *30*, 2001557.

[70] M. T. Sirtl, R. Hooijer, M. Armer, F. G. Ebadi, M. Mohammadi, C. Maheu, A. Weis, B. T. van Gorkom, S. Häringer, R. A. J. Janssen, T. Mayer, V. Dyakonov, W. Tress, T. Bein, *Adv. Energy Mater.* **2022**, *12,* 2103215.

[71] K. A. Kurdi, D. P. McCarthy, D. P. McMeekin, S. O. Furer, M.-H. Tremblay, S. Barlow, U. Bach, S. R. Marder, *Mater. Chem. Front.* **2021**, *5*, 450.

[72] J. H. Heo, S.-C. Lee, S.-K. Jung, O.-P. Kwon, S. H. Im, *J. Mater. Chem. A* **2017**, *5*, 20615.

[73] S.-K. Jung, J. H. Heo, D. W. Lee, S.-C. Lee, S.-H. Lee, W. Yoon, H. Yun, S. H. Im, J. H. Kim, O.-P. Kwon, *Adv. Funct. Mater.* **2018**, *28*, 1800346.

[74] S.-K. Jung, J. H. Heo, D. W. Lee, S.-H. Lee, S.-C. Lee, W. Yoon, H. Yun, D. Kim, J. H. Kim, S. H. Im, O.-P. Kwon, *ChemSusChem* **2019**, *12*, 224.

[75] S.-K. Jung, J. H. Heo, B. M. Oh, J. B. Lee, S.-H. Park, W. Yoon, Y. Song, H. Yun, J. H. Kim, S. H. Im, O.-P. Kwon, *Adv. Funct. Mater.* **2020**, *30*, 1905951.

[76] T. Nakamura, N. Shioya, T. Shimoaka, R. Nishikubo, T. Hasegawa, A. Saeki, Y. Murata, R. Murdey, A. Wakamiya, *Chem. Mater.* **2019**, *31*, 1729.

[77] K. Rundel, S. Maniam, K. Deshmukh, E. Gann, S. K. K. Prasad, J. M. Hodgkiss, S. J. Langford, C. R. McNeill, *J. Mater. Chem. A* **2017**, *5*, 12266.

[78] J. Hong, Y. H. Ha, H. Cha, R. Kim, Y. J. Kim, C. E. Park, J. R. Durrant, S.-K. Kwon, T. K. An, Y.-H. Kim, *ACS Appl. Mater. Interfaces* **2017**, *9*, 44667.

[79] M. T. Sirtl, M. Armer, L. K. Reb, R. Hooijer, P. Dörflinger, M. A. Scheel, K. Tvingstedt, P. Rieder, N. Glück, P. Pandit, S. V. Roth, P. Müller-Buschbaum, V. Dyakonov, T. Bein, *ACS Appl. Energy Mater.* **2020**, *3*, 11597.

Chapter 2

Experimental Procedures

Theory and experimental methodologies

This chapter elaborates on the theory behind the most relevant experimental techniques employed in the development of this thesis as well as detailed experimental procedures followed.

Part of this chapter is a modified version from the experimental section in:

''Benzodithiophene-based Spacers for Layered and Quasi-layered Lead Halide Perovskite Solar Cells''

B. Primera Darwich, N. Guijarro, H.-H. Cho, L. Yao, L. Monnier, P. Schouwink, M. Mensi, J.-H. Yum, K. Sivula, *ChemSusChem* **2021**, *14*, 3001.

2.0 Preparatory protocols

2.0.1 Lead-based perovskites (Chapters 3 and 4)

Chemicals and Materials employed: PbI_2 (99.999%, Sigma), methylammonium iodide (Greatcell solar), phenylethylammonium iodide (Sigma Aldrich), N,N-Dimethylformamide (extra dry, 99.8%, Acros Organics), dimethyl sulfoxide (>99.5%, Sigma Aldrich), ethyl acetate (anhydrous, 99.8%, Sigma Aldrich), chlorobenzene (extra dry, 99.8%, Acros Organics), Spiro-MeOTAD (Luminescence Technology Corp), LiTFSI (99.95%, Sigma Aldrich), 4-tert-butylpyridine (>96%, TCI), acetonitrile (anhydrous, 99.8%, Sigma Aldrich), TiO_2 paste (18 NR-T, Greatcell Solar), titanium (IV) isopropoxide (≥ 97%, Sigma Aldrich), PEDOT:PSS (M124 HTL Solar, Ossila), benzo[1,2-*b*:4,5-*b′*]dithiophene (BDT, TCI, 98%), *n*-butyllithium solution (*n*-BuLi, 1.6 M in hexane, Sigma), 1,4-dibromobutane (Fluorochem, 99%), 1,6-dibromohexane (Fluorochem, 95%), ammonium acetate (ABCR, 97%), nitromethane (Sigma, 95%), *N,N*-dimethylformamide (DMF, Sigma, 99.8%), lithium aluminum hydride ($LiAlH_4$, Sigma, 95%), potassium phthalimide (Sigma, 98%), and hydrazine hydrate (Alfa Aesar, 98%) were used as received. Conductive patterned FTO was purchased from Lyoyang Guluo Glass Co. with a resistance of 7 Ω/sq.

NDI amino chromophore synthesis: The detailed reaction schemes are provided on **Scheme A1.1** and ^1H NMR spectra on **Figure A1.1**

***NDI-Bu-NBoc**:* NDA (8.0 g, 30 mmol), NH_2-Bu-NBoc (13.2 g, 70 mmol) and DMF (80 mL) were mixed a flask and heated under Argon atmosphere for 24 h. After cooling to room temperature, 100 mL of water was added in the reaction. Ethyl acetate was used to extract NDI-Bu-NBoc and evaporated with rotavapor. The crude product of NDI-Bu-NBoc was purified through silica gel chromatography using dichloromethane/ethyl acetate (5:1) as eluent. ^1H NMR (400 MHz, $CDCl_3$, 25 °C, TMS) $\delta = 8.69$ (s, 4H), 4.53 (s, 2H), 4.15 (t, 4H), 3.14 (m, 4H), 1.*72 (m, 4H), 1.55 (m, 4H), 1.36 (s, 18H).*

NDI-dibutylamino: NDI-Bu-NBoc (4.5 g, 7.4 mmol) were suspended in 40 mL dichloromethane. Trifluoroacetic acid (20 mL) was dropped into the suspension. The reaction was stirred at room temperature for overnight. After that, the solvent was evaporated with rotavapor. The product was washed with dichloromethane containing a small amount of ethanol, without further purification. ^{1}H NMR (400 MHz, DMSO, 25 °C, TMS) δ = 8.70 (s, 4H), 7.74 (s, 4H), 4.10 (t, 6H), 2.85 (t, 4H), 1.74 (m, 4H), 1.63 (m, 4H).

NDI-Et-NBoc: NDA (1.1 g, 4 mmol), NH_2-Et-NBoc (1.3 g, 8 mmol) and DMF (40 mL) were mixed a flask and heated under Argon atmosphere for 24 h. After cooling to room temperature, 100 mL of water was added in the reaction. Ethyl acetate was used to extract NDI-Et-NBoc and evaporated with rotavapor. The crude product of NDI-Et-NBoc was purified through silica gel chromatography using dichloromethane/ethyl acetate (3:1) as eluent. ^{1}H NMR (400 MHz, $CDCl_3$, 25 °C, TMS) δ = 8.80 (s, 4H), 4.88 (s, 2H), 4.41 (t, 4H), 3.59 (m, 4H), 1.25 (s, 18H).

NDI-diethylamino: NDI-Et-NBoc (750 mg) were suspended in 10 mL dichloromethane. Trifluoroacetic acid (10 mL) was dropped into the suspension. The reaction was stirred at room temperature for overnight. After that, the solvent was evaporated with rotavapor. The product was washed with dichloromethane containing a small amount of ethanol, without further purification. ^{1}H NMR (400 MHz, DMSO, 25 °C, TMS) δ = 8.73 (s, 4H), 7.88 (s, 6H), 4.36 (t, 6H), 3.21 (m, 4H).

NDI-monoNBoc: NDA (8.04 g, 30 mmol), NH_2-Et-NBoc (4.75 mL), 1-propylamine (2.48 mL) and DMF (80 mL) were mixed a flask and heated under Argon atmosphere for 24 h. After cooling to room temperature, 100 mL of water was added in the reaction. Ethyl acetate was used to extract NDI-monoNBoc and evaporated with rotavapor. The crude product of NDI-monoNBoc was purified through silica gel chromatography using dichloromethane/ethyl acetate (20:1) as eluent. ^{1}H NMR (400 MHz, $CDCl_3$, 25 °C, TMS) δ = 8.79 (s, 4H), 4.87 (s, 1H), 4.41 (t, 2H), 4.20 (t, 2H), 3.58 (m, 2H), 1.80 (m, 2H), 1.25 (s, 9H), 1.06 (t, 4H).

NDI-monoamino: NDI-Et-NBoc (1.2 g, 2.6 mmol) were suspended in 12 mL dichloromethane. Trifluoroacetic acid (10 mL) was dropped into the suspension. The reaction was stirred at room temperature for overnight. After that, the solvent was evaporated with rotavapor. The product was washed with dichloromethane containing a small amount of ethanol, without further purification. ^{1}H NMR (400 MHz, DMSO, 25 °C, TMS) δ = 8.71 (s, 4H), 7.83 (s, 3H), 4.35 (t, 2H), 4.05 (t, 2H), 3.19 (t, 2H), 1.70 (m, 2H), 0.96 (m, 3H).

BDT amino molecule synthesis: BDT cation synthesis reactions were adapted from literature reports[1] and are described in detail in **Scheme A2.1** for BDT-C2 and **Scheme A2.2** for BDT-C4 and BDT-C6.[2] Characterizations of the final cations and reaction intermediates by ^{1}H NMR are given in **Appendix 2.1** in **Figure A2.1** and **Figure A2.2** for BDT-C2, in **Figure A2.3** and **Figure A2.4** for BDT-C4 and finally in **Figure A2.5** and **Figure A2.6**, for BDT-C6. All reactions were carried out under an inert Ar atmosphere unless otherwise specified. The ^{1}H NMR spectra were obtained at room temperature using $CDCl_3$ as internal standard on a 400 MHz NMR Bruker AVANCE III-400 spectrometer (Bruker, Rheinstetten, Germany). Tetrahydrofuran (THF) and DMF were purified using a Pure Solv-MD solvent purification system (Innovative Technology, Amesbury, United States). Silica gel chromatography was carried out with technical grade silicon dioxide (Acros Organics, pore size 60 Å and 40–50 µm particle size).

Molecular amino to salt synthesis: Each of the amine-functionalized molecules synthesized were combined with a stoichiometric amount of 57 wt% hydriodic acid (HI) (1:1 for monoamino systems and 2:1 for diamino systems) and allowed to stir for 2 hours in methanol in an ice bath. The salt products were washed three times with diethyl ether, collected and dried.

NDI incorporation into PEA_2PbI_4: A naphthalene diimide-based chromophore (NDI-E) functionalized with an $NH_3^+I^-$ anchoring group (NDI-E salt) was tested as a preliminary chromophore candidate; solutions with various compositions of both phenylethylammonium iodide (PEAI) and NDI-E salt were prepared (as listed on **Chapter 3**) and mixed with PbI_2 resulting in a total 0.2 M cation concentration and a 0.1 M PbI_2 concentration in dimethylformamide (DMF):

The solutions were each spun-coat onto a glass substrate at 3000 rpm for 30 s. The films were then annealed for 10 minutes at 100 ^{0}C on a hot plate. Fabrication took place inside an argon-filled glovebox. All additional thin films in this work were deposited with these conditions unless otherwise noted.

Powder synthesis (two-layer method for NDI incorporation into PEA_2PbI_4)**:** The procedure reported in the literature[3] for the two-layer 2D halide perovskite formation was adapted as follows: 27 mg PbI_2 were dissolved in 500 µL of 57 wt% HI and placed on a 2 ml vial as the bottom layer. In order to attempt the preparation of the halide perovskite structures (see

Chapter 3 for PEA-NDI-E ratios) on top of this layer, the respective chromophore cation solutions in 1 ml methanol were deposited as the top layer. The collected crystals were washed with diethyl ether, re-dissolved in DMF (at 0.4 M concentration) and spun-coat onto thin films at 3000 rpm for 30 s in an Ar glovebox.

***PbI_2 film dip-coating into an NDI-E chromophore solution*:** A film of PbI_2 (spun-coat from a 0.5 M PbI_2 solution in DMF at 3000 rpm for 30 s) was immersed into a 0.0125 M NDI salt solution in isopropyl alcohol (IPA) for 48 h.

***Powder synthesis (solvent evaporation)*:** A solution of 0.25 M PbI_2 and 0.5 M NDI-E chromophore in DMF was placed in a small vial sealed with a septum with an Argon inflow as well as a solvent outlet (**Figure 2.1** a).

***Powder synthesis (solvent transport/antisolvent diffusion)*:** The procedure reported in the literature for the antisolvent vapor diffusion method[4] was adapted as follows: A solution of 0.25 M PbI_2 and 0.5 M chromophore in DMF was placed in a small unsealed vial placed inside a larger sealed flask containing toluene antisolvent (**Figure 2.1** b). This was heated to 110 ^{0}C for 48 h after which a powder product could be collected. The powder was later dissolved in DMF and drop-cast for further analysis.

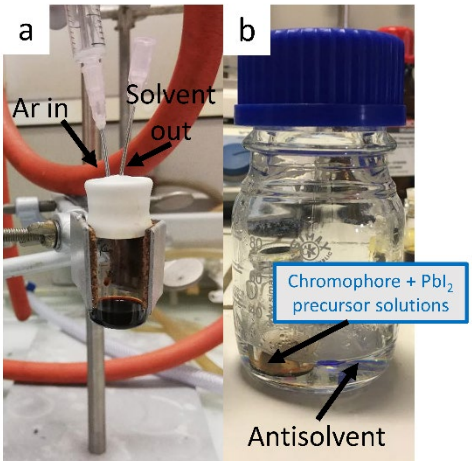

Figure 2.1. Setup of powder synthesis methods tested, namely (a) solvent evaporation and (b) solvent transport/antisolvent diffusion.

Perovskite thin film fabrication: For $MAPbI_3$, the procedure reported by Huang *et al.*[5] was followed, namely 1.6 M solutions with 1:1 ratio of PbI_2:MAI were prepared in a 8.9:1.1 (v/v)

DMF:DMSO mixture. For the QLLHPs, the PEA or BDT ligands were mixed with PbI_2 and methylammonium iodide (MAI) according to the specified stoichiometry. All perovskite solutions were spun coat in an Argon environment with a 2-step program: namely, a first step of 3000 rpm for 10 s, followed by 6000 rpm for 25 s at the beginning of which 500 µL of chlorobenzene antisolvent were spun coat onto the perovskite in formation. For the N20 series of perovskites, an antisolvent composition of 50:50 (v/v) chlorobenzene:ethyl acetate was found to improve the film appearance and were therefore implemented. For the $n = 1$ LLHPs films, stoichiometric amounts of the cations were added to a 0.1 M PbI_2 solution in DMF, spun coat at 3000 rpm for 30s. All perovskite films were annealed at 130°C for 10 minutes, unless otherwise noted.

Device fabrication: Photovoltaic devices with the n-i-p structure were fabricated starting with FTO substrates, which were sequentially ultrasonically cleaned in acetone, aqueous Hellmanex solution, water, and isopropyl alcohol. A compact TiO_2 layer was prepared from a titanium isopropoxide-based precursor solution spun coat at 5000 rpm for 40 seconds, following the procedure reported by Yan *et al.*.[6] The films were then thermally annealed, following a ramped annealing step to 500°C (dwell 45 minutes). Furthermore, a mesoporous TiO_2 layer was formed via diluting the precursor paste in a 1:5 ratio (w/w) with ethanol and spin coating at 4000 rpm for 40 seconds, followed by a ramping program[7] to 450°C, held for 30 minutes. The perovskite films were then deposited as described above. This was followed by the deposition of the Spiro-OMeTAD layer,[7] from a solution consisting of 72.3 mg of Spiro dissolved in 1 ml of chlorobenzene, to which 28.8 µl tBP and 17.5 µL LiTFSI (520 mg/ml acetonitrile) were added; the solution was spun coat at 4000 rpm for 25 seconds, these were then oxidized in air for 12 hours. Lastly, 100 nm Au electrodes were deposited by evaporation (mask area 0.16 cm^2**).**

2.0.2 Lead-free based perovskites (Chapters 5 and 6)

Chemicals and Materials employed: Cesium bromide (99.999%, ABCR), silver bromide (99.999%, ABCR), Bismuth(III) bromide (99%, ABCR), lithium bromide (99%, Chemie Brunschwig), methylammonium bromide (Greatcell solar), lithium hydroxide (98%, Sigma Aldrich), ammonium thiocyanate (99.9%, Sigma Aldrich), Spiro-MeOTAD (Luminescence Technology Corp), LiTFSI (99.95%, Sigma Aldrich), 4-tert-butylpyridine (>96%, TCI), acetonitrile (anhydrous, 99.8%, Sigma Aldrich), Chlorobenzene (99.8%, Chemie Brunschwig), 2-propanol (99.5+%, anhydrous, VWR), dimethyl sulfoxide (>99.5%, Sigma Aldrich), TiO_2 paste (18 NR-T, Greatcell Solar), Titanium diisopropoxide bis(acetylacetonate) (75 wt. % in isopropanol, Sigma Aldrich) were used as received. Conductive patterned FTO was purchased from Lyoyang Guluo Glass Co. with a resistance of 7 Ω/sq.

Anhydrous LiSCN synthesis: The procedure reported by Lee *et al.* was followed.[8] Namely, LiOH hydrate was mixed with ammonium thiocyanate and heated until the hydrate dissolved the salts. The solution was filtered and placed under vacuum to remove the remaining solvent. Ether solvents were used to wash and recrystallize the product. The product was extracted and dried for 48 hours.

Perovskite thin film fabrication: CsBr (212.81 mg), AgBr (93.89 mg) and $BiBr_3$ (224.36 mg) were dissolved in 1 ml DMSO to prepare a 0.5 M stock solution which was allowed to heat at 90°C overnight in an argon glovebox. The solutions were spun coat on plasma-cleaned substrates in the argon glovebox, with the following procedure: 4000 rpm, 60s. 200 μl of isopropanol antisolvent were dropped just before the last 20 seconds of spinning. These were then annealed at 310°C for 10 minutes. For the CsBr excess samples, 5-15 mol% CsBr excess (with respect to the stoichiometric CsBr amount) were added into the precursor solution, likewise for the LiBr, MABr and LiSCN additive experiments in mol% of 1-6.

Device fabrication: Photovoltaic devices with the n-i-p structure were fabricated starting with FTO substrates, which were sequentially ultrasonically cleaned in acetone, aqueous Hellmanex solution, water, and isopropyl alcohol. A compact TiO_2 layer was prepared from a titanium diisopropoxide-based precursor using spray pyrolysis, following the procedure of Saliba *et al.*. at 450°C.[7] Furthermore, a mesoporous TiO_2 layer was formed via diluting the precursor paste in a 1:10 ratio (w/w) with ethanol and spin coating at 4000 rpm for 40 seconds, followed by a ramping program[7] to 450°C, held for 1h30 minutes. The perovskite films were then deposited as described above. This was followed by the deposition of the Spiro-OMeTAD layer which was modified from that reported by Greul *et al.*,[9] namely, 73 mg of spiroOMeTAD were dissolved in 1 ml chlorobenzene. To this solution, 10 µl tert-butyl pyridine and 30 µl of a 170 mg/ml in acetonitrile LiTFSI solution were added, the solution was spun coat on top of the double perovskite layers at 4000 rpm for 60 seconds. The samples were then oxidized in air overnight. The devices were then placed in an evaporator where a 1 nm MoO_3 layer was deposited. For the devices in Chapter 5, 100 nm Au electrodes were deposited by evaporation (mask area 0.16 cm^2), whereas for the devices in Chapter 6, 8 nm Au were deposited.

2.1 Physical Characterization

2.1.1 X-ray diffraction measurements

X-ray diffraction (XRD) allows to identify the crystal structure of a material.[10] Here, an incident beam of X-rays is diffracted and reflected by the material under analysis. The condition to observe constructive interferences in the diffracted beam is given by Bragg's law:

$$n\lambda = 2d\ sin\theta$$

where λ is the wavelength of the incident beam, d is the distance between two crystallographic planes of the material, n is a constant given the order of the reflection, and θ is the angle of incidence of the incident beam on the crystallographic plane. Broadly speaking, constructive interferences are obtained when the difference between the optical path of two beams is a multiple of the wavelength (**Figure 2.2**). In practice, the wavelength of the X-ray beam is kept constant, while the incidence angle θ is modified. Generally speaking, at those θ where Bragg's law is satisfied, a peak is measured in the diffractogram and the corresponding d can be determined. The set of peaks measured in a diffractogram provide information on the crystalline planes of the material, and therefore constitute a signature for the crystalline structure. Indeed, each crystalline structure has a distinct diffractogram.

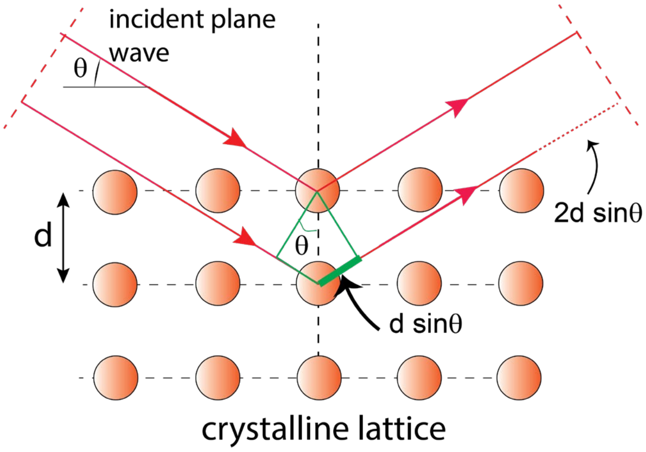

Figure 2.2. Scheme of the diffraction of X-rays (red lines) by a crystalline lattice of atoms (orange spheres). The difference in the optical path between the two beams reflected by two crystalline planes separated by a distance d is $2d\ sin\theta$. Therefore, constructive interferences between the two beams are obtained when Bragg's law is validated, that is, when $2d\ sin\theta = n\ \lambda$.

XRD patterns shown in Chapters 3-6 were performed on a Bruker D8 Advanced diffractometer with a 0.154 nm Cu X-ray source. Interlayer spacings for 2D halide perovskites were then calculated from the first diffraction peak using Bragg's law of diffraction.[11] X-ray diffraction measurements were taken in Bragg-Brentano geometry using non-monochromated Cu-K-alpha radiation on a Bruker D8 Discover instrument equipped with a LynxEYE XE detector. The films were mounted in a N_2-filled glovebox on custom sample holders that allow measuring under inert conditions. Moreover, Grazing-Incidence Wide-Angle X-ray Scattering (GIWAXS) measurements shown in Chapters 3-4 were conducted at the European Synchrotron Radiation Facility (ESRF) on beamline BM01 with a 0.064066 nm x-ray source. For synchrotron powder x-ray diffraction the samples were constantly rotated to avoid any preferred orientations.[12] GIWAXS images shown on Chapter 5 were taken with a D8 Discover Plus instrument.

2.2 Microscopy techniques

2.2.1 Transmission and Scanning electron Microscopy

Scanning electron microscopy (SEM) and transmission electron microscopy (TEM) use electrons that are beamed at a sample and collected after the interaction for imaging purposes. The main difference between SEM and TEM is that SEM creates the image by analyzing the reflected or knocked-off electrons, whereas the TEM uses transmitted electrons to create an image. Therefore, TEM could be used to visualize the spacing and the morphology of nanoscopic samples, whereas SEM affords to monitor the morphology of thin films as well as their thicknesses.

Aside from imaging the sample, TEM and SEM are coupled to an energy-dispersive X-ray (EDX) spectrometer. This analytical tool is used for elemental analysis of the sample. In this case, a high-energy incident beam excites an electron in an inner shell of the atom, causing its ejection and rendering a hole. The filling of this hole with an electron from an outer layer triggers the emission of energy in the form of X-rays. Given the discrete energy distribution, the emitted radiation is characteristic of each specimen (element). In this way, it is possible to simultaneously take images of the sample, while mapping the elemental composition.

The TEM images shown in Chapter 4 were collected with a high resolution (HR) TEM Advanced Tecnai Osiris at an electron beam voltage of 200 kV. The samples were deposited on micrometric copper grids by scratching part of the films on a droplet of toluene solution, and transfer the droplet loaded with particles of the film on the grid by drop casting. The SEM images shown in Chapters 3-6 were obtained with a SEM Gemini 300 Microscope.

2.2.2 Conductive- Atomic Force Microscopy

Atomic force microscopy (AFM) is a high-resolution imaging technique that relies on the atomic forces that arise from the interaction of the surface of the sample and a sharp tip connected to a cantilever. The movement of the tip (attracted/repulsed by the surface) is measured by monitoring a laser reflected on a cantilever. Overall, by monitoring the variation of the cantilever position as the tip scans the surface it is possible to map the topography of the surface.

Among the many techniques that could be coupled to the AFM platform, the conductive AFM (C-AFM) affords to map local variations in the sample's conductivity with a nanoscale resolution. Here, a conductive tip is placed in contact with the sample, while a bias voltage is applied between the tip and the sample- As a result, the current flow is measured between the sample (or the sample's contact) and the tip, while the latter maps moves throughout the surface creating a conductivity or current map. Generally, sets of information on the topography, recorded by the deflection of the cantilever while scanning the surface, as well as on the current, are collected simultaneously.

In Chapter 4, C-AFM was utilized to probe the surface photocurrent generated in quasi-2D perovskites loaded with BDT and PEA spacers. The samples were prepared directly on FTO. C-AFM were performed with an Asylum Research Cypher S AFM using the conductive mode and a Pt-coated tip. Note that the contact on the sample was made on the FTO substrate.

2.3 Spectroscopy techniques

2.3.1 UV-Visible absorption spectroscopy

Assessing light harvesting is crucial in the assessment of materials for photovoltaic applications. Steady-state absorption spectroscopy allows to evaluate the light absorption caused by electronic transitions within solutions and thin films. The transmitted, absorbed and reflected light intensities (I_T, I_{ABS}, I_R, respectively) are related to the incident light (I_0) as follows:

$$I_0 = I_T + I_{ABS} + I_R$$

Note that the transmittance T, Absorptance A and reflectance R are defined as:

$$T = \frac{I_T}{I_0};\ A = \frac{I_{ABS}}{I_0};\ R = \frac{I_R}{I_0}$$

whereby,

$$100\% = T + A + R$$

UV-Visible absorption spectroscopy can be used to determine the band gap of a semiconductor material by using the Tauc relationship,[13] whereby:

$$(\alpha h\nu)^{1/n} = \left(h\nu - E_g\right)$$

where h is Planck's constant, ν is the frequency of the photon, α is the absorption coefficient, E_g is the band gap, and n is a parameter linked to the nature of the band gap transition. More specifically, these relationships will describe (i) a direct allowed transition when $n = {}^{1}/_{2}$; (ii) a direct forbidden transition when $n = {}^{3}/_{2}$; (iii) an indirect allowed transition when $n = 2$; and (iv) an indirect forbidden transition when $n = 3$. E_g can be determined by plotting $(\alpha h\nu)^{1/n}$ as a function of $h\nu$. This is the so-called Tauc plot, and measuring the energy at which the linear part of the representation intercepts the x-axis will provide an estimate of the E_g.

UV-Visible absorption spectra were recorded using a UV-3600 (Shimadzu) spectrophotometer. It is worth noting that in Chapters 5-6, to determine the absorption of the different materials deposited on FTO-coated glass substrates, the following equation was utilized:

$$A(\%) = 100\% - T(\%) - R(\%)$$

For each sample, the total transmission (T) and total reflectance (R) were measured using an integrating sphere. The absorptance (A) was determined using the equation above.

2.3.2 Steady-state emission spectroscopy (Photoluminescence)

An emission spectrum entails recording the intensity of the light emitted by a sample as a function of the wavelength upon exciting with monochromatic radiation. Commonly, a Xe lamp is used as a light source, and a monochromator placed between the lamp and the sample affords to select the excitation wavelength. Upon excitation, the emission is collected and passed through a monochromator to select and analyze a particular wavelength.

The emission spectra shown in Chapters 3-6 were obtained using a Horiba Jobin Yvon Fluorolog-3 spectrofluorometer.

2.3.3 Intensity-Modulated Photovoltage Spectroscopy

The intensity-modulated photovoltage spectroscopy (IMVS) is a frequency-resolved technique that allows the determination of the electron lifetime in the device. Broadly speaking, the IMVS technique was originally developed to analyze the recombination characteristics of dye-sensitized solar cells,[14] but it has been recently implemented to analyze the charge recombination dynamics in perovskite solar cells.[15]

In brief, the device is held at open circuit under a constant illumination intensity upon which an small AC perturbation is applied to the illumination intensity (**Figure 2.3a**), following:

$$I(t) = I + I_0 sin(\omega t)$$

where I is the constant base illumination intensity, I_0 refers to the amplitude (i.e., illumination intensity) of the sinusoidal waveform that is superimposed, and ω corresponds to the angular frequency.

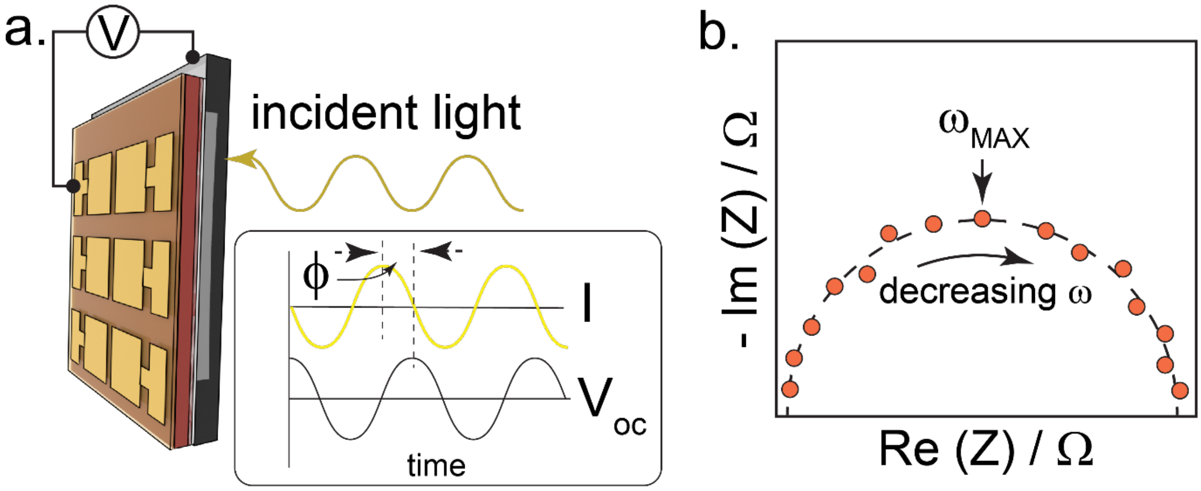

Figure 2.3. Scheme of the IMVS setup including the detail of the phase shift in between the illumination intensity and the V_{OC} response (a). Example of the IMVS response highlighting the characteristic point ω_{MAX} from which τ_{rec} is calculated (b).

Likewise, during the experiment the resulting open circuit voltage ($V_{OC}(t)$) generated by the device will have two components, a constant component and a sinusoidal component originating from the applied perturbation:

$$V_{OC}(t) = V_{OC} + V_{OC,0} sin(\omega t + \phi)$$

Note that the intrinsic delayed response of the system, caused mostly by the charge recombination dynamics within the device, will cause the appearance of a phase shift (Φ) in the response. The IMVS transfer function could be defined considering the perturbation components as:[16]

$$F_{IMVS} = \frac{|V_{OC,0}| exp(i\omega t + i\phi)}{|I_0| exp(i\omega t)} = F_{IMVS,0} exp(i\phi)$$

During a conventional IMVS measurement the angular frequency (*ω=2πf*), or in other words, the frequency (f) at which the light intensity is modulated, will take a range of values to construct the so-called Nyquist plot (**Figure 2.3b**). Here, both the imaginary (Im) and real (Re) components of the IMVS transfer function are plotted as a function of the frequency of the light perturbation. The frequency at which the maximum point (ω_{MAX}) is obtained is inversely proportional to the electron recombination time constant (τ_{rec}), according to:

$$\tau_{rec} = \frac{1}{\omega_{MAX}}$$

The IMVS measurements reported in Chapter 6 were carried out using a potentiostat Biologic SP300 which was both controlling the source of illumination as well as recording the IMVS response. A white LED (Cree XLamp MC-E White) running at 3 V (200 mA) DC background was used as the light source. A peak amplitude of 200 mV and a modulation frequency range from 100 kHz to 50 mHz were used.

2.3.4 Fourier transformed infrared spectroscopy

Infrared (IR) spectroscopy is an absorption technique that monitors low-energy transitions, such as the vibrations in the molecules. Bearing in mind that molecular vibrations reflect the chemical characteristics of a molecule, it can be used to identify molecular bonds and chemical structures. In addition, as the interaction with the surrounding environment affects the energy of the bonds, this will in turn alter the molecular vibrations that could be readily detected by IR spectroscopy.[17]

Being an absorption spectroscopy technique it relies on measuring the amount of light absorbed (or transmitted) by the sample at each wavelength. In fact, conventional IR spectra depicts the frequency along the horizontal axis in the form of wavenumbers (cm^{-1}), while the transmittance T (%) or absorbance (A) is expressed along the vertical axis. Currently, IR spectrometers operate using an interferometer which speeds up the measurement compared to dispersive measurements, wherein the sample is irradiated with different single wavelength beams analyzing the absorption of light. Here, an IR beam that contains a broad range of IR wavelengths is passed through a beam splitter, which ideally transmits and reflects 50% of the incident radiation (**Figure 2.4**). One beam reaches the fixed mirror and reflects back, whereas the second beam reaches the moving mirror and reflects back to the beam splitter. Both are recombined at the beam splitter and pass through sample where part of the energy is absorbed, and detected. By changing the position of the moving mirror (over time) the beams will recombine constructively or cause a fringe pattern. The movement of the mirror, hence, causes an interference pattern that is "time-dependent" according to the movement of the mirror. Eventually, the detector records the total intensity as a function of time, that is, the raw response produces an interferogram. It is worth emphasizing that the interferogram does not separate the source radiation into individual frequencies. By using the Fourier transform algorithm, the interferogram is converted to a spectrum. One of the particular setup configurations of the FTIR is the so-called attenuated total reflectance (ATR), whereby the sample is placed on top of an ATR crystal (typically germanium) from where the IR beam protrudes into the sample via an evanescence wave.

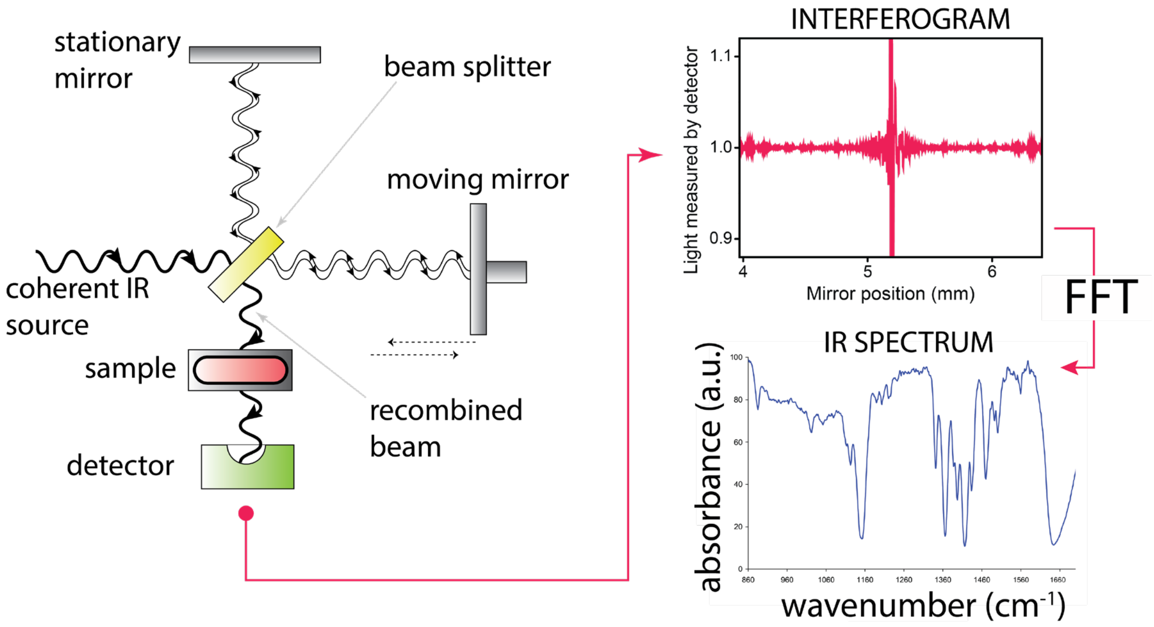
stationary mirror
beam splitter
moving mirror
coherent IR source
sample
detector
recombined beam
INTERFEROGRAM
Light measured by detector
1.1
1.0
0.9
4
5
6
Mirror position (mm)
FFT
IR SPECTRUM
absorbance (a.u.)
100
80
60
40
20
0
860
960
1060
1160
1260
1360
1460
1560
1660
wavenumber (cm-1)

Figure 2.4. Block scheme of a FT-IR instrument and of the conversion from the interferogram to the IR spectrum applying Fourier transform.

The FTIR spectra shown in Chapter 4 corresponds to samples deposited on glass and they were collected using an attenuated total reflectance (ATR)-FTIR setup by means of a Perkin Elmer Spectrum 100 Series FTIR spectrometer.

2.3.5 Solid-state nuclear magnetic resonance

^{133}Cs ssNMR: ^{133}Cs MAS NMR spectra were recorded on a 500 MHz Bruker spectrometer (11.7 T) equipped with an Avance III console and a 1.3 mm three-channel low temperature MAS probe. Samples were packed into 1.3 mm zirconia rotors under ambient conditions and spun up to a 40 kHz spinning speed using nitrogen gas. All spectra were recorded using a Hahn echo pulse sequence with $\pi/8$ and $\pi/4$ pulses of 0.75 and 1.5 μs, which selectively excite the central transition. Up to 1024 transients were accumulated. Recycle delays were set to 1.3 times T_1, the latter exceeding 300 s in the double perovskite samples and reaching almost 800 s for CsBr. ^{133}Cs chemical shifts were referenced to 0.1 M $CsNO_3$ aqueous solution. Long experimental times of around 5 days allowed for full relaxation while a reduced excitation angle allowed for the achievement of a homogeneous excitation.

^{7}Li ssNMR: ^{7}Li MAS NMR spectra were recorded on a 500 MHz Bruker spectrometer (11.7 T) equipped with an Avance III console and a 1.3 mm three-channel low temperature MAS probe. Samples were packed into 1.3 mm zirconia rotors under ambient conditions and spun up to a 40 kHz spinning speed using nitrogen gas. All spectra were recorded using a one-pulse sequence with $\pi/2$ pulses of 2.6 μs. For LiBr, a single scan provided sufficient signal intensity whereas for the other samples up to 69’632 transients were accumulated. Recycle delays were set to 1.3 times T_1. Due to the very low amount of lithium in the double perovskite samples, quantitative data was not collected in this case. For the LiBr sample T_1 was 74 s (low intensity peak) and 945 s (high intensity peak) with a recycle delay of 1228 s. For the LiBr diffusion sample, T_1 was 2.4 s with a recycle delay of 3.12 s. The LiBr additive in the double perovskite samples showed weak signals for which T_1 could not be specifically determined, in both cases the recycle delay was set to 5 s. ^{7}Li chemical shifts were referenced to 9.7 m LiCl aqueous solution.

2.3.6 Photoemission and x-ray spectroscopy

Photoemission spectroscopy measures the energy distribution of electrons emitted by atoms and molecules in various charge and energy states. A material irradiated with ultraviolet light (Ultraviolet photoelectron spectroscopy - UPS) or X rays (X-ray photoelectron spectroscopy -XPS) can emit electrons called photoelectrons from atomic energy levels with a kinetic energy (KE) equal to the difference between the photon energy $h\nu_{ph}$ and the ionization energy E_{ion}, which is the energy required to completely remove an electron from an atomic energy level:

$$KE = h\nu_{ph} - E_{ion}$$

In a more specific sense, XPS and UPS are quantitative surface-sensitive techniques wherein the analysis of the characteristic KE of the photoelectrons brings out information on the oxidation state and the chemical environment of species as well as the overall electronic structure and density of the electronic states within the material. It is worth noting that on the basis of the KE, the electron binding energy of each emitted electron can be determined by following the photoelectric effect equation:

$$E_{binding} = E_{incident} - (E_{kinetic} + \phi)$$

where $E_{incident}$ refers to the energy of the incident monochromatic beam, $E_{kinetic}$ refers to the KE of the ejected electrons and ϕ is a known offset coming from the absorption of the electron by the detector. In the case of an XPS spectrum, the electron counts will be shown as a function of their binding energy, displaying bands at $E_{binding}$ values that are characteristic of the atoms present in the sample and of their immediate chemical environment.

The peaks observed in an XPS spectrum are characteristic of the material, i.e., binding energies and Auger transitions can be precisely associated to an element of the periodic table, while small changes in shape and/or position of the bands (or peaks) can be linked to the chemical environment of this element inside the sample (*e.g.* oxidation state). In addition, if several elements are present in the material, the relative abundance can be measured by integrating their XPS signal. Finally, it is possible to probe the abundance underneath the surface by either a destructive process where the surface is progressively etched with a beam of Ar^+ ion while the acquisition of the spectra is performed, or a non-destructive process whereby the angle of incidence of the beam is altered to penetrate up to a few nm in the surface. The latter is known as angle-resolved XPS (ARXPS), which is implemented in Chapters 5-6.

The valence band maxima (VBM) energy levels with respect to vacuum were deduced from UPS linear extrapolations for the VBM, secondary electron cut-off (SECO) (from the respective regions of the He-I spectra), and the corresponding ionization energy calculations.[18,19] In detail:

The work function, ϕ, is first determined following the formula:[20]

$$\phi = hv - \text{SECO}$$

where hv is the energy of the incident beam (21.22 eV). The ionization energy may then be obtained from:

$$I_E = \phi + VBM$$

XPS measurements shown in Chapters 4-6 were carried out on an Axis Supra (Kratos Analytical) instrument, where a monochromated Kα X-ray line of an aluminum anode was used. The pass energy was set to 20 eV with a step size of 0.1 eV. The samples were grounded to the sample holder by connecting the FTO underlayer to the sample stage. UPS measurements were also carried out on an Axis Supra (Kratos Analytical) using 21.22 eV photons emitted by an He-I UV source. The pass energy was set to 10 eV with a step size of 0.025 eV. Samples were electrically grounded to limit charging effects. The photoelectron intensity is presented as a function of the binding energy referenced at the Fermi level of the analyzer.

2.4 Solar Cell Characterization

2.4.1 *JV* curves

The performance of the solar cells was evaluated by recording the current-voltage (J-V) profile under illumination. The J-V profile allows to obtain key performance indicators such as the short circuit current (J_{SC}), that is, the current density achieved under illumination at zero bias; the open circuit potential (V_{OC}) which denotes the applied bias necessary to make zero the current flowing through the device. The point where the maximum power (P_{MAX}) is generated is termed as the "maximum power point", and a current density and a voltage ($P_{MAX} = J_{mp}\, V_{mp}$) are associated to it. There exist two characteristic values calculated directly from the J-V data. The fill factor (FF), which is defined as:

$$FF = \frac{J_{mp}\, V_{mp}}{J_{SC}\, V_{OC}}$$

Finally, the power conversion efficiency (PCE) of the devices is calculated as:

$$PCE = \frac{J_{SC}\, V_{OC}\, FF}{P_{in}}$$

where P_{in} is the incident power intensity.

J-V characteristics shown along Chapters 4-6 were obtained under standard AM1.5G (1 Sun) illumination using a 300 W Xe arc lamp set to 100 mW cm^{-2} with a calibrated Si photodiode (Thorlabs). The curves were recorded using a Keithley 2401 source measure unit using a scan rate of 100 mV s^{-1}. In all cases, testing was performed under nitrogen atmosphere and the active area was 0.09 cm^{2}, unless otherwise noted.

2.4.2 Incident Photon-to-current efficiency

The Incident photon-to-current efficiency (IPCE) or external quantum efficiency (EQE) refers to the charge collected per incident photon. The IPCE values are typically reported as a function of the incident wavelength, in the form of a spectrum, by using the following expression:

$$IPCE(\lambda) = \frac{1240\, J_{\lambda}\, (Acm^{-2})}{\lambda\, (nm)\, P_{\lambda}(Wcm^{-2})}$$

where λ denotes the wavelength of the monochromatic light irradiating the sample, J_{λ}denotes the short circuit current under illumination and P_{λ} refers to the incident irradiance.

The IPCE was measured by employing a tunable PowerArc illuminator (Optical Building Blocks Corporation) for monochromatic illumination and measured at short circuit conditions.

2.4.3 Transient Photocurrent measurement

Transient photocurrent (TPC) measurements consist of tracking the photocurrent response after a short light pulse. Depending on the relaxation dynamics of the photocurrent, information on the transport and recombination properties within the active film can be obtained.

The TPC results shown in Chapter 4 were obtained using a pulsed laser system (EKSPLA, NT230-50-SF-2H) at 550 nm with a 5 ns pulse duration and a 50 Hz repetition rate (12.0 nJ cm^{-2}) was employed as light source. A digital oscilloscope (Tektronix DPO7254C) was employed to record the photocurrent decay using a differential probe (TDP3500, Tektronix) under light bias. During the TPC measurements, the differential probe was connected to a sampling resistor of 50 Ω wired in series to the solar cell.

Appendix 1: Full synthetic details for NDI-based organic cations

The synthesis of NDI-diB (NDI-dibutyl), NDI-diE (NDI-diethyl) and NDI-E (NDI ethyl) were performed by Dr. Liang Yao.

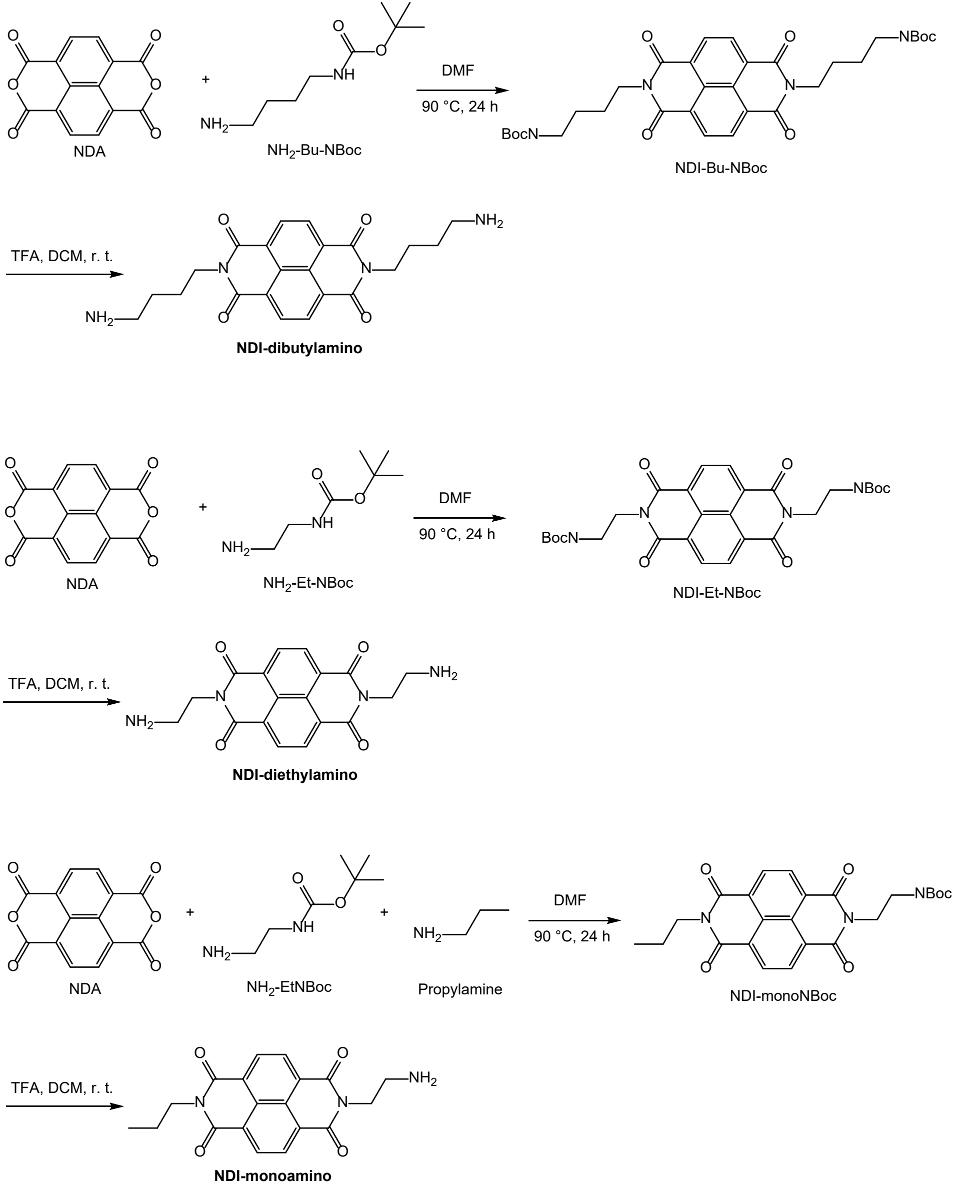
NDA
NH2-Bu-NBoc
DMF
90 °C, 24 h
NDI-Bu-NBoc
TFA, DCM, r. t.
NDI-dibutylamino
NDA
NH2-Et-NBoc
DMF
90 °C, 24 h
NDI-Et-NBoc
TFA, DCM, r. t.
NDI-diethylamino
NDA
NH2-EtNBoc
Propylamine
DMF
90 °C, 24 h
NDI-monoNBoc
TFA, DCM, r. t.
NDI-monoamino

Scheme A1.1. NDI-diB, NDI-diE and NDI-E amino synthesis

For the formation of the ammonium iodide salt of the NDI compounds, hydriodic acid (HI, 57% wt. in H_2O), with a 25% vol. excess, was added dropwise to a chilled solution of each NDI-monoamino (1:1), NDI-diethylamino (2:1) and NDI-dibutylamino (2:1). The salt crystals were then washed with diethyl ether five times and vacuum dried. The crystals were further allowed to sit and dry overnight before use.

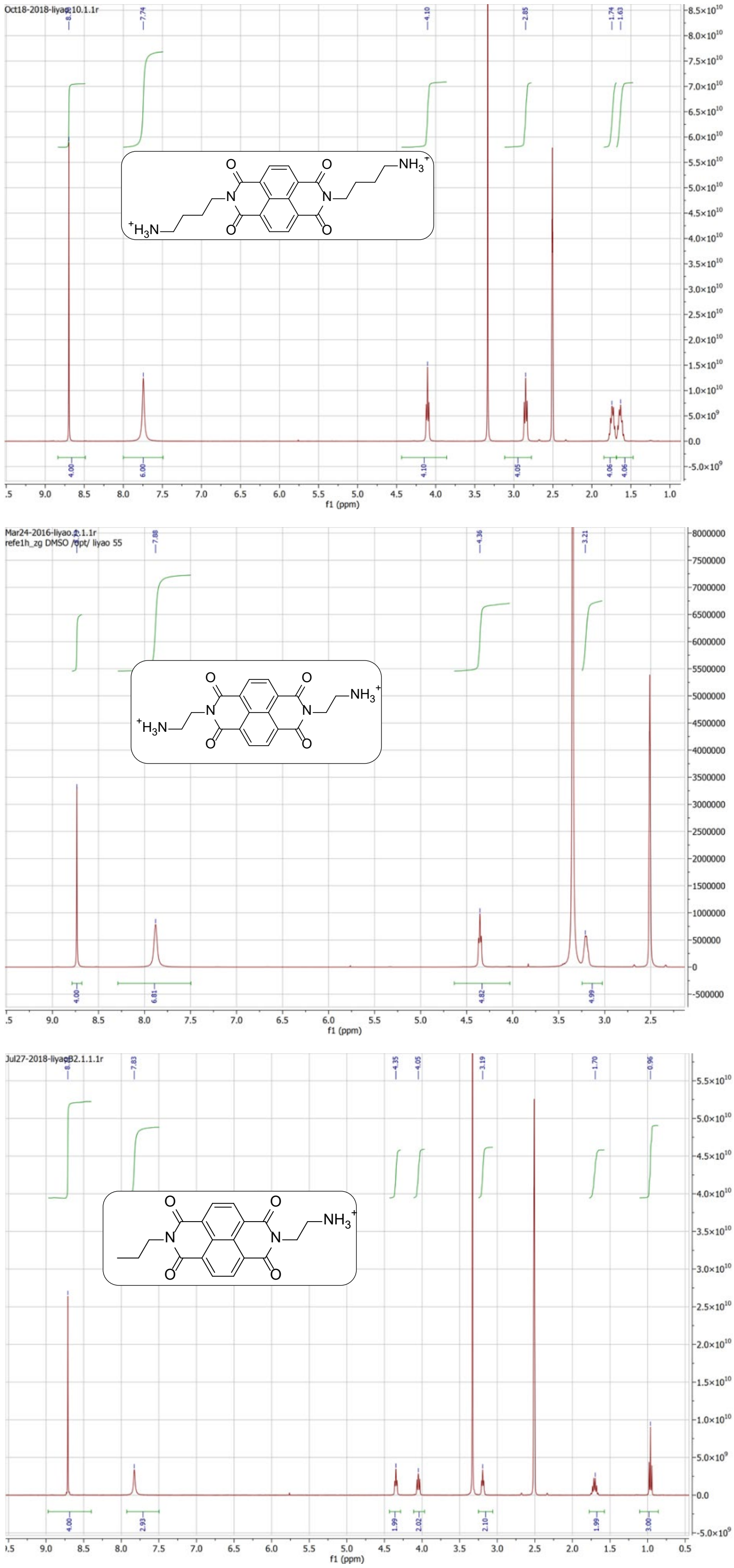

Figure A1.1. ^{1}H NMR of NDI-dibutylammonium, -diethylammonium, -monoammonium cations.

Appendix 2: Full synthetic details for BDT-based organic cations

BDT molecule synthesis and characterization were performed by Dr. Han-Hee Cho.

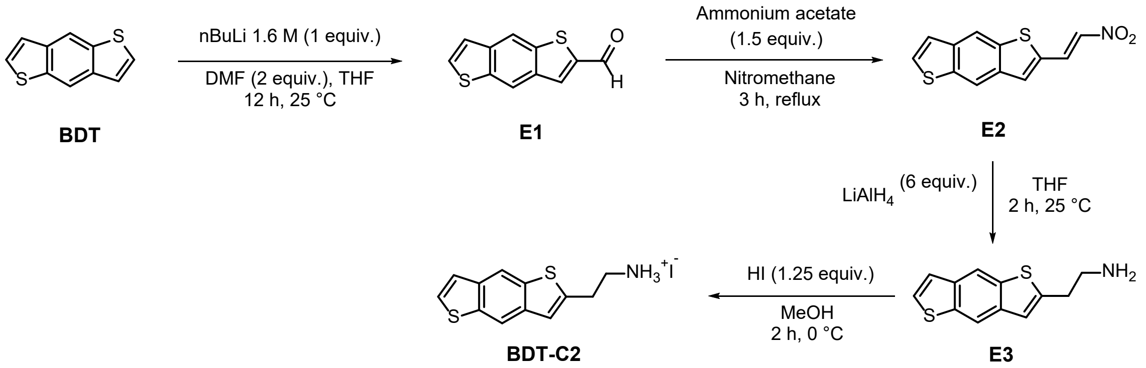
BDT
nBuLi 1.6 M (1 equiv.)
DMF (2 equiv.), THF
12 h, 25 °C
E1
Ammonium acetate
(1.5 equiv.)
Nitromethane
3 h, reflux
E2
LiAlH4 (6 equiv.)
THF
2 h, 25 °C
E3
HI (1.25 equiv.)
MeOH
2 h, 0 °C
BDT-C2

Scheme A2.1. Synthetic routes for the preparation of **BDT-C2**

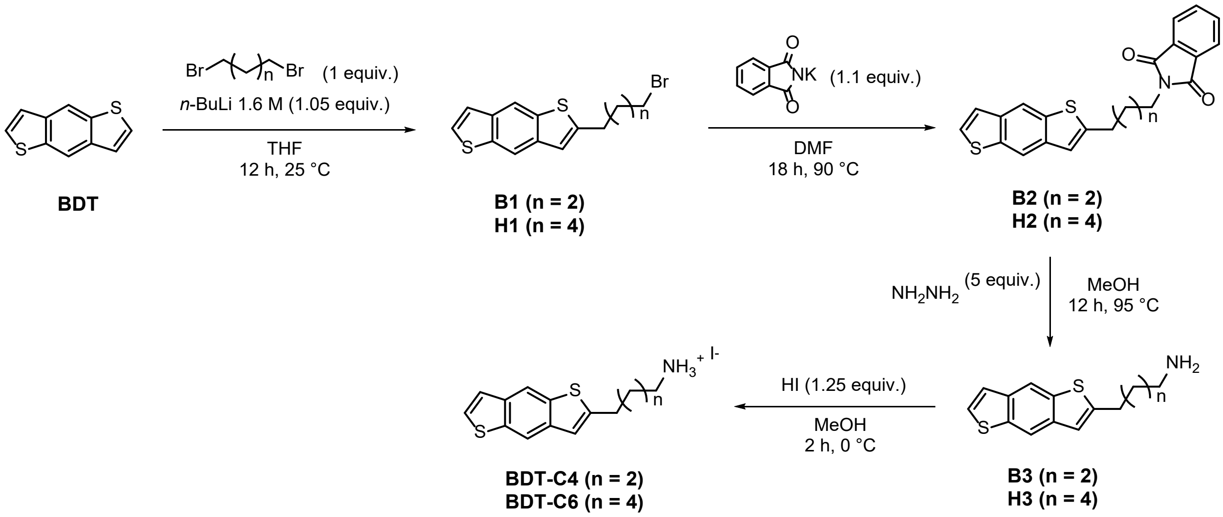
BDT
Br–(–)n–Br (1 equiv.)
n-BuLi 1.6 M (1.05 equiv.)
THF
12 h, 25 °C
B1 (n = 2)
H1 (n = 4)
NK (1.1 equiv.)
DMF
18 h, 90 °C
B2 (n = 2)
H2 (n = 4)
NH2NH2 (5 equiv.)
MeOH
12 h, 95 °C
B3 (n = 2)
H3 (n = 4)
HI (1.25 equiv.)
MeOH
2 h, 0 °C
BDT-C4 (n = 2)
BDT-C6 (n = 4)

Scheme A2.2. Synthetic routes for the preparation of **BDT-C4** and **BDT-C6**[2]

Benzo[1,2-b:4,5-b′]dithiophene-2-carbaldehyde (**E1**).

Compound **E1** was prepared following the reported procedure in the literature.[1] To a solution of BDT (2 g, 10.5 mmol) in dry THF (50 mL) *n*-BuLi (7.3 mL, 1.6 M in hexane, 11.6 mmol) was added dropwise at −78 °C and the resulting solution was stirred for 1 h at the same temperature. DMF (1.2 mL, 15.8 mmol) was added dropwise and the resulting mixture was stirred for 3 h at −78 °C. Then, the reaction was quenched by adding 100 mL of saturated aqueous NH_4Cl DI water and the aqueous solution was extracted with ethyl acetate (3 × 50 mL). The combined organic phase was washed with brine (100 mL), dried over anhydrous $MgSO_4$, and concentrated in vacuo. The residue was purified by chromatography on silica gel using hexane/DCM mixture (1:1 (v/v)) to afford **E1** as a yellow solid. Yield: 1.88 g (82%). ^1H NMR (400 MHz, $CDCl_3$) δ 10.12 (s, 1H), 8.45 (s, 1H), 8.32 (s, 1H), 8.08 (s, 1H), 7.60 (d, *J* = 5.5 Hz, 1H), 7.38 (d, *J* = 5.5 Hz, 1H).

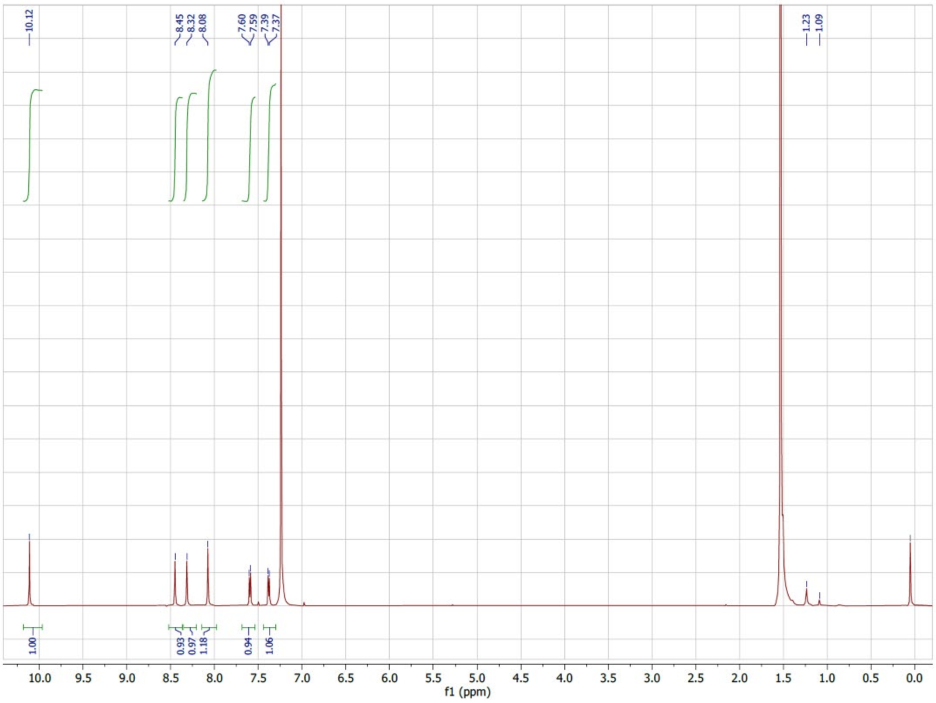

Figure A2.1. ^1H NMR spectrum of **E1**

(E)-2-(2-Nitrovinyl)benzo[1,2-b:4,5-b′]dithiophene (**E2**).

A mixture of **E1** (0.94 g, 4.3 mmol) and ammonium acetate (0.50 g, 6.5 mmol) in nitromethane (50 mL) was refluxed for 3 h and quenched by adding DI water (20 mL). The mixture was extracted with ethyl acetate (3 × 50 mL) and the combined organic phase was dried over anhydrous $MgSO_4$ and concentrated in vacuo. The residue was purified by chromatography on silica gel using hexane/DCM mixture (3:1 (v/v)) to afford **E2** as a yellow solid. Yield: 0.69 g (61%). ^1H NMR (400 MHz, $CDCl_3$) δ 8.32 (s, 1H), 8.27 (s, 1H), 8.27 (d, *J* = 13.4 Hz, 1H), 7.73 (s, 1H), 7.58 (d, *J* = 5.5 Hz, 1H), 7.47 (d, *J* = 13.4 Hz, 1H), 7.37 (d, *J* = 5.5 Hz, 1H).

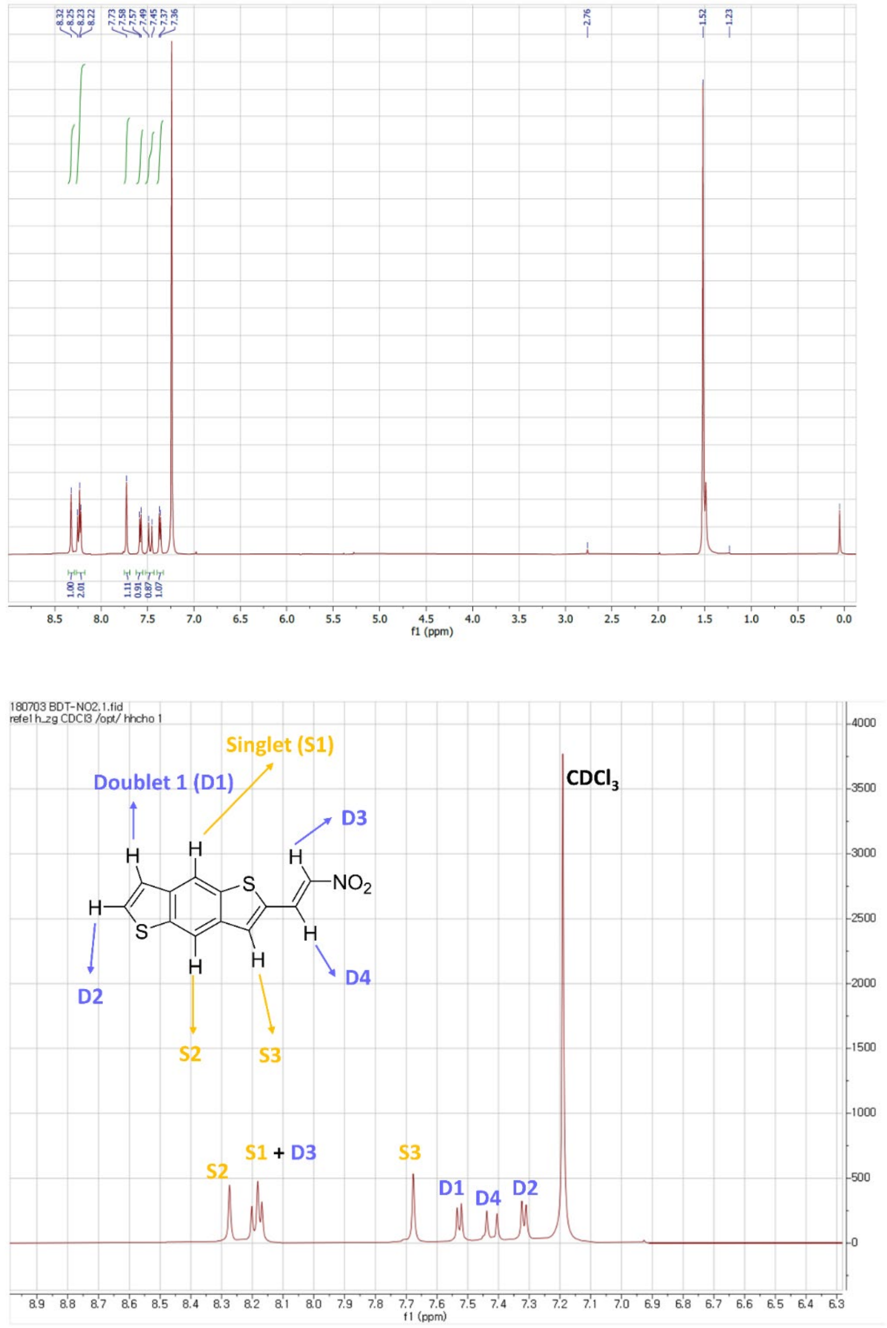

Figure A2.2. ^{1}H NMR spectrum of E2 (top) and closer view of the area of interest (bottom).

2-(Benzo[1,2-b:4,5-b′]dithiophen-2-yl)ethan-1-amine (**E3**).

To a solution of **E2** (0.36 g, 1.4 mmol) in dry THF (15 mL) was added dropwise $LiAlH_4$ (0.32 g, 8.4 mmol) in dry THF (5 mL) at 0 °C. The mixture was warmed to room temperature and stirred for 2 h. Then, the mixture was cooled to 0 °C and quenched by adding DI water (0.3 mL) slowly, followed by addition of 15% NaOH (0.3 mL) and DI water (0.9 mL). The residue was extracted with DCM (3 × 50 mL), dried over anhydrous $MgSO_4$, and concentrated in vacuo to afford **E3**. The compound **E3** was used to prepare **BDT-C2** without further purification. Yield: 0.14 g.

2-(Benzo[1,2-b:4,5-b′]dithiophen-2-yl)propan-1-aminium iodide (**BDT-C2**).

For the formation of the ammonium iodide salt of BDT-C2, hydriodic acid (HI, 57% wt. in H_2O), with a 25% vol. excess, was added dropwise to a chilled solution of **E3**. The salt crystals were then washed with diethyl ether five times and vacuum dried. The crystals were further allowed to sit and dry overnight before use.

2-(4-Bromobutyl)benzo[1,2-b:4,5-b′]dithiophene (**B1**).

To a solution of BDT (2.20 g, 11.6 mmol) in dry THF (80 mL) was added dropwise *n*-BuLi (7.6 mL, 1.6 M in hexane, 12.1 mmol) at −78 °C and the resulting solution was stirred for 1 h at the same temperature. 1,4-dibromobutane (1.4 mL, d = 1.81 g mL^{-1}, 11.6 mmol) was rapidly added. The resulting mixture was allowed to warm to room temperature slowly and stirred for overnight. Then, the reaction was quenched by adding 100 mL of DI water; the aqueous solution was then extracted with diethyl ether (3 × 100 mL). The combined organic phase was washed with brine (150 mL), dried over anhydrous $MgSO_4$, and concentrated in vacuo. The residue was purified by chromatography on silica gel using hexane/DCM mixture (4:1 (v/v)) to afford **B1** as a pale-yellow solid. Yield: 1.28 g (34%). ^1H NMR (400 MHz, $CDCl_3$): δ 8.19 (d, *J* = 17.2 Hz, 2H), 7.45 (d, *J* = 5.6 Hz, 1H), 7.36 (d, *J* = 5.5 Hz, 1H), 7.06 (s, 1H), 3.48 (t, *J* = 6.0 Hz, 2H), 2.99 (t, *J* = 6.8 Hz, 2H), 2.01 – 1.73 (m, 4H).

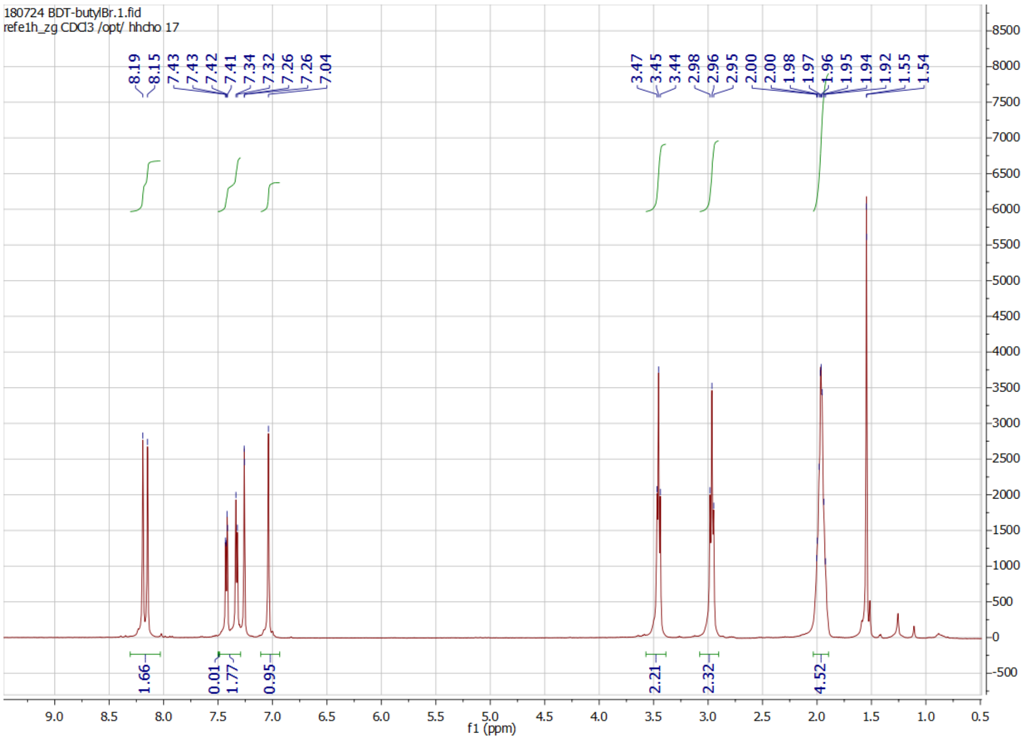

Figure A2.3. ^{1}H NMR spectrum of **B1**

2-(4-(Benzo[1,2-b:4,5-b']dithiophen-2-yl)butyl)isoindoline-1,3-dione (**B2**).

A mixture of **B1** (1.28 g, 4.0 mmol) and potassium phthalimide (0.76 g, 4.2 mmol) in DMF (50 mL) was stirred at 90 °C for 18 h. After cooling, the mixture was poured into DI water (200 mL) and extracted with DCM (150 mL). The combined organic phase was washed with 0.2 M KOH (100 mL), DI water (200 mL), and saturated aqueous NH_4Cl. Then, the resulting organic phase was dried over anhydrous $MgSO_4$ and concentrated in vacuo. The residue was purified by chromatography on silica gel using hexane/DCM mixture (1:1.5 (v/v)) to afford **B2** as a white solid. Yield: 1.30 g (84%). ^{1}H NMR (400 MHz, $CDCl_3$) δ 8.12 (d, *J* = 13.4 Hz, 2H), 7.81 (dd, *J* = 5.4, 3.2 Hz, 1H), 7.68 (dd, *J* = 5.5, 3.0 Hz, 1H), 7.39 (d, *J* = 5.5 Hz, 1H), 7.30 (d, *J* = 5.5 Hz, 1H), 7.01 (s, 1H), 3.73 (t, *J* = 6.5 Hz, 2H), 2.95 (t, *J* = 6.8 Hz, 2H), 1.90 – 1.71 (m, 4H).

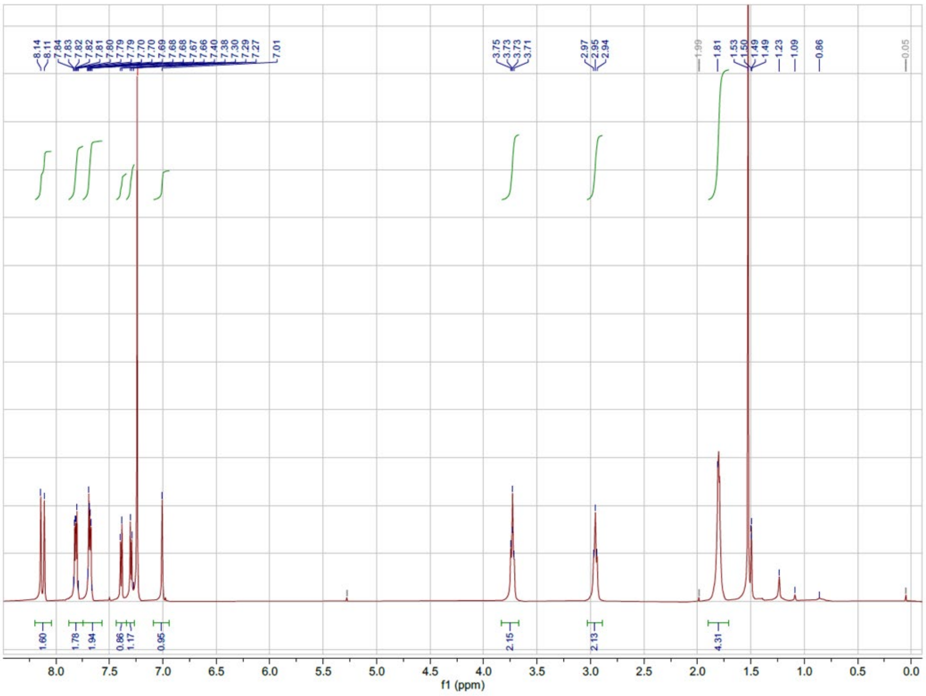

Figure A2.4. ^{1}H NMR spectrum of **B2**

4-(Benzo[1,2-b:4,5-b′]dithiophen-2-yl)butan-1-amine (**B3**).

To a solution of **B2** (1.3 g, 3.3 mmol) in methanol (100 mL) hydrazine hydrate (0.81 mL, 16.5 mmol) was added slowly and the reaction mixture was refluxed for 12 h. After cooling to room temperature, methanol was removed under reduced pressure and DCM (200 mL) was added. The organic phase was washed with 10% KOH (50 mL) and dried over anhydrous $MgSO_4$. After filtration, the solvent was evaporated to afford **B3** as a yellow solid. The compound **B3** was used to prepare **BDT-C4** without further purification. Yield: 0.84 g.

4-(Benzo[1,2-b:4,5-b′]dithiophen-2-yl)butan-1-aminium iodide (**BDT-C4**).

For the formation of the ammonium iodide salt of BDT-C4, hydriodic acid (HI, 57% wt. in H_2O), with a 25% vol. excess, was added dropwise to a chilled solution of **B3**. The salt crystals were then washed with diethyl ether five times and vacuum dried. The crystals were further allowed to sit and dry overnight before use.

2-(6-Bromohexyl)benzo[1,2-b:4,5-b′]dithiophene (**H1**).

Compound **H1** was prepared by a similar procedure described for **B1** using 1,4-dibromohexane (3.2 mL, d = 1.59 g mL^{-1}, 21.0 mmol). Yield: 2.52 g (34%). ^{1}H NMR (400 MHz, $CDCl_3$) δ 8.15 (d, *J* = 18.7 Hz, 2H), 7.39 (d, *J* = 5.6 Hz, 1H), 7.31 (d, *J* = 14.2 Hz, 1H), 7.00 (s, 1H), 3.39 (t, *J* = 6.8 Hz, 2H), 2.90 (t, *J* = 7.8 Hz 2H), 1.89 – 1.63 (m, 4H), 1.50 – 1.36 (m, 4H).

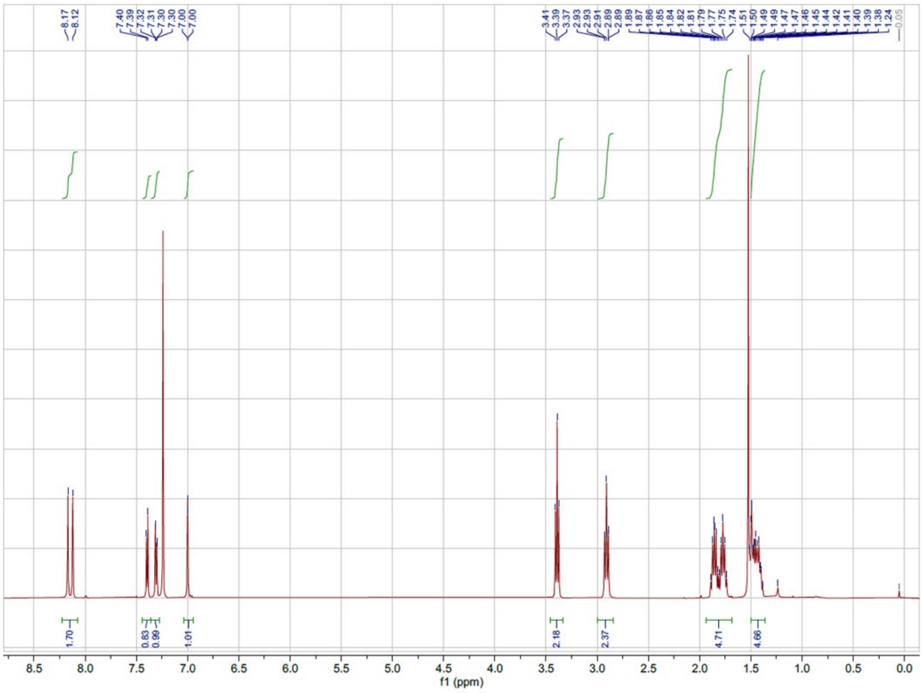

Figure A2.5. ^{1}H NMR spectrum of **H1**

2-(6-(Benzo[1,2-b:4,5-b′]dithiophen-2-yl)hexyl)isoindoline-1,3-dione (**H2**).

Compound **H2** was prepared by a procedure similar to that described for **B2** using **H1** (2.52 g, 7.1 mmol). Yield: 2.66 g (89%). ^{1}H NMR (400 MHz, $CDCl_3$) δ 8.13 (d, *J* = 19.4 Hz, 2H), 7.81 (dd, *J* = 5.4, 3.0 Hz, 2H), 7.68 (dd, *J* = 5.5, 3.1 Hz, 2H), 7.39 (d, *J* = 5.5 Hz, 1H), 7.30 (d, *J* = 5.6 Hz, 1H), 6.98 (s, 1H), 3.67 (t, *J* = 7.2 Hz, 2H), 2.89 (t, *J* = 7.5 Hz, 2H), 1.81 – 1.63 (m, 4H), 1.48 – 1.33 (m, 4H).

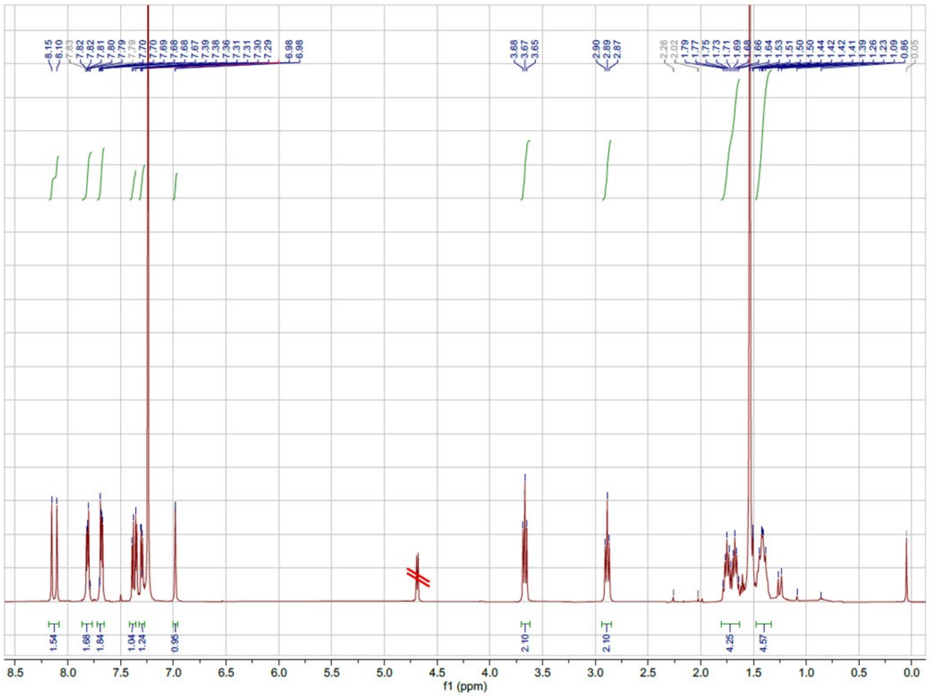

Figure A2.6. ^1H NMR spectrum of **H2**

6-(Benzo[1,2-b:4,5-b′]dithiophen-2-yl)hexan-1-amine (**H3**).

Compound **H3** was prepared by a procedure similar to that for **B3** using **H2** (2.66 g, 6.3 mmol). Yield: 1.81 g.

6-(Benzo[1,2-b:4,5-b′]dithiophen-2-yl)hexan-1-aminium iodide (**BDT-C6**).

For the formation of the ammonium iodide salt of BDT-C6, hydriodic acid (HI, 57% wt. in H_2O), with a 25% vol. excess, was added dropwise to a chilled solution of **H3**. The salt crystals were then washed with diethyl ether five times and vacuum dried. The crystals were further allowed to sit and dry overnight before use.

References

[1] N. Gigant, E. Claveau, P. Bouyssou, I. Gillaizeau, *Org. Lett.* **2012**, *14*, 844.

[2] X. A. Jeanbourquin, A. Rahmanudin, X. Yu, M. Johnson, N. Guijarro, L. Yao, K. Sivula, *ACS Appl. Mater. Interfaces* **2017**, *9*, 27825.

[3] K. Du, Q. Tu, X. Zhang, Q. Han, J. Liu, S. Zauscher, D. B. Mitzi, *Inorganic Chemistry* **2017**, *56*, 9291.

[4] J. V. Passarelli, D. J. Fairfield, N. A. Sather, M. P. Hendricks, H. Sai, C. L. Stern, S. I. Stupp, *J. Am. Chem. Soc.* **2018**, *140*, 7313.

[5] Z. Huang, D. Wang, S. Wang, T. Zhang, *Materials (Basel)* **2018**, *11*, 778.

[6] K. Yan, M. Long, T. Zhang, Z. Wei, H. Chen, S. Yang, J. Xu, *Journal of the American Chemical Society* **2015**, *137*, 4460.

[7] M. Saliba, J.-P. Correa-Baena, C. M. Wolff, M. Stolterfoht, N. Phung, S. Albrecht, D. Neher, A. Abate, *Chem. Mater.* **2018**, *30*, 4193.

[8] D. A. Lee, *Inorg. Chem.* **1964**, *3*, 289.

[9] E. Greul, M. L. Petrus, A. Binek, P. Docampo, T. Bein, *J. Mater. Chem. A* **2017**, *5*, 19972.

[10] A. A. Bunaciu, E. G. Udriştioiu, H. Y. Aboul-Enein, *Crit Rev Anal Chem* **2015**, *45*, 289.

[11] Å. Kvick, in *Encyclopedia of Spectroscopy and Spectrometry* (Ed.: J.C. Lindon), Elsevier, Oxford, **1999**, pp. 1248–1257.

[12] H. Cheng, C. Lu, J. Liu, Y. Yan, X. Han, H. Jin, Y. Wang, Y. Liu, C. Wu, *Progress in Natural Science: Materials International* **2017**, *27*, 66.

[13] J. Tauc, R. Grigorovici, A. Vancu, *physica status solidi (b)* **1966**, *15*, 627.

[14] J. Halme, *Phys. Chem. Chem. Phys.* **2011**, *13*, 12435.

[15] N. Parikh, S. Narayanan, H. Kumari, D. Prochowicz, A. Kalam, S. Satapathi, S. Akin, M. M. Tavakoli, P. Yadav, *Phys. Status Solidi RRL* **2021**, 210051.

[16] E. Ghahremanirad, A. Bou, S. Olyaee, J. Bisquert, *J. Phys. Chem. Lett.* **2017**, *8*, 1402.

[17] B. Campanella, V. Palleschi, S. Legnaioli, *ChemTexts* **2021**, *7*, 5.

[18] B. Philippe, T. J. Jacobsson, J.-P. Correa-Baena, N. K. Jena, A. Banerjee, S. Chakraborty, U. B. Cappel, R. Ahuja, A. Hagfeldt, M. Odelius, H. Rensmo, *J. Phys. Chem. C* **2017**, *121*, 26655.

[19] A. Agresti, A. Pazniak, S. Pescetelli, A. Di Vito, D. Rossi, A. Pecchia, M. Auf der Maur, A. Liedl, R. Larciprete, D. V. Kuznetsov, D. Saranin, A. Di Carlo, *Nat. Mater.* **2019**, *18*, 1228.

[20] H. Zhang, D. Zhang, X. Lu, C. Liu, G. Zhou, X. Ma, L. Wang, P. Jiang, Q.-K. Xue, X. Bao, *Nat. Commun.* **2017**, *8*, 214.

Chapter 3

NDI Layered Lead-Halide Perovskites

Synthesis attempts of 2D perovskites based on Naphthalene Diimide functional molecules

This Chapter covers synthesis attempts of NDI-based layered lead halide perovskites via several methods, a solution-based approach, a powder synthesis approach and a mixed-cation approach together with a well-established cation system. Namely, for the latter, attempts at the gradual incorporation of NDI-based layered perovskites into the well-established phenyl ethyl ammonium (PEA)-based layered perovskite structure are presented in order to understand if the PEA-based 2D perovskite can serve as a scaffold structure for the guiding and eventual incorporation of larger, and functional, organic cations such as NDI. In this work, three different NDI molecular variants with various salt side chain conformations are tested. Findings from this initial chapter are informative with regards to the design rules and limitations of functional cation incorporation into layered lead halide perovskite structures.

3.1 Introduction

The realm of organic chemistry provides an infinite library of chromophore cation candidates to be tested as viable active spacer options for the fabrication of layered lead-halide perovskites. Indeed, the viability of the cationic incorporation depends on limitations such as cation size, for which the boundaries have not yet been established in the literature, while playing a crucial role in the outcome of photogenerated carriers.[1] In fact, chromophore cations would allow for elegant modifications of layered perovskite energy levels, bandgaps and charge carrier transport properties.[2] For instance, for benzylammonium, naphtylmethylammonium and pyrenemethylammonium-based molecular cations, Elshanawany *et al.*, have observed the ultrafast energy transfer between the lead halide inorganic layers and the singlet and triplet states of the molecular cation layers.[3] Moreover, large organic cations can likewise serve the purpose of increasing the moisture resistance of lead halide perovskites, a well-known trigger for perovskite instability, while also contributing towards structural stability via appropriate and rigid organic-inorganic layer chemical bonding.[4]

The naphthalene diimide molecule (NDI), absorbing light in the range of 300 to 500 nm, stands out as an interesting candidate for chromophore incorporation into 2D halide perovskites, by improving the visible light-absorbing capabilities of the resulting perovskite, if successfully formed, while harnessing the charge-transporting abilities of the NDI molecular structure. In fact, numerous works have reported the implementation of the NDI molecule as an effective electron transport layer in perovskite photovoltaic devices, for instance those by Kurdi et.al,[5] Heo *et al.*,[6] Jung *et al.*,[7–9] Nakamura *et al.*,[10] to name a few. The NDI molecule has great potential applications in perovskite photovoltaics, given the versatility of the core in attaching solubilizing functional groups, which could prevent aggregate formation and enhance its solubility.[11] Furthermore, as reported in computational studies, the NDI molecule can act as an electron-withdrawing group in the 2D halide perovskite structure while also participating in charge transport.[12] Given the many encouraging reports on the versatility and prospects of the NDI molecule, this work attempts the incorporation of various NDI molecular cation derivatives into layered lead halide perovskites.

3.2 Results and Discussion

In this work, three NDI molecule variants were studied (**Figure 3.1**) for implementation as cations in lead-based layered lead halide perovskites. These are, namely, a non-symmetric NDI ethyl ammonium (**NDI-E**) (with a light absorption onset at 550 nm) cation and the symmetric NDI diethyl ammonium (**NDI-diE**) (with a light absorption onset at 600 nm) and NDI dibutyl ammonium (**NDI- diB**) (with a light absorption onset at 670 nm) cations (**Figure 3.2b**).

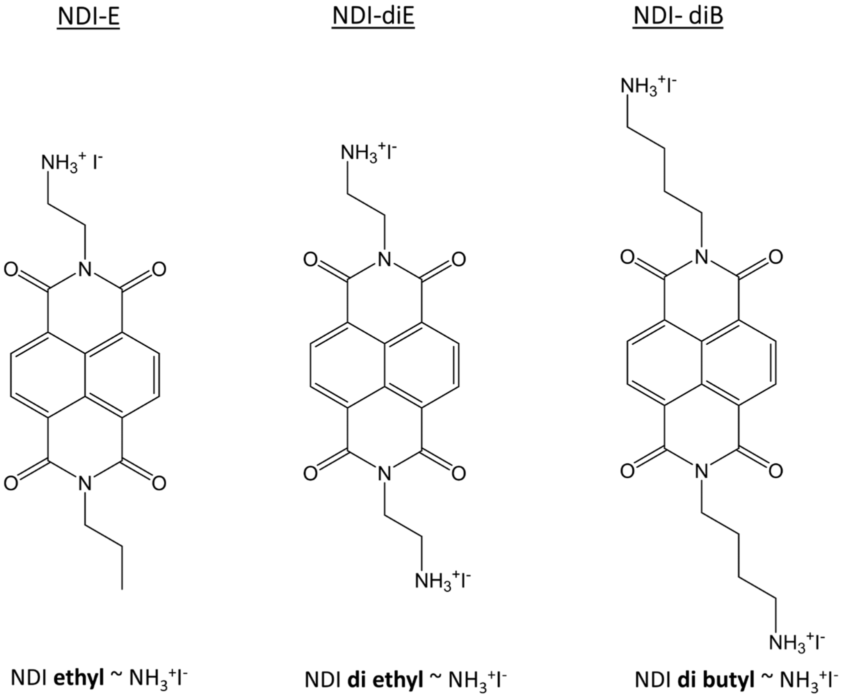

Figure 3.1. NDI molecular variants: (a) NDI ethyl ammonium iodide (NDI-E), (b) NDI diethyl ammonium iodide (NDI-diE) and (c) NDI dibutyl ammonium iodide (NDI-diB).

Namely, for the asymmetric cationic structure, the formula corresponding to a well-formed single-layered lead halide perovskite structure is: A_2PbI_4, corresponding to a Ruddlesden-Popper structure, where A represents the asymmetric cation, *i.e.* NDI-E. Whereas, for a symmetric cation, a Dion-Jacobson perovskite structure would instead be formed, with perovskite inorganic slabs stacking exactly one over the other (as opposed to a slight stacking distortion, as is the case with the Ruddlesden-Popper structures) while the symmetric cationic species place themselves as anchored interlayers.[13] Given the double cationic charge nature of symmetric cationic structures, the formula for a single layered lead halide perovskite structure formed from these would now be $APbI_4$. Being aware of the two different types of perovskite structures that could be synthesized either with asymmetric or symmetric NDI cations, thin films from each were prepared in the relevant stoichiometries (synthetic details for the NDI cations and the perovskites are presented in **Chapter 2**).

The photoluminescence (PL) spectra as well as X-ray diffraction (XRD) patterns for the NDI chromophores alone were first studied, these are helpful in later determining whether any chromophore precursor aggregates remain in the final perovskite structures to be synthesized. Namely, the NDI-E chromophore presents strong x-ray diffraction with the initial peaks within the range of interest for 2D halide perovskites (at low 2θ diffraction angles) at 3.8, 7.47 and 11.13 ^{0} (2θ); the NDI-diE presents weaker crystallinity (as defined from the observable wider peak widths) with diffraction at 8.15 ^{0} (2θ) within the range of interest while the NDI-diB presents diffraction at 4.77, 8.76 and 9.50 ^{0} (2θ) (**Figure 3.2a**). The NDI-E chromophore variant exhibits a photoluminescence peak at 415 nm, while NDI-diE and NDI-diB have photoluminescence peaks at 410 and 405 nm (less-defined), respectively (**Figure 3.2c**).

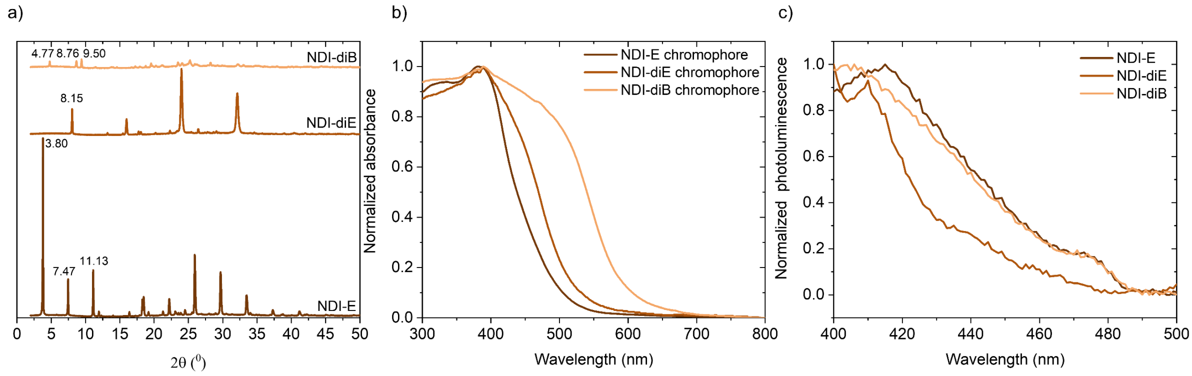

Figure 3.2. NDI-based chromophore characterization. (a) X-ray diffraction patterns, (b) UV-vis absorption and (c) photoluminescence spectra (375 nm excitation).

3.2.1 The Solution-based Approach

As an initial approach, the solution-based incorporation of NDI-E into Pb-I-based octahedral layers was attempted. Both partial and full incorporation of NDI-E into layered perovskites was attempted, where full incorporation means only the NDI-E was included as the A-site cation in the precursor solution, whereas in partial incorporation attempts several ratios of NDI-E and the well-known 2D perovskite A-site cation, phenylethylammonium, or PEAI, were tested.

Solutions were prepared following the conditions indicated on **Table 3.1**.

Table 3.1. Stoichiometries for partial and full NDI-E incorporation attempts into 2D perovskites

Desired 2D halide perovskite formula	**NDI-E mol fr.**	**PEA mol fr.**	**PbI_2 mol fr.**
PEA_2PbI_4	0.00	0.67	0.33
$PEA_{1.9}NDI\text{-}E_{0.1}PbI_4$	0.03	0.63	0.33
$PEA_{1.75}NDI\text{-}E_{0.25}PbI_4$	0.08	0.58	0.33
$PEA_{1.5}NDI\text{-}E_{0.5}PbI_4$	0.17	0.50	0.33
$PEA_1NDI\text{-}E_1PbI_4$	0.33	0.33	0.33
$NDI\text{-}E_2PbI_4$	0.67	0.00	0.33

The respective solutions of NDI-E and PbI_2 in DMF were combined, resulting in a NDI-E + PbI_2 solution with a 2:1 ratio of chromophore to PbI_2 as described on **Chapter 2**, following 2D halide perovskite stoichiometry for an asymmetric cation; the mixture solution was spun coat into a thin film at 3000 rpm for 30 s (followed by thermal annealing at 100 ˚C for 10 min). This method along with others that will be further presented on this work are schematically depicted on **Figure 3.3**.

A complete description of the experimental details can be found in **Chapter 2**.

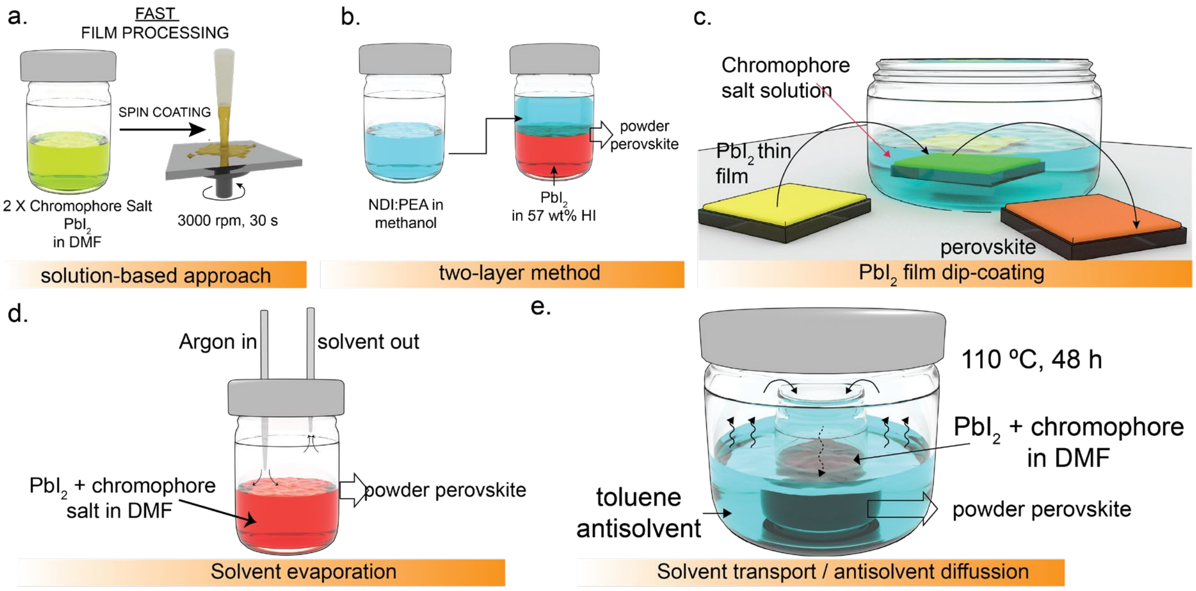
a.
FAST FILM PROCESSING
SPIN COATING
2 X Chromophore Salt
PbI2
in DMF
3000 rpm, 30 s
solution-based approach
b.
NDI:PEA in methanol
PbI2 in 57 wt% HI
powder perovskite
two-layer method
c.
Chromophore salt solution
PbI2 thin film
perovskite
PbI2 film dip-coating
d.
Argon in
solvent out
PbI2 + chromophore salt in DMF
powder perovskite
Solvent evaporation
e.
110 °C, 48 h
PbI2 + chromophore in DMF
toluene antisolvent
powder perovskite
Solvent transport / antisolvent diffussion

Figure 3.3. Chromophore molecular cation incorporation methods studied towards 2D halide perovskite synthesis. (a) Solution-based method, (b) two-layer method, (c) PbI_2 film dip-coating into a chromophore solution, (d) solvent evaporation and (e) solvent transport/antisolvent diffusion.

The solution-based approach (**Figure 3.3a**), however, led to no thin film crystallization for a full incorporation attempt of NDI-E, as confirmed by the absence of X-ray diffraction peaks, especially around 5 degrees (2θ), corresponding to diffraction signals for interlayer spacings of 2D halide perovskite materials (**Figure 3.3a**, 67 mol% NDI-E). Hence the partial incorporation of NDI-E, *i.e.* in 3, 8, 17 and 33 mol% NDI-E mixed in with PEA_2PbI_4 was attempted, where crystallinity was strongly conserved for 3 mol% NDI-E incorporation, and consecutively weakened until 33 mol% NDI-E incorporation in the system, while a clear increase in the interlayer spacing was observed (**Figure 3.4a**, 3-33 mol% NDI-E). Namely, interplanar spacings were calculated from the first diffraction peak following Bragg's law. First, the corresponding d-spacing of 16Å was calculated for PEA_2PbI_4, with a P21/c space group;[14] Moreover, a greater amount of NDI-E in the system correlated with a greater interlayer spacing (**Figure 3.4a**). Moreover, incorporation of NDI-E demonstrated to induce a slight blue shifting of the UV-vis absorption spectrum, which suggests that the incorporated NDI-E is affecting the optoelectronic properties of the host PEA-based halide perovskite. It has been reported that as a result of increased spacing, reduced orbital overlap between the lead iodide planes leads to an increase in the band gap of the resulting material.[15] In addition, the sharp absorption peak centered around 510 nm decreases with NDI-E incorporation

(**Figure 3.4b**). This trend appears to go in parallel with the loss in crystallinity of the system, and probably emerges from the structural disruption caused by increased amounts of NDI-E.

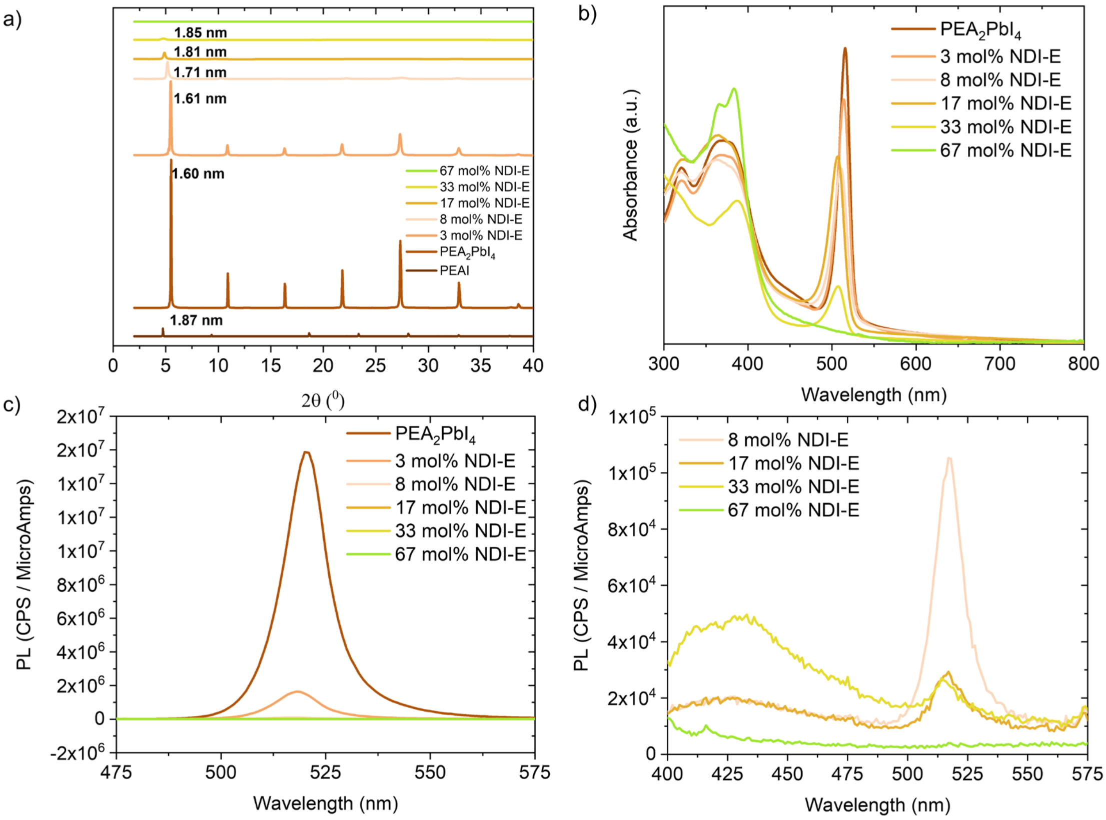

Figure 3.4. (a) XRD patterns, (b) UV-vis absorption and (c) photoluminescence spectra (d) including a zoom-in, for PEA_2PbI_4 thin films prepared by the solution-based approach and varying NDI-E contents from 0 to 67 mol% (375 nm excitation).

Note that for 67 mol% incorporation of NDI-E, only an absorption band at around 375-400 nm which matches quite well with that of NDI-E is observed. The photoluminescence peak around 520 nm characteristic of the PEA_2PbI_4 perovskite is similarly blue-shifted for increasing amounts of NDI (**Figure 3.4 c** and **d**), possibly indicating charge transfer from the Pb-I-based octahedral layers to the organic NDI-E chromophore.

Furthermore, GIWAXS data (**Figure 3.5a-f**) show a decrease in the degree of out-of-plane orientation of the 2D halide perovskite grains with an increasing percentage of NDI-E, which correlates with and can be expected from the decreased degree of crystallinity observed in the XRD thin film measurements (**Figure 3.4a**).

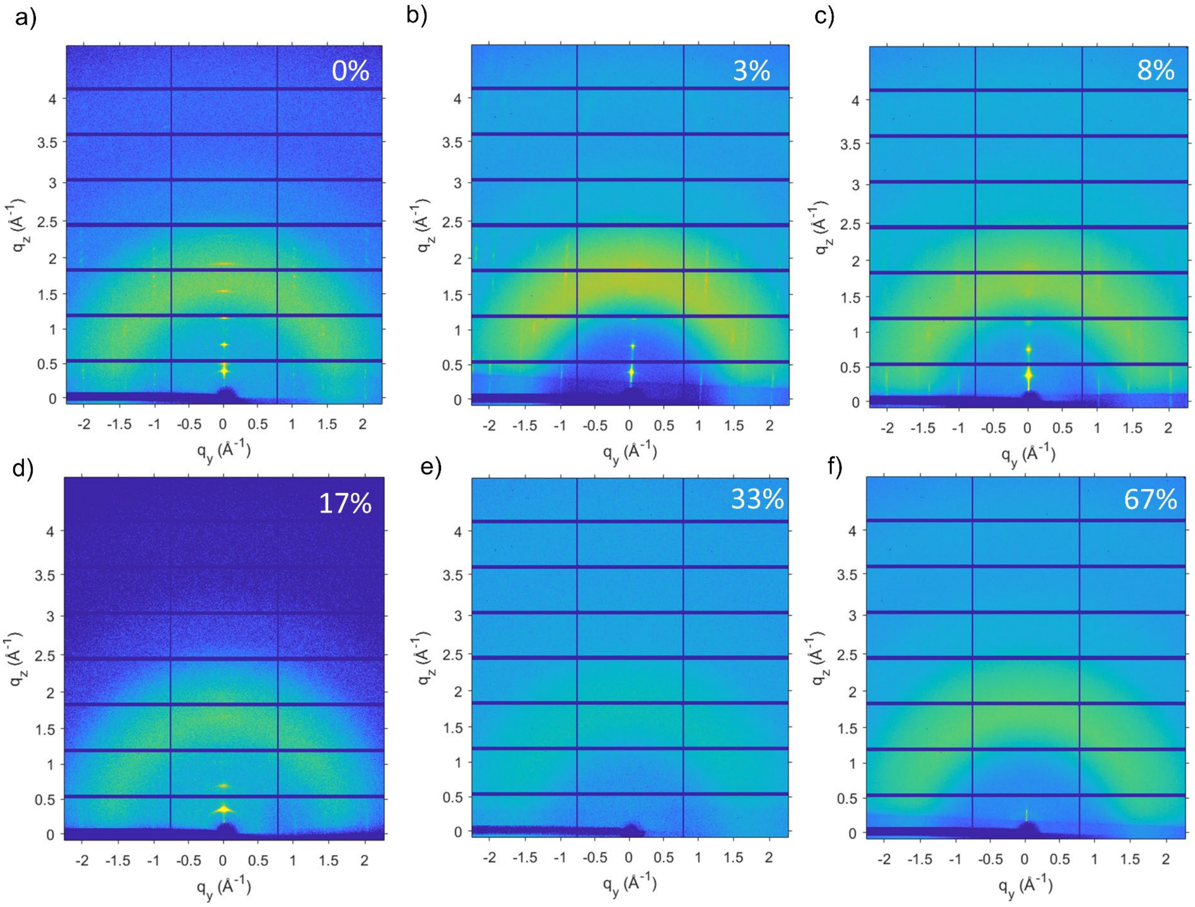

Figure 3.5. GIWAXS data for all prepared films with (PEA and/or NDI-E)$_2$PbI$_4$.

In view of these preliminary measurements, it was hypothesized that the thin film deposition method would kinetically trap the structure into an amorphous state originating from a kinetically-fast attempt at thin film crystallization. Therefore, a kinetically slower 2D halide perovskite formation method, more specifically a two-layer 2D halide perovskite single crystal synthesis method (**Figure 3.3b**), adapted from that reported in the literature was attempted.[16]

3.2.2 The Two-layer Method

For the two-layer method, a solution of an NDI-E:PEAI mixture in methanol was prepared and placed on top of a PbI$_2$ in hydriodic acid (HI) solution, allowing the cations to slowly diffuse to the interface. From the stoichiometries listed on **Table 3.1**, the two-layer systems presented on **Figure 3.6** were established. However, solubility constraints arose for systems with 8-33 mol% NDI-E, whereby the mixture of NDI-E and PEAI in the methanol top layer led to a precipitate. Nevertheless, powder products could be collected from all two-layer systems.

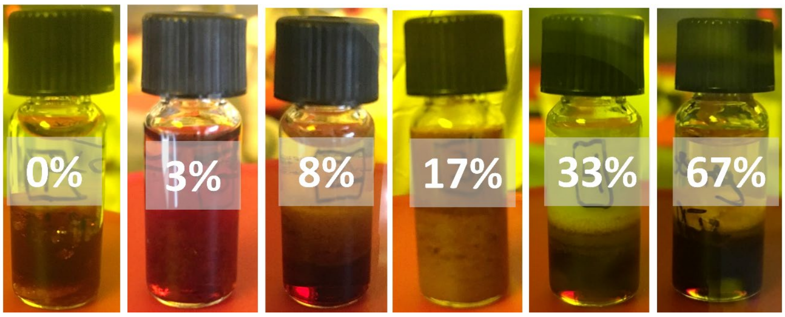

Figure 3.6. Solutions prepared with the two-layer method for PEA_2PbI_4 (0% NDI-E) and PEA_2PbI_4 with 3-67 mol% NDI-E in the system.

The films resulting from the re-dissolution of the crystals/powders obtained from the two-layer method resulted in a lower degree of system crystallinity with NDI-E present in the system compared to that obtained with the solution-based approach; with the two-layer method system crystallinity could only be conserved up until 3 mol% NDI-E in the system (Figure 3.7**a**), whereas with the solution-based approach crystallinity in the system could be conserved with up to 33 mol% NDI-E in the system. Furthermore, absorbance peaks corresponding to PEA_2PbI_4 are absent for samples with 8 mol% NDI-E in the system and above (**Figure 3.7b**), as well as the corresponding photoluminescence (**Figure 3.7c** and **d**). However similarly to the solution-based approach, comparing the 0 mol% NDI-E system with the 3 mol% NDI-E system, a greater amount of NDI-E leads to both greater interplanar spacings as well as to a blue-shifting of the absorption and photoluminescence peaks. In the case of the two-layer method, clear photoluminescence around 420 nm corresponding to NDI-E (**Figure 3.2c**) is observed for all samples, however, interestingly this photoluminescence decreases for increasing percentages of NDI-E in the system without any rising photoluminescence elsewhere in the spectrum; this indicates the possibility of a higher degree of NDI-E stacking for greater NDI-E amounts, leading to quenching of the photoluminescence, such stacking effects on photoluminescence quenching were similarly observed for increasing concentrations of asymmetric i-Indigo molecules, as reported.[17] For the 3 mol% NDI-E system however, the NDI-E photoluminescence is lower than that for greater NDI-E percentages, indicating the possible charge transfer from NDI-E to the Pb-I octahedral layers, which is otherwise not possible given the stacking as well as the more amorphous nature that arises with greater NDI-E content.

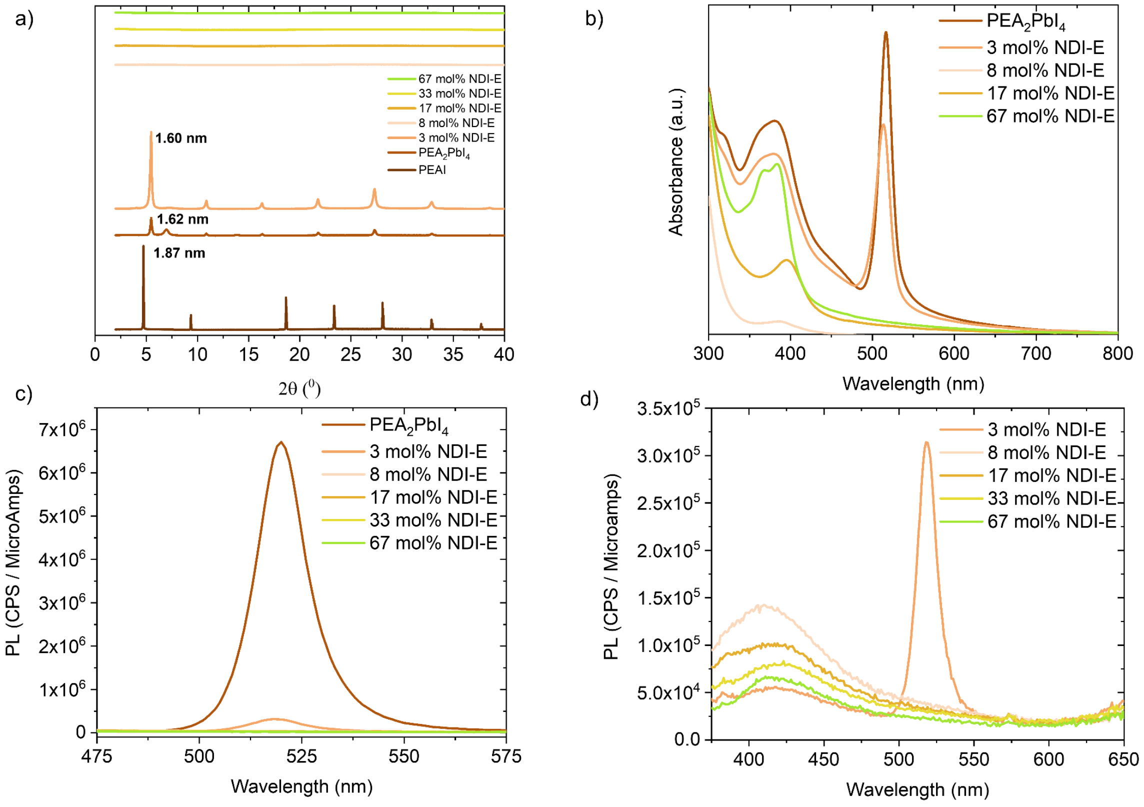

Figure 3.7. NDI-E incorporation into PEA_2PbI_4 for samples with 0-67 mol% NDI-E content with the two-layer method. (a) XRD patterns of NDI-E containing samples in addition to the PEAI precursor, (b) UV-vis absorption spectra, (c) photoluminescence spectra and (d) zoom-in photoluminescence spectra of samples with 8-67% NDI-E (350 nm excitation).

It is important to note that the powders obtained with the two-layer method were re-dissolved and spun coat, hence the kinetically fast method still plays a role in the two-layer method for film deposition though crystals/powders are first synthesized with a kinetically slow procedure. Furthermore, the precipitate formation for samples with 8 mol% NDI-E and greater could have led to the improper incorporation of NDI-E in the system.

3.2.3 The PbI_2 Film Dip-coating Method

Given the low degree of incorporation and solubility issues for NDI-E incorporation with the kinetically slower two-layer method, a two-step deposition method was attempted (**Figure 3.3c**), which would bring about a kinetically-slower method and would simultaneously lead to a film deposition method without the need for powder re-dissolution. However, the film resulting from immersion of a PbI_2 thin film into an NDI-E solution in isopropyl alcohol (IPA) was not uniformly coated with the halide perovskite product, where patches of the NDI-E containing halide perovskite form on the surface; these were analyzed with X-ray diffraction (**Figure 3.8**):

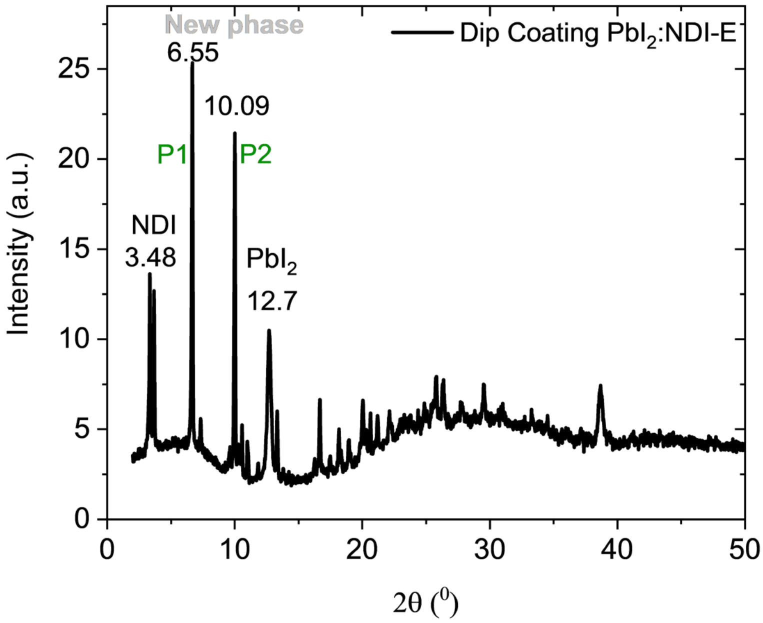

Figure 3.8. X-ray diffraction pattern of the film resulting from dip coating PbI_2 into an NDI-E solution in IPA, P1 and P2 represent new phases not ascribed to either precursor and could possibly represent a new 2D halide perovskite phase.

The film resulting from the dip-coating method displayed the first peaks under 10° (2θ) observed for the NDI-E in PbI_2 system, not corresponding to the NDI precursor, (**Figure 3.8**), however, still a certain degree of amorphous character and impurity in the system are observed through the remaining peaks, which are assigned to NDI-E and PbI_2; these impurities were clearly visible with the naked-eye. Following the NDI-E chromophore precursor XRD peaks on **Figure 3.2a**, the peak at 3.48° (2θ) (**Figure 3.8**) was assigned to the NDI-E 3.80° (2θ) peak, whereas the peaks at 6.55° and 10.09° (2θ) (P1 and P2, respectively) were assigned to the possibly new 2D halide perovskite phase, though there are two similar peaks for the NDI-E chromophore precursor within approximately 1° (2θ) from these at 7.47° and 11.13° (2θ), respectively (**Figure 3.2a**). Nevertheless, given the non-uniformity of the film, a further kinetically slow method for single crystal synthesis was attempted, the solvent evaporation system and consequently the solvent transport/antisolvent diffusion method.

3.2.4 The Solvent evaporation and solvent transport/antisolvent diffusion methods

Following evaporation of the DMF solvent from an NDI-E and PbI_2 solution (**Figure 3.3d**), remaining PbI_2 could be clearly observed instead of the desired homogenous halide perovskite powder. Hence the product was not collected and was instead re-dissolved for the solvent transport/antisolvent diffusion method (**Figure 3.3e**). In this case, after 48 h of heating the solution in the toluene antisolvent environment at 110 °C, a brown powder could be collected which was dissolved in DMF and drop cast, yielding once again the peaks under 10° (2θ) observed with the PbI_2 film dip-coating in NDI-E solution (**Figure 3.9d**). The peak at 3.96° (2θ) was assigned similarly to the 3.80° (2θ) peak corresponding to NDI-E, similarly the peaks at 7.99° and 11.4° (2θ) were assigned to the 7.47° and 11.13° (2θ) NDI-E peaks. The peak at 5.89° (2θ) was assigned to a new possible 2D halide perovskite phase; in this case only a minor PbI_2 peak is observed at 12.52° (2θ), however it remains evident that NDI-E is in excess.

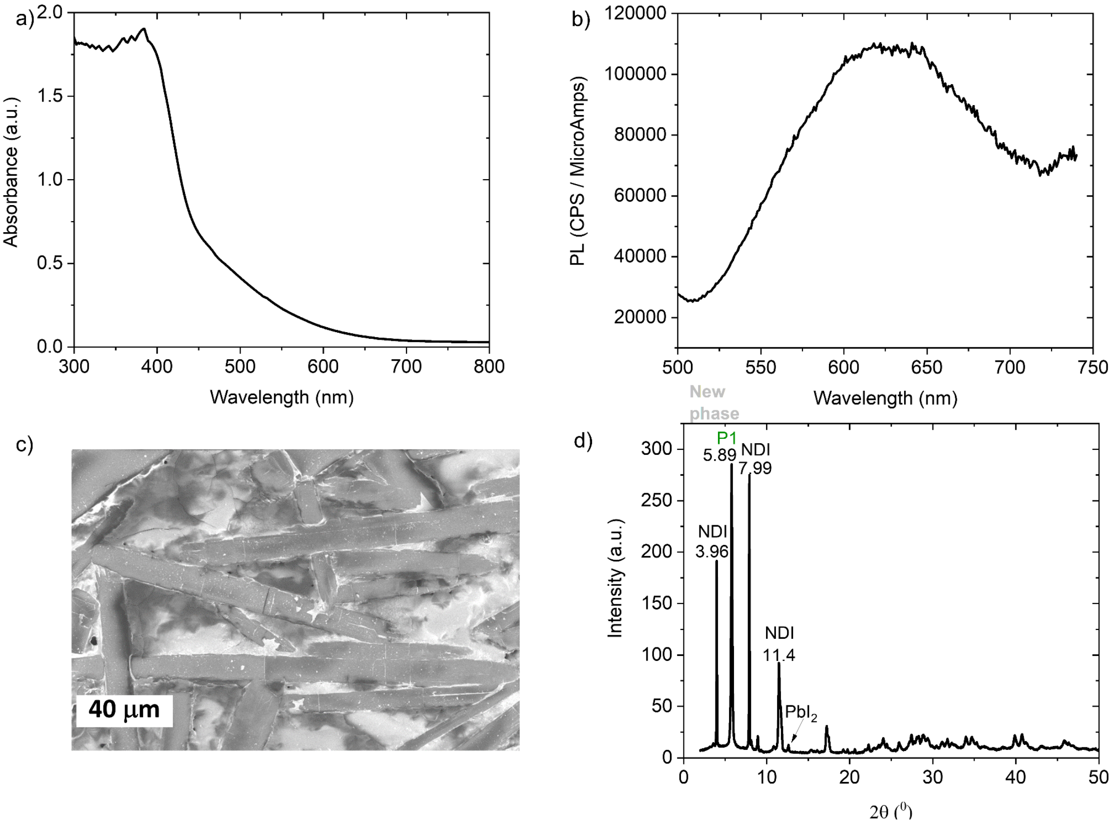

Figure 3.9. NDI-E incorporation attempt into Pb-I octahedral layers with the solvent transport/antisolvent diffusion method. (a) UV-visible absorption spectrum, (b) photoluminescence (475 nm excitation), (c) SEM image and (d) X-ray diffraction pattern of the drop cast redissolved powder in DMF, P1 represents a new phase not ascribed to either precursor and could possibly represent a new 2D halide perovskite phase.

Furthermore, the drop cast film exhibited an absorption onset at approximately 650 nm with an absorption maximum at 383 nm (**Figure 3.9a**). The new photoluminescence peak at 625 nm, different from the pure NDI-E photoluminescence observed at 415 nm (**Figure 3.2c**) as well as the PbI_2 photoluminescence at 525 nm, would support halide perovskite formation (**Figure 3.9b**). However, higher resolution X-ray diffraction data with lower angles (2θ) diffraction would be required to confirm 2D halide perovskite formation. Furthermore, scanning electron microscopy (SEM) images show long crystals with a length of about 160 μm (**Figure 3.9c**). We note that the drop cast deposition approach could in fact allow for a slower crystallization process.

Moreover, synchrotron powder X-ray diffraction of the NDI-E + PbI_2 powder resulting from the solvent transport/antisolvent diffusion method demonstrated clear diffraction peaks below 5° (2θ), corresponding to 2D halide perovskite formation. Furthermore, a reversible phase transformation upon initial cooling from a ramp of 300 K to 100 K followed by ramp-heating the sample back up to 300 K is evident through the reduction and re-appearance of the diffraction peak at 10.68° (2θ) (**Figure 3.10b**), signaling at two possible temperature-dependent powder 2D halide perovskite conformations with the NDI-E chromophore.

Following Bragg's law of diffraction, the powder 2D halide perovskite interlayer spacings were calculated to be 2.89 nm from the first diffraction peak at 1.27° (2θ) (**Figure 3.10b**), slightly (0.19 nm) greater than 2 x the 1.35 nm NDI-E molecular length calculated from molecular dynamics with the Chem3D software (**Figure 3.10a**). This is reasonable given the proposed 2D halide perovskite structure with the NDI-E molecules anchoring at the corners shared by adjacent Pb-I octahedra, positioned at the interlayer spacings on **Figure 3.11**, where the interlayer spacing is shown to be slightly greater than the size of two NDI-E molecules extended out on the conformation shown.

The calculated interlayer spacing of 2.89 nm would be larger than that corresponding to phenylethylammonium incorporation into Pb-I octahedral layers on a spun-coat film, with a first XRD peak corresponding to a 1.60 nm interlayer spacing in that case (**Figure 3.4a**). This is reasonable given the significantly larger size of the organic molecular cation.

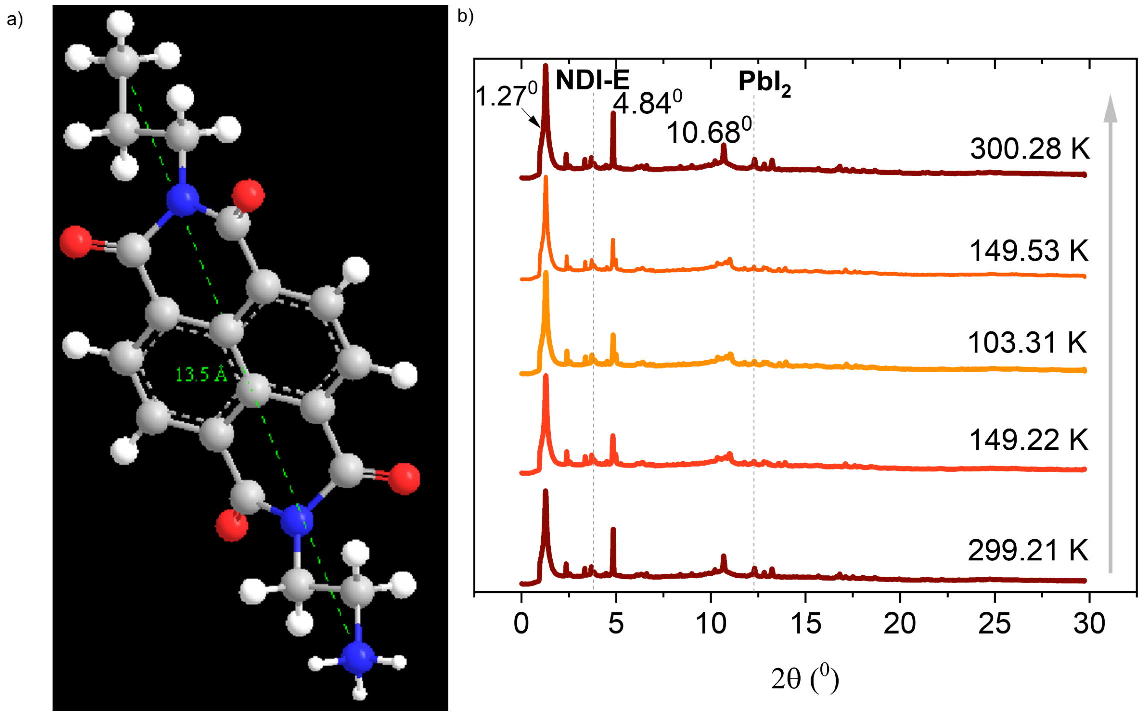

Figure 3.10. 2D halide perovskite interlayer spacing determination from synchrotron powder X-ray diffraction data for the powder resulting from the solvent transport/antisolvent diffusion method on a solution of NDI-E and PbI_2. (a) Chem3D software simulation of NDI-E molecular length (13.5 Å), (b) synchrotron powder X-ray diffraction data for sample temperatures ramped from 300 to 100 K and back, and interlayer spacing corresponding to the 1.27° (2θ) first diffraction peak.

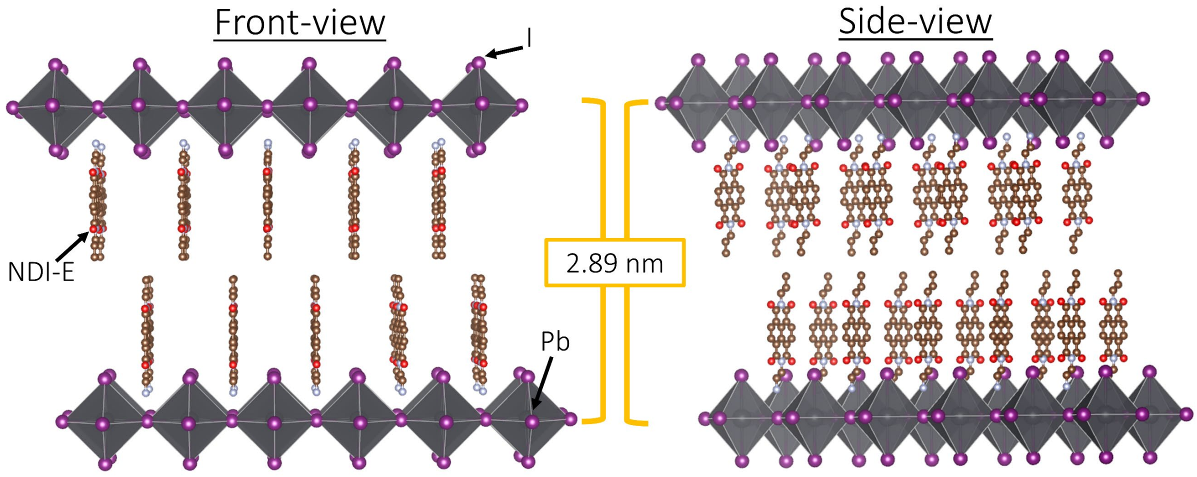

Figure 3.11. NDI-E anchoring at the corners of Pb-I octahedra: front-view and side-view, with the NDI-E groups oriented perpendicular to the inorganic layers (models generated with the VESTA software[18]).

The possibility of anchoring NDI molecules with yet longer alkyl linker chain lengths and with a symmetric nature (*i.e.*, with a possibility of enhanced anchoring at the top and bottom octahedral layers simultaneously) was also attempted with the NDI-diE and NDI-diB variants displayed on **Figure 3.1**, with the solution-based approach. Furthermore, NDI-diE and NDI-diB are interesting as they would enhance the visible light absorption properties of the chromophore compared to NDI-E (**Figure 3.2b**). Several spin coating speeds (3000 and 1500 rpm) and solvent systems were tested in order to ensure a kinetically-slower spin-coating method; in addition to processing in dimethyl formamide (DMF b.p. 153 °C), higher boiling point solvents such as dimethyl sulfoxide (DMSO b.p. 189 °C) as well as a 50/50 DMF/DMSO mixture (in order to slow down the solvent evaporation rate and allow for a longer crystallization time) were also used (**Figure 3.12**).

These however led to no thin film crystallinity (**Figure 3.12 c** and **f**); UV-visible light absorbance (**Figure 3.12 a** and **d**) and photoluminescence peaks (**Figure 3.12 b** and **e**) corresponding to NDI-diE and NDI-diB precursors (**Figure 3.2b,c**) remained present in the film resulting from the chromophores blend with PbI_2, indicating mostly the precursors remained and no 2D halide perovskites were formed. Namely, the NDI-diE blend with PbI_2 and NDI-diB blend with PbI_2 mostly displayed PL around 420 nm while NDI-diE and NDI-diB alone each display PL at 410 and 405 nm, respectively. Both blend systems exhibit minor photoluminescence around 575 nm, possibly indicating the partial formation of a 2D halide perovskite phase with the NDI-diE and NDI-diB systems but to a very small extent.

NDI-diE and NDI-diB incorporation into Pb-I octahedral layers was also attempted with the solvent transport/antisolvent diffusion method, however this led to no crystallinity of the resulting drop cast powder.

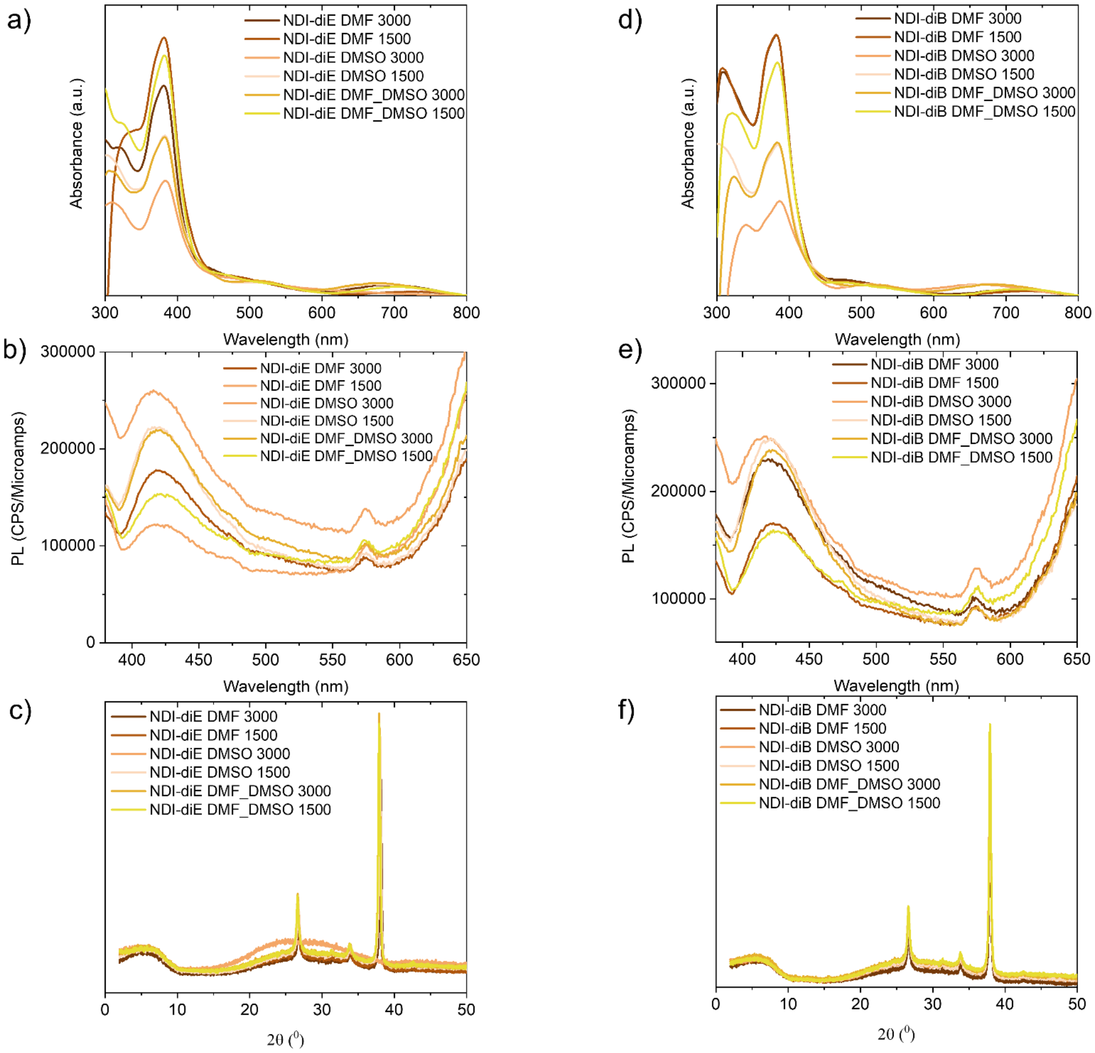

Figure 3.12. UV-vis spectra (a,d), PL spectra (b,e) (350 nm excitation) and XRD spectra (c,f) for NDI di-E and NDI-diB incorporation attempts into layered lead halide perovskites, respectively.

3.3 Conclusion

In conclusion, chromophore cations have the potential to enhance the light absorption capabilities as well as ameliorate the stability of conventional 2D halide perovskite materials. In this work thus far, three NDI chromophore variants have been studied, one asymmetric and two symmetric cations with 2- and 4-carbon side chains. The non-symmetric molecule tested contained a 2-carbon ammonium alkyl linker, for which full incorporation was not possible with the kinetically-fast solution-based deposition method. Namely, for NDI-E incorporation into PEA_2PbI_4, while crystallinity is somewhat conserved for low NDI-E mole percentages, higher molar percentages still present lower degrees of crystallinity. This may be due to improper dimensions of the octahedral layer in accommodating larger NDI molecules compared to the smaller PEAI molecules with the kinetically fast solution-processing method. Nevertheless, the results are encouraging given the observed activity of the NDI molecule in the optical properties of the material.

The kinetically-slower powder synthesis approach with the solvent transport/antisolvent diffusion method does display more 2D-like characteristics in the X-ray diffraction data; the resulting new phase is however not pure. Nevertheless, the formation of this new phase aids in understanding and characterizing this novel 2D halide perovskite structure. However, the structure seems unable to be conserved in the thin film fabrication approach, which would be otherwise ideal for photovoltaic device applications. Furthermore, synchrotron powder X-ray diffraction data for the NDI-E + PbI_2 powder obtained show two possible temperature-dependent phases.

Symmetric di-ammonium alkyl linker NDI systems with 2 and 4-carbon chain lengths were also tested, leading to no system crystallinity, which aligns well with reports from Proppe *et al.* for the NDI-diE system.[19] However, it is important to emphasize that in this work we find that tuning the NDI cation molecular form towards an asymmetric cation and exploring further synthesis routes, such as a modification of the powder synthesis approach, could open new gateways to incorporate NDI cations into layered perovskites, though a pure 2D perovskite phase, free of remaining precursors, could not be fabricated.

This work although preliminary represented a stepping stone towards the rational design of this new family of emerging chromophore-hybrid halide perovskites, providing a solid platform to advance on the understanding of these barely explored systems which also provided great insights for the functional molecular cation system to be presented in Chapter 4. Namely, given the chemical availabilities and challenge of incorporating the NDI molecular variants NDI-E, NDI-diE and NDI-diB as a pure 2D phase into [PbI_6] octahedral layers in a facile solution-based approach, the family of chromophore systems under examination was further expanded on to a smaller functional molecule based on benzodithiophene (BDT). This different approach at incorporating functional molecules into 2D perovskite structures will be discussed in the following Chapter. Moreover, the feedback obtained from this system is helpful for further developing NDI molecular variants for incorporation into 2D halide perovskites and could guide the design rules for large molecule/chromophore incorporation into layered lead halide perovskites in general.

3.4 References

[1] M. Righetto, D. Giovanni, S. S. Lim, T. C. Sum, *Applied Physics Reviews* **2021**, *8*, 011318.

[2] M. P. Hautzinger, D. Pan, A. K. Pigg, Y. Fu, D. J. Morrow, M. Leng, M.-Y. Kuo, N. Spitha, D. P. Lafayette, D. D. Kohler, J. C. Wright, S. Jin, *ACS Energy Lett.* **2020**, *5*, 1430.

[3] M. M. Elshanawany, A. Gaetano Ricciardulli, M. Saliba, J. Wachtveitl, M. Braun, *Nanoscale* **2021**, *13*, 15668.

[4] B. Kim, S. I. Seok, *Energy Environ. Sci.* **2020**, *13*, 805.

[5] K. A. Kurdi, D. P. McCarthy, D. P. McMeekin, S. O. Furer, M.-H. Tremblay, S. Barlow, U. Bach, S. R. Marder, *Mater. Chem. Front.* **2021**, *5*, 450.

[6] J. H. Heo, S.-C. Lee, S.-K. Jung, O.-P. Kwon, S. H. Im, *J. Mater. Chem. A* **2017**, *5*, 20615.

[7] S.-K. Jung, J. H. Heo, D. W. Lee, S.-C. Lee, S.-H. Lee, W. Yoon, H. Yun, S. H. Im, J. H. Kim, O.-P. Kwon, *Advanced Functional Materials* **2018**, *28*, 1800346.

[8] S.-K. Jung, J. H. Heo, D. W. Lee, S.-H. Lee, S.-C. Lee, W. Yoon, H. Yun, D. Kim, J. H. Kim, S. H. Im, O.-P. Kwon, *ChemSusChem* **2019**, *12*, 224.

[9] S.-K. Jung, J. H. Heo, B. M. Oh, J. B. Lee, S.-H. Park, W. Yoon, Y. Song, H. Yun, J. H. Kim, S. H. Im, O.-P. Kwon, *Advanced Functional Materials* **2020**, *30*, 1905951.

[10] T. Nakamura, N. Shioya, T. Shimoaka, R. Nishikubo, T. Hasegawa, A. Saeki, Y. Murata, R. Murdey, A. Wakamiya, *Chem. Mater.* **2019**, *31*, 1729.

[11] M. A. Jameel, T. C.-J. Yang, G. J. Wilson, R. A. Evans, A. Gupta, S. J. Langford, *J. Mater. Chem. A* **2021**, *9*, 27170.

[12] S. Maheshwari, T. J. Savenije, N. Renaud, F. C. Grozema, *J. Phys. Chem. C* **2018**, *122*, 17118.

[13] X. Li, W. Ke, B. Traoré, P. Guo, I. Hadar, M. Kepenekian, J. Even, C. Katan, C. C. Stoumpos, R. D. Schaller, M. G. Kanatzidis, *J. Am. Chem. Soc.* **2019**, *141*, 12880.

[14] H.-H. Fang, J. Yang, S. Tao, S. Adjokatse, M. E. Kamminga, J. Ye, G. R. Blake, J. Even, M. A. Loi, *Advanced Functional Materials* **2018**, *28*, 1800305.

[15] M. Safdari, P. H. Svensson, M. T. Hoang, I. Oh, L. Kloo, J. M. Gardner, *J. Mater. Chem. A* **2016**, *4*, 15638.

[16] K. Du, Q. Tu, X. Zhang, Q. Han, J. Liu, S. Zauscher, D. B. Mitzi, *Inorganic Chemistry* **2017**, *56*, 9291.

[17] A. K. Singh, K. Krishnamoorthy, *Langmuir* **2017**, *33*, 13401.

[18] K. Momma, F. Izumi, *J Appl Cryst* **2011**, *44*, 1272.

[19] A. H. Proppe, M.-H. Tremblay, Y. Zhang, Z. Yang, R. Quintero-Bermudez, S. O. Kelley, S. Barlow, S. R. Marder, E. H. Sargent, *J. Phys. Chem. C* **2020**, *124*, 24379.

Chapter 4

BDT Layered Lead-Halide Perovskites

Synthesis attempts of 2D perovskites based on BDT functional molecule spacers

This chapter discusses the importance of tailoring the alkyl linker chain length on benzodithiophene (BDT) functional molecular spacers incorporated first into pure 2D lead halide perovskite structures, followed by incorporation into high *n* number quasi-layered lead halide perovskites (QLLHP) according to the formula $(R)_2A_{n-1}Pb_nX_{3n+1}$. A comparative study with the common phenylethylammonium (PEA) insulating spacer is first presented and the resulting effects of the functional BDT spacer on perovskite stability, defect mitigation and therefore device performance are revealed.

This Chapter is in part a modification of the following publication:

''Benzodithiophene-based Spacers for Layered and Quasi-layered Lead Halide Perovskite Solar Cells''

B. Primera Darwich, N. Guijarro, H.-H. Cho, L. Yao, L. Monnier, P. Schouwink, M. Mensi, J.-H. Yum, K. Sivula, *ChemSusChem* **2021**, *14*, 3001.

4.1 Introduction

While a multitude of optoelectronically-innocent organic spacers have been reported for layered lead-halide perovskites (LLHPs), an exciting emergent trend is the incorporation of aromatic moieties with extended π-conjugation that can offer supplementary semiconducting properties such as controlled electronic conductivity, increased light absorption, enhanced photo-induced charge transfer, and tunable quantum well electronic structures.[1] This trend has been inspired by the success of molecular engineering in the field of organic semiconductors, where judicious design has afforded unprecedented tunability of material properties.[2] To this end, cation-functionalized organic semiconductor building blocks based on pyrene,[3–5] perylene,[6,7] carbazole,[8] and thiophene,[9–11] have been recently reported in layered and quasi-layered hybrid perovskites.

While these demonstrations are encouraging steps towards merging the fields of organic electronics and hybrid perovskites, the ability to successfully incorporate conjugated organics in LLHPs is severely limited by their size and their intramolecular π-π stacking. Indeed, the size of the PbX_6 octahedra defines a constraint on the width/depth of the organic. Moreover the presence of an increasing number of heteroatoms (sulfur and nitrogen) in the aromatic structure, which is generally favorable for the semiconducting properties,[12] also increases the strength of the π-π interactions[13,14] disrupting the formation of LLHPs via self-aggregation of the organic. Recently, Dou and coworkers have engineered steric effects in a benzothiadiazole-containing cation to reduce π-stacking and facilitate incorporation.[15] While this approach allowed the integration of an impressively long conjugated system, the use of steric hinderance also reduces the intermolecular conjugation and limits the extent of energy level control in the organic. Thus, there remains a need to develop strategies and understanding towards the incorporation of large, rigid and heteroatom-containing conjugated organic cations in LLHPs. Progress can be made in this aspect by continuing to demonstrate the incorporation of diverse organic semiconductor building blocks in LLHPs and by recognizing how to engineer their incorporation via structural modification.

Benzodithiophene (BDT) is a widely successful planar conjugated building block in the field of organic semiconductors due to its excellent semiconducting properties and its ease of synthesis and functionalization.[16] However, its incorporation in LLHPs has not been previously reported. In view of the known ability of electron-donating thiophene-based small molecules as passivating agents for defects in the perovskite structure,[17–19] we further hypothesized that the incorporation of a BDT-based cation in LLHPs in the layered or quasi-layered structure, if possible, could also act to passivate halide defects via a Lewis base mechanism. Herein, we prepare BDT-based cations with different alkane linkers and find that the linker length is critical for incorporation into LLHPs. Furthermore, via incorporation into photovoltaic devices in a quasi-layered structure, and in comparison to the standard PEA-based spacer, we present evidence for an additional passivation mechanism in the BDT-based system.

4.2 Results and Discussion

4.2.1 Benzodithiophene incorporation in layered perovskites

To demonstrate the incorporation of the conjugated BDT core we first hypothesized that the length of an alkyl chain linking the BDT to an aminium ion (commonly called ammonium) could be an important factor. To test this, we prepared three versions of the iodide salts of m-(benzo[1,2-b:4,5-b']dithiophen-2-yl)alkan-1-aminium with m =2,4,6 (see chemical structures in **Figure 4.1a**) using the synthesis routes described in the experimental chapter of this thesis work to yield the cations coded as BDT-C2, BDT-C4, and BDT-C6 for 2, 4, and 6 carbon linkers, respectively. Indeed, while the $(BDT\text{-}C6)_2PbI_4$ thin film showed clear and intense diffraction peaks (**Table 4.1**) which can be indexed to a RP phase,[20] peaks for the BDT-C4 version were drastically diminished and no RP phase peaks were evident on the BDT-C2-based film. The absence of a strong diffraction peak around $2\theta = 12.5°$ for all BDT cations discounts the formation of crystalline PbI_2 domains, suggesting a homogeneous mixture of the organic cation and lead iodide even for the BDT-C2-based film. Interestingly, the UV-Vis absorption spectrum of the BDT-C2-based film (**Figure 4.1c**) shows an extended absorption shoulder until ~700 nm, similar to drop-cast films of pure BDT.[21]

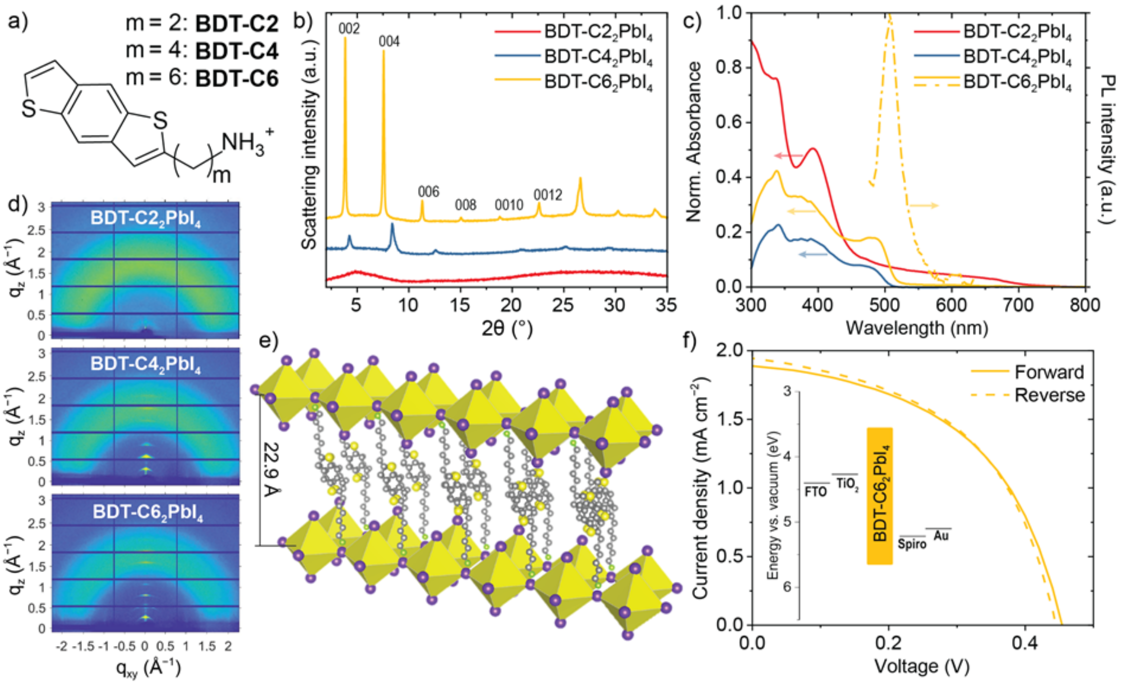

Figure 4.1. (a) Benzodithiophene-based ligand chemical structures where m represents the number of carbon atoms in the alkyl chain between the aminium cation and the conjugated BDT core. (b) X-ray diffraction patterns of (BDT-Cm)$_2$PbI$_4$ thin films and (c) corresponding UV-vis absorption and photoluminescence (PL) spectra. Note that PL is only observed for (BDT-C6)$_2$PbI$_4$. (d) GIWAXS patterns of (BDT-Cm)$_2$PbI$_4$ thin films. (e) shows a schematic of a proposed layer arrangement of the (BDT-C6)$_2$PbI$_4$ perovskite (drawn with the Vesta software[22]). (f) J-V curve for a (BDT-C6)$_2$PbI$_4$ -based photovoltaic device under 1-sun illumination (energy levels of the device in the inset).* For (BDT-C2)$_2$PbI$_4$, the formula denotes the stoichiometry of the fabrication solution and not the final crystal, which is not formed.

Table 4.1. XRD plane and corresponding d-spacing calculation for (BDT-C6)$_2$PbI$_4$

hkl plane	XRD 2θ peak position	d-spacing (Å)
002	3.86	22.9
004	7.55	23.4
006	11.31	23.4
008	15.00	23.6
0010	18.83	23.5
0012	22.63	23.5
0014	26.53	23.5

Indeed, the absorption spectrum for the BDT-C2 drop-cast film alone shows an absorption shoulder, also evident of extended j-aggregation as well as significant light scattering due to morphological effects, which is no longer present in the BDT-C4 and BDT-C6 drop-cast films (**Figure 4.2**).

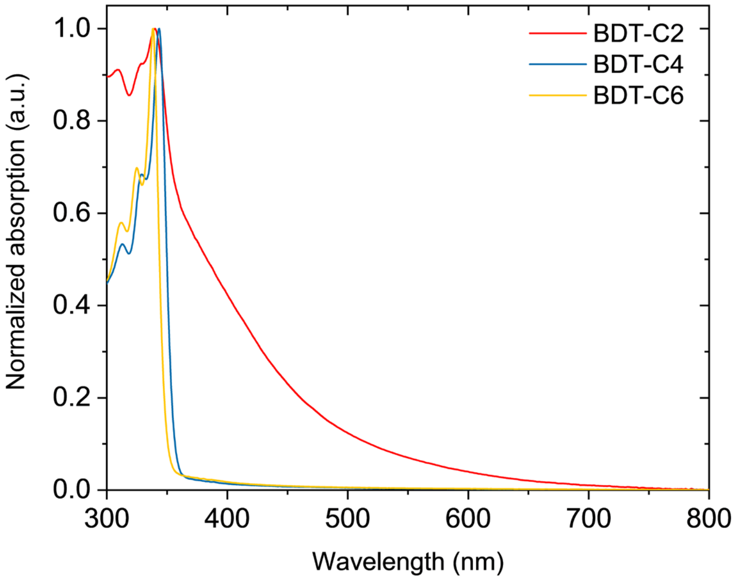

Figure 4.2. UV-vis absorption spectra of BDT-C2, BDT-C4 and BDT-C6 drop-cast films.

The absence of this absorption shoulder in the BDT-C4- and the BDT-C6- based films further supports their formation of a RP phase without an extended π-π stacking of the BDT cation. Despite the characteristic, though weaker, XRD peaks of a RP phase, the $(BDT\text{-}C4)_2PbI_4$ thin film does not exhibit the distinctive excitonic UV-Vis absorption peak of a LLHP and no strong photoluminescence (PL) was observed for this film. In contrast, the $(BDT\text{-}C6)_2PbI_4$ thin film shows a clear absorption peak at 490 nm and a strong, well-defined PL emission was observed centered at 510 nm. These features are hypsochromic to $(PEA)_2PbI_4$ (**Figure 4.3**) suggesting that the conjugated BDT core is optoelectronically-uncoupled from the layers of lead iodide—consistent with a larger separation distance expected from the hexyl-linker in BDT-C6.

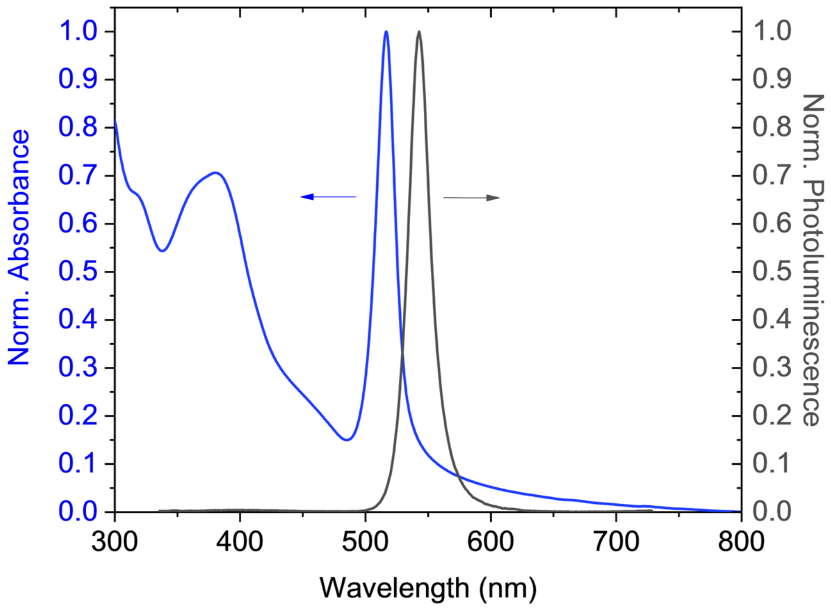

Figure 4.3. UV-vis absorption spectrum and photoluminescence of a thin film of $(PEA)_2PbI_4$ prepared on a glass substrate.

Additional information on the crystallinity of the BDT-based LLHPs is given by grazing incidence wide angle X-ray scattering (GIWAXS) diffraction patterns (**Figure 4.1d**), which confirm the strong out-of-plane orientation for $(BDT\text{-}C6)_2PbI_4$ with the (00l) planes oriented parallel to the substrate. The $(BDT\text{-}C4)_2PbI_4$ film shows a similar orientation despite its poorer crystallinity, while the amorphous nature of the $(BDT\text{-}C2)_2PbI_4$ is confirmed. Overall, the XRD and GIWAXS data of the $(BDT\text{-}C6)_2PbI_4$ film suggest an interlayer spacing of 22.9 Å. Considering this distance and the BDT-C6 molecular length of 16.1 Å (obtained via DFT calculations with SCIGRESS™) an overlapping of the BDT core is inferred consistent with the schematic structure shown in **Figure 4.1e**, where π-π interactions between opposite BDT units are influential towards the interlayer spacing. However, as forming single crystals of $(BDT\text{-}C6)_2PbI_4$ was not possible despite significant efforts, further insight into the precise hexyl chain orientation and π-π interactions of the BDT core in the RP phase are out of the scope of this work. Despite this, the effect of the changing alkyl chain length remains a significant observation and suggests an important design rule for incorporating rigid conjugated moieties in LLHPs.

To verify whether the thin film annealing temperature was a limiting factor in the poor optoelectronic and crystallographic properties of the BDT-C4-based layered perovskite, a series of annealing temperatures ranging from 100°C to 180°C were tested, where similar XRD-patterns were observed and no particular improvement in crystallinity could be observed at any specific annealing temperature (**Figure 4.4a**). Moreover, the clear excitonic absorption peak observed for (BDT-C6)$_2$PbI$_4$ was absent as similar UV-vis spectra were observed for (BDT-C4)$_2$PbI$_4$ at all annealing temperatures tested (**Figure 4.4b**), whereas only weak and wide photoluminescence signals appeared centered at 510 nm (**Figure 4.4c**). Photoluminescence spectra further revealed annealing temperatures higher than 150°C are detrimental to the (BDT-C4)$_2$PbI$_4$ structure.

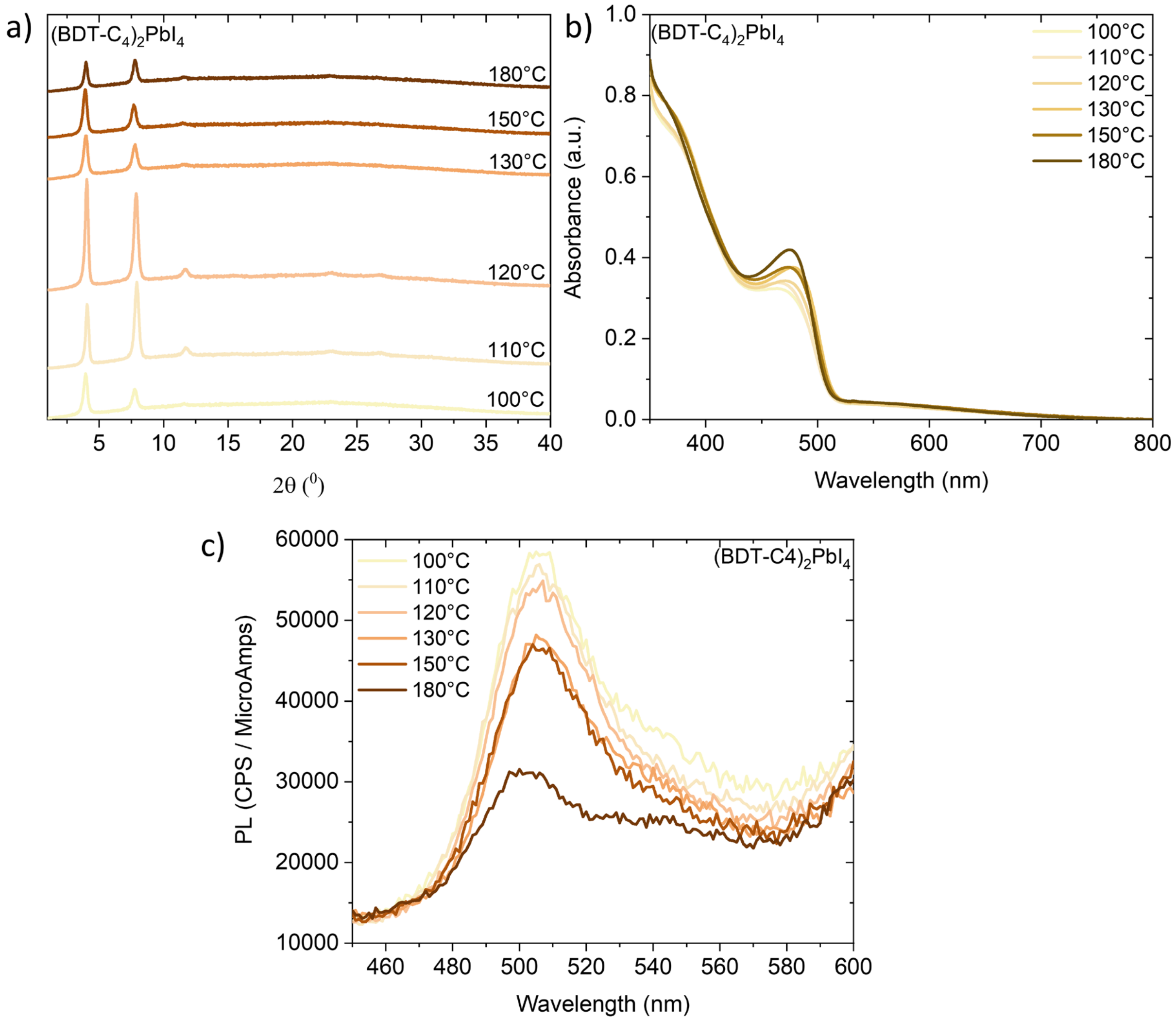

Figure 4.4. a) X-ray diffraction patterns for (BDT-C4)$_2$PbI$_4$ thin films annealed at 100, 110, 120, 130, 150 and 180°C b) corresponding UV-vis spectra and c) photoluminescence spectra.

With this information in hand, it became evident that the BDT-C6 conformation was the best candidate to proceed with, when compared to the BDT-C4 and BDT-C2 species. Considering the success at incorporating the BDT-C6 cation into a RP LLHP, we gathered additional data on this version for further optoelectronic application (**Figure 4.5**).

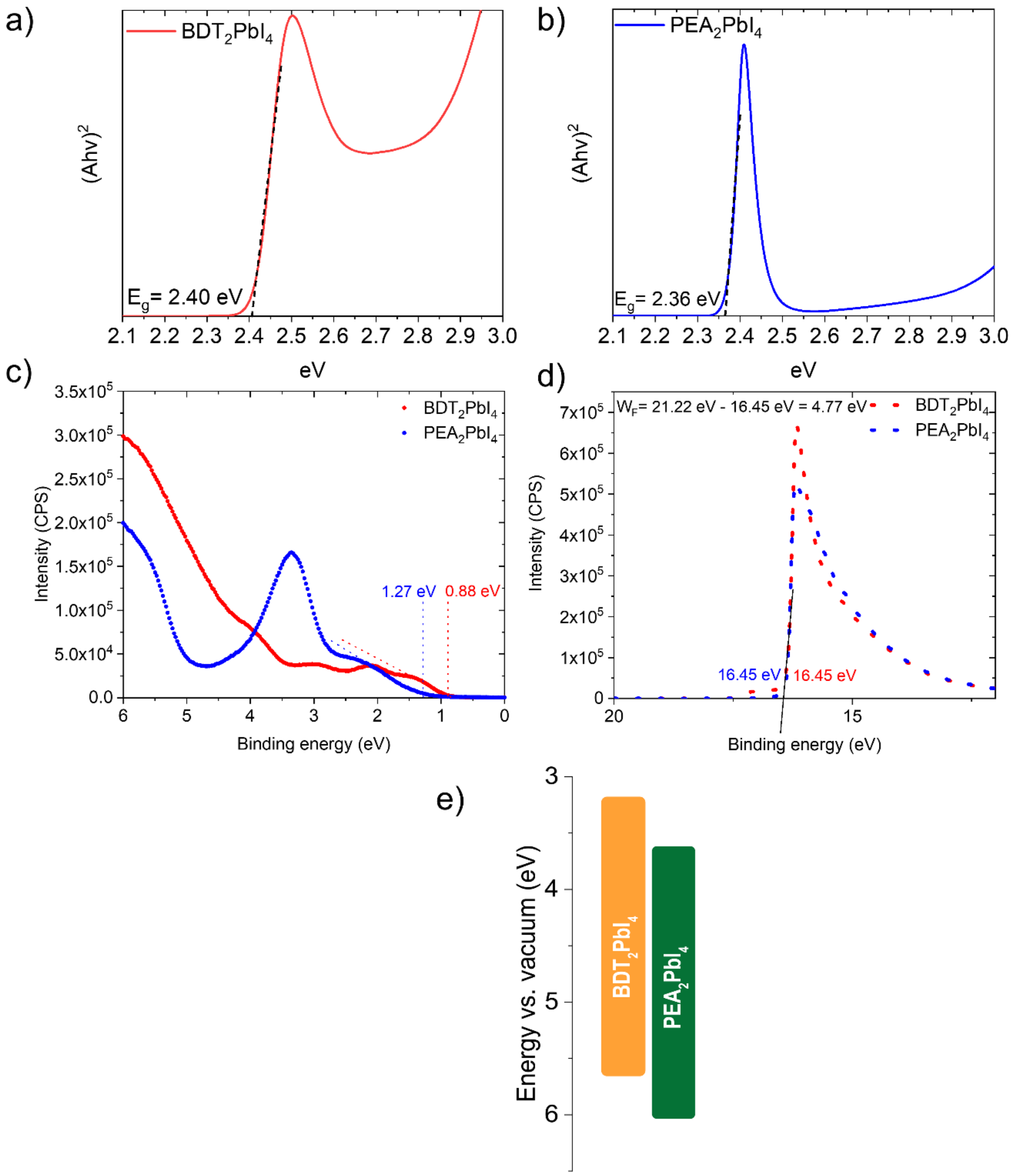

Figure 4.5. Tauc plots for (a) (BDT-C6)$_2$PbI$_4$ (simply called BDT$_2$PbI$_4$ here) and (b) PEA$_2$PbI$_4$ and UPS linear scale plots with a fitting of the VBM for (c) BDT$_2$PbI$_4$ and PEA$_2$PbI$_4$ (d) UPS linear scale plots with a fitting of the secondary electron cut-off for BDT$_2$PbI$_4$ and PEA$_2$PbI$_4$ as well as (e) the corresponding energy levels (see the corresponding method of calculation in the experimental section of **Chapter 2**).

The optical band gap of $(BDT\text{-}C6)_2PbI_4$ was found to be 2.40 eV (**Figure 4.5a**) via Tauc plot analysis compared to 2.36 eV (**Figure 4.5b**) for $(PEA)_2PbI_4$. In addition, the valence band maxima were determined by ultraviolet photoelectron spectroscopy (UPS) measurements following linear extrapolations for the valence band maximum (VBM), secondary electron cut-off and the corresponding ionization energy calculations (**Figure 4.5c,d**).[23,24] These data were combined to locate the VBM of $(BDT\text{-}C6)_2PbI_4$ at 5.7 eV vs. vacuum compared to 6.0 eV for PEA_2PbI_4 (**Figure 4.5e**).

The good crystallinity, strong PL, and suitable energy levels of the $(BDT\text{-}C6)_2PbI_4$ were next put to test in a standard n-i-p photovoltaic device with a fluorine-doped tin oxide (FTO) substrate, compact + mesoporous TiO_2 as the electron transport layer (ETL), spiro-OMeTAD as the hole transporting layer (HTL), and Au as the top electrode. **Figure 4.1f** shows the energy level alignment of the device and the best current density-voltage (J-V) curves under 1 sun illumination, which showed negligible hysteresis between forward and reverse scans. However, generally low performance parameters were observed with a short circuit current density, $J_{SC} = 1.9$ mA cm^{-2}, open circuit potential $V_{OC} = 0.46$ V and a fill factor, $FF = 0.5$ resulting in a power conversion efficiency of only 0.42 %. This modest performance is similar to other "single-layered" LLHPs[25] and is limited by the alignment of the layers parallel with the substrate, which prevents charge transport to the electrodes of the device.

4.2.2 Quasi-layered photovoltaic devices

Increasing the number of inorganic layers, n, with respect to the bulky organic cation as represented by the chemical formula $(R)_2A_{n-1}Pb_nX_{3n+1}$, where A is a small organic cation (e.g. MA=methylammonium) to yield a quasi-layered semiconductor material is a well-established route to improve the performance of LLHP-based solar cells. Indeed, quasi-layered lead halide perovskites (QLLHPs) exhibit a reduction in band gap energy, smaller exciton binding energy, and improved layer orientation with respect to the substrate compared to LLHPs (where $n = 1$), while generally also improving active layer stability versus their bulk counterparts ($n = \infty$).[26–28]

Thus, we next investigated the performance of the BDT-C6 cation (referred to hereafter as the BDT cation for simplicity) compared to the standard PEA cation in quasi-layered solar cells, following the formulas $(BDT)_2MA_{N-1}Pb_NI_{3N+1}$ and $(PEA)_2MA_{N-1}Pb_NI_{3N+1}$, respectively in the precursor solution preparation. Note that, unlike n which refers to the actual number of layers sandwiched in between the spacers, N denotes the stoichiometric feed ratio. Indeed, it has been reported that 2D structures with $n \geq 6$ are experimentally unlikely and thus not formed.[29] While we did not focus on quasi-layered cells with $N < 20$ due to poor morphology, we noted a significant performance difference for medium and high *N* numbers which are represented by $N = 20$ and 100, respectively. To prepare thin films of the quasi-layered lead halide perovskites (QLLHPs) we employed the antisolvent approach shown schematically in **Figure 4.6**.

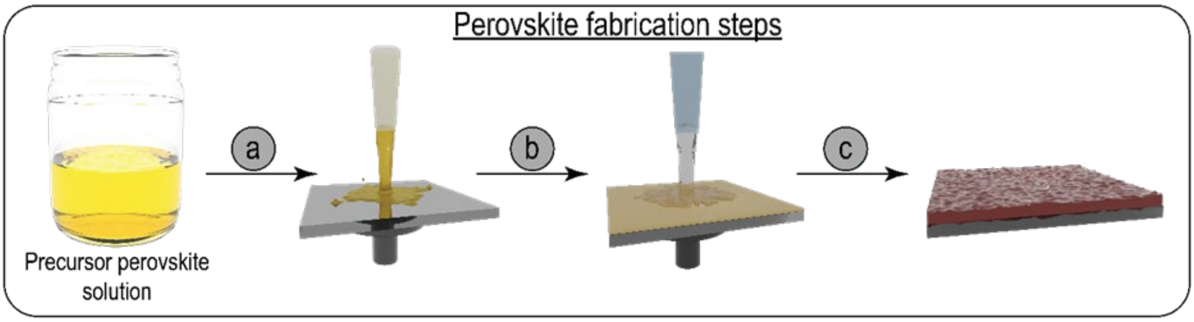

Figure 4.6. Schematic representation of the quasi-layered perovskite fabrication steps (a) spin-coating of precursor solution, (b) antisolvent dripping, and (c) thermal annealing (see experimental section in **Chapter 2** for further details).

We denote the $(BDT)_2MA_{N-1}Pb_NI_{3N+1}$ films as N20 MBDT and N100 MBDT for $N = 20$ and 100, respectively, and similarly for N20 MPEA and N100 MPEA to simplify the compositional notation for the reader. Although the XRD patterns of both the N20 and N100 series of perovskites with BDT and PEA ligands exhibit mainly the principal $MAPbI_3$ phase due to its majority content (**Figure 4.7a** and **b**) similar to comparable reports,[30,31] high-resolution transmission electron microscopy, HRTEM, measurements (**Figure 4.8**) and corresponding fast Fourier transforms (FFT) of the N20 and N100 films indicate regions with interlayer spacings of 7.4 and 7.8 Å for MPEA and MBDT, respectively, suggesting the presence of low *n* layered domains existing together with $n = \infty$ domains (with interlayer spacing of 3.1 Å), similar to a previously-described QLLHP with butylammonium.[32]

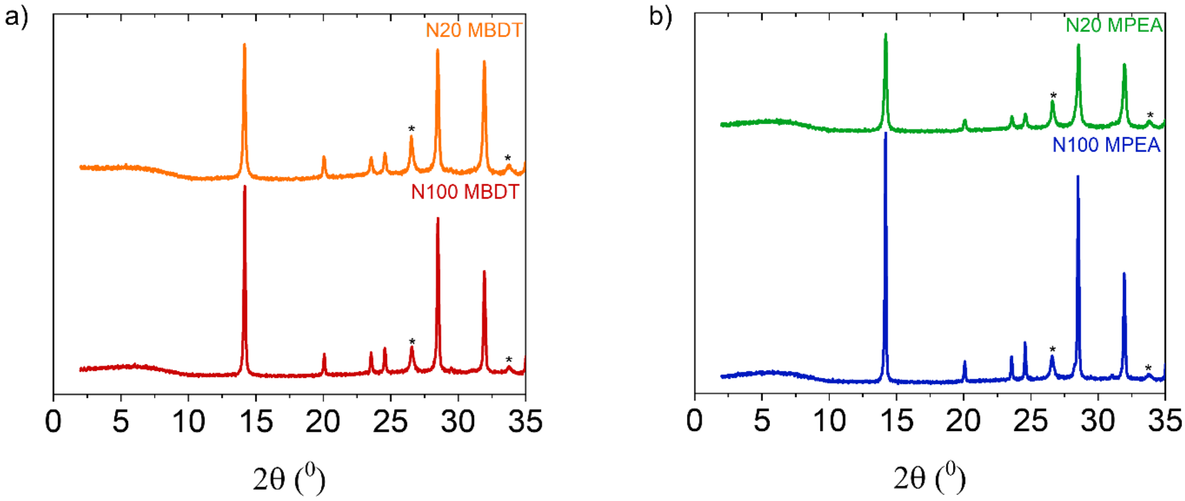

Figure 4.7. X-ray diffraction patterns of thin films of the quasi-layered perovskites studied in this work, as prepared on FTO(*) substrates, for the (a) MBDT series and (b) MPEA series.

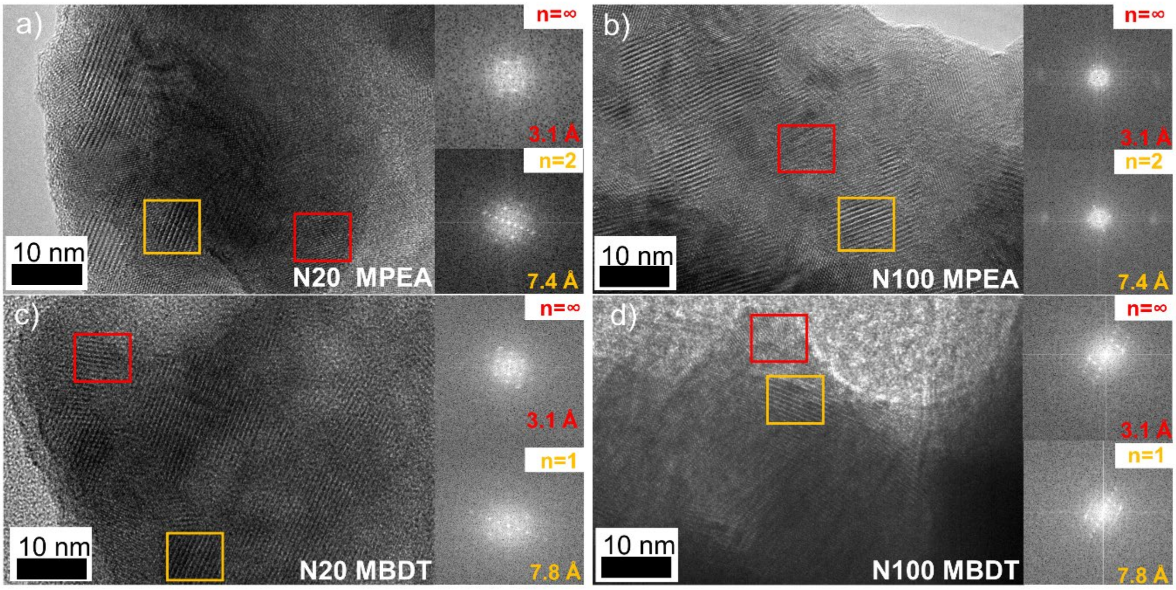
a)
10 nm
N20 MPEA
n=∞
3.1 Å
n=2
7.4 Å
b)
10 nm
N100 MPEA
n=∞
3.1 Å
n=2
7.4 Å
c)
10 nm
N20 MBDT
n=∞
3.1 Å
n=1
7.8 Å
d)
10 nm
N100 MBDT
n=∞
3.1 Å
n=1
7.8 Å

Figure 4.8. Investigating the crystalline distribution of mixed N-number perovskites with high resolution transmission electron microscopy (HRTEM) of (a) N20 MPEA, (b) N100 MPEA, (c) N20 MBDT, and (d) N100 MBDT. The red rectangles represent the $n = \infty$ regions analyzed in the Fourier transform images, whereas the yellow rectangles similarly represent the layered perovskite regions analyzed in the Fourier transform.

In addition, a homogeneous distribution of sulfur, lead, and iodide is observed on a > 100 nm length scale throughout a portion of an N20 MBDT film with transmission electron microscopy with energy dispersive X-ray spectroscopy (TEM-EDX), suggesting that the BDT cation is evenly distributed in the film (**Figure 4.9**).

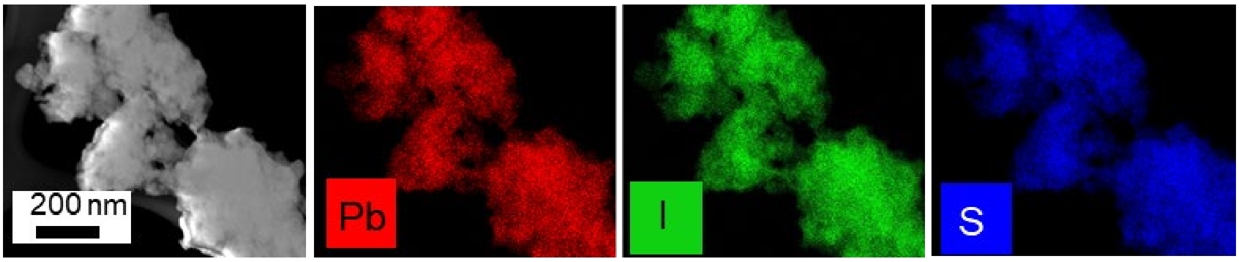

Figure 4.9. TEM image and the corresponding EDX maps (for the element indicated) of a portion of an N20 MBDT film removed from a substrate.

PL measurements also suggest the formation of the QLLHPs (**Figure 4.10**), where hypsochromic shifts of the emission maximum wavelength are observed for the N20 and N100 MBDT and MPEA samples, with respect to the $MAPbI_3$ reference, further supporting the existence of homogeneously-distributed bulky cations in the quasi-layered film.

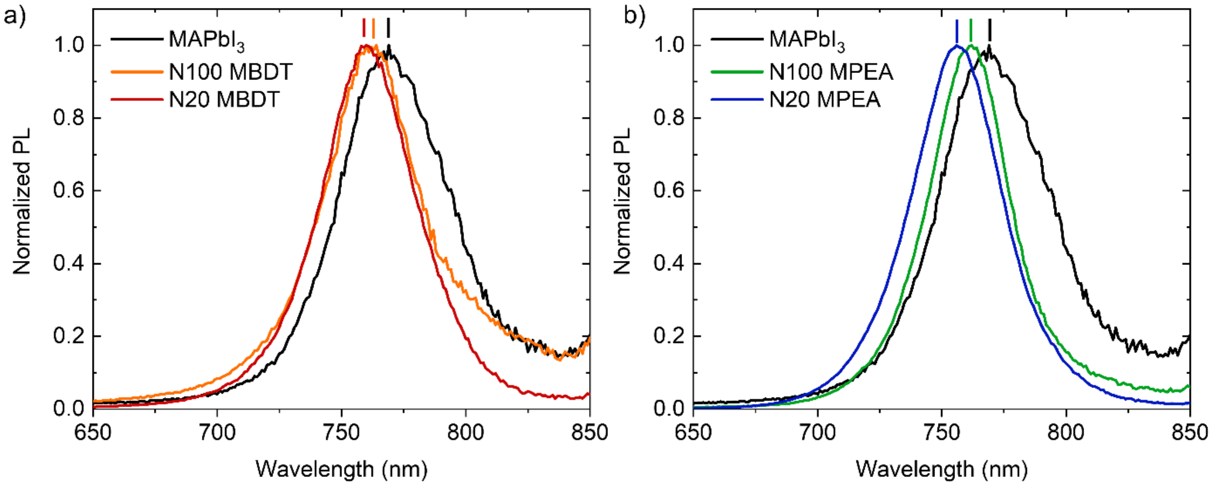

Figure 4.10. Steady-state photoluminescence of (a) N20 & N100 MBDT and (b) N20 & N100 MPEA and the $MAPbI_3$ reference shown in both cases. The excitation wavelength was 450 nm.

The bandgap energies of the QLLHPs were determined from UV-vis spectra (**Figure 4.11**) by means of the corresponding Tauc plots (**Figure 4.12**). It is worth noting that no noticeable changes in the band gap were detected upon the incorporation of the spacers.

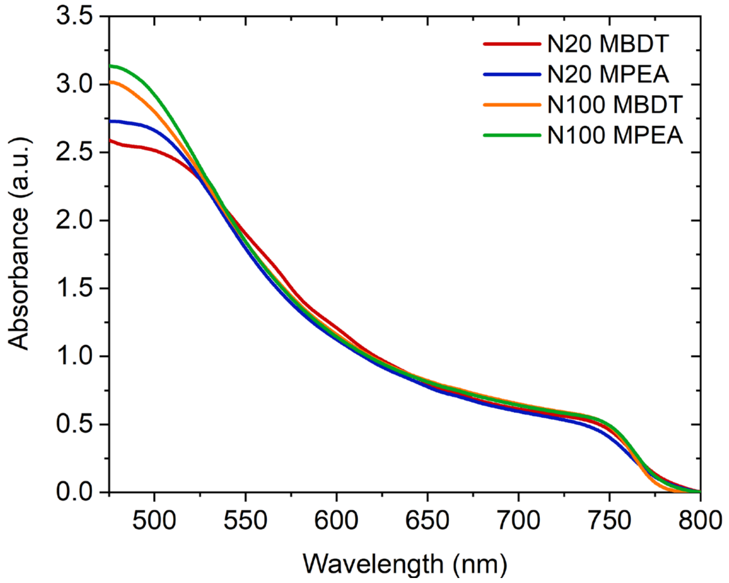

Figure 4.11. UV-visible absorption spectra of the QLLHPs N20 MBDT, N20 MPEA, N100 MBDT and N100 MPEA prepared on glass substrates.

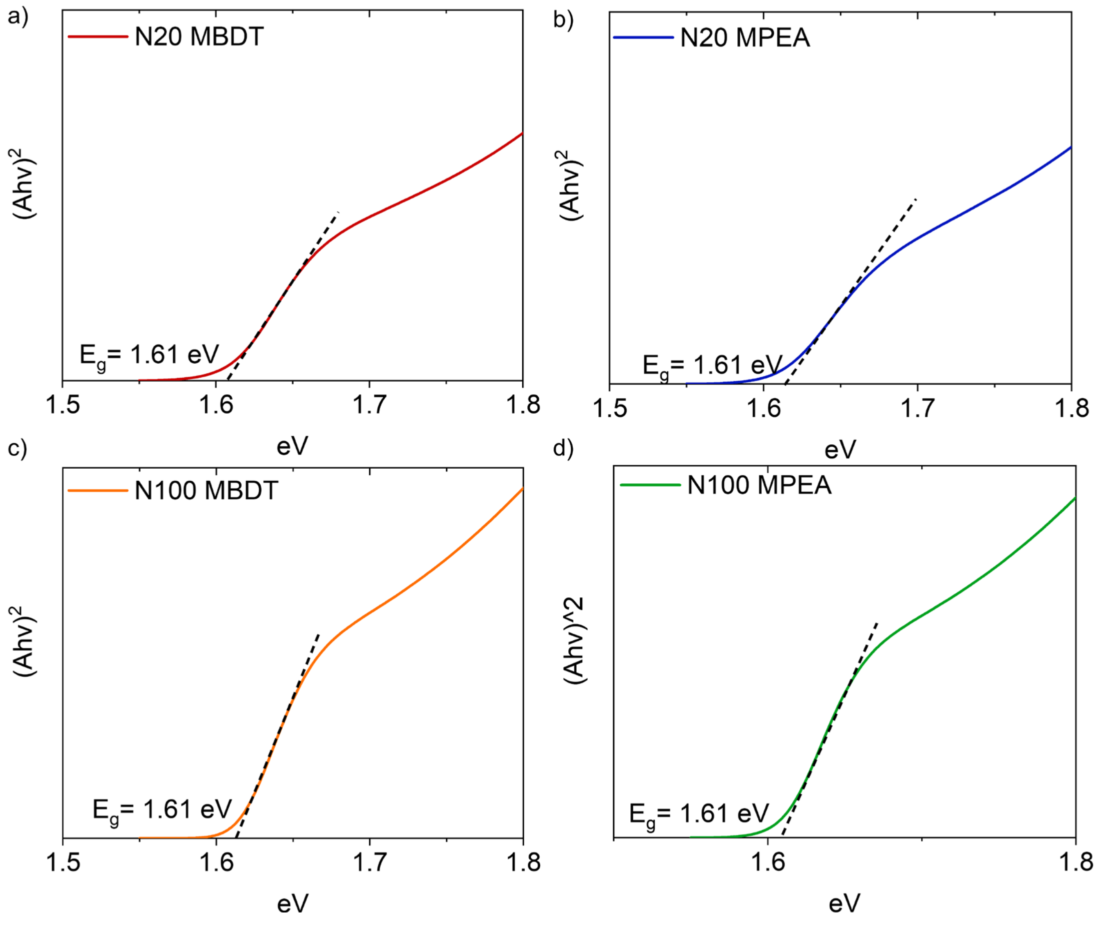

Figure 4.12. QLLHP band gap energy determination via Tauc plot analysis for (a) N20 MBDT, (b) N20 MPEA, (c) N100 MBDT, and (d) N100 MPEA.

With the band gap in hand and with the aim of positioning the corresponding valence and conduction band edges, the valence band maxima (VBM) energy levels with respect to vacuum were deduced from UPS linear extrapolations for the VBM (**Figure 4.13**), secondary electron cut-off (**Figure 4.14**), and the corresponding ionization energy calculations (**Figure 4.15**).[23,24] In view of the relative position of the energy bands it is worth highlighting two observations. Firstly, the incorporation of the spacers, both PEA and BDT, causes the VB edge to shift towards lower energy values, indeed, the higher the spacer's content the deeper the band. Secondly, the lowering in the VB is more significant when implementing BDT.

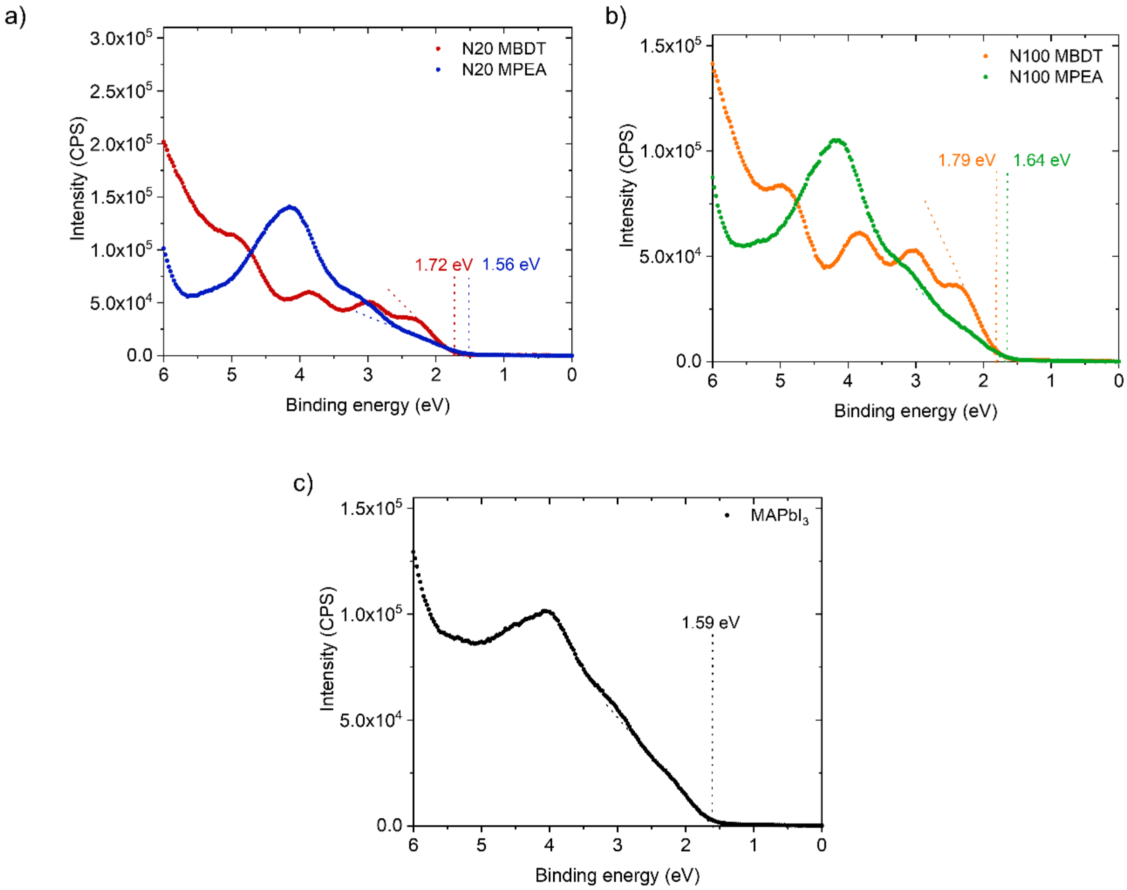

Figure 4.13. UPS linear scale plots with a fitting of the VBM for (a) the N20 series, (b) the N100 series, and (c) $MAPbI_3$.

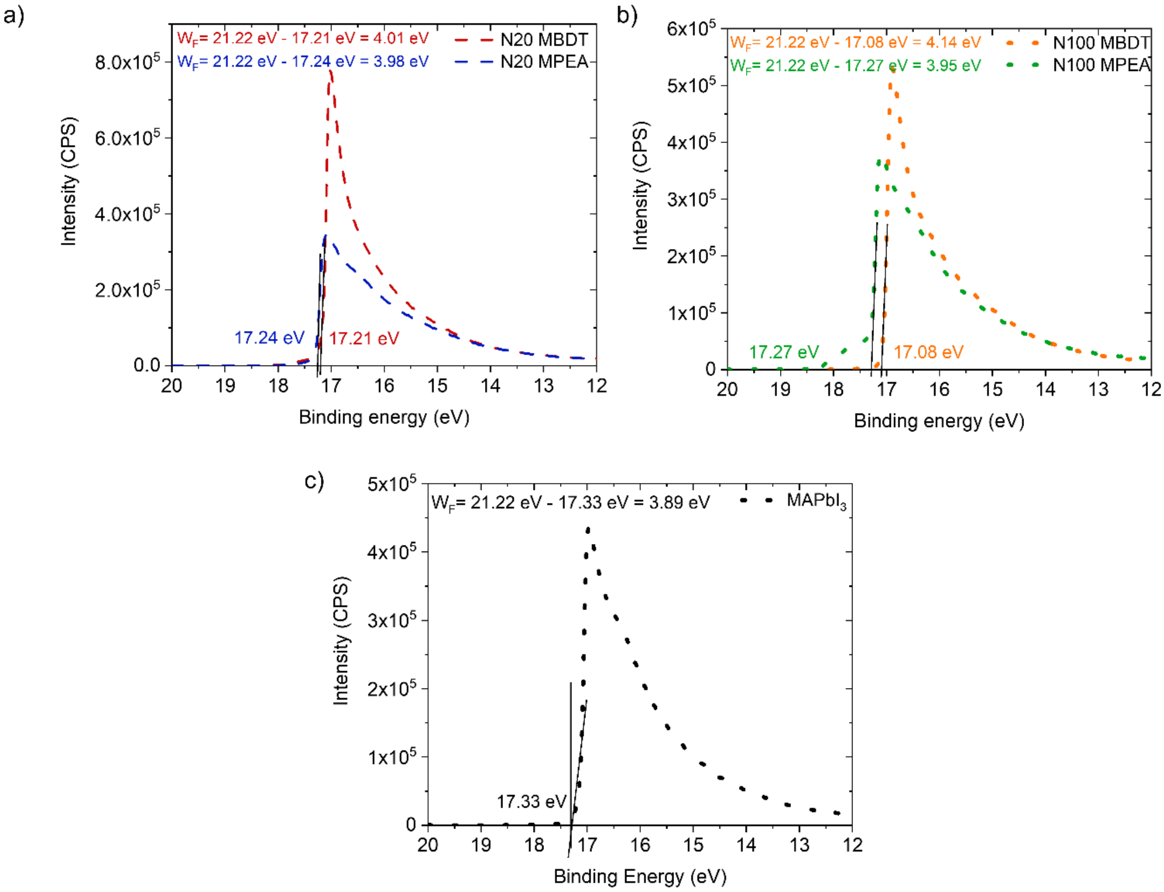

Figure 4.14. UPS linear scale plots with a fitting of the secondary electron cut-off for (a) the N20 series, (b) the N100 series, and (c) $MAPbI_3$.

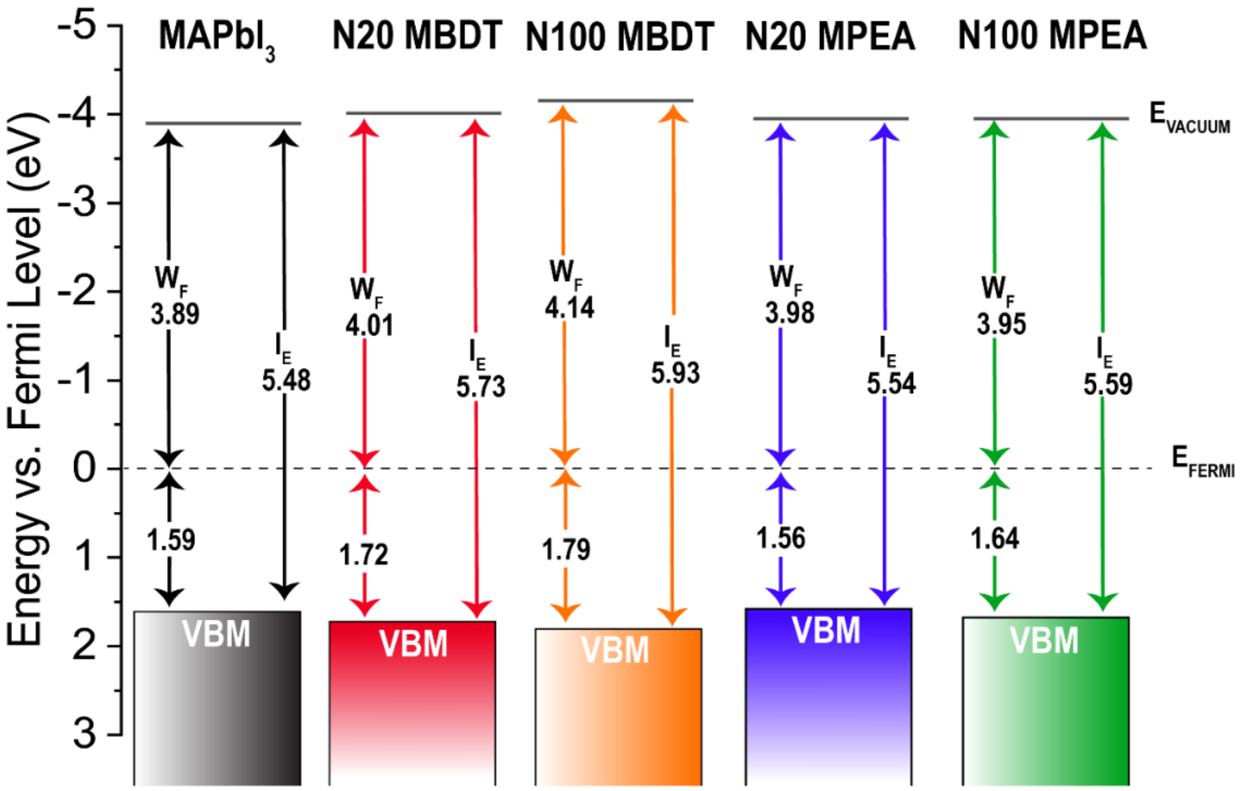

Figure 4.15. Summary of calculated VBM, work function (W_F) and ionization energy (I_E) values for $MAPbI_3$, the N100 series and the N20 series.

In order to compare the photovoltaic performance of the BDT-based QLLHP to the PEA version, devices were next fabricated: FTO/TiO_2/QLLHP/Spiro/Au. Band alignments with the electron and hole contacts[33] and calculated energy levels of the QLLHPs implemented are presented in **Figure 4.16a** (note only one of the four active materials was used for each device). Furthermore, the one-sun J-V curves of the best-performing devices for each of the active layers are reported in **Figure 4.16b**. For the N100 series, the N100 MBDT device outperforms N100 MPEA with a PCE of 14.7% vs. 13.7%, which is mainly due to an enhanced J_{SC} and a moderate FF increase. We note that the performance of the MPEA devices is comparable to previous reports with similar *n*,[34] but slightly lower likely due to the larger aperture area (0.09 cm^2 vs. 0.05 cm^2) used in our work. The enhancement of the J_{SC} of the BDT vs. that of the PEA QLLHP becomes more evident at lower *N* values, where the N20 MBDT best-performing device resulted in a PCE of 8.5% vs. 5.3% for the best N20 MPEA device. It is worth noting that the observed higher J_{SC} values in the BDT-based devices are not due to a light absorption increase, as the PEA and BDT devices exhibited similar light absorbance (**Figure 4.11**).

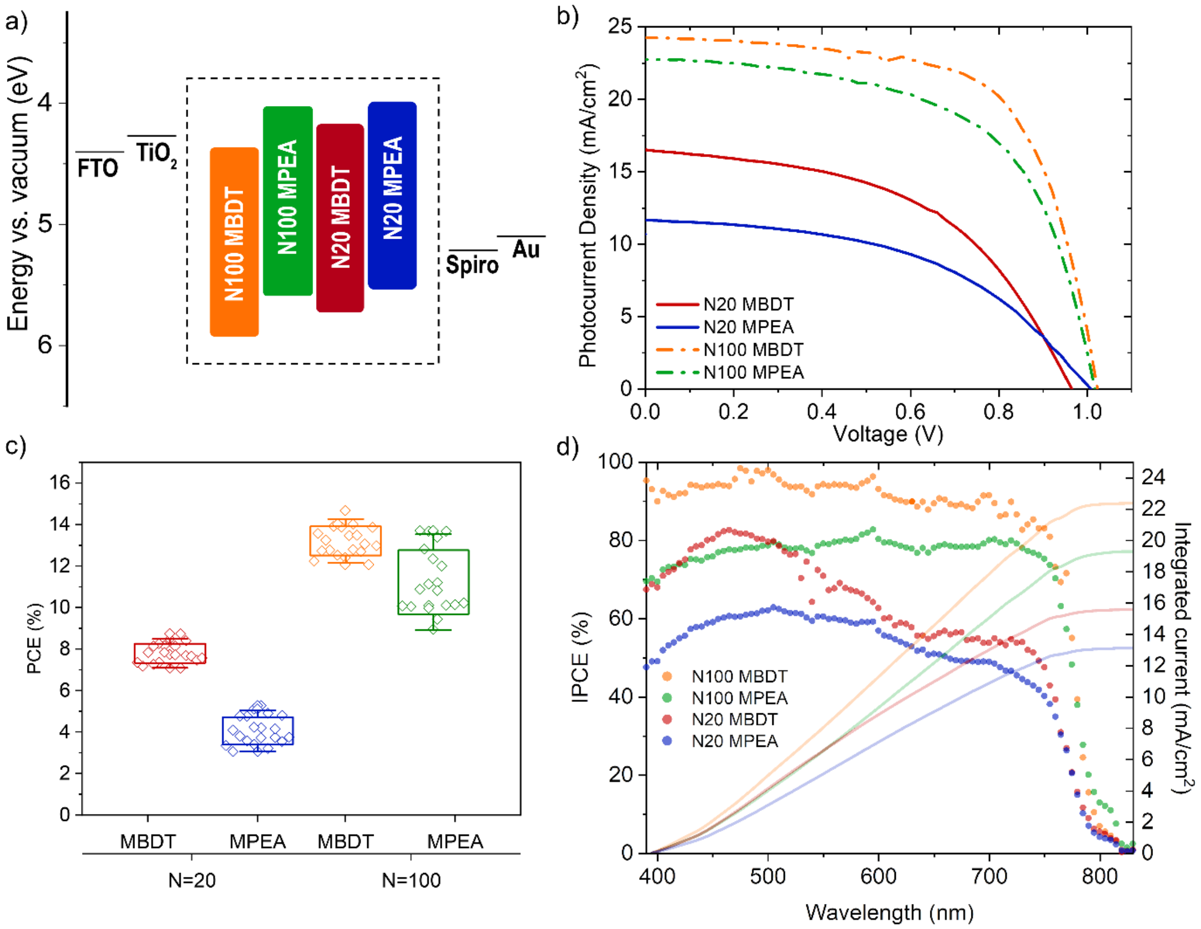

Figure 4.16. Quasi-layered devices. (a) Energy level and band gap alignment of the four QLLHP materials tested (inside the dashed box) with respect to the hole-transporting and electron-transporting contacts used. (b) Champion cell J-V curves obtained with a 0.09 cm² active area and AM 1.5G illumination. (c) Box plots with results of 20 devices for each QLLHP material and (d) device incident photon-to-current efficiency (IPCE) and integrated currents with respect to illumination wavelength.

In addition to the best-performing devices, both the N20 and the N100 MBDT devices display a more reproducible and narrower device PCE distribution compared to the N20 and N100 MPEA devices, respectively, as shown by box plots presented in **Figure 4.16c** representing the PCE results from 20 devices prepared for each material tested (average and champion values for J_{SC}, V_{OC}, and *FF* are listed in **Table 4.2**).

Table 4.2. Comparative numerical photovoltaic results for QLLHP-based solar cells (reverse scans)

	J_{SC} [mAcm^{-2}] [a]	V_{OC} [V] [a]	*FF* [a]	PCE [%][a]	J_{SC} [mAcm^{-2}][b]	V_{OC} [V] [b]	*FF* [b]	PCE [%] [b]
N20 MBDT	15.91	0.96	0.50	7.80	16.51	0.97	0.50	8.48
N20 MPEA	10.46	1.02	0.40	4.07	11.66	1.01	0.48	5.27
N100 MBDT	22.03	1.00	0.61	13.22	24.25	1.02	0.65	14.67
N100 MPEA	21.24	1.01	0.54	11.24	22.74	1.02	0.59	13.68

[a] Average over 20 devices; [b] Champion device

The J_{SC}, V_{OC} and *FF* distributions for all devices are displayed in more detail on **Figure 4.17**.

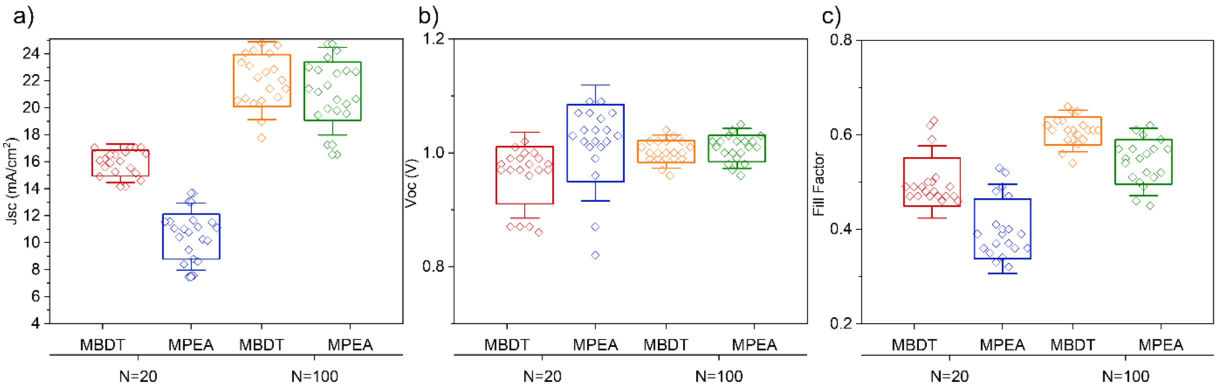

Figure 4.17. (a) *Jsc*, (b) *Voc* and (c) FF distributions for 20 devices of N20 MBDT, N20 MPEA, N100 MBDT and N100 MPEA devices (reverse curves)

Moreover, we note that hysteresis decreases significantly for higher *N* number perovskites (**Figure 4.18**, **Table 4.3**).

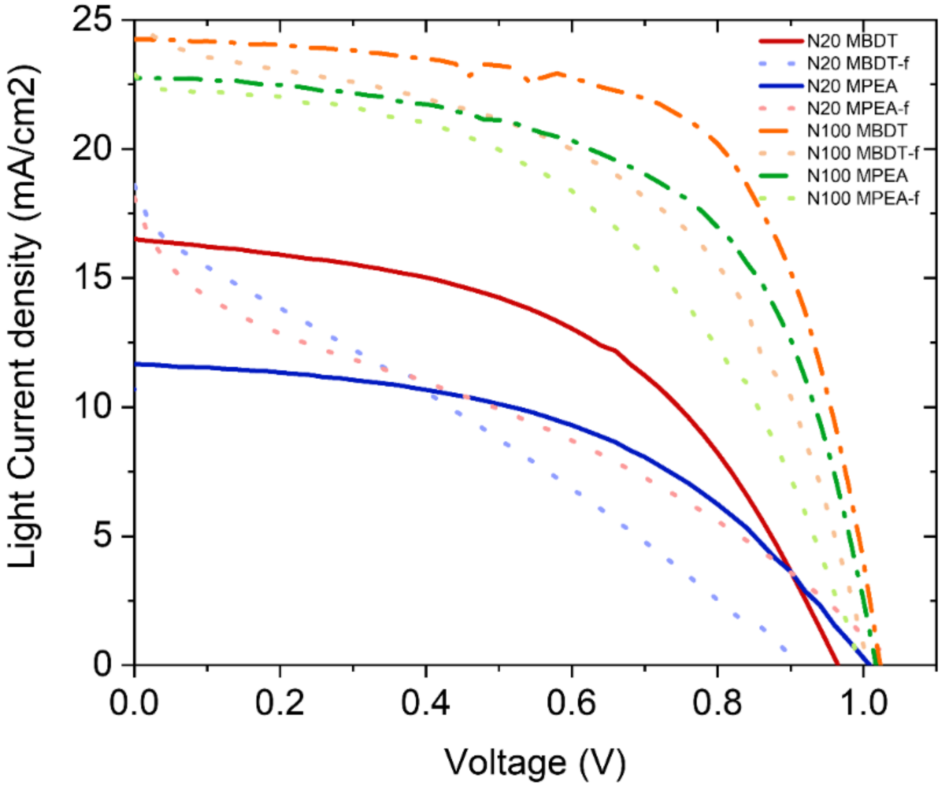

Figure 4.18. Forward and reverse J-V curves for the N20 MBDT, N20 MPEA, N100 MBDT and N100 MPEA devices

Table 4.3. Comparative numerical photovoltaic results for QLLHP-based solar cells in the reverse (-r) and forward (-f) scans

	J_{SC} [mAcm^{-2}] [a]	V_{OC} [V] [a]	FF [a]	PCE [%] [a]	J_{SC} [mAcm^{-2}] [b]	V_{OC} [V] [b]	FF [b]	PCE [%] [b]
N20 MBDT-r	15.91	0.96	0.50	7.80	16.51	0.97	0.50	8.48
N20 MBDT-f	16.71	0.88	0.30	4.42	18.60	0.91	0.26	4.63
N20 MPEA-r	10.46	1.02	0.40	4.07	11.66	1.01	0.48	5.27
N20 MPEA-f	12.88	1.00	0.24	2.90	18.12	1.05	0.28	4.84
N100 MBDT-r	22.03	1.00	0.61	13.22	24.25	1.02	0.65	**14.67**
N100 MBDT-f	22.64	0.98	0.43	9.41	25.29	1.01	0.50	11.63
N100 MPEA-r	21.24	1.01	0.54	11.24	22.74	1.02	0.59	**13.68**
N100 MPEA-f	22.12	0.98	0.44	9.34	22.88	0.99	0.49	11.16

[a] Average over 20 devices; [b] Champion device

To further verify the performance of the MBDT and MPEA devices, the incident photon to current efficiency (IPCE) was measured as a function of illumination wavelength at short-circuit conditions (**Figure 4.16d**). Integrating the data with the standard solar spectrum resulted in theoretical one-sun J_{SC} values of 22.36 mA cm^{-2} for N100 MBDT, 19.28 mA cm^{-2} for N100 MPEA, 15.56 mA cm^{-2} for N20 MBDT and 13.10 mA cm^{-2} for N20 MPEA, which match well with the J_{SC} found in the J-V curve.

4.2.3 Origin of the device performance difference

In an effort to rationalize the performance difference between the BDT and PEA QLLHP solar cells we first examined the morphology of the active layer.

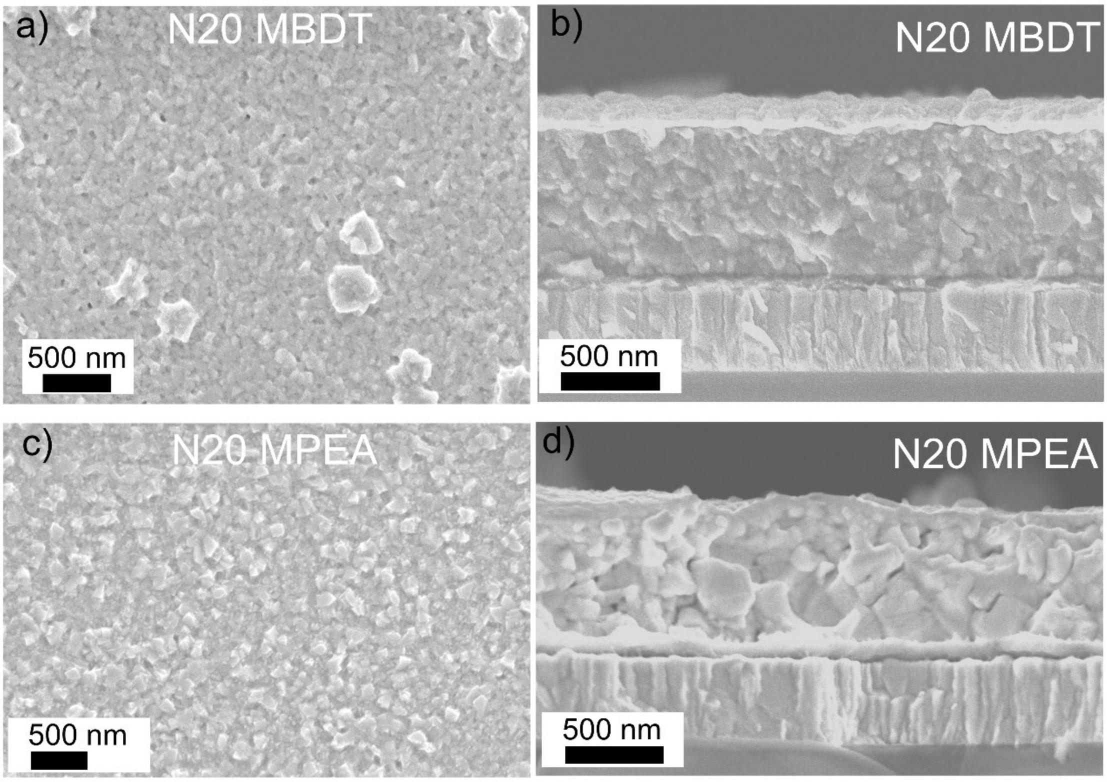

Figure 4.19. (a) Top and (b) cross-sectional SEM images of N20 MBDT and (c) top and (d) cross-sectional SEM images of N20 MPEA layers solution-processed onto FTO substrates. Note cross-sectional images show films capped with an Au overlayer (to facilitate measurement).

Interestingly, despite the identical processing conditions, we observed a significantly different morphology of the active layer with scanning electron microscopy (SEM) showing a considerably smaller grain size for the BDT-containing QLLHP active layers compared to PEA. This is illustrated by the top-down SEM images for the bare films of N20 MBDT (**Figure 4.19a**) and N20 MBDT (**Figure 4.19c**) as well as the corresponding cross-sectional images for the N20 QLLHP layers prepared on FTO and capped with Au shown in **Figure 4.19b** and **d**, respectively. For the N20 case, the average grain size (calculated over 20 grains) was calculated to be 153 ± 48 nm for N20 MBDT and 227 ± 58 nm for N20 MPEA, using the ImageJ software[35], as tabulated on **Table 4.4**.

Table 4.4. Domain size for N20 MBDT and MPEA series

Domain	N20 MBDT (nm)	N20 MPEA (nm)
1	213	360
2	83	325
3	108	314
4	125	213
5	184	213
6	220	208
7	192	279
8	162	244
9	189	245
10	155	279
11	129	199
12	226	197
13	174	213
14	218	205
15	131	144
16	144	172
17	136	157
18	83	162
19	77	198
20	102	216
Average (nm):	153	227

This trend is consistent in the N100 devices (see top-down and cross-sectional images on **Figure 4.20a,b** (N100 MBDT films) and **c,d** (N100 MPEA), respectively) where average grain sizes of 182 ± 37 nm and 291 ± 86 nm were calculated for the BDT- and PEA- containing films, respectively (See **Table 4.5**). The significantly smaller grain size for the BDT-containing active layer could result from the lower solubility of this cation in the DMF:DMSO solvent mixture (53 mg mL^{-1}) compared to PEA (83 mg mL^{-1}), leading to a greater amount of seeding during film formation and hence smaller grain size. However, despite the smaller grain size and the associated increased density of grain boundaries, which are a well-known source of defects and charge carrier traps,[36] the performance of the BDT-containing devices is improved compared to that of the PEA-based devices.

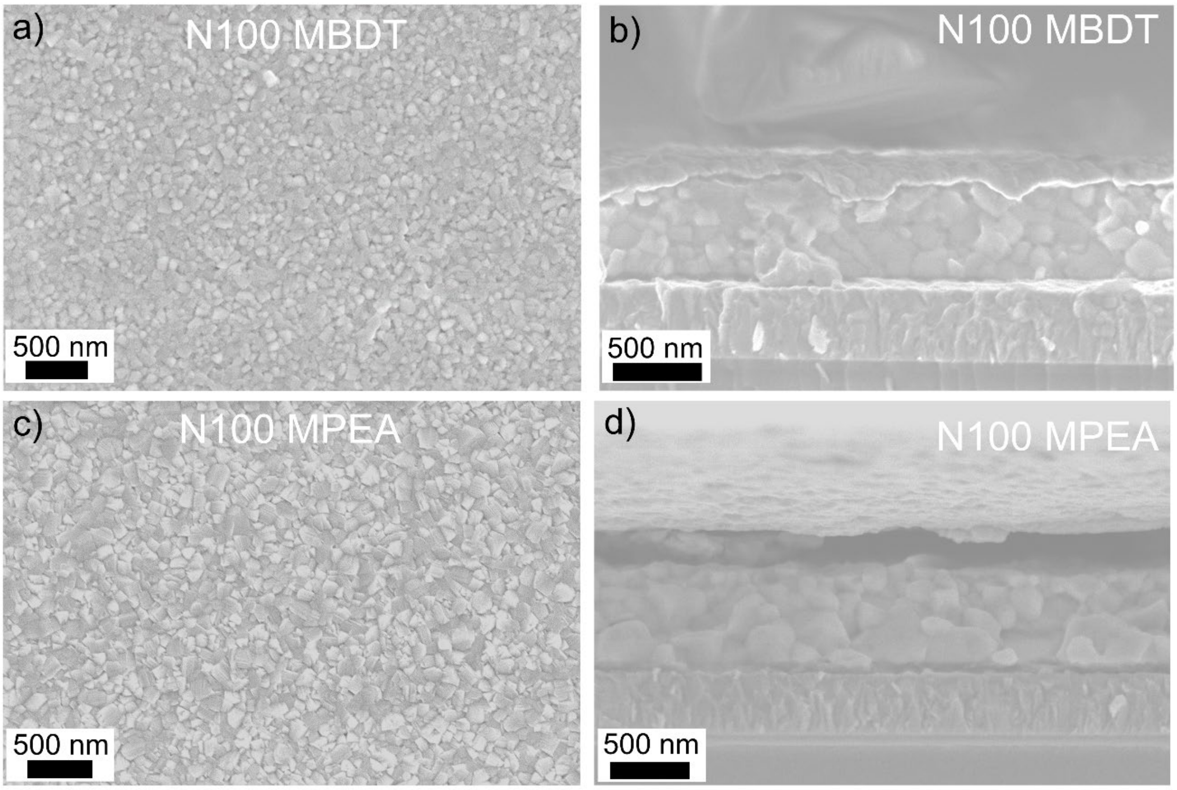
a)
N100 MBDT
500 nm
b)
N100 MBDT
500 nm
c)
N100 MPEA
500 nm
d)
N100 MPEA
500 nm

Figure 4.20. (a) Top and (b) cross-sectional SEM images of N100 MBDT and (c) top and (d) cross-sectional SEM images of N100 MPEA layers solution-processed onto FTO substrates. Note cross-sectional images show films capped with an Au overlayer (to facilitate measurement).

Table 4.5. Domain size for N100 MBDT and MPEA series

Domain	N100 MBDT (nm)	N100 MPEA (nm)
1	231	322
2	172	230
3	162	272
4	254	283
5	147	239
6	230	489
7	173	418
8	153	339
9	165	316
10	217	184
11	165	361
12	181	402
13	191	283
14	267	298
15	139	265
16	157	284
17	141	199
18	177	324
19	165	195
20	163	126
Average (nm):	182	291

Considering that PEA addition to lead halide perovskites is known to passivate defects at the grain boundaries,[30] and knowing that the BDT cation results in more grain boundaries which are commonly conducive to a higher defect density, we hypothesized that the BDT proceeded to passivate the defects in the device active layer in an alternative form. To investigate this possibility, we performed transient photocurrent (TPC) measurements at short circuit conditions using a 5 ns pulsed laser (550 nm wavelength) at a fluence of 0.96 μJ cm^{-2}. The TPC dynamics for representative devices with each active layer are shown in **Figure**

4.21 over two different time scales (short time response in the inset). While the TPC decay dynamics have been determined to be influenced by both the charge carrier transport in the device and the recombination at the transport layers/absorber interfaces,[37] given the identical charge transport layers in our devices, we attribute differences in the TPC dynamics mainly toward charge transport in the active layer. The extracted TPC exponential decay times (τ_c) are given in **Table 4.6** for short and long time scales (τ_{c1} and τ_{c2}, respectively), and a significantly faster decay for the BDT-containing devices is seen over both time scales as also evident from qualitative inspection of **Figure 4.21** (e.g. τ_{c1} = 2.17 and 8.93 μs for the N100 MBDT and MPEA, respectively).

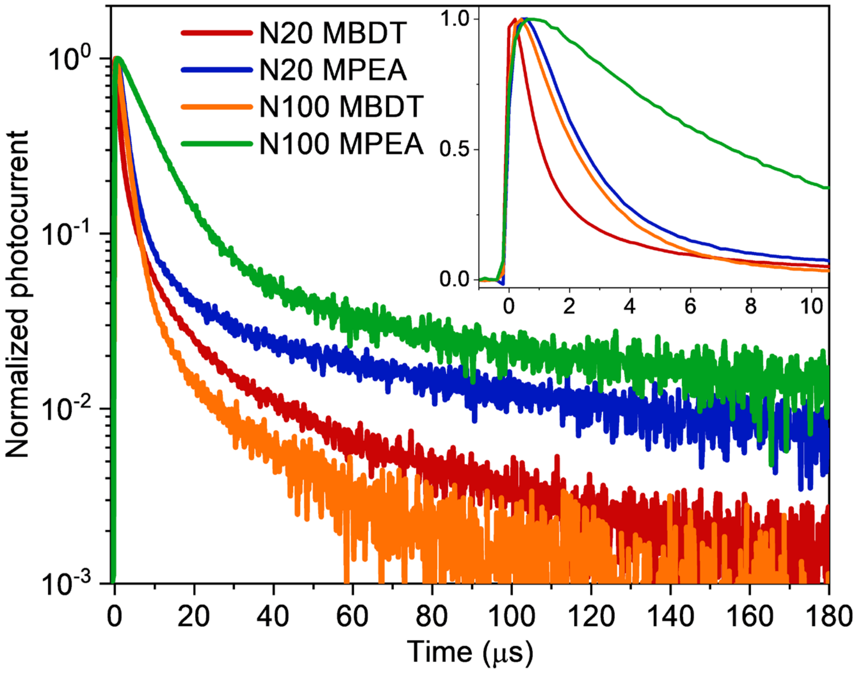

Figure 4.21. Normalized device photocurrent as a function of time after a 5 ns pulse (550 nm wavelength) shown in the log scale over the long time frame and a linear scale for the short time regime (inset).

Table 4.6. Extracted TPC exponential decay times (τ_c) for QLLHP-based devices (standard errors given in parenthesis).

	τ_{c1} [μs] [a]	τ_{c2} [μs] [b]
N20 MBDT	1.07 (0.02)	34.8 (0.77)
N20 MPEA	2.13 (0.02)	50.8 (1.99)
N100 MBDT	2.17 (0.007)	23.2 (1.92)
N100 MPEA	8.93 (0.23)	38.0 (1.42)

[a] Short timescale < 10 μs; [b] long timescales (between 40-180 μs)

Moreover, **Figure 4.22** further corroborates the above observations, where conductive atomic force microscopy images under illumination (right) (displayed together with their corresponding topography images on the left, for the N100 series of samples shows a clear surface current increase of one order of magnitude for the N100 MBDT (**Figure 4.22**) sample (up to 680 pA) vs. the N100 MPEA (**Figure 4.22b**) sample (up to 53 pA). While the N100 MBDT's topography leads to a somewhat increased segregation of the conductive regions, the enhanced overall conductivity of the N100 MBDT sample can be confirmed, further representing the optoelectronic activity of the BDT spacer.

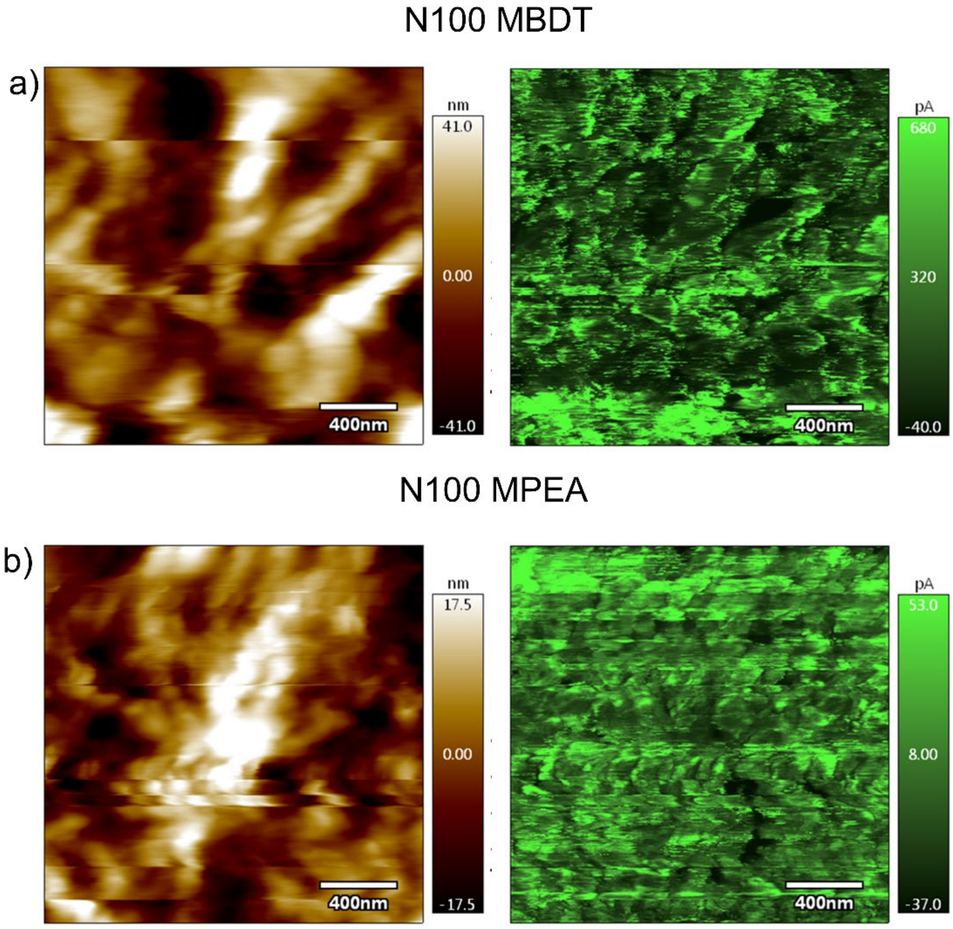
N100 MBDT
a)
nm
41.0
0.00
-41.0
400nm
pA
680
320
-40.0
400nm
N100 MPEA
b)
nm
17.5
0.00
-17.5
400nm
pA
53.0
8.00
-37.0
400nm

Figure 4.22. (Left) Atomic force microscopy (AFM) and (right) conductive atomic force microscopy images of (a) N100MBDT and (b) N100 MPEA

These consistently faster decays, together with the larger J_{SC} of the devices, are in line with the view that charge carrier transport is improved in the BDT-containing devices over a wide range of photogenerated charge densities in the device.[38,39] This would be expected if charge trapping states at the grain boundaries are energetically altered when the BDT ligand is employed. Insights into energetic differences of the trapping states at the grain boundaries was next sought by examining the UV photoelectron spectra for the different active layers (**Figure 4.23a**) near the valence band maximum (VBM).

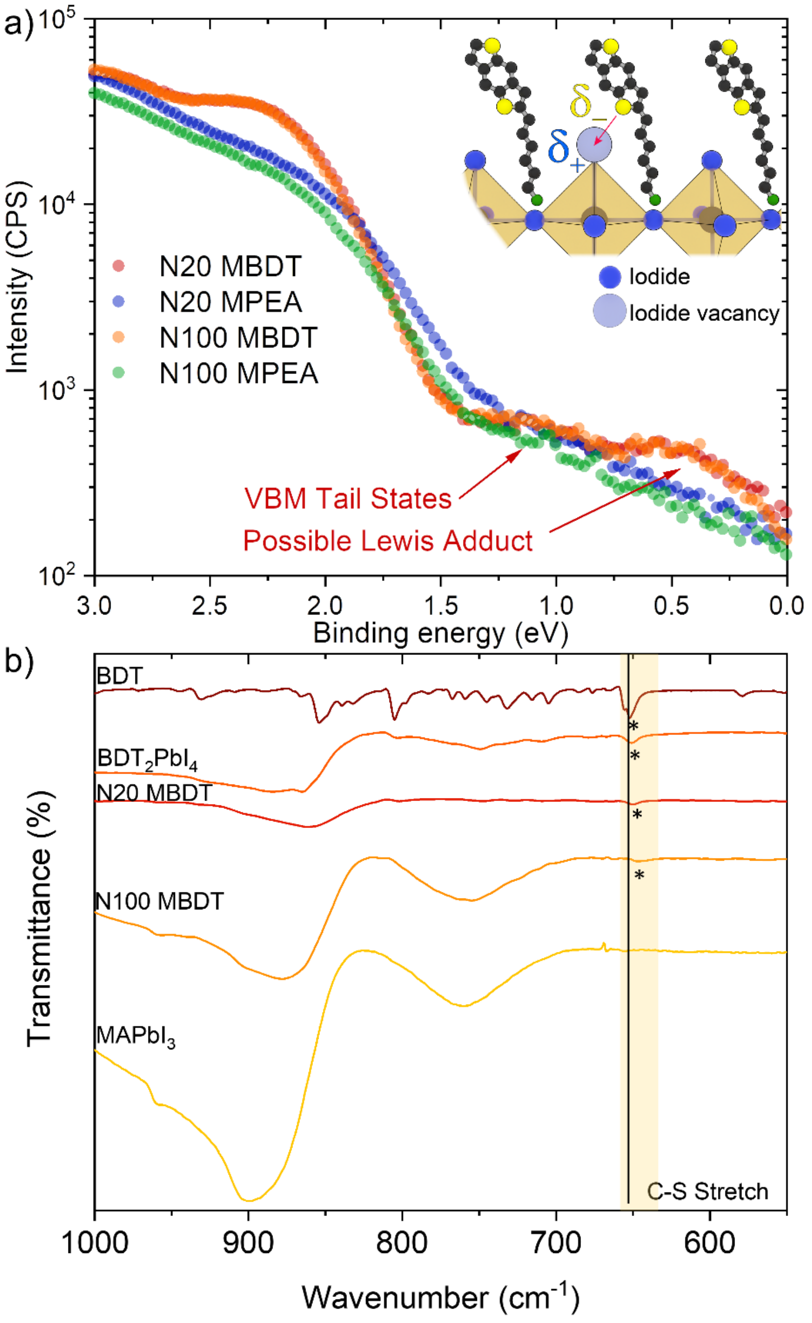

Figure 4.23. (a) UV photoelectron spectroscopy measurements of the perovskite thin films deposited on FTO substrates. The inset shows a schematic of hypothesized undercoordinated Pb passivation via $v_I^{\bullet}$ – S (thiophene) Lewis adduct formation (b) ATR-FTIR data for a BDT drop cast film, BDT_2PbI_4, N20 MBDT, N100 MBDT and $MAPbI_3$ reference thin films with a highlight of the C-S stretch peak shift, the asterisks represent the peak positions.

While the region between the VBM, which is at a binding energy of approximately 1.5 eV, and the Fermi energy level (E_F = 0 eV) is expected to contain band tail states, an increased density of states in this region (closer to the E_F) is observed for both the N20 and N100 MBDT layers compared to the MPEA. Previously, a similar increase in the UPS signal in this region has been attributed to the presence of metallic/reduced Pb species.[40] However, X-ray Photoelectron Spectroscopy (XPS) measurements did not reveal the presence of metallic Pb nor a loss of Pb cationic character on the octahedral central Pb ion (**Figure 4.24**).

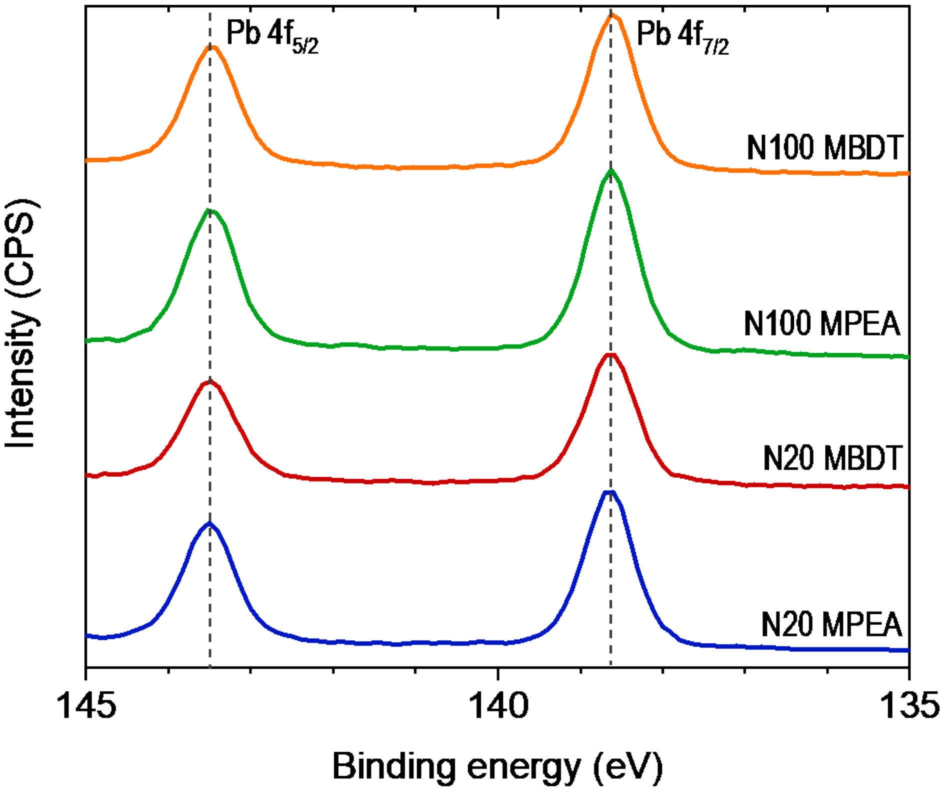

Figure 4.24. Narrow-scan XPS Pb 4f spectra of the QLLHP samples N20 MPEA, N20 MBDT, N100 MPEA, N100 MBDT.

This is not unexpected given the differences in probing depth (i.e. approximately 5 nm for XPS compared to the ca. 1 nm for UPS) suggesting the observed states are localized at the surface and grain boundaries. In view of the electron-donating nature of the BDT cation via the sulfur atom in the thiophene,[17,19] and the frequent presence of iodide vacancies ($v_I^{\bullet}$ in Kröger–Vink notation) at the surface,[41,42] it is plausible to propose the existence of Lewis acid-base interactions between the BDT cation and the undercoordinated Pb atoms in the vicinity. Given the positive charge on the aforementioned vacancies, and their corresponding function as electron traps, forming $v_I^{\bullet}$ – S (thiophene) adducts as shown in **Figure 4.23a** (inset schematic) could alleviate such defects.

In order to support our observations of reduced Pb species on the UPS measurements on **Figure 4.23a**, we have carried out attenuated total reflectance-fourier transform infrared spectroscopy (ATR-FTIR) measurements on a pure BDT-C6 sample, BDT_2PbI_4, N20 MBDT, N100 MBDT and an $MAPbI_3$ reference sample (**Figure 4.23b**). From the resulting spectra, a clear shift of the 652 cm^{-1} C-S stretch peak in the pure BDT sample towards lower wavenumbers for all the perovskite samples synthesized with BDT can be observed.[43] Namely, in BDT_2PbI_4, the peak shifts towards 651 cm^{-1} while for N20 MBDT and N100 MBDT, the peak shifts to 650 cm^{-1} and 646.5 cm^{-1}, respectively. The shift towards lower wavenumbers indicates the weakening of the C-S (thiophene) bond which aligns well with the participation of S (thiophene) as an electron-donating species. Bearing in mind that UPS revealed the partial reduction of Pb in the presence of BDT, it is plausible to consider that the S (thiophene) acts as a Lewis base donating electrons to the undercoordinated Pb centers. The results obtained from UPS and ATR-FTIR data thus support the formation of a Pb – S Lewis adduct. Indeed, similar shifts towards lower wavenumbers have been reported for Lewis acid-base adducts passivating undercoordinated lead defects.[44,45]

We further speculate that these resulting energy states improve the charge carrier transport between grain boundaries and between the active layer and the hole transporting Spiro overlayer, which could be possible if a formed Lewis adduct brings the BDT moiety into an improved electronic communication with the perovskite material. Indeed, an increased charge carrier transport at these grain boundaries reasonably explains the increased performance of the BDT-containing devices despite the increased concentration of grain boundaries. Moreover, since BDT is known to operate as a good hole transport moiety in OPV devices, and the “Lewis-adduct” energy states observed by UPS are well aligned with the energy level of Spiro, an improved hole transfer of the MBDT films to Spiro is a reasonable conclusion.

4.2.4 Device stability comparison

Since the formation of QLLHPs is a well-established route to increase device stability by preventing ionic migration in the active layer and also the diffusion of water molecules,[25] we next probed the effect of the BDT cation's bulkier nature compared to PEA on the stability of solar cells. The N100 series of devices were subjected to photovoltaic stability measurements in a dry N_2 environment under constant one-sun illumination where the N100 MBDT device showed a significantly improved performance after 130 h conserving 64% of the initial performance while the N100 MPEA device conserved only 31% of its initial performance (**Figure 4.25a**).

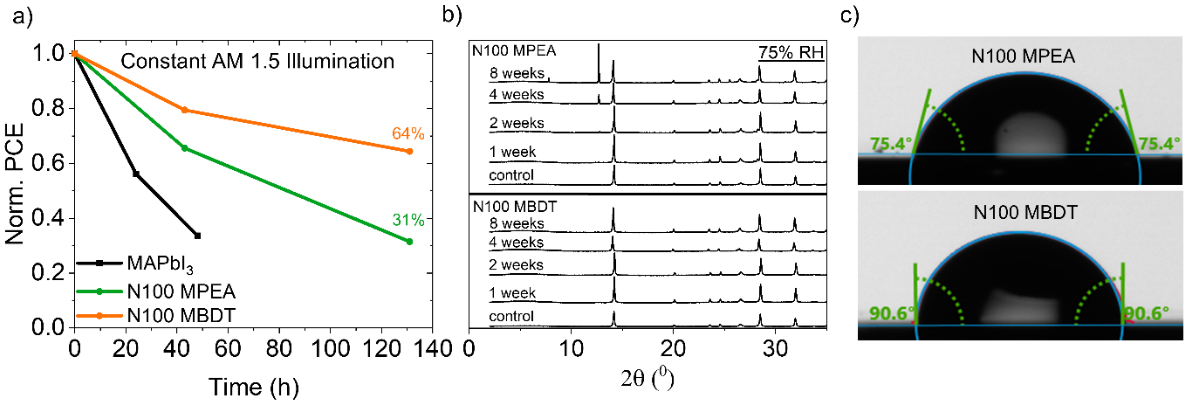

Figure 4.25. QLLHP stability and moisture resistance measurements. (a) Normalized PCE of the N100-based devices (and an $n = \infty$ control) with respect to time in a dry N_2 environment under constant one-sun illumination (open circuit conditions) (b) XRD patterns of bare QLLHP active layers exposed to 75% RH air (25°C) for different times. (c) water contact angle measurements for bare films of N100 MPEA (top) and N100 MBDT (bottom).

In comparison, an $MAPbI_3$ ($n = \infty$) device dropped to 34% of the initial performance after only 48 h. The normalized performance parameters for the J_{SC}, V_{OC} and FF can be found on **Figure 4.26a**, **b** and **c**, respectively. Under these conditions (dry N_2), the enhanced stability of the MBDT device is reasonably ascribed to an improved ability of the bulkier pi-conjugated BDT cation to suppress MA leakage from the main perovskite ($n = \infty$) domains in the active layer.[46,47] The N100 QLLHP active layers were also submitted to high humidity environments (75% relative humidity, RH) for 8 weeks, and examined periodically by XRD to track the phase stability (**Figure 4.25b**). After 4 weeks the N100 MPEA samples began to show signs of degradation with the emergence of a new peak at around 2θ = 12.5° indicative of PbI_2 segregation from the main perovskite phase, which was not observed for the N100 MBDT perovskite. The improved resistance to water was further confirmed by contact angle measurements (**Figure 4.25c**), where an enhanced hydrophobicity was observed for the N100 MBDT (exhibiting a water contact angle of 90.6° compared to 75.4° for the N100 MPEA). Overall, these experiments support the view that the bulky BDT, when incorporated into a QLLHP even at a small quantity (*i.e.* at $N = 100$) can successfully improve both material and device stabilities compared to the standard PEA cation.

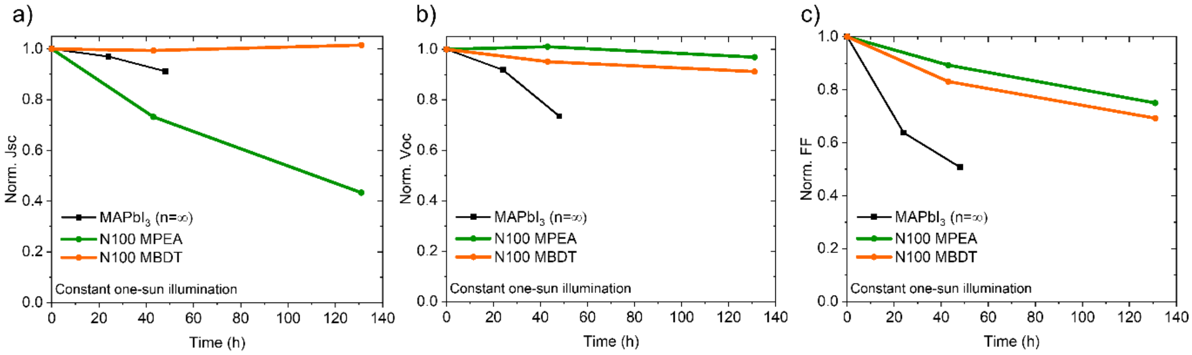

Figure 4.26. Normalized (a) *Jsc* (b) *Voc* and (c) FF performance parameters for constant one-sun illumination stability studies on N100 MPEA, N100 MBDT and $MAPbI_3$ reference devices.

4.3 Conclusions

In summary, motivated by the aspiration to integrate diverse organic semiconductor species into layered perovskites we have demonstrated the incorporation of a benzodithiophene (BDT)-based organic cation in layered and quasi-layered lead halide perovskites. We found that tuning the length of the alkyl chain between the BDT group and the ammonium ion was critical to the successful formation of a Ruddlesden-Popper ($n = 1$) phase, with only the hexyl BDT-C6 version resulting in a photoactive RP phase. The resulting $(BDT\text{-}C6)_2PbI_4$ perovskite thin films were found to form with layers parallel to the substrate and gave modest photovoltaic device performance. In contrast, the active BDT cation gave superior device performance compared to PEA in quasi-layered lead iodide-based devices with $N = 20$ or 100, due to an increase in J_{SC}. The increased performance, despite a smaller domain size and increase in grain boundaries in the BDT-containing active layers, was correlated to a faster TPC decay time likely due to superior charge transport/transfer in the

BDT devices compared to PEA. In fact, N20-fabricated perovskite photovoltaic devices with BDT display an increase of 60% of the performance of the corresponding PEA devices, whereas the N100 devices lead to a performance increase of 8% of that from the corresponding PEA devices. Moreover, evidence of Lewis acid-base interactions between the BDT cation and undercoordinated Pb atoms (likely present due to iodide vacancies at grain boundaries and active layer interfaces) as acquired by UPS and ATR-FTIR data, suggests an electronic influence of the BDT cation on the defects and rationalizes the improved performance. In addition, due to its bulkier nature, the BDT-cation-based photovoltaic devices showed an increased device stability compared to PEA-based devices. We further note that only a small BDT cation loading is enough for material stabilization, harnessing the advantages of the better-performing high N number perovskites. These results underline the importance of molecular engineering π-conjugated organic cations to tune their ability of incorporation in layered lead halide perovskite thin films. The findings further highlight the possibility to harness functionality in π-conjugated organic cations to improve performance in layered and quasi-layered lead halide perovskite solar cells.

4.4 References

[1] Y. Gao, Z. Wei, S.-N. Hsu, B. W. Boudouris, L. Dou, *Mater. Chem. Front.* **2020**, *4*, 3400.

[2] H. Bronstein, C. B. Nielsen, B. C. Schroeder, I. McCulloch, *Nat. Rev. Chem.* **2020**, *4*, 66.

[3] F. Yang, P. Zhang, M. A. Kamarudin, G. Kapil, T. Ma, S. Hayase, *Adv. Funct. Mater.* **2018**, *28*, 1804856.

[4] W. T. M. Van Gompel, R. Herckens, K. Van Hecke, B. Ruttens, J. D'Haen, L. Lutsen, D. Vanderzande, *Chem. Commun.* **2019**, *55*, 2481.

[5] W. T. M. Van Gompel, R. Herckens, K. Van Hecke, B. Ruttens, J. D'Haen, L. Lutsen, D. Vanderzande, *ChemNanoMat* **2019**, *5*, 323.

[6] J. V. Passarelli, D. J. Fairfield, N. A. Sather, M. P. Hendricks, H. Sai, C. L. Stern, S. I. Stupp, *J. Am. Chem. Soc.* **2018**, *140*, 7313.

[7] J. Yang, C. Liu, C. Cai, X. Hu, Z. Huang, X. Duan, X. Meng, Z. Yuan, L. Tan, Y. Chen, *Adv. Energy Mater.* **2019**, *9*, 1900198.

[8] R. Herckens, W. T. M. V. Gompel, W. Song, M. C. Gélvez-Rueda, A. Maufort, B. Ruttens, J. D'Haen, F. C. Grozema, T. Aernouts, L. Lutsen, D. Vanderzande, *J. Mater. Chem. A* **2018**, *6*, 22899.

[9] Y. Gao, Z. Wei, P. Yoo, E. Shi, M. Zeller, C. Zhu, P. Liao, L. Dou, *J. Am. Chem. Soc.* **2019**, *141*, 15577.

[10] D. Lu, G. Lv, Z. Xu, Y. Dong, X. Ji, Y. Liu, *J. Am. Chem. Soc.* **2020**, *142*, 11114.

[11] Y. Dong, D. Lu, Z. Xu, H. Lai, Y. Liu, *Adv. Energy Mater.* **2020**, *10*, 2000694.

[12] G. Gryn'ova, C. Corminboeuf, *J. Phys. Chem. Lett.* **2016**, *7*, 5198.

[13] E. G. Hohenstein, C. D. Sherrill, *J. Phys. Chem. A* **2009**, *113*, 878.

[14] R. G. Huber, M. A. Margreiter, J. E. Fuchs, S. von Grafenstein, C. S. Tautermann, K. R. Liedl, T. Fox, *J. Chem. Inf. Model.* **2014**, *54*, 1371.

[15] Y. Gao, E. Shi, S. Deng, S. B. Shiring, J. M. Snaider, C. Liang, B. Yuan, R. Song, S. M. Janke, A. Liebman-Peláez, P. Yoo, M. Zeller, B. W. Boudouris, P. Liao, C. Zhu, V. Blum, Y. Yu, B. M. Savoie, L. Huang, L. Dou, *Nat. Chem.* **2019**, *11*, 1151.

[16] H. Yao, L. Ye, H. Zhang, S. Li, S. Zhang, J. Hou, *Chem. Rev.* **2016**, *116*, 7397.

[17] N. K. Noel, A. Abate, S. D. Stranks, E. S. Parrott, V. M. Burlakov, A. Goriely, H. J. Snaith, *ACS Nano* **2014**, *8*, 9815.

[18] L. Zhang, F. Yu, L. Chen, J. Li, *Appl. Surf. Sci.* **2018**, *443*, 176.

[19] T. Y. Wen, S. Yang, P. F. Liu, L. J. Tang, H. W. Qiao, X. Chen, X. H. Yang, Y. Hou, H. G. Yang, *Adv. Energy Mater.* **2018**, *8*, 1703143.

[20] S.-Y. Kim, J.-M. Yang, E.-S. Choi, N.-G. Park, *Nanoscale* **2019**, *11*, 14330.

[21] M. A. M. Leenen, F. Cucinotta, L. Viani, A. Mavrinskiy, W. Pisula, J. Gierschner, J. Cornil, A. Prodi-Schwab, H. Thiem, K. Müllen, L. De Cola, *J. Phys. Chem. B* **2010**, *114*, 14614.

[22] K. Momma, F. Izumi, *J. Appl. Cryst.* **2011**, *44*, 1272.

[23] B. Philippe, T. J. Jacobsson, J.-P. Correa-Baena, N. K. Jena, A. Banerjee, S. Chakraborty, U. B. Cappel, R. Ahuja, A. Hagfeldt, M. Odelius, H. Rensmo, *J. Phys. Chem. C* **2017**, *121*, 26655.

[24] A. Agresti, A. Pazniak, S. Pescetelli, A. Di Vito, D. Rossi, A. Pecchia, M. Auf der Maur, A. Liedl, R. Larciprete, D. V. Kuznetsov, D. Saranin, A. Di Carlo, *Nature Materials* **2019**, *18*, 1228.

[25] C. Ortiz-Cervantes, P. Carmona-Monroy, D. Solis-Ibarra, *ChemSusChem* **2019**, *12*, 1560.

[26] A. Krishna, S. Gottis, M. K. Nazeeruddin, F. Sauvage, *Adv. Funct. Mater.* **2018**, *29*, 1806482.

[27] C. C. Stoumpos, M. G. Kanatzidis, *Adv. Mater.* **2016**, *28*, 5778.

[28] D. T. Gangadharan, D. Ma, *Energy Environ. Sci.* **2019**, *12*, 2860.

[29] E. S. Vasileiadou, B. Wang, I. Spanopoulos, I. Hadar, A. Navrotsky, M. G. Kanatzidis, *J. Am. Chem. Soc.* **2021**, *143*, 2523.

[30] J.-W. Lee, Z. Dai, T.-H. Han, C. Choi, S.-Y. Chang, S.-J. Lee, N. D. Marco, H. Zhao, P. Sun, Y. Huang, Y. Yang, *Nat. Commun.* **2018**, *9*, 3021.

[31] W. Fu, H. Liu, X. Shi, L. Zuo, X. Li, A. K. -Y. Jen, *Adv. Func. Mater.* **2019**, *29*, 1900221.

[32] Y. Lin, Y. Fang, J. Zhao, Y. Shao, S. J. Stuard, M. M. Nahid, H. Ade, Q. Wang, J. E. Shield, N. Zhou, A. M. Moran, J. Huang, *Nat Commun* **2019**, *10*, 1008.

[33] Z. Zhou, J. Xu, L. Xiao, J. Chen, Z. Tan, J. Yao, S. Dai, *RSC Advances* **2016**, *6*, 78585.

[34] L. N. Quan, M. Yuan, R. Comin, O. Voznyy, E. M. Beauregard, S. Hoogland, A. Buin, A. R. Kirmani, K. Zhao, A. Amassian, D. H. Kim, E. H. Sargent, *J. Am. Chem. Soc.* **2016**, *138*, 2649.

[35] M. D. Abramoff, P. J. Magalhaes, S. J. Ram, *Biophotonics International* **2004**, *11*, 36.

[36] H. Jin, E. Debroye, M. Keshavarz, I. G. Scheblykin, M. B. J. Roeffaers, J. Hofkens, J. A. Steele, *Mater. Horiz.* **2020**, *7*, 397.

[37] Y. Li, Y. Li, J. Shi, H. Li, H. Zhang, J. Wu, D. Li, Y. Luo, H. Wu, Q. Meng, *Appl. Phys. Lett.* **2018**, *112*, 053904.

[38] W. Chen, Y. Wu, Y. Yue, J. Liu, W. Zhang, X. Yang, H. Chen, E. Bi, I. Ashraful, M. Grätzel, L. Han, *Science* **2015**, *350*, 944.

[39] J. Xue, R. Wang, K.-L. Wang, Z.-K. Wang, I. Yavuz, Y. Wang, Y. Yang, X. Gao, T. Huang, S. Nuryyeva, J.-W. Lee, Y. Duan, L.-S. Liao, R. Kaner, Y. Yang, *J. Am. Chem. Soc.* **2019**, *141*, 13948.

[40] F.-S. Zu, P. Amsalem, I. Salzmann, R.-B. Wang, M. Ralaiarisoa, S. Kowarik, S. Duhm, N. Koch, *Advanced Optical Materials* **2017**, *5*, 1700139.

[41] B. Wang, F. Wu, S. Bi, J. Zhou, J. Wang, X. Leng, D. Zhang, R. Meng, B. Xue, C. Zong, L. Zhu, Y. Zhang, H. Zhou, *J. . Mater. Chem. A* **2019**, *7*, 23895.

[42] F. Zhang, K. Zhu, *Advanced Energy Materials* **2020**, *10*, 1902579.

[43] J. D. Magdaline, T. Chithambarathanu, *IOSR-JAC* **2015**, *8*, 9.

[44] X. Wu, L. Zhang, Z. Xu, S. Olthof, X. Ren, Y. Liu, D. Yang, F. Gao, S. (Frank) Liu, *J. Mater. Chem. A* **2020**, *8*, 8313.

[45] R. Wang, J. Xue, L. Meng, J.-W. Lee, Z. Zhao, P. Sun, L. Cai, T. Huang, Z. Wang, Z.-K. Wang, Y. Duan, J. L. Yang, S. Tan, Y. Yuan, Y. Huang, Y. Yang, *Joule* **2019**, *3*, 1464.

[46] D. Wei, F. Ma, R. Wang, S. Dou, P. Cui, H. Huang, J. Ji, E. Jia, X. Jia, S. Sajid, A. M. Elseman, L. Chu, Y. Li, B. Jiang, J. Qiao, Y. Yuan, M. Li, *Adv. Mater.* **2018**, *30*, 1707583.

[47] J. A. McLeod, L. Liu, *J. Phys. Chem. Lett.* **2018**, *9*, 2411.

Chapter 5

Homogeneous Bromide Treatment on Lead-free $Cs_2AgBiBr_6$ Double Perovskites

Defect mitigation by means of stoichiometry tuning and interfacial engineering

This chapter introduces the first stoichiometric tuning attempt of this thesis work for the $Cs_2AgBiBr_6$ double perovskite as well as modification of the perovskite-electron transport layer interface via lithium salt doping of the mesoporous titanium dioxide layer (n-i-p configuration). The interaction between sequentially-added CsBr excess amounts (considered homogeneous as they are also the same as some of the perovskite precursor salts) into the double perovskite and the bulk structure are carefully studied to better understand their impact on the optoelectronic properties of the reference material. Overall, these results pave the pathway for a better understanding of the defect mitigation that is required in this double perovskite to advance its performance.

5.1 Introduction

The $Cs_2AgBiBr_6$ double perovskites represent very promising alternatives to lead-based double perovskites for photovoltaic applications given that toxicity is no longer a concern in addition to their enhanced thermal stabilities, while still leveraging the cost advantages of thin film photovoltaic active layers. Nevertheless, the reported performances of $Cs_2AgBiBr_6$-based photovoltaic devices remain well below the maximum established by the Shockley-Queisser limit, namely, 16.4%.[1,2] Indeed, currently double perovskites still lag behind in terms of photovoltaic efficiencies, which has been reported to be mainly due to a high density of electron traps and short electron diffusion lengths in the material.[3] This could be very well due to several stoichiometric defects in the material representing either shallow or deep trap states which have been reported by Xiao *et al.* as well as Li *et al.* to be tunable by means of bromine-poor or -rich growth conditions based on their computational work on the thermodynamic stability of $Cs_2AgBiBr_6$.[4,5]

Being inspired by the aforementioned work, during the development of this thesis preliminary studies in which all precursor stoichiometries in the $Cs_2AgBiBr_6$ were tuned were carried out, where the CsBr stood out due to noticeable changes to the double perovskite structure and photovoltaic activity. In effect, Sirtl *et al.* interestingly reported several combinations of AgBr and $BiBr_3$ precursor stoichiometric ratios (i.e. several deficit and/or excess ratios) which further corroborated our experimental observations whereby the reference material's crystallinity and photoluminescent properties are clearly affected.[6] Following the encouraging literature and preliminary experimental observations, and in the quest for better understanding the stoichiometric and defect-tuning requirements of double perovskites, an in-depth study was developed to probe and rationalize the effects of a CsBr excess on the stoichiometric $Cs_2AgBiBr_6$ reference material, which is set out in the following pages. Note that CsBr has been chosen as the bromide source to carry out these experiments. This has the advantage of circumventing the introduction of "impurities" or altering the elemental composition, as it would happen using other salts. It is worth noting that the effect of the concomitant "excess" Cs will also be explored.

5.2 Sample preparation and identification

In this work, the solution-based approach to synthesize $Cs_2AgBiBr_6$ double perovskites, as opposed to the vacuum-deposition method, was implemented. The fabrication method is represented on **Scheme 5.1**.

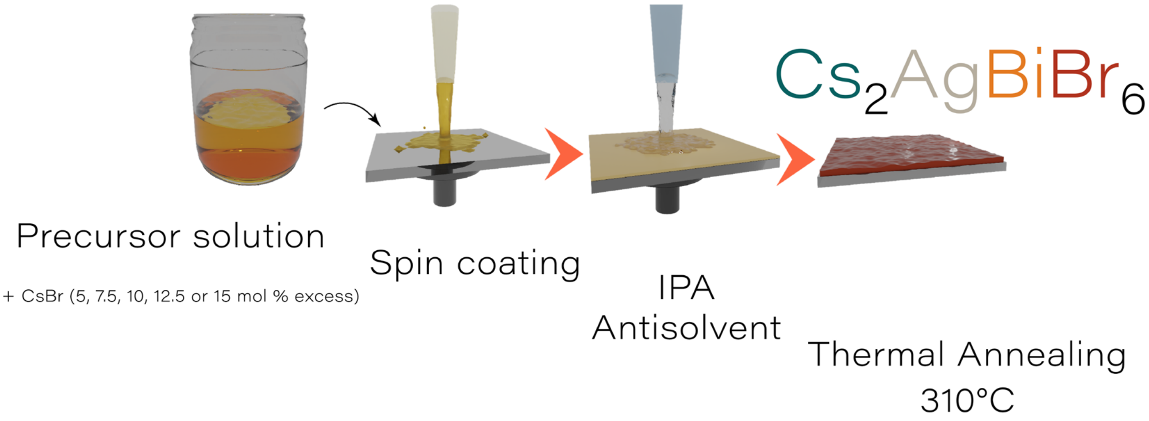

Scheme 5.1. $Cs_2AgBiBr_6$ fabrication steps with the solution-processing method with isopropanol (IPA) antisolvent. In addition to the control sample, samples with 5, 7.5, 10, 12.5 and 15 mol% CsBr excess (with respect to the stoichiometric CsBr content) were prepared by adding the corresponding CsBr excess amount to the precursor solution in DMSO solvent.

Namely, in addition to the reference $Cs_2AgBiBr_6$ material, samples with 5, 7.5, 10, 12.5 and 15 mol% CsBr excess with respect to the original molar amount of CsBr present in a stoichiometric sample, were prepared by adding the corresponding amount of excess CsBr to the perovskite precursor solution in DMSO solvent.

5.3 Results and Discussion

5.3.1 Material's Characterization

Upon initial inspection of the X-ray diffraction (XRD) patterns for the resulting double perovskite thin films, a clearly enhanced crystallographic orientation of the $Cs_2AgBiBr_6$ crystals with the addition of a CsBr excess in the precursor solution becomes apparent along the (00n) crystallographic plane direction. **Figure 5.1a** depicts the XRD patterns of the reference and cesium bromide excess samples studied where a clear enhancement of the (002) and (004) peak intensities with respect to the other diffraction peaks can be observed. In this sense, **Table 5.1** summarizes the (002) and (004) peak intensity ratios with respect to the (442) peak which has been taken as a reference as its intensity remains virtually unchanged for all samples whose thicknesses also do not vary. Interestingly, both (004)/(442) and (002)/(442) peak intensity ratios reach a maximum at a 12.5% CsBr loading with ratios of 18.22 and 4.24, respectively. It is worth mentioning that the 10% CsBr excess sample does nearly approach these values as well, with ratios of 15.51 and 4.00, respectively, which are both quite increased with respect to the corresponding ratios of the $Cs_2AgBiBr_6$ reference film, namely, 3.75 and 1.25, respectively. Moreover, starting from a 15% CsBr additive excess, this orientational preference is diminished, however not lost, with corresponding ratios of 11.01 and 2.75 for the (004)/(442) and (002)/(442) peak intensity ratios, respectively. Similar characterization methods have been employed by Sirtl *et al.*, where they have interestingly also observed enhanced crystallographic orientation with the addition of an AgBr excess while also introducing $BiBr_3$ precursor deficiencies in the material.[6]

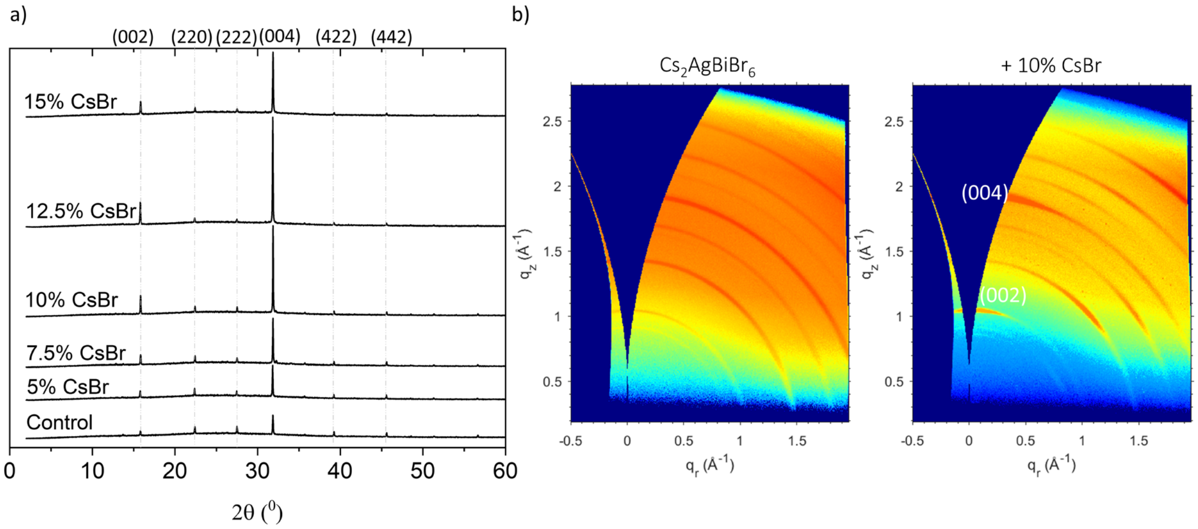

Figure 5.1. (a) X-ray diffraction patterns for the $Cs_2AgBiBr_6$ reference samples and samples with progressive addition of CsBr excess (b) GIWAXS patterns for the $Cs_2AgBiBr_6$ reference and 10% excess CsBr thin films.

In order to further investigate the crystallographic orientation of the double perovskite material with a given CsBr excess, Grazing-Incidence Wide Angle X-ray Scattering (GIWAXS) measurements were carried out. In effect, **Figure 5.1b** (right) further corroborates the preferred orientation of $Cs_2AgBiBr_6$ films already with a 10% CsBr excess by means of the aforementioned 2D X-ray diffraction measurement. Here, one may clearly observe particularly enhanced signal intensity for Bragg spots along the q_r= 0 A^{-1} positions, namely representing out-of-plane preferred alignment of the (002) and (004) crystallographic planes, whereas no preferred orientation can be identified for the $Cs_2AgBiBr_6$ reference sample as clearly distinct Debye-Scherrer rings are instead observed in **Figure 5.1b**(left). This represents still strong crystallinity however with random orientation. Furthermore, given the identical XRD peak positions (*i.e.*. no XRD peak shifts) observed on **Figure 5.1a**, no crystallographic strain may be inferred from the addition of a CsBr excess into the $Cs_2AgBiBr_6$ structure, thereby maintaining consistent characteristic interplanar spacings. Furthermore, identical XRD patterns between the CsBr excess samples and the $Cs_2AgBiBr_6$ reference suggest that no (crystalline) secondary phases resulting from the excess CsBr are present in the perovskite thin film. We note that Raman spectra of the films were also recorded without noticing any significant change between the control and CsBr-loaded samples (results not shown), hence, corroborating the lack of segregated phases. In addition, Sirtl *et al.* also indicated that the diffraction pattern of CsBr could be obscured by the signal of $Cs_2AgBiBr_6$.

Table 5.1. X-ray diffraction peak intensities for the (442) (reference), (004) and (002) peaks and the (004) and (002) peak intensity ratios versus the (442) peak intensity for the $Cs_2AgBiBr_6$ and CsBr excess samples

	Diffraction Peak Intensities			Peak Intensity Ratios	
	(442)	**(004)**	**(002)**	**(004)/(442)**	**(002)/(442)**
$Cs_2AgBiBr_6$	511	1917	639	3.75	1.25
5% CsBr	512	3068	894	5.99	1.75
7.5% CsBr	511	4219	1150	8.26	2.25
10% CsBr	511	7925	2045	15.51	4.00
12.5% CsBr	512	9331	2172	18.22	4.24
15% CsBr	511	5624	1406	11.01	2.75

Aside from leading to the enhanced preferred orientation, the excess CsBr brings about greater crystallographic feature sizes as is evidenced by Scanning Electron Microscopy (SEM) (**Figure 5.2**). It is worth noting that although samples with 12.5% and 15% excess CsBr display crystal domains larger than those with 10% excess CsBr , their crystal size distribution does however increase as well. It is further worth noting that the mechanism whereby the excess CsBr promotes crystallization along the (00n) direction and increases the grain size is yet not clear. Moreover, ions such as SCN$^-$, when mixed within lead perovskite precursors, have been consistently reported to increase the average crystal size and result in preferential orientations.[7] Here, the specific interaction between the ions and particular planes of the perovskite during the crystallization afford this result. It is, therefore, plausible to consider that the excess CsBr promotes an additional stabilization of some planes during the crystallization, promoting, hence, specific orientations.

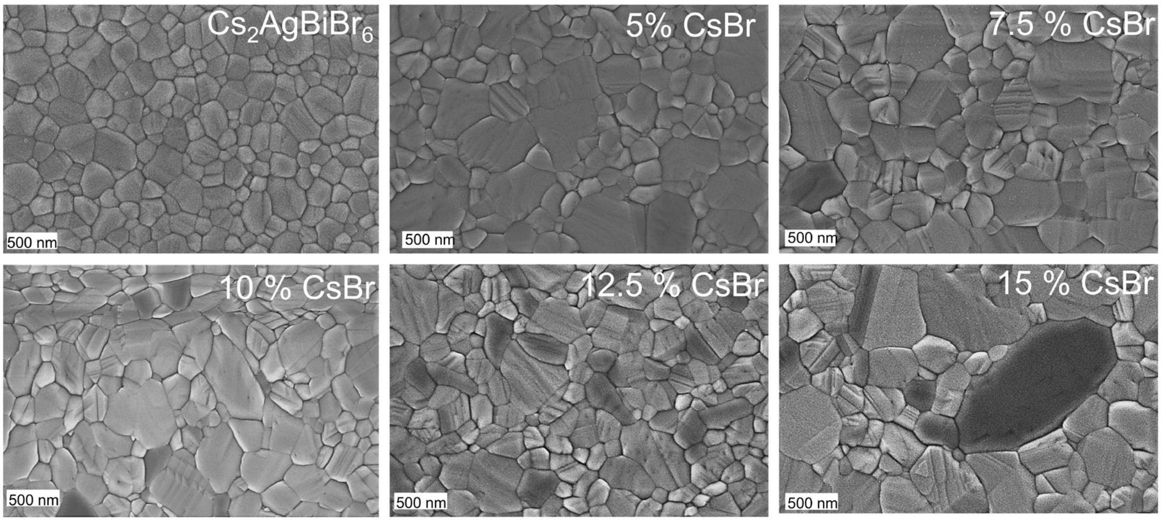

Figure 5.2. Scanning electron microscopy (SEM) images of $Cs_2AgBiBr_6$ thin films and the films with 5, 7.5, 10, 12.5 and 15% CsBr in excess.

5.3.2 Optoelectronic properties

The photoluminescence (PL) spectra of $Cs_2AgBiBr_6$ recorded as a function of different CsBr content is shown in (**Figure 5.3**). As first glance it is observed that the enlarged crystallite sizes correlate with improve emission signal, reaching the maximum intensity for a 10% CsBr excess. In addition, a slight red-shift of the emission peak is detected with the addition of excess CsBr. This shift, which is of approximately 5 nm when comparing the stoichiometric sample to the 10% excess CsBr, could be accounted for by the red-shift noticed in the UV-visible absorption spectra which points at a reduced bandgap (**Figure 5.3a).**

The increased emission signal with respect to the stoichiometric $Cs_2AgBiBr_6$ could be explained by the mitigation of the non-radiative recombination pathway, likely because of the reduced density of charge carrier traps that act as recombination centers. It is worth noting that the intensity of the emission peak reaches a maximum for a 10%-excess CsBr while decaying henceforth for higher loadings. This suggests an increased non-radiative recombination, likely related to the loss of preferential orientation since energy traps could be generated at the interface between domains with different orientation.

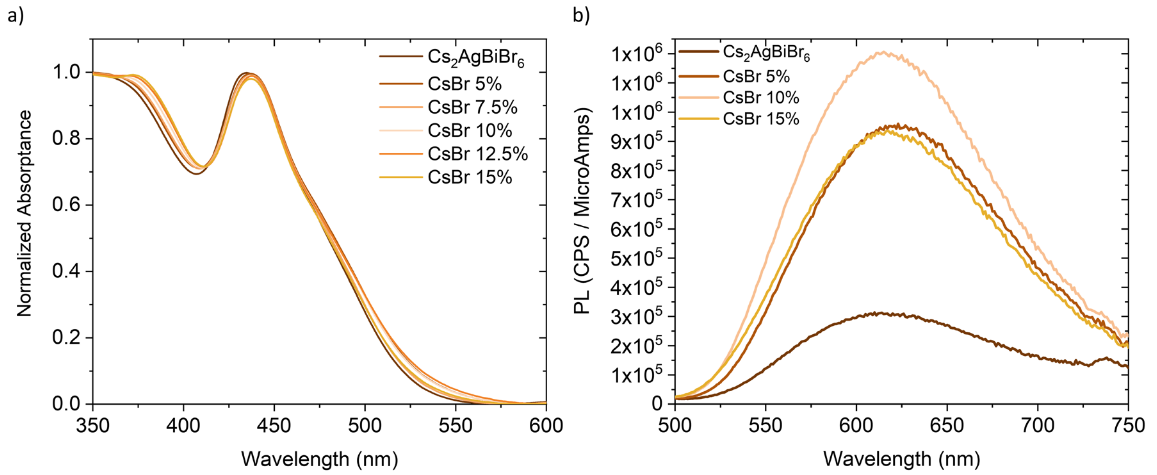

Figure 5.3. (a) Spectral absorptance for the $Cs_2AgBiBr_6$ reference sample and films with 5 to 15% CsBr in excess (b) Corresponding steady-state photoluminescence spectra for the $Cs_2AgBiBr_6$ reference film and samples with 5, 10 and 15% CsBr in excess

In order to further investigate the presence of traps and the hypothesized trap-healing effect of the excess CsBr, space-charge limited current (SCLC) measurements were carried out on electron-only devices to better understand the density of electron traps together with the electron mobility in the $Cs_2AgBiBr_6$ reference sample as well as in the sample with a 5% excess CsBr. **Figure 5.4a** displays the resulting SCLC curves for the electron-only device structures depicted on **Figure 5.4b**.

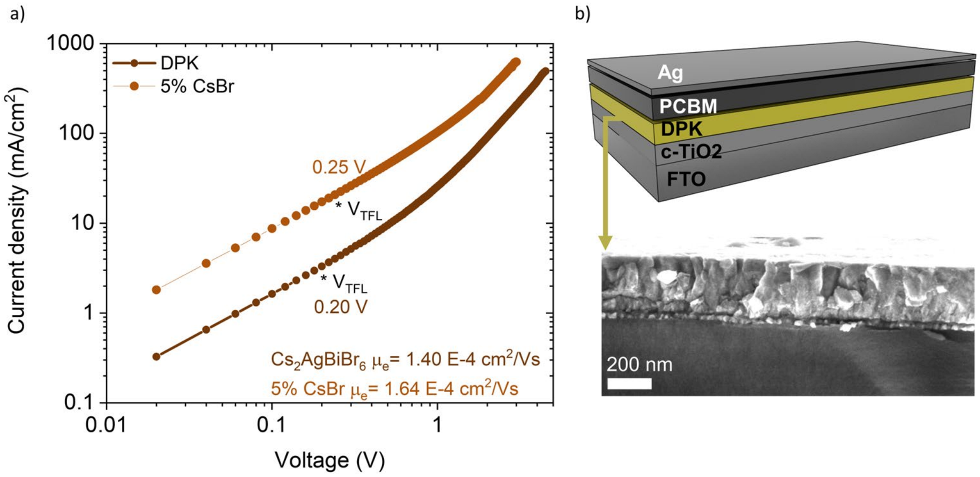

Figure 5.4. (a) Space-charge-limited current (SCLC) curves for electron-only devices with a $Cs_2AgBiBr_6$ reference layer and one with a 5% excess CsBr (b) corresponding SCLC device schematic with a sample cross-sectional SEM image of the 5% excess CsBr device.

The electron-only devices are namely comprised of a fluorine-doped tin oxide (FTO) substrate, a compact TiO_2 ($cTiO_2$) electron transport underlayer, the double perovskite under study, a PCBM electron transport overlayer and a silver electrode. While the trap-filled limit voltages (V_{TFL}) for both the reference and 5% excess CsBr samples are similar, indicating a comparable density of electron traps, the calculated electron mobility in the 5% excess CsBr sample does increase slightly to 1.64 x 10^{-4} cm^2/ Vs compared to 1.40 x 10^{-4} cm^2/ Vs for the $Cs_2AgBiBr_6$ reference sample. We note that while we expect an overall decrease in the density of charge carrier traps, following the results of the PL spectra, one may conclude that the excess CsBr mainly leads to a reduction in hole traps in the material, given the comparable electron trap densities observed on **Figure 5.4a**.

With these observed optoelectronic properties in hand, photovoltaic devices were next fabricated in order to better understand the modified charge-transporting and optoelectronic properties of the CsBr excess double perovskite thin films in comparison to the reference.

5.3.3 Photovoltaic devices

5.3.3.1 Perovskite-electron transport layer interfacial engineering

Before proceeding to the fabrication of photovoltaic devices based on double perovskites with a CsBr excess, some further optimizations were performed on the basic photovoltaic device structure. Namely, an n-i-p structure was implemented, consisting of an electron-transporting underlayer (compact and mesoporous titanium dioxide, TiO_2) to the double perovskite and a hole-transporting overlayer comprised of Spiro-OMeTAD, followed by a thin layer of MoO_3 (1 nm) and gold (100 nm), as depicted on **Figure 5.5a**. Given the initially poor open circuit voltages of the reference device, a previously reported lithium bis-trifluoromethanesulfonimide (LiTFSI) salt treatment on the mesoporous TiO_2 electron transport layer was explored,[8,9] yielding very positive results and greatly improving the open circuit potential (*Voc*) of the reference device, as observed on the current-density-voltage (*J-V*) curve on **Figure 5.5b** and as summarized with the results on **Table 5.2.** Comparative numerical photovoltaic results for LiTFSI treated and untreated $mpTiO_2$ layers under the $Cs_2AgBiBr_6$ active layer in the forward (f) and reverse (r) scans. Moreover, **Figure 5.6** depicts the box plot distribution of the aforementioned devices in further detail, summarizing the different measured power conversion efficiencies (**a**), short-circuit current densities (**b**), open circuit voltages (**c**) and fill factors (**d**). Despite the small loss in fill factor upon LiTFSI-treatment of the mpTiO$_2$ layer, a significant enhancement of the V_{OC} in average leads to improved photovoltaic device performances.

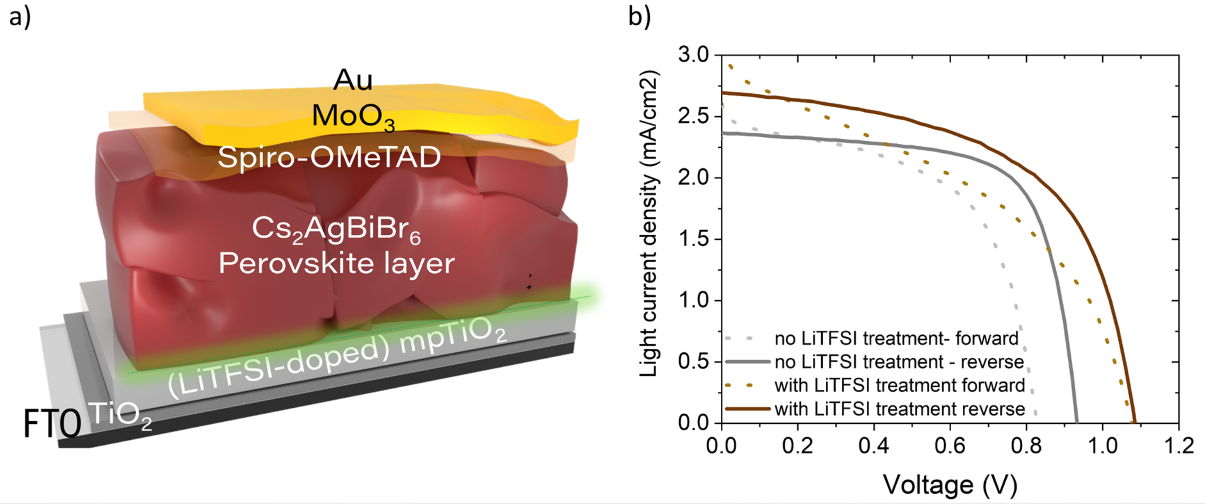

Figure 5.5. (a) Schematic diagram of the implemented n-i-p photovoltaic device structure and (b) resulting photovoltaic forward and reverse scan curves from the best devices with and without LiTFSI-treated mpTiO$_2$ electron transport layer.

Table 5.2. Comparative numerical photovoltaic results for LiTFSI treated and untreated mpTiO$_2$ layers under the Cs$_2$AgBiBr$_6$ active layer in the forward (f) and reverse (r) scans

	J_{SC} [mAcm^{-2}] [a]	V_{OC} [V] [a]	FF [a]	PCE [%][a]	J_{SC} [mAcm^{-2}][b]	V_{OC} [V] [b]	FF [b]	PCE [%] [b]
With LiTFSI (f)	2.83	1.03	0.35	1.02	3.59	1.08	0.34	1.30
With LiTFSI (r)	2.18	1.04	0.58	1.26	2.70	1.09	0.57	1.66
No LiTFSI (f)	3.35	0.90	0.40	1.04	2.60	0.83	0.54	1.16
No LiTFSI (r)	2.10	0.92	0.67	1.16	2.37	0.93	0.69	1.52

[a] Average over at least 10 devices; [b] Champion device

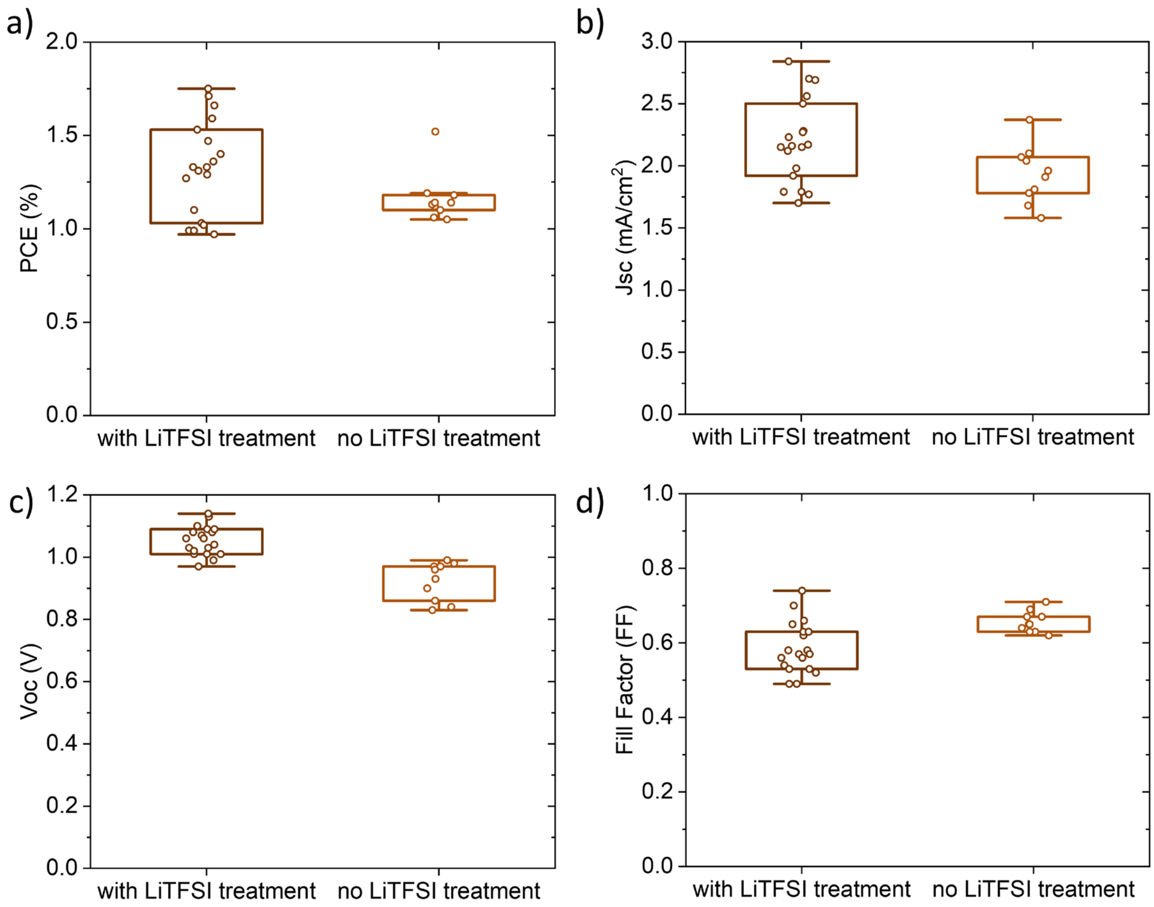

Figure 5.6. Photovoltaic results (reverse scan) for LiTFSI-treated and untreated (a) mpTiO_2 layers under the $Cs_2AgBiBr_6$ active layer (a) Power conversion efficiencies (b) Short-circuit current densities (c) Open circuit voltages and (d) fill factors.

Therefore, for the following devices to be presented, a LiTFSI treatment of the mpTiO_2 is consistently implemented.

5.3.3.2 Photovoltaic results for stoichiometrically-tuned double perovskites (CsBr excess)

Following the n-i-p structure with the LiTFSI-treated mpTiO_2 electron transport layer, photovoltaic devices with several different CsBr excess amounts were fabricated. **Figure 5.7** shows the box plot distributions of each of the four key photovoltaic device parameters, (**a**) power conversion efficiency, (**b**) short-circuit current density, (**c**) open circuit voltage and (**d**) fill factor, for the reference $Cs_2AgBiBr_6$ sample together with the 5%, 10% and 15% CsBr excess devices. In **Figure 5.7a** one may observe a clear trend towards enhanced power conversion efficiencies (PCE) up until a 10% CsBr excess loading, after which device performance decreases. While device fill factors are comparable for the 10 and 15% CsBr devices when set side by side those of the reference (**Figure 5.7d**), the short-circuit photocurrents do appear to be somewhat compromised (**Figure 5.7b)**; this is however offset by the enhancement of the open circuit voltage (**Figure 5.7c).**

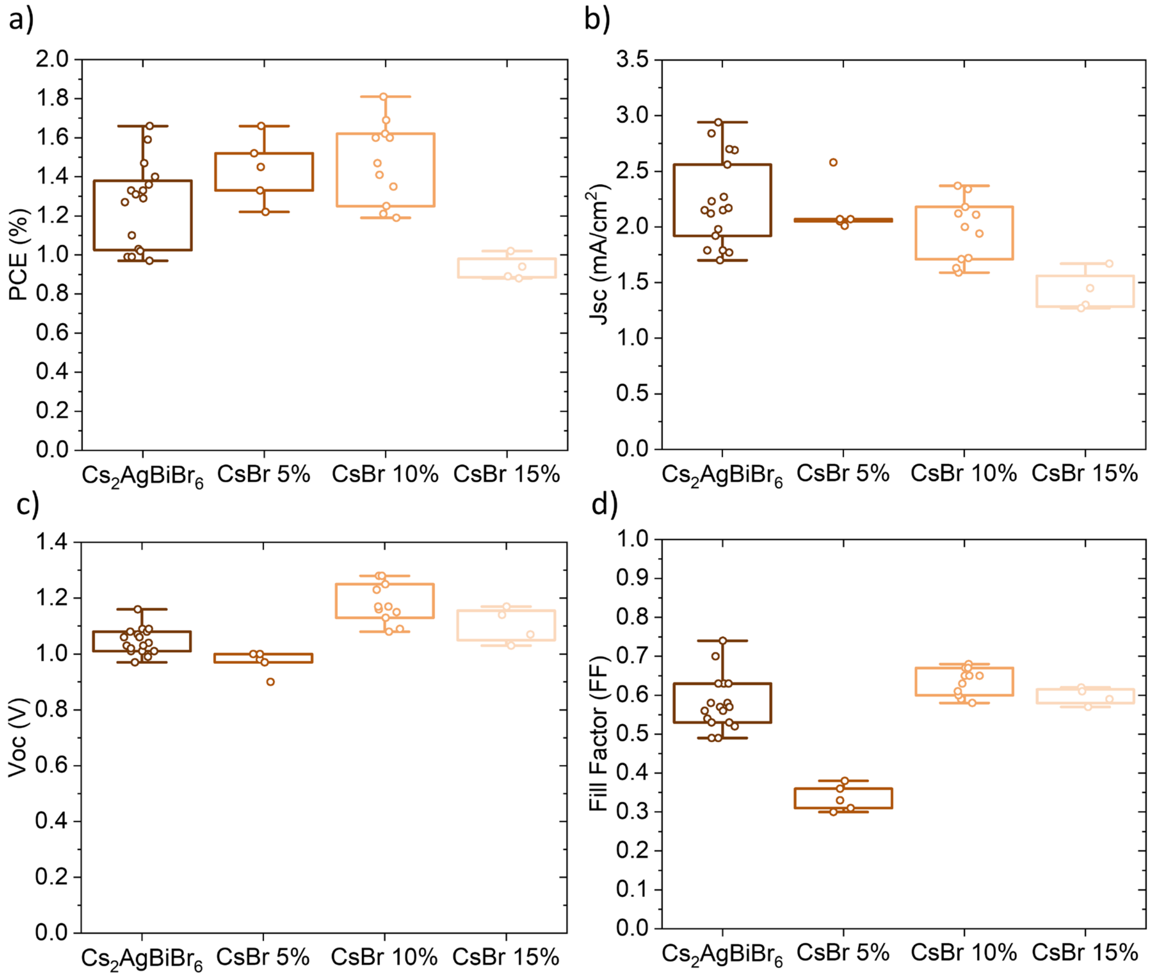

Figure 5.7. Photovoltaic device box plots depicting (a) power conversion efficiencies (b) short-circuit current densities (c) open circuit voltages and (d) fill factors for the $Cs_2AgBiBr_6$ reference and 5, 10 and 15% CsBr excess devices.

Moreover, **Figure 5.8** displays the current-density-voltage (*J-V*) curves for both the best reference device as well as the best-performing CsBr excess-containing photovoltaic device, corresponding to the 10% CsBr excess. Indeed, the double perovskite PV device with a 10% CsBr excess outperforms the reference device. Not surprisingly, thin films of the double perovskite fabricated with a 10% CsBr excess also showed the best photoluminescent peak intensity (as was shown on **Figure 5.3b**) alongside a larger crystal domain size (**Figure 5.2**).

The enhanced crystal domain sizes , which likely result in a lower density of recombination sites at the grain boundaries, could account for the enhanced *Voc* of the device. The photovoltaic device results for the average and best devices are summarized on **Table 5.3**.

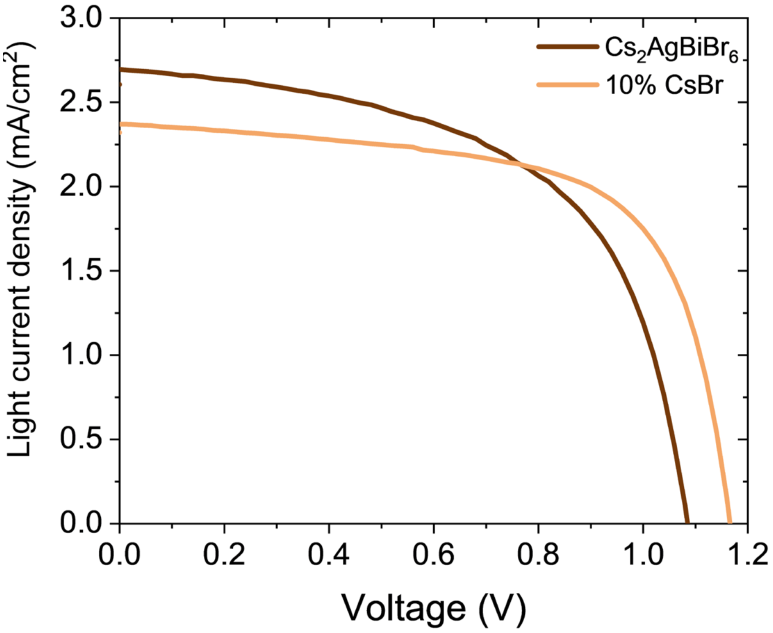

Figure 5.8. Photovoltaic J-V curves for the best performing $Cs_2AgBiBr_6$ reference device and the 10% CsBr device.

Table 5.3. Comparative numerical photovoltaic results (reverse scans) for the reference $Cs_2AgBiBr_6$-based devices and those with 5, 10 and 15% CsBr excess

	J_{SC} [mAcm^{-2}] [a]	V_{OC} [V] [a]	*FF* [a]	PCE [%][a]	J_{SC} [mAcm^{-2}][b]	V_{OC} [V] [b]	*FF* [b]	PCE [%] [b]
$Cs_2AgBiBr_6$	2.18	1.04	0.58	1.26	2.70	1.09	0.57	1.66
5% CsBr	2.16	0.97	0.69	1.44	2.58	1.00	0.65	1.66
10% CsBr	1.97	1.18	0.63	1.47	2.37	1.17	0.65	1.81
15% CsBr	1.42	1.10	0.60	0.93	1.67	1.07	0.57	1.02

[a] Average over at least 5 devices; [b] Champion device

Following observations on the significantly enhanced V_{OC} of the photovoltaic devices involving excess amounts of CsBr in the $Cs_2AgBiBr_6$ layer, the effect of the CsBr excess was further investigated with additional spectroscopy techniques to better understand the working mechanism of the additive's activity as well as to better identify more preferable future treatments of the double perovskite for yet further enhanced optoelectronic properties, as follows.

5.3.4 Further spectroscopic analysis

Ultraviolet-photoelectron spectroscopy (UPS) was next employed to determine the valence band for the reference and the CsBr-excess samples. **Figure 5.9a** depicts the fitting of the secondary electron cut-off whereas the **Figure 5.9b** portrays the fitting of the valence band maximum.

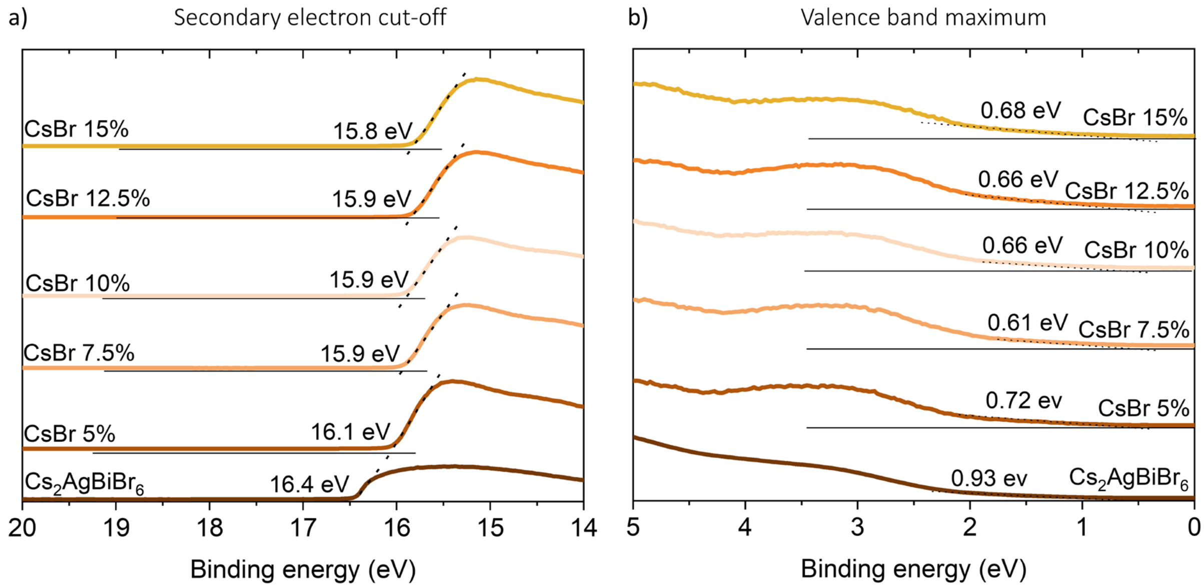

Figure 5.9. (a) Secondary electron cut-off fittings and (b) valence band maximum fittings for the $Cs_2AgBiBr_6$ double perovskite film as well as the double perovskite with several different CsBr excess amounts

In order to determine the distinct energy levels for the samples under study, a Tauc plot analysis was further carried out based on the spectra obtained from UV-visible spectroscopy in order to determine the bandgap, following the indirect bandgap formula (as described in more detail in **Chapter 2**) (**Figure 5.10a**). With the band gaps in hand, the ionization energy calculations were implemented, together with the linear fits of the valence band maxima and secondary electron cut-off, following the procedure described in **Chapter 2**,[10,11] resulting in the energy levels depicted on **Figure 5.10b**. Note that the FTO, TiO_2, Spiro, MoO_3 and Au energy levels are obtained from literature references.[12,13]

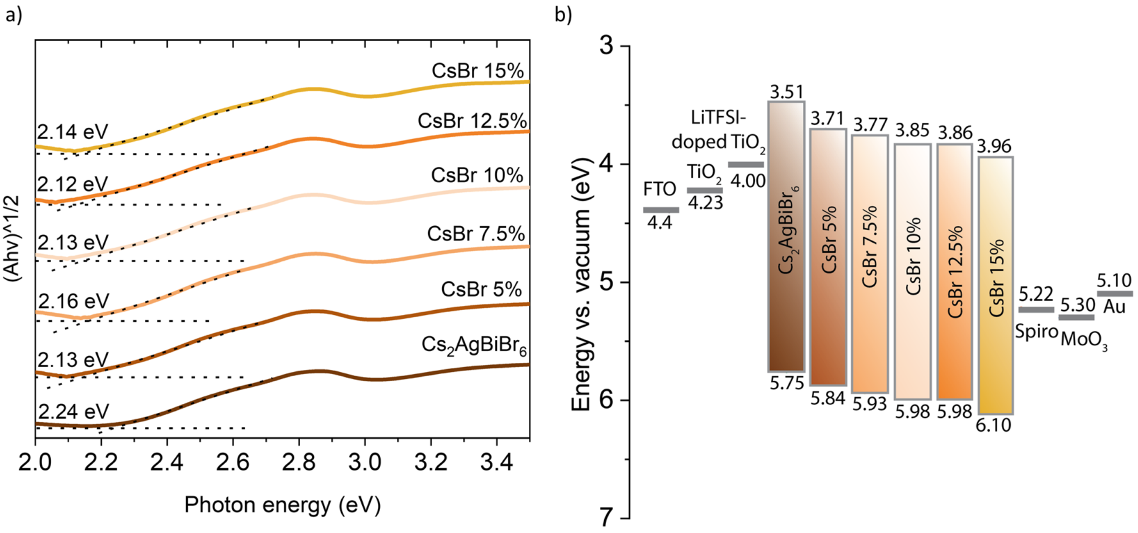

Figure 5.10. (a) Indirect bandgap Tauc plot analysis for the $Cs_2AgBiBr_6$ reference sample in addition to different CsBr excess loadings and (b) resulting calculated energy levels

From the calculated energy levels one may observe in general both deeper conduction band minima and valence band maxima values for the $Cs_2AgBiBr_6$ double perovskite when an excess CsBr is added into the precursor solution. Overall, the deeper the conduction band minima, the lower the voltage losses at that interface provided that sufficient driving force for electron transfer exists. As a consequence, high *Voc* values are observed with a CsBr excess. However, the driving force for electron transfer could also be decreased, which could explain the loss in *Jsc* with increased CsBr excess loading. Likewise, in the case of the interface with the Spiro-OMeTAD a large energy gap could adversely affect hole transfer and as a consequence the performance, causing severe voltage losses and even hampering the hole extraction. Therefore, a more appropriate energy level alignment together with the enhanced morphology and charge carrier recombination mitigation may be the contributing factors allowing the 10% excess CsBr to represent the optimal excess condition.

In order to further understand the chemical interaction between the excess CsBr and the reference $Cs_2AgBiBr_6$ perovskite film, solid state nuclear magnetic resonance (ssNMR) spectroscopy measurements to track the ^{133}Cs chemical shift were carried out, whereby thin films of the perovskite samples were scratched and the powder loaded into an NMR rotor (see **Chapter 2** for details). In addition to the $Cs_2AgBiBr_6$ reference sample, samples with 10% CsBr excess and a much larger 17.5% CsBr excess were measured. As a control, in order to further verify the possible presence of CsBr aggregates, the ^{133}Cs chemical shift signal for the CsBr powder was also recorded. The collected ssNMR spectra are presented on **Figure 5.11**, where new ^{133}Cs environments different from those of CsBr (261 ppm) and the $Cs_2AgBiBr_6$ (83 ppm) sample appear for the 10% CsBr sample (230 ppm) and the large CsBr excess (17.5%) sample (229 ppm), in addition to the characteristic 83 ppm ^{133}Cs chemical shift of the double perovskite.

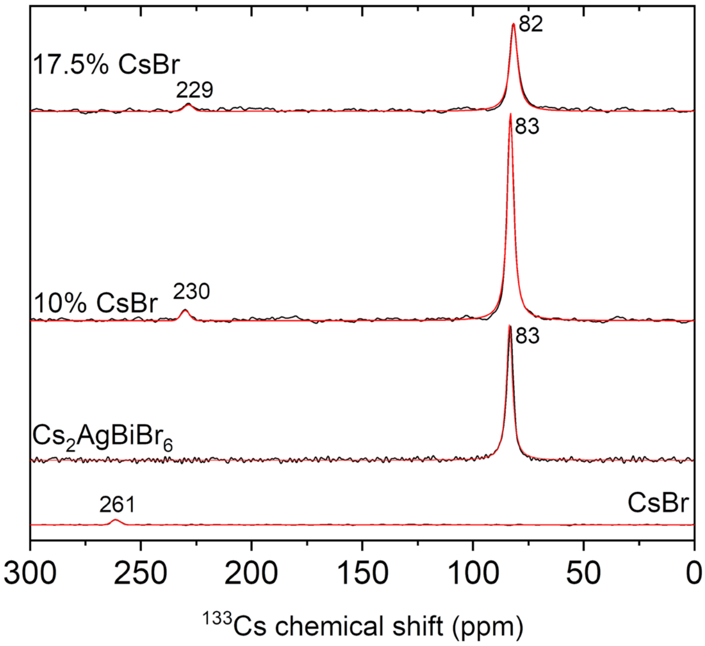

Figure 5.11. ^{133}Cs solid state NMR spectra for CsBr, $Cs_2AgBiBr_6$ and double perovskite samples with a 10% and 17.5% CsBr excess.

Indeed, the appearance of new ^{133}Cs chemical environments different from both the ^{133}Cs chemical environment in the reference double perovskite and the ^{133}Cs chemical environment in the pure CsBr salt indicates a distinct interaction between some of the Cs in the structure and its distinct surrounding chemical environment in the CsBr excess double perovskite samples. We hypothesize that this new ^{133}Cs signal could be related to the defect-healing nature of the CsBr excess. Indeed, we propose that this distinct signal corresponds to the excess Cs positioned at the surface of the crystal resulting in "cesium-terminated surfaces."[14] Simultaneously, Br^- ions will heal the defects associated to vacancies on the surface, which are common defects on this material.[5] A schematic portraying this healing mechanism is depicted in **Figure 5.12**.

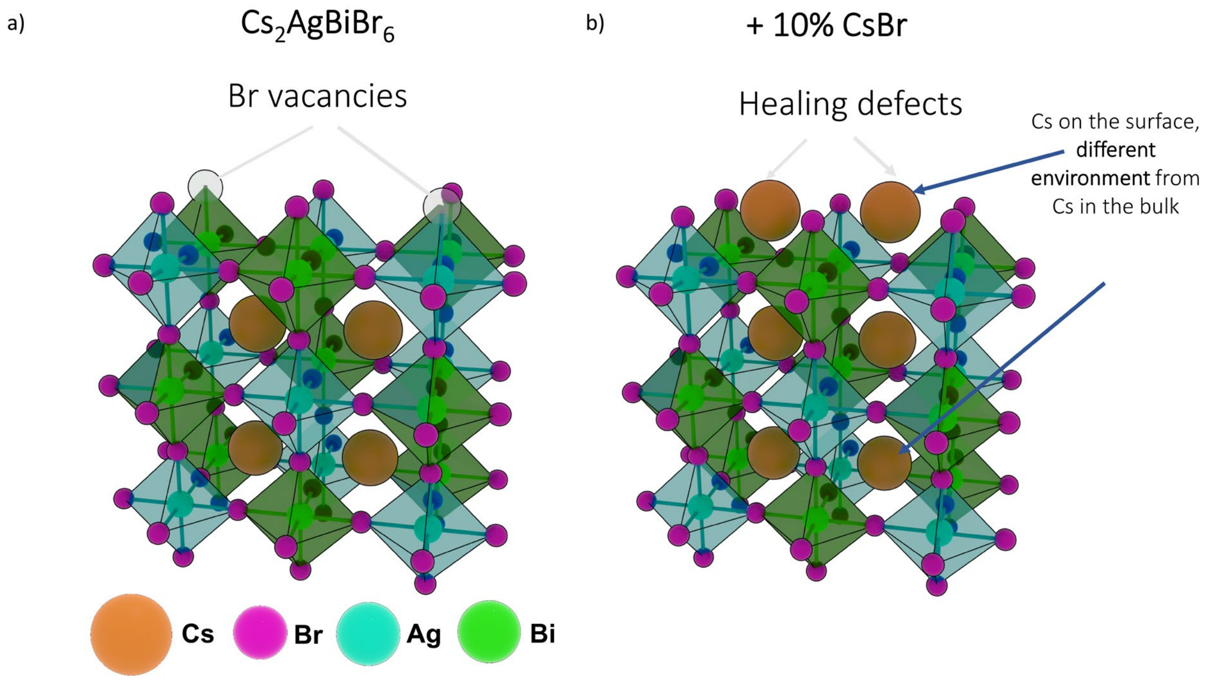

Figure 5.12. (a) Proposed schematic of the suggested Br vacancy defects on the $Cs_2AgBiBr_6$ reference material based on experimental observations and (b) the CsBr terminated surface on the 10% CsBr excess sample providing a healing treatment for these defects.

Table 5.4 summarizes both the spin-lattice relaxation times (obtained by saturation recovery experiments) and the peak full width at half maxima (FWMH) for the characteristic *bulk* double perovskite ^{133}Cs chemical shift of each of the perovskite samples measured, where a clear increase of the spin-lattice relaxation time is observed upon excess CsBr presence in the double perovskite, reaching a maximum for the 10% excess CsBr sample, whereas a clear broadening of the characteristic ^{133}Cs chemical shift signal in the double perovskite, as observed by means of the full width at half maxima, continues to be observed up until even larger CsBr excess loadings. The greater spin-lattice relaxation times for the bulk ^{133}Cs chemical shift 10% excess CsBr double perovskite sample could indeed imply the stronger Cs excess activity in promoting a bromine-richer chemical environment that can indeed be sensed by the Cs in the perovskite bulk (which could serve as an evidence for the healing of bromide vacancies in the double perovskite structure). In fact, Lim *et al.* have reported longer ^{133}Cs relaxation times for Cs atoms surrounded by 11 bromide ions versus shorter relaxation times for Cs atoms surrounded by less bromides (for Cs_2BBr_4 (B=^{57}Co, ^{63}Cu, and ^{65}Zn) structures).[15] The maximum ^{133}Cs relaxation times for the 10% CsBr sample could therefore represent a maximum healing capacity. Therefore, when far too much CsBr is added into the structure, as is the case for the 17.5% CsBr excess sample, disorder is now introduced intro the structure by means of the additional excess CsBr which is probably no longer included within the structure for purposes of bromide vacancy healing. The latter would nevertheless still lead to bulk ^{133}Cs chemical shift peak broadening, given the continuously wider range of chemical states around the Cs brought about by the additional disorder and large Cs, which is less so the case for the 10% CsBr excess sample.

Table 5.4. ^{133}Cs solid state NMR results for the reference $Cs_2AgBiBr_6$-based devices and those with 10 and 17.5% CsBr excess

	^{133}Cs peak position (ppm)	**Spin-Lattice Relaxation Time T_1 (s)**	**Peak FWHM (ppm)**
$Cs_2AgBiBr_6$	83	190	3.2
10% CsBr	83	272	3.5
17.5% CsBr	82	233	4.2

Furthermore, angle-dependent X-ray photoelectron spectroscopy (XPS) was carried out to evaluate the atomic concentration of the components of the reference $Cs_2AgBiBr_6$ as well as the sample with 10% excess CsBr as a function of the depth in the thin film (**Figure 5.13a** and **b**, respectively). The aim was to observe the distribution of the key elements on the first 10 nm of the film; namely, a 70° sample tilt angle corresponds to the surface whereas a 0° tilt angle corresponds to the first 10 nm of the sample. It is worth noting that bromide outgassing is a common bottleneck in XPS measurements, which can explain the Br atomic concentrations lower than 60% for the $Cs_2AgBiBr_6$ reference samples which also carries on to the 10% CsBr excess sample (and which therefore leads to overestimated Cs atomic concentration values as a result).[16–18] Analyzing this data form a qualitative standpoint, it is worth noting that a greater Cs content is indeed observed towards the bulk (at a 0° sample tilt angle) for the 10% excess CsBr sample (**Figure 5.13b**), which also translates to a slight Cs excess at the surface, compared to the reference (**Figure 5.13a**).

The detailed Cs atomic concentration values for the reference and 10% CsBr excess samples are listed on **Table 5.5**, together with the corresponding ratio between them as a function of the depth or tilt angle. One may observe that the 10% excess CsBr sample does maintain a nearly 10% (within experimental error) Cs excess throughout the first 10 nm of the sample. We note that the % increase in Cs excess near the surface of the 10% excess CsBr sample does appear less due to the likely greater overestimation of Cs atomic concentration near the surface of the reference sample as a consequence of the likely greater bromine outgassing under high vacuum. Moreover, despite the significant bromide outgassing in both samples, the 10% excess CsBr does maintain a higher bromide content towards the surface in comparison to the reference. The slightly greater presence of both Cs and Br at the surface could therefore support the conclusions from the ss NMR analysis, whereby the additional excess CsBr allows for the filling of bromide vacancies, healing thus, some of the surface defects on the crystal structure.

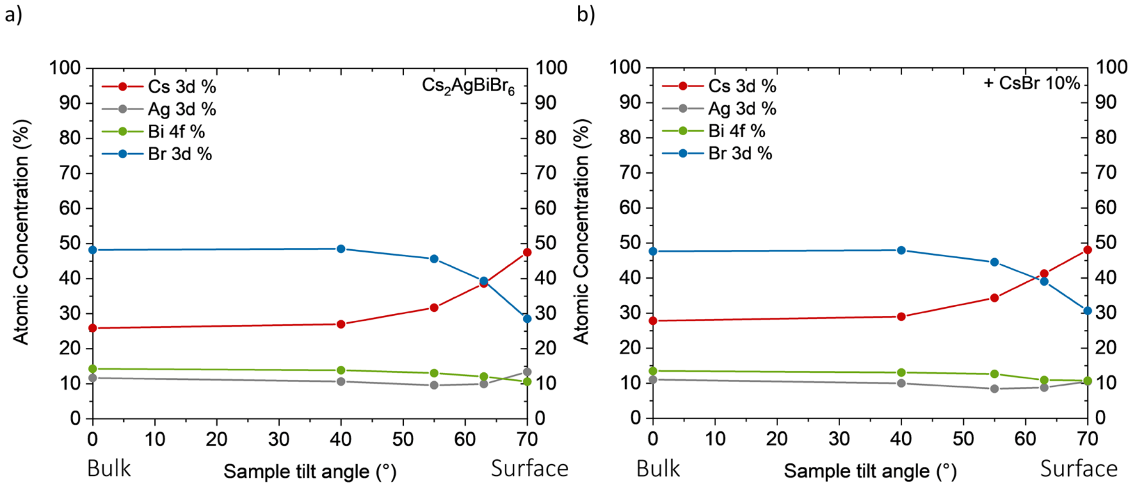

Figure 5.13. Angle-dependent X-ray photoelectron spectroscopy (XPS) of (a) $Cs_2AgBiBr_6$ and (b) the double perovskite with 10% CsBr in excess tracking the Cs, Ag, Bi and Br content from the surface to about the first 10 nm of the films.

Table 5.5. Angle-dependent XPS Cs atomic concentration results for the $Cs_2AgBiBr_6$ reference sample and the double perovskite sample with 10% CsBr in excess, distributed along the approximately first 10 nm of the sample

	Cs Atomic Concentration		
	$Cs_2AgBiBr_6$ (DPK) (%)	**10% CsBr (DPK10) (%)**	**DPK10/DPK percent increase (%)**
0 (first 10 nm)	25.88	27.81	7.44
40	26.99	29.00	7.43
55	31.72	34.36	8.30
63	38.64	41.28	6.83
70 (surface)	47.47	48.05	1.22

5.4 Conclusions

The above-presented data demonstrate a clear effect of the excess CsBr presence in double perovskites, first of all in terms of the crystallinity, where preferred orientation of the crystallites along the (00n) plane direction is evidenced by means of XRD and GIWAXS measurements. Furthermore, this preferred orientation is hypothesized to promote crystal growth, leading to larger crystal domain sizes as observed with scanning electron microscopy, which contribute to an enhancement of the photoluminescence signal of the bare perovskite films without the presence of charge collecting layers. In effect, a maximum PL signal was observed for the 10% excess CsBr sample, after which CsBr excess loading appears far greater than that required by the system.

SsNMR spectroscopy targeting the ^{133}Cs chemical shift signal reveals the appearance of new ^{133}Cs chemical environments in the CsBr excess samples, distinct from those of the pure CsBr salt and the pure reference $Cs_2AgBiBr_6$ material. Together with the positive steady-state PL results, it is hypothesized that the new Cs environment could indeed be attributed to a Cs-rich surface, that could accompany the passivation of the Br^- vacancies with the incoming Br^- from the excess CsBr. Moreover, angle-dependent X-ray photoelectron spectroscopy was implemented to confirm the Cs excess presence throughout the first 10 nm of the perovskite films for the samples with an excess CsBr, which, despite the expected halide outgassing were qualitatively compared to the spectra of the reference sample.

Photovoltaic devices with the n-i-p structure were constructed, where first a LiTFSI salt treatment of the mpTiO_2 layer allowed for better-performing reference devices. Photovoltaic results show an enhancement of PCEs, where on average much larger V_{OC} values are obtained when the double perovskite active layer contains some excess CsBr in the precursor solution, the optimum value for the photovoltaic devices was also found at 10% CsBr excess loading, which corroborates with observations made from the steady-state photoluminescence measurements. From Tauc plot analysis it was observed that a CsBr excess in the double perovskite led to a slight decrease of the band gap as well as a deepening of the valence band maxima and conduction band minima. The former appears to be detrimental to photovoltaic device performance, especially after a 12.5% excess CsBr loading, given the large energy gap for the hole extraction that could cause important voltage losses, whereas the small driving force for the electron injection into the TiO_2 could reduce the charge transfer efficiency. Although the best photovoltaic device (1.81% PCE), obtained for the 10% excess CsBr loading, outperforms the best-performing reference device (1.66% PCE), on average some photocurrent losses are observed for the 10% CsBr excess devices at the expense of greater open circuit potentials, which present room for further improvement. Indeed, the rather large size of the Cs ion complicates its insertion within the structure being limited to the outer layer. We believe that using smaller cations in combination with the bromide could offer alternative benefits, leveraging the passivation effect of the bromide with other doping or healing phenomena caused by smaller cations. Overall, this work paves way for the exploration of further forms of bromine vacancy healing in double perovskites in the quest to reduce the inherent losses and boost PCEs to values closer to the theoretical limit.

5.5 References

[1] S. Rühle, *physica status solidi (a)* **2017**, *214*, 1600955.

[2] E. Greul, M. L. Petrus, A. Binek, P. Docampo, T. Bein, *J. Mater. Chem. A* **2017**, *5*, 19972.

[3] G. Longo, S. Mahesh, L. R. V. Buizza, A. D. Wright, A. J. Ramadan, M. Abdi-Jalebi, P. K. Nayak, L. M. Herz, H. J. Snaith, *ACS Energy Lett.* **2020**, *5*, 2200.

[4] Z. Xiao, W. Meng, J. Wang, Y. Yan, *ChemSusChem* **2016**, *9*, 2628.

[5] T. Li, X. Zhao, D. Yang, M.-H. Du, L. Zhang, *Phys. Rev. Applied* **2018**, *10*, 041001.

[6] M. T. Sirtl, M. Armer, L. K. Reb, R. Hooijer, P. Dörflinger, M. A. Scheel, K. Tvingstedt, P. Rieder, N. Glück, P. Pandit, S. V. Roth, P. Müller-Buschbaum, V. Dyakonov, T. Bein, *ACS Appl. Energy Mater.* **2020**, *3*, 11597.

[7] X. Zhang, G. Wu, W. Fu, M. Qin, W. Yang, J. Yan, Z. Zhang, X. Lu, H. Chen, *Advanced Energy Materials* **2018**, *8*, 1702498.

[8] F. Giordano, A. Abate, J. P. Correa Baena, M. Saliba, T. Matsui, S. H. Im, S. M. Zakeeruddin, M. K. Nazeeruddin, A. Hagfeldt, M. Graetzel, *Nat. Commun.* **2016**, *7*, 10379.

[9] M. Kim, I. Choi, S. J. Choi, J. W. Song, S.-I. Mo, J.-H. An, Y. Jo, S. Ahn, S. K. Ahn, G.-H. Kim, D. S. Kim, *Joule* **2021**, *5*, 659.

[10] B. Philippe, T. J. Jacobsson, J.-P. Correa-Baena, N. K. Jena, A. Banerjee, S. Chakraborty, U. B. Cappel, R. Ahuja, A. Hagfeldt, M. Odelius, H. Rensmo, *J. Phys. Chem. C* **2017**, *121*, 26655.

[11] A. Agresti, A. Pazniak, S. Pescetelli, A. Di Vito, D. Rossi, A. Pecchia, M. Auf der Maur, A. Liedl, R. Larciprete, D. V. Kuznetsov, D. Saranin, A. Di Carlo, *Nat. Mater.* **2019**, *18*, 1228.

[12] Z. Zhou, J. Xu, L. Xiao, J. Chen, Z. Tan, J. Yao, S. Dai, *RSC Adv.* **2016**, *6*, 78585.

[13] J.-H. Li, Y. Li, J.-T. Xu, C. K. Luscombe, *ACS Appl. Mater. Interfaces* **2017**, *9*, 17942.

[14] B.-H. Wang, B. Gao, J.-R. Zhang, L. Chen, G. Junkang, S. Shen, C.-T. Au, K. Li, M.-Q. Cai, S.-F. Yin, *Phys. Chem. Chem. Phys.* **2021**, *23*, 12439.

[15] A. R. Lim, S. H. Kim, *Solid State Sci.* **2017**, *67*, 93.

[16] S. Tan, T. Huang, I. Yavuz, R. Wang, M. H. Weber, Y. Zhao, M. Abdelsamie, M. E. Liao, H.-C. Wang, K. Huynh, K.-H. Wei, J. Xue, F. Babbe, M. S. Goorsky, J.-W. Lee, C. M. Sutter-Fella, Y. Yang, *J. Am. Chem. Soc.* **2021**, *143*, 6781.

[17] Y. Jiang, S.-C. Yang, Q. Jeangros, S. Pisoni, T. Moser, S. Buecheler, A. N. Tiwari, F. Fu, *Joule* **2020**, *4*, 1087.

[18] C. Das, M. Wussler, T. Hellmann, T. Mayer, W. Jaegermann, *Phys. Chem. Chem. Phys.* **2018**, *20*, 17180.

Chapter 6

Heterogeneous Bromide Treatments on Lead-free $Cs_2AgBiBr_6$ Double Perovskites

Bromide defect mitigation with foreign species

This chapter summarizes work on alternative treatments for bromide introduction into $Cs_2AgBiBr_6$ double perovskites with heterogeneous species, meaning those not native to the perovskite's structure as was the case on Chapter 5 with cesium bromide. In this chapter, interesting findings are revealed with respect to the bromide introduction into the double perovskite by means of lithium bromide salt addition into the perovskite via several incorporation methods which are each also optimized. The activity of both the lithium and bromide additives is verified by means of separate lithium and bromine incorporation experiments with volatile carrying counterions. Photovoltaic devices are fabricated and the results are presented which evidence the enhanced optoelectronic activity of the LiBr-treated double perovskites.

6.1 Introduction

Findings from **Chapter 5** have revealed that the addition of CsBr into the double perovskite precursor solution led to several advantages pertaining to the optoelectronic activity of the material, likely by bromide vacancy defect passivation via the localization of CsBr towards the crystallite surface for effective healing. Nevertheless, the resulting photovoltaic device photocurrents appeared compromised at the expense of higher device open circuit voltages which present the motivation for the following work: the exploration of alternative routes of bromide replenishment into the double perovskite. It is hypothesized that the cesium presence as a bromide counterionic carrier increases intrinsic resistance in the perovskite active layer, given the large atomic size of the cesium atoms without any particular role. Therefore, this observation, along with the positive results of the CsBr activity in the double perovskite material, motivated the search for alternative bromide carrying salts, this time with smaller cations.

Previous works have reported the substitution of some of the CsBr in the double perovskite precursor with alkali metal salts, such as rubidium bromide (RbBr), potassium bromide (KBr) and sodium bromide (NaBr) up until a 2 mol % substitution,[1] or even further for Rb substitution of Cs up until 10 mol%,[2] where enhanced optoelectronic properties were mainly observed for Rb substitution of the A-site Cs cation in the double perovskite. Namely, Rb substitution was responsible for enhanced X-ray sensitivity in the 2 mol% substitution experiments, whereas the 10 mol% experiments led to a moderate increase in photovoltaic device performance, as reported. Furthermore, Li *et al.* have reported partial Li substitution (1 mol%) of the A-site Cs cation in $Cs_2AgBiBr_6$ where an enhanced photovoltaic performance could be observed for a hole transport material-free photovoltaic device, from 1.77% to 2.57%.[3]

However, reports on the addition of a bromine excess into the double perovskite via the introduction of bromine-containing additives are rare to this date. Thus far such reports include for instance the addition of methyl ammonium bromide (MABr) into the double perovskite precursor solution, which has been reported to increase the photovoltaic efficiency of the resulting double perovskite-based device from 1.43% to 2.53% by promoting an intermediate $Cs_{2-x}MA_xAgBiBr_6$ species formation during the double perovskite fabrication process, leading to enhanced film qualities and a lowering of the charge carrier trap densities.[4] Identifying the need to explore the replenishment of bromine in the double perovskite based on the previous observations on Chapter 5 and the above-mentioned literature reports, justifies the idea of studying the effects of alkali metal bromide additives (as opposed to substituents) into the double perovskite. As a result, in the following work, LiBr additives are introduced into the double perovskite via a solution-based approach, where the aim is to also harness the small cationic size of lithium by equally introducing a bromide excess or replenishment into the double perovskite. The LiBr additives are referred to as heterogeneous additives as they are not native to the double perovskite structure as was the case with CsBr on the previous chapter.

6.2 Sample preparation and identification

In order to introduce different amounts of LiBr into the $Cs_2AgBiBr_6$ double perovskite precursor solution two different methods were employed, namely: **Method 1)** the direct addition of the salt into the perovskite precursor solution in dimethysulfoxide solvent (DMSO) in molar percentages ranging from 1 to 6% with respect to the CsBr amount (**Scheme 6.1**), followed by spin-coating and isopropanol (IPA) antisolvent dripping and thermal annealing at 310°C, and, **Method 2)** LiBr diffusion into the perovskite thin film after thermal annealing by immersion into an LiBr solution in isopropanol, followed by an additional thermal annealing post-treatment.

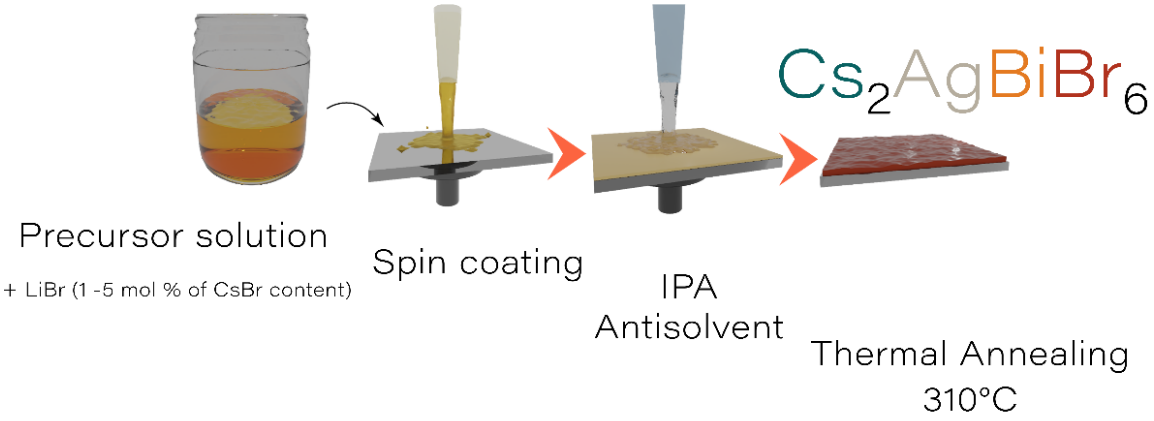

Scheme 6.1. Preparation method for introducing the LiBr additive into the perovskite precursor solution, following the solution-based approach

Namely, for the LiBr diffusion method, the perovskite thin films are prepared as described on **Scheme 6.1** (without the addition of the LiBr salt into the precursor solution), after which they are submitted to the processing described on **Scheme 6.2**. Details on the perovskite film preparation and deposition are presented on the Experimental **Chapter 2**.

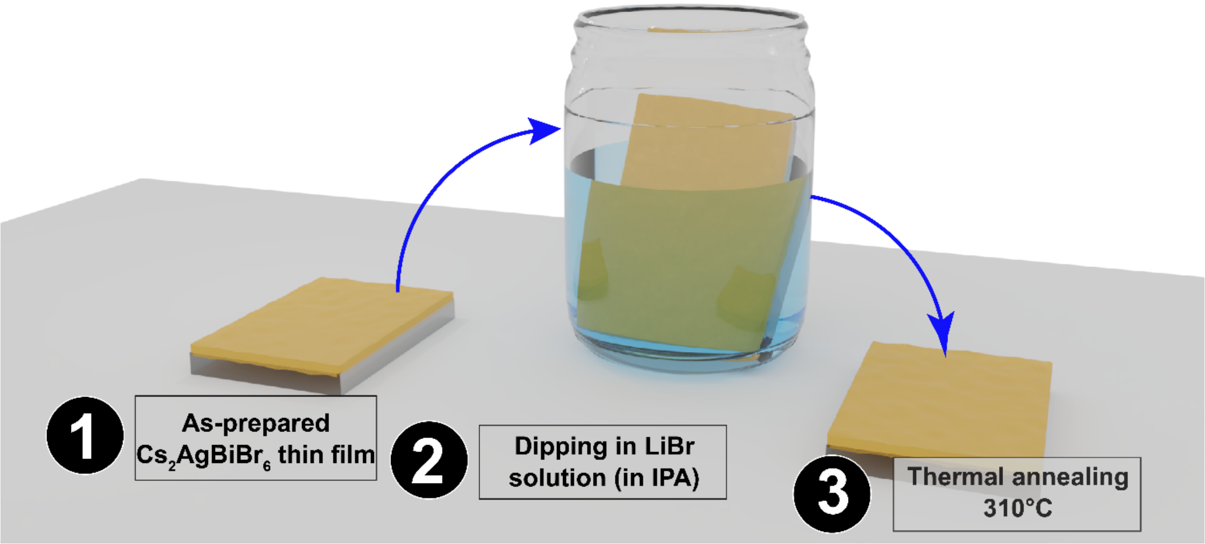
1
As-prepared $Cs_2AgBiBr_6$ thin film
2
Dipping in LiBr solution (in IPA)
3
Thermal annealing 310°C

Scheme 6.2. LiBr diffusion and thermal annealing post-treatment on the $Cs_2AgBiBr_6$ thin film

6.3 Results and Discussion

6.3.1 Material's Characterization

The double perovskite materials with LiBr introduced both via additive addition (Method 1) and LiBr diffusion (Method 2) were characterized by means of X-ray diffraction (**Figure 6.1a**), where one may observe the presence of identical XRD peaks, meaning the conservation of the $Cs_2AgBiBr_6$ perovskite phase without apparent crystalline impurities. However, as observed on **Figure 6.1b**, some lattice distortion is introduced, more specifically, lattice shrinking can be observed through the shifting of all diffraction peaks towards higher 2θ degrees, this is exemplified for the most prominent (004) X-ray diffraction signal.

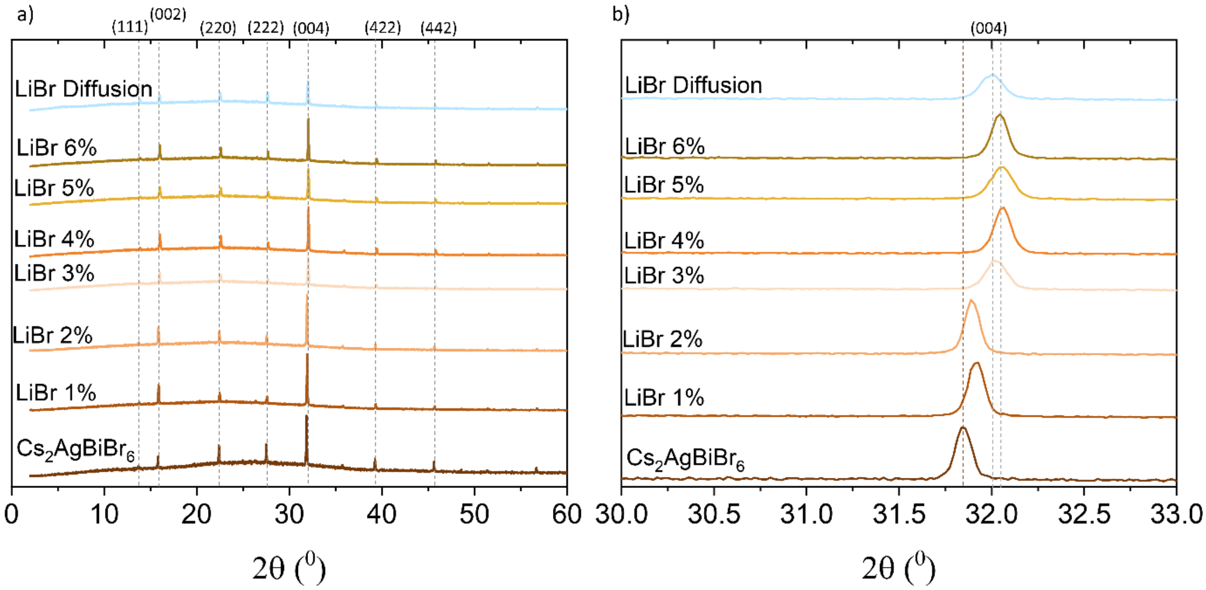

Figure 6.1. (a) X-ray diffraction patterns of the $Cs_2AgBiBr_6$ reference sample, as well as with 1 to 6% LiBr addition, and a diffraction pattern for a $Cs_2AgBiBr_6$ sample with a LiBr diffusion post-treatment (b) close-up image of the (004) XRD peaks for the aforementioned samples

In order to discern the possibility of a partial double perovskite formation in which the Li ions have replaced some of the Cs A-site cations, the Goldschmidt tolerance factor was calculated.[5] In effect, the Goldschmidt tolerance factor model determines the feasibility of a stable perovskite phase formation based on the ionic radii of the A and B site cations and X site anions in the ABX_3 perovskite structure. This model may be applied to double perovskites after some modifications, given their different structural formula: $A_2B_1B_2X_6$.

One may derive a Goldschmidt tolerance factor (t) formula for double perovskites analogous to that for ABX_3-type perovskites.[6] Namely, for ABX_3-type perovskites, the Goldschmidt tolerance factor is:

$$t = \frac{r_A + r_x}{\sqrt{2}(r_{B+}r_x)}$$

Where r_A, r_B and r_x are the ionic radii of the A-site cation, B-site cation and X anion, respectively. Therefore, for double perovskites one may infer:

$$t = \frac{r_A + r_x}{\sqrt{2}(\frac{r_{B_1} + r_{B_2}}{2} + r_x)}$$

For double perovskites, the limits of stability are set from *t*=0.82 to 1.08.[6] **Table 6.1** below lists the reported ionic radii of the cations and anions of interest,[7] with the respective Goldschmidt tolerance factor calculations for the $Cs_2AgBiBr_6$ perovskite and a potential $Li_2AgBiBr_6$ structure.

Table 6.1. Reported ionic radii and calculated tolerance factors for $Cs_2AgBiBr_6$ and $Li_2AgBiBr_6$ perovskite structures

Ionic Radii (Angstroms)			**Goldschmidt tolerance factor**	
r_A	Cs^+	1.67	$Cs_2AgBiBr_6$	1.03
r_A	Li^+	0.76	$Li_2AgBiBr_6$	0.77
r_{B1}	Ag^+	1.15		
r_{B2}	Bi^{3+}	1.03		
r_X	Br^-	1.89		

While the $Cs_2AgBiBr_6$ results in a tolerance factor of 1.03, well within the allowed range for structural stability, the much lower tolerance factor of 0.77 indicates the unfeasibility of the $Li_2AgBiBr_6$ double perovskite structure. Indeed, the $Li_2AgBiBr_6$ has been reported to be thermodynamically unstable by other computational methods.[8] Moreover, as reported by Li *et al.*, even after the substitution of 1 mol% of Cs^+ ions by Li^+ ions, the formation of new perovskite phases was not observed due to the small substitution amount and the effective formation of a solid solution instead.[3] Therefore, one may discard the possibility of a $Li_2AgBiBr_6$ phase formation. Moreover, the presence of an identical, yet shifted, X-ray diffraction pattern for the LiBr-treated $Cs_2AgBiBr_6$ films more likely indicates the introduction of some strain into the structure. For instance, Wu *et al.* have observed that the Ag-Br and Bi-Br bonds were affected by the presence of methyl ammonium during the film formation process when methylammonium bromide was inserted as an additive to the double perovskite.[4,9] Similar conclusions can be made from the shifts exemplified on **Figure 6.1b**, where the presence of lithium ions, for instance as interstitials, could indeed increase structural strain and reduce the lattice distances in the double perovskite. For instance, a similar placement of atomic hydrogen at interstitial positions of $Cs_2AgBiBr_6$ has been reported by Zhang *et al.*.[10] Expecting similar sizes for atomic hydrogen and ionic lithium makes the positioning of lithium ions at interstitial positions of the double perovskite therefore plausible.

Moreover, we hypothesize that interstitial Li^+ will strengthen the positively-charged environment established by Cs^+, Ag^+, or Bi^{3+}, hence accounting for the slight shrinkage of the lattice detected. We note that the degree of lattice shrinking as observed on **Figure 6.1b** is gradual, where the LiBr 1-2% films lead to an XRD peak shift with respect to the reference of no more than 0.07° 2θ, whereas LiBr 3% films show a distinct peak shift of 0.17° 2θ. Then, LiBr 4-6% films show similar extents of XRD peak shifting of approximately 0.20° 2θ. Lastly, and interestingly, the extent of XRD peak shifting for the LiBr diffusion sample matches that of the LiBr 3% sample.

In order to evaluate the possible optoelectronic benefit of the addition of LiBr into the $Cs_2AgBiBr_6$ bulk, steady state photoluminescence measurements were carried out, the results of which are shown on **Figure 6.2**. Indeed, an optimum LiBr loading appears to be reached at 3% LiBr where a maximum photoluminescence emission intensity is achieved, thereafter the excess presence of LiBr seems to be detrimental to the structure. An enhanced photoluminescence of double perovskite films treated with up to 3% LiBr could signify the healing of defects otherwise resulting in charge carrier traps and nonradiative recombination.

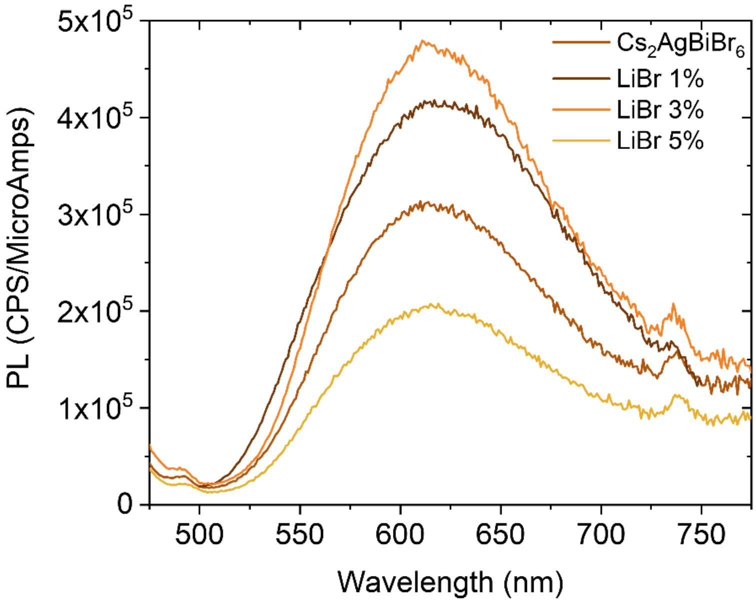

Figure 6.2. Steady-state photoluminescence measurements of the $Cs_2AgBiBr_6$ reference thin film and films with a 1, 3 and 5% LiBr loading.

Moreover, while the introduction of LiBr as an additive in the precursor solution leads a slight increase in the crystal domain sizes up until a 2% LiBr loading, loadings of 3% LiBr and higher in particular lead to the formation of aggregates (**Figure 6.3**), as observed with scanning electron microscopy (SEM) images of the thin films. In particular, loadings of 5% LiBr and greater already lead to smaller crystal domain sizes, which could also explain the reduced photoluminescence signal observed on **Figure 6.2** for the 5% LiBr film, as indeed films with smaller crystals have a higher density of grain boundaries which are sites for non-radiative recombination. More interestingly, a LiBr diffusion post-treatment of the double perovskite leads to a significant enhancement of the crystal domain sizes.

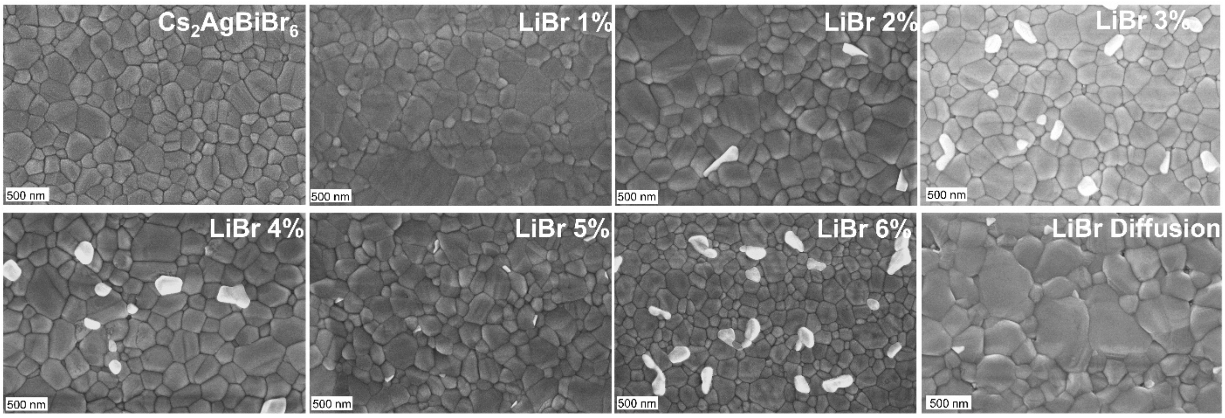

Figure 6.3. SEM images of the reference $Cs_2AgBiBr_6$ thin film and films fabricated with method 1, *i.e.* LiBr additives in the double perovskite precursor solution (1-6%, with respect to CsBr) and lastly a $Cs_2AgBiBr_6$ thin film after an LiBr diffusion post-treatment (Method 2).

6.3.2 Photovoltaic Device Results and Characterization

In order to evaluate the optoelectronic activity of the LiBr-treated double perovskites both via methods 1 and 2, photovoltaic devices were fabricated and optimized. Namely, devices with the n-i-p conformation were fabricated consisting of a compact and mesoporous titanium dioxide, TiO_2, electron transport layer, followed by the (treated) double perovskite and Spiro-OMeTAD hole transport layer, followed by a thin layer of MoO_3 (1 nm) and gold (8 nm). Note that devices in this chapter were further optimized using a thinner gold layer. Further details on device fabrication and measurements can be found on the experimental **Chapter 2**.

Figure 6.4a depicts the power conversion efficiency (PCE) box plots for the reference $Cs_2AgBiBr_6$ devices and those with LiBr loadings ranging from 1 to 6% LiBr, where an optimum is reached at a 3% LiBr loading. This optimum amount could be due to detrimental effects on the solubility of precursors at amounts greater than 3% LiBr as well as increased unwanted aggregate formation. These observations match the optimal photoluminescence signal intensity observed in **Figure 6.2,** corroborating the possibility of a defect-healing nature to the LiBr additive**.** Moreover, while the open circuit potentials (**Figure 6.4c**) and fill factors (**Figure 6.4d**) of LiBr additive devices are relatively comparable to the reference device, some devices with a 3% LiBr loading do generate significantly enhanced photocurrents **(Figure 6.4b).** These results, for the average and champion devices, are presented on **Table 6.2.**

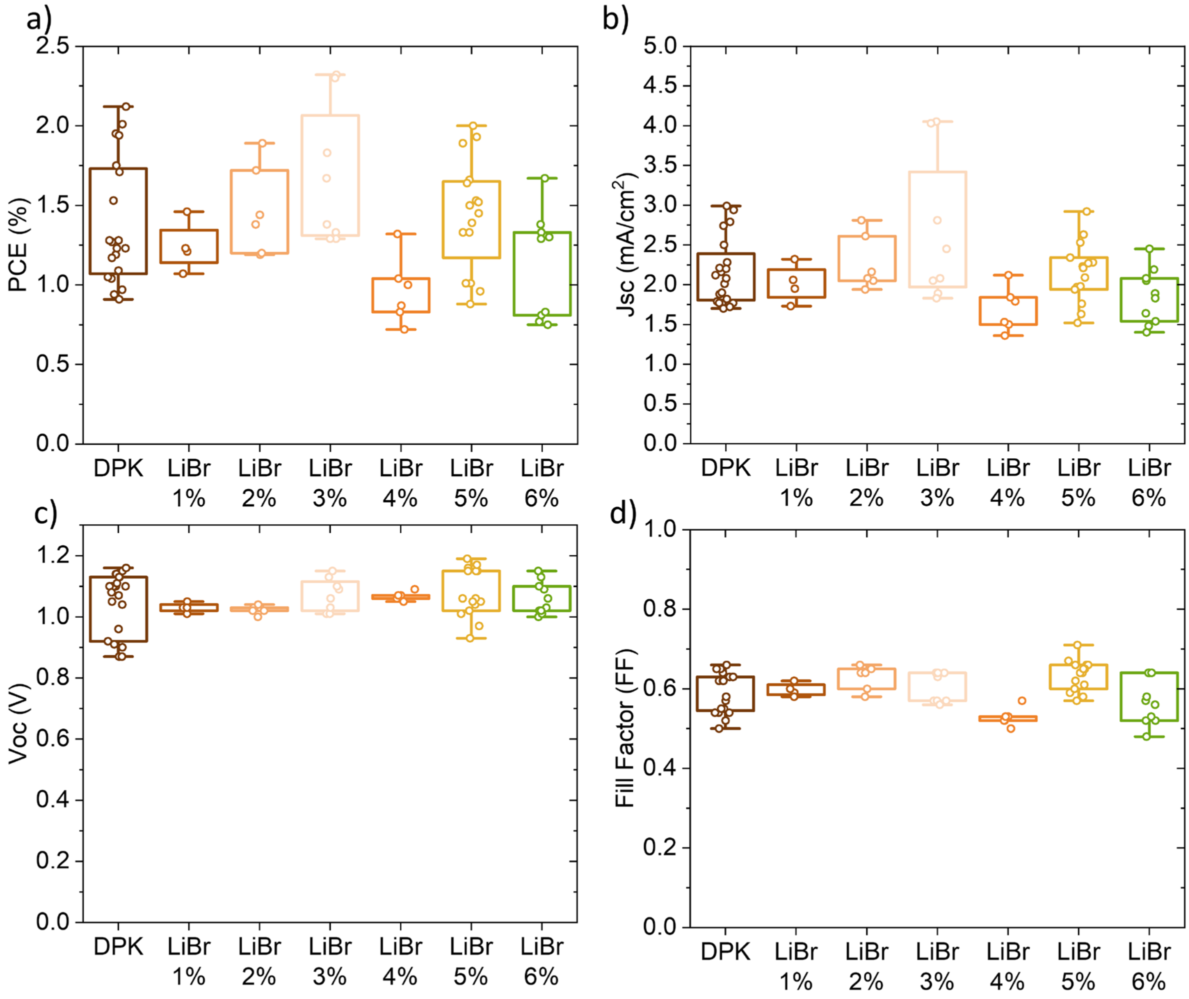

Figure 6.4. (a) Power conversion efficiencies, (b) short-circuit current densities, (c) open-circuit voltages and (d) fill factors for photovoltaic devices made from the reference $Cs_2AgBiBr_6$ perovskite active layer and double perovskites prepared with a 1 to 6% LiBr additive loading (Method 1).

Table 6.2. Comparative numerical photovoltaic results (average and champion) for the reference photovoltaic devices with a $Cs_2AgBiBr_6$ active layer and devices with 1-6% LiBr additive loadings.

	J_{SC} [mAcm^{-2}] [a]	V_{OC} [V] [a]	FF [a]	PCE [%] [a]	J_{SC} [mAcm^{-2}] [b]	V_{OC} [V] [b]	FF [b]	PCE [%] [b]
$Cs_2AgBiBr_6$	2.17	1.07	0.59	1.38	2.94	1.16	0.63	2.12
LiBr 1%	2.06	1.01	0.59	1.23	2.32	1.01	0.62	1.46
LiBr 2%	2.28	1.02	0.63	1.47	2.81	1.02	0.66	1.89
LiBr 3%	**2.68**	**1.07**	**0.59**	**1.67**	**4.05**	**1.01**	**0.57**	**2.32**
LiBr 4%	1.69	1.07	0.53	0.96	2.12	1.09	0.57	1.32
LiBr 5%	2.15	1.08	0.63	1.48	2.63	1.15	0.66	2.00
LiBr 6%	1.86	1.06	0.57	1.14	2.45	1.06	0.64	1.67

[a] Average over at least 5 devices; [b] Champion device

The J-V curves for both the best reference and 3% LiBr loading devices are presented on **Table 6.5.**

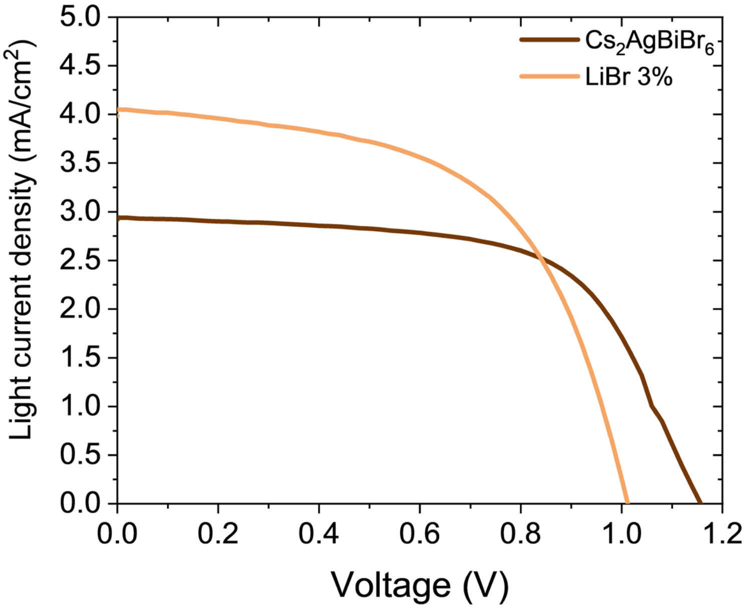

Figure 6.5. Current-density(J)-voltage(V) curves for the champion $Cs_2AgBiBr_6$ and 3% LiBr photovoltaic devices.

Although a moderate increase in photovoltaic performance could be observed at the optimal 3% LiBr loading, further LiBr incorporation methods, such as method 2, were also explored for the fabrication of a (LiBr-treated) double perovskite active layer for photovoltaic applications. The initial experiments involved the immersion of the spun-coat and already thermally-annealed double perovskite film into a solution of LiBr in isopropanol for 10 minutes. Different sets of LiBr solution concentrations were tested, namely 5 mg/ml, 10 mg/ml and 15mg/ml. Box plots for the resulting device PCEs are displayed on **Figure 6.6a**, and likewise for the short circuit current densities (**Figure 6.6b**), open circuit voltages (**Figure 6.6**) and fill factors (**Figure 6.6d**).

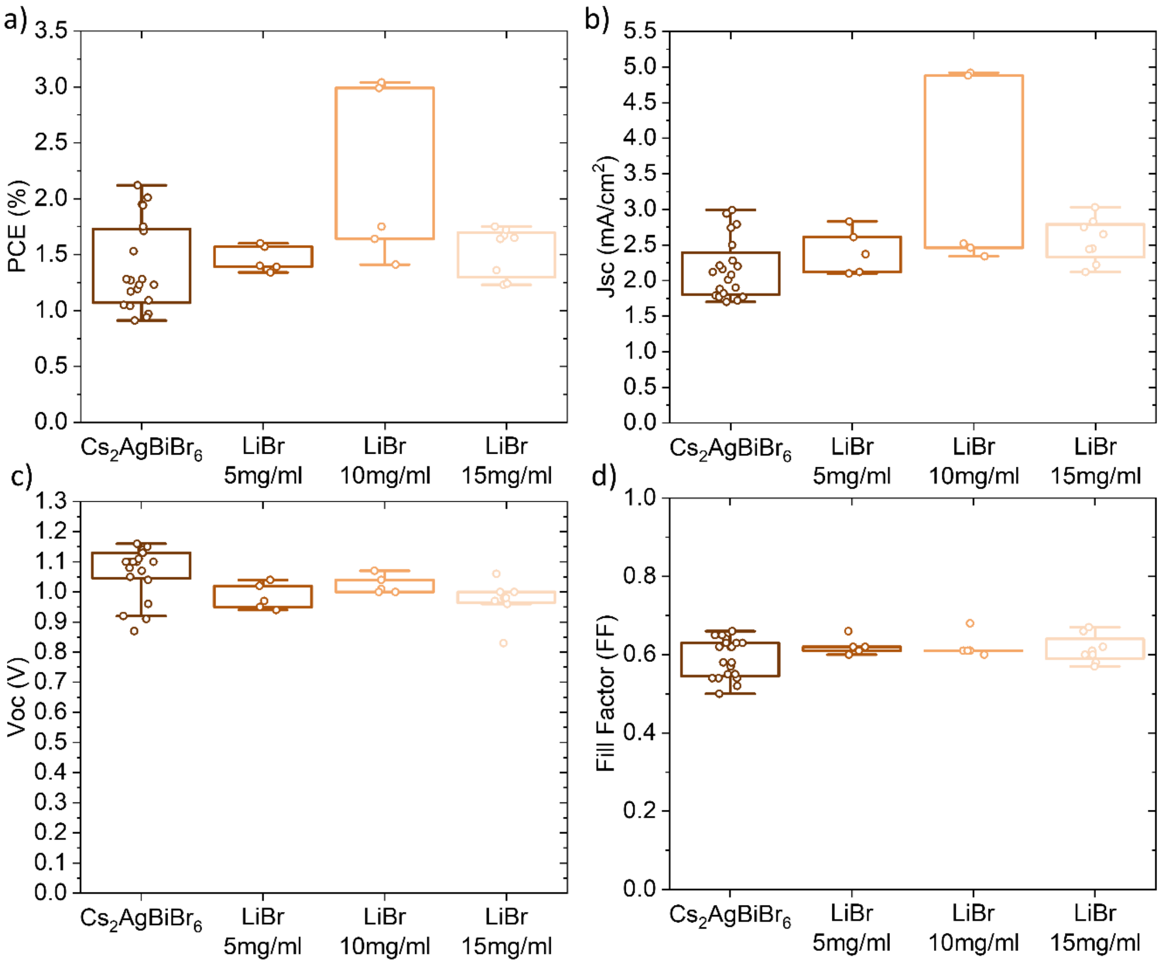

Figure 6.6. (a) Power conversion efficiencies, (b) short-circuit current densities, (c) open-circuit voltages and (d) fill factors for photovoltaic devices made from the reference $Cs_2AgBiBr_6$ perovskite active layer and double perovskites immersed for 10 minutes in LiBr solutions of various concentrations (Method 2).

The average and champion photovoltaic device performances from the LiBr solution concentration optimizations are presented on **Table 6.3**, where the optimal LiBr solution concentration can be identified at 10 mg/ml of isopropanol.

Table 6.3. Comparative numerical photovoltaic results (average and champion) for the reference $Cs_2AgBiBr_6$ devices and devices with an LiBr diffusion post-treatment of the double perovskite with different LiBr solution concentrations.

	J_{SC} [mAcm^{-2}] [a]	V_{OC} [V] [a]	*FF* [a]	PCE [%][a]	J_{SC} [mAcm^{-2}][b]	V_{OC} [V] [b]	*FF* [b]	PCE [%] [b]
$Cs_2AgBiBr_6$	2.17	1.07	0.59	1.38	2.94	1.16	0.63	2.12
LiBr 5 mg/ml	2.41	0.98	0.62	1.46	2.83	0.95	0.60	1.6
LiBr 10 mg/ml	**3.42**	**1.02**	**0.62**	**2.17**	**4.92**	**1.01**	**0.61**	**3.04**
LiBr 15 mg/ml	2.56	0.97	0.61	1.53	2.75	0.97	0.66	1.75

[a] Average over at least 5 devices; [b] Champion device

Next, with these encouraging results, the diffusion times were optimized, and photovoltaic devices prepared. **Figure 6.7** displays the photovoltaic devices for the LiBr diffusion time optimization. From the box plots of the power conversion efficiencies in **Figure 6.7a**, one may observe an optimum at 5 minutes of LiBr diffusion, likely since longer diffusion times could lead to unwanted aggregate formation. While fill factors after an LiBr diffusion treatment are comparable to those of the reference devices (**Figure 6.7d**), there is a significant enhancement of the short-circuit current densities of the LiBr diffusion devices (**Figure 6.7b**), however at the expense of slightly lower device open circuit potentials (**Figure 6.7c**), which leaves room for improvement. The effect of the LiBr diffusion time on the photovoltaic results is summarized on **Table 6.4**. Here one may observe the optimal LiBr diffusion time of 5 minutes, in comparison to 1 and 10 minute diffusion times, yields a champion device power conversion efficiency of 3.37% versus 2.12% for the best control device. The improvement in power conversion efficiency is brought about by the significantly enhanced device short-circuit current density from 2.94 mA/cm^2 in the reference to 5.93 mA/cm^2. While device fill factors are comparable, the open circuit potential is reduced at the expense of the increased photocurrent, providing again room for improvement regarding the LiBr diffusion method.

Table 6.4. Comparative numerical photovoltaic results (average and champion) for the reference $Cs_2AgBiBr_6$ devices and devices with an LiBr diffusion post-treatment (10 mg/ml) of the double perovskite with different LiBr diffusion times.

	J_{SC} [mAcm^{-2}] ^{a}	V_{OC} [V] ^{a}	FF ^{a}	PCE [%]^{a}	J_{SC} [mAcm^{-2}]^{b}	V_{OC} [V] ^{b}	FF ^{b}	PCE [%] ^{b}
$Cs_2AgBiBr_6$	2.17	1.07	0.59	1.38	2.94	1.16	0.63	2.12
LiBr 1 minute	3.42	1.05	0.54	1.89	5.27	1	0.54	2.84
LiBr 5 minutes	**4.60**	**1.00**	**0.57**	**2.59**	**5.93**	**0.96**	**0.60**	**3.37**
LiBr 10 minutes	3.42	1.02	0.62	2.17	4.92	1.01	0.61	3.04

^{a} Average over at least 5 devices; ^{b} Champion device

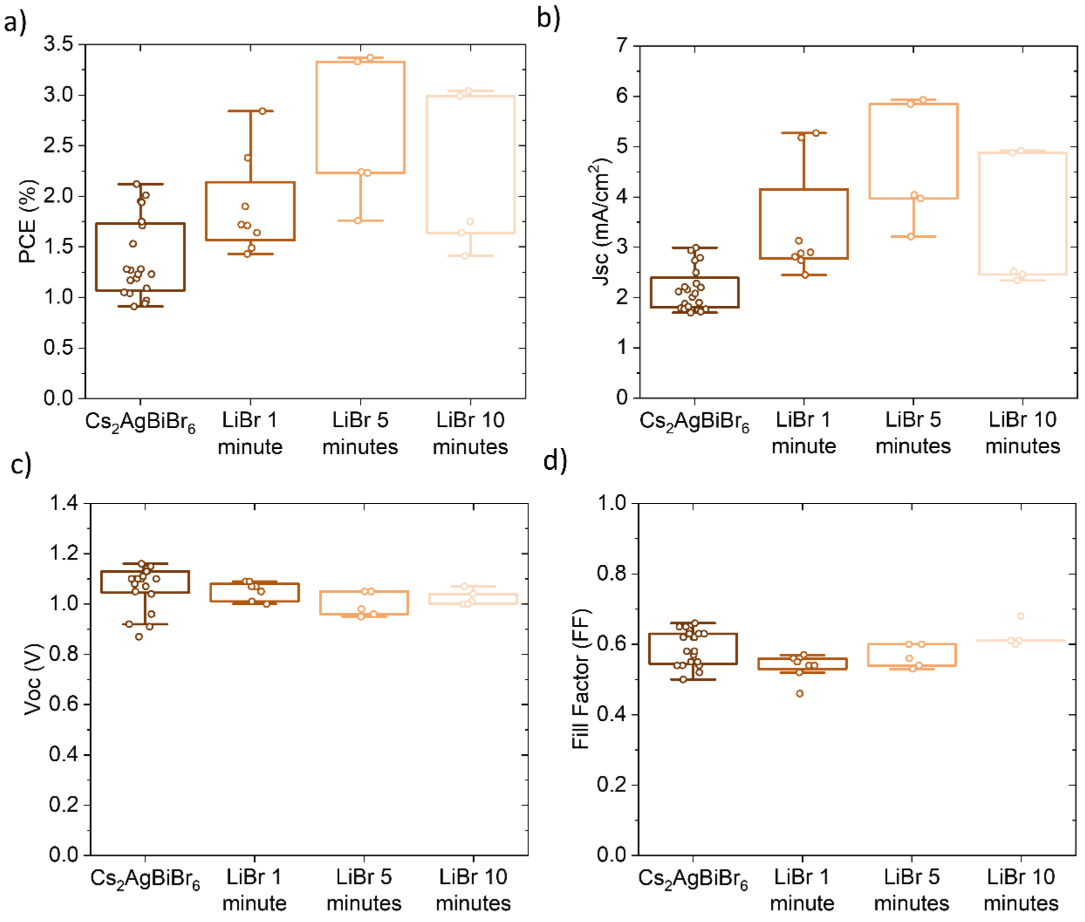

Figure 6.7. (a) Power conversion efficiencies, (b) short-circuit current densities, (c) open-circuit voltages and (d) fill factors for photovoltaic devices made from the reference $Cs_2AgBiBr_6$ perovskite active layer and double perovskites immersed for 1, 5 and 10 minutes in LiBr solutions (10 mg/ml in isopropanol) (Method 2).

Figure 6.8 displays the J-V curves for the best-performing $Cs_2AgBiBr_6$ reference photovoltaic device in comparison to the best-performing devices for a 5 and 10 minute LiBr diffusion treatment of the double perovskite.

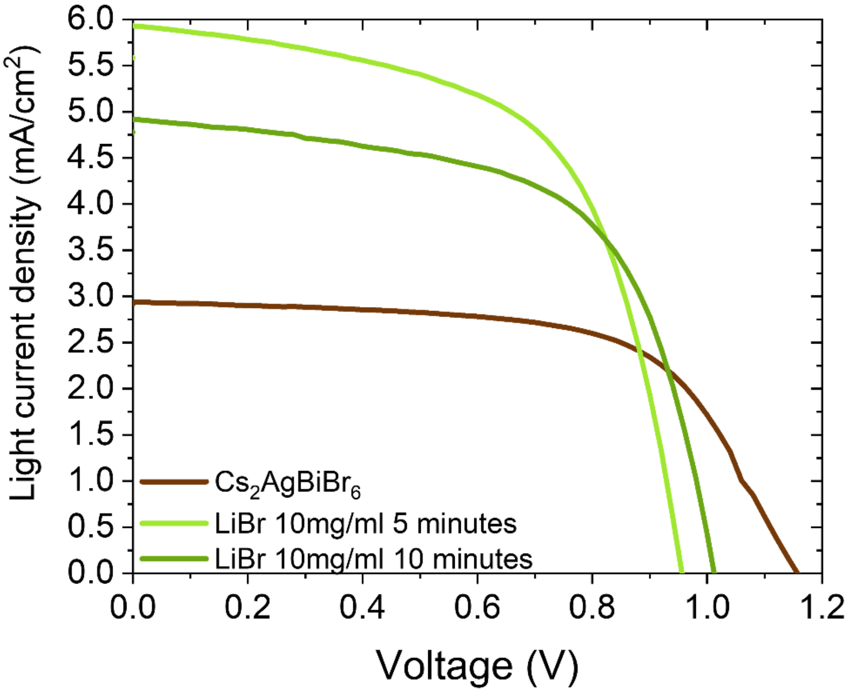

Figure 6.8. Current density(*J*)-voltage(*V*) curves for the champion $Cs_2AgBiBr_6$ and the 5 and 10 minute LiBr diffusion photovoltaic devices.

Moreover, reference samples were also dipped in isopropanol solvent as a control experiment, to discard the possibility of a beneficial isopropanol post-treatment. While the isopropanol treatment proved to lead to a slight benefit in the average device performance, the best device does not however outperform the best reference photovoltaic device. These data are respectively presented on **Table 6.5**. It is, therefore, plausible to conclude that the LiBr diffusion is principally responsible for the improved photovoltaic performance observed, as opposed to just the additional treatment in isopropanol.

Table 6.5. Comparative numerical photovoltaic results (average and champion) for the reference $Cs_2AgBiBr_6$ devices and devices with the double perovskite dipped in isopropanol (IPA) as a control

	J_{SC} [mAcm^{-2}] [a]	V_{OC} [V] [a]	FF [a]	PCE [%] [a]	J_{SC} [mAcm^{-2}] [b]	V_{OC} [V] [b]	FF [b]	PCE [%] [b]
$Cs_2AgBiBr_6$	2.17	1.07	0.59	1.38	2.94	1.16	0.63	2.12
IPA dipping	2.60	1.13	0.58	1.71	2.52	1.14	0.64	1.83

[a] Average over at least 4 devices; [b] Champion device

Nevertheless, optimal devices with an LiBr diffusion treatment of the double perovskite as well as a bulk additive incorporation of LiBr still experience significant levels of hysteresis which present a point for further work and device optimization, as presented on **Figure 6.9**.

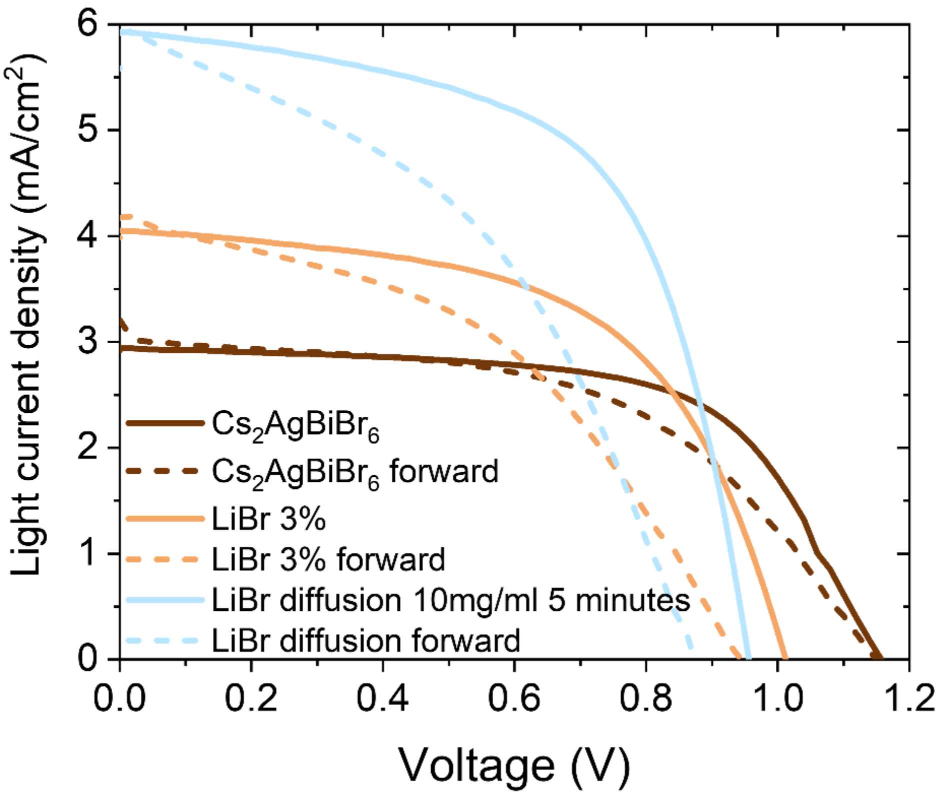

Figure 6.9. Forward and reverse scan current density(J)-voltage(V) curves for the champion $Cs_2AgBiBr_6$ device, the 3% LiBr device fabricated through Method 1 and the optimized LiBr diffusion device fabricated through Method 2.

Next, intensity-modulated photovoltage spectroscopy (IMVS) was used to investigate electron lifetime which, with this method, can be estimated under open circuit conditions.[11] This could serve to understand the reasoning behind the enhanced photovoltaic device performance of devices fabricated with method 2. Namely, the IMVS measurements were carried out both on the reference $Cs_2AgBiBr_6$ devices as well as on optimized devices treated with LiBr diffusion. **Table 6.6** summarizes the average charge carrier recombination lifetimes extracted from 3 devices of each the reference and LiBr-treated cells. Detailed information on these calculations may be found on the experimental section in **Chapter 2**.

Table 6.6. Average recombination lifetime results of $Cs_2AgBiBr_6$ and LiBr-treated photovoltaic cells from intensity modulated photovoltage spectroscopy measurements

	Average τ_{rec} (ms)
$Cs_2AgBiBr_6$	5.13
LiBr diffusion	22.5

The recombination lifetimes (t_{rec}) presented on **Table 6.6** are calculated from the equation below,[12] where f is the frequency corresponding to the maximum point in the IMVS transfer function as represented on the Nyquist curves, displayed on **Figure 6.10.**

$$t_{rec} = \frac{1}{2\pi f}$$

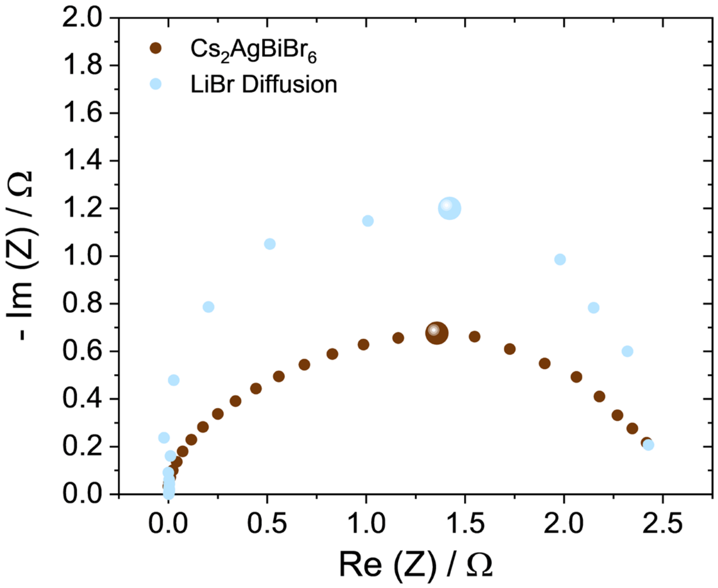

Figure 6.10. Nyquist plots (real, Re, and imaginary, - Im, components) of intensity-modulated photovoltage spectroscopy measurements on a $Cs_2AgBiBr_6$ reference device and a device prepared with Method 2 (LiBr diffusion).

As observed, samples prepared with LiBr diffusion showed a longer recombination lifetime, indicating that the charge separated species survive for longer time in the material prior recombination.[13] Broadly speaking, this is beneficial when considering assembling this material in a device, since it will increase the probability of charge extraction prior to recombination.[14] It is reasonable to consider that the larger crystal sizes of the samples prepared by LiBr diffusion could reduce the overall trap density, since the latter is commonly located at the grain boundaries. However, we cannot rule out the potential role of LiBr as a passivating agent. This will be explored below.

The calculated recombination lifetimes might appear rather long compared to other devices or even the reported picosecond to 1.4 microsecond lifetimes for $Cs_2AgBiBr_6$ perovskites.[15] It is worth noting that recombination processes at sub-microsecond timescales could be occurring, but not detected, being out of the scope of the IMVS technique, limited to probe the recombination dynamics in the range of tens of microseconds to milliseconds. Given the relatively low photocurrents reported for this class of material, it is not unreasonable to think that a massive loss (recombination) of photogenerated charges occurs at the early stages upon excitation, while being the recombination dynamics of the remaining charges the ones probed by IMVS.

Moreover, in order to discern whether the presence of additional bromide anions, lithium cations or both was a requirement for device performance improvement. A further series of control experiments were prepared, where first bromide salts with volatile cations (*i.e.* methyl ammonium bromide) were introduced into the double perovskite over a wide range of concentrations spanning those employed in Method 1 for LiBr. Indeed, at annealing temperatures of 310°C, the methyl ammonium cations are expected to volatilize and are chosen for this purpose. The box plots for devices fabricated by introducing methyl ammonium bromide at concentrations of 5, 10 and 15 mol% (with respect to CsBr content) are presented on **Figure 6.11**.

We note that, in order to remain comparable to the optimized LiBr addition experiments, further MABr concentrations were not tested, as opposed to the work of Wu *et al.*, which targets higher MABr concentrations for device optimization via intermediate species formation during double perovskite synthesis, where an enhancement of power conversion efficiencies could be observed at much greater MABr loadings. In this work however, we do not observe any particular short-circuit current density (**Figure 6.11b**), open circuit voltage (**Figure 6.11c**), fill factor (**Figure 6.11d**) and therefore power conversion efficiencies (**Figure 6.11a**) of double perovskite devices treated with an MABr additive, in the range of interest.

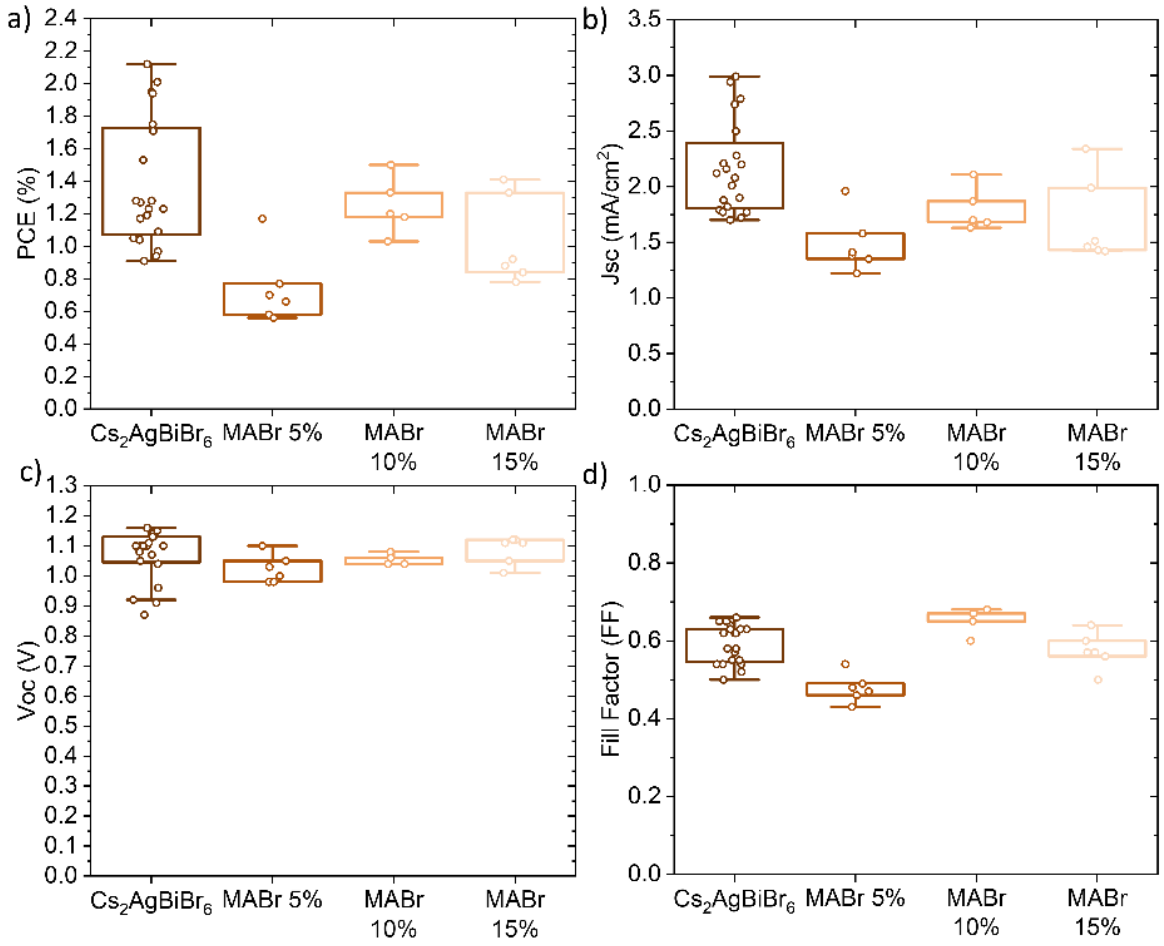

Figure 6.11. (a) Power conversion efficiencies, (b) short-circuit current densities, (c) open-circuit voltages and (d) fill factors for photovoltaic devices made from the reference $Cs_2AgBiBr_6$ perovskite active layer and double perovskites with MABr additive in concentrations ranging from (1-15 % with respect to CsBr content).

Similarly, methylammonium bromide diffusion (via a method comparable to Method 2 for LiBr diffusion) into the double perovskite was also tested with MABr solutions at concentrations of 10 mg/ml in isopropanol. Box plots for devices fabricated by allowing methyl ammonium bromide to diffuse into the double perovskite at times of 1, 5 and 10 minutes are presented on **Figure 6.12**. While an optimum condition for MABr diffusion, as evidenced by somewhat higher power conversion efficiencies (**Figure 6.12a**) appears to be reached at 5 minutes of diffusion time, mainly due to an enhancement of fill factors (**Figure 6.12d**), device short circuit current densities (**Figure 6.12b**) and open circuit voltages (**Figure 6.12c**) do not see any particular improvement and, overall, there is no improvement of the photovoltaic device performance.

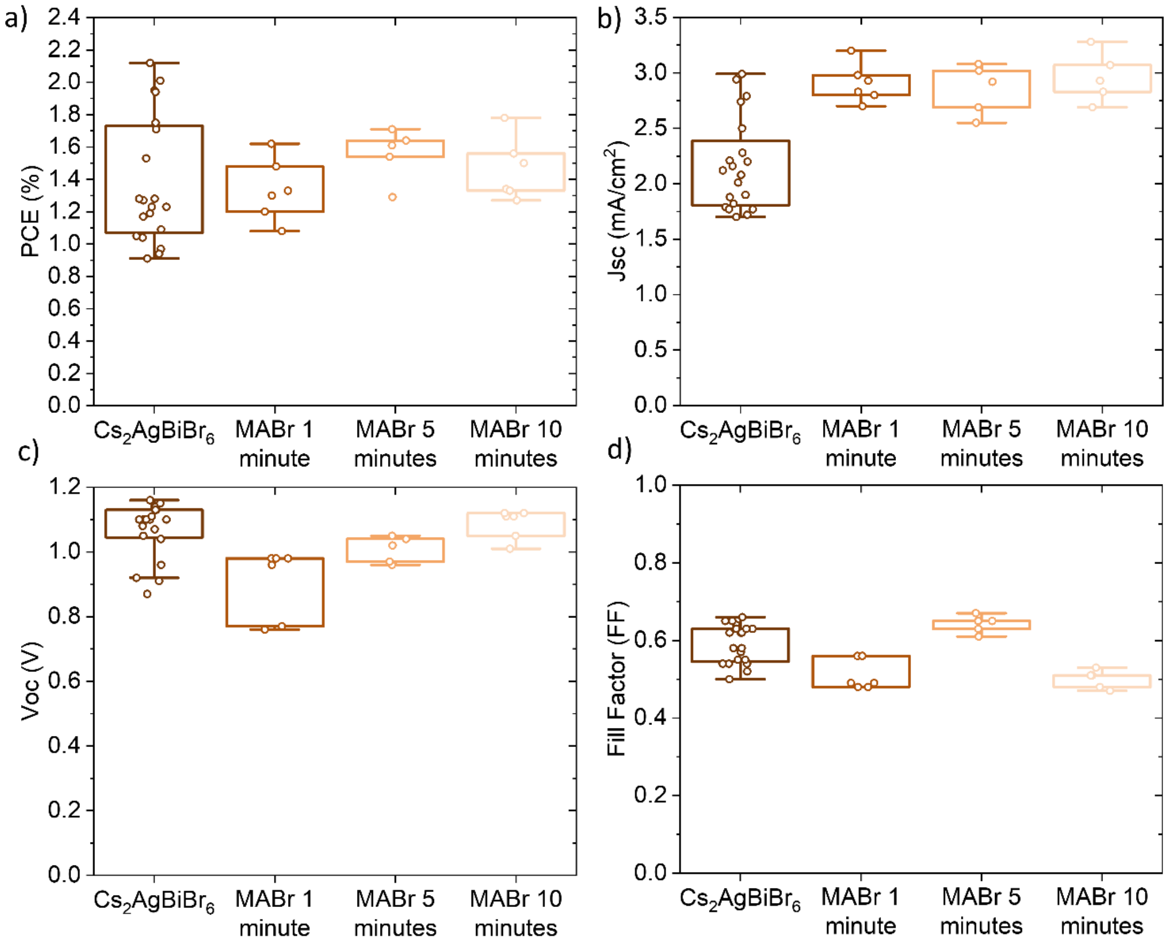

Figure 6.12. (a) Power conversion efficiencies, (b) short-circuit current densities, (c) open-circuit voltages and (d) fill factors for photovoltaic devices made from the reference $Cs_2AgBiBr_6$ perovskite active layer and double perovskites after MABr diffusion after 1, 5 and 10 minutes.

Further bromide incorporation was attempted via a bromine vapor annealing treatment, by which the thermally annealed solution-processed double perovskite was then placed in an enclosed container with bromine vapor at 50°C for 10 minutes, followed by an additional thermal annealing step. This however did not lead to any noticeable improvement in photovoltaic device performance as exemplified by the resulting photovoltaic device box plots in **Figure 6.13a-d**. It is plausible that this method is not valid for bromide introduction purposes, as indeed bromine molecules are present in the surrounding environment to the double perovskite instead of bromide anions.

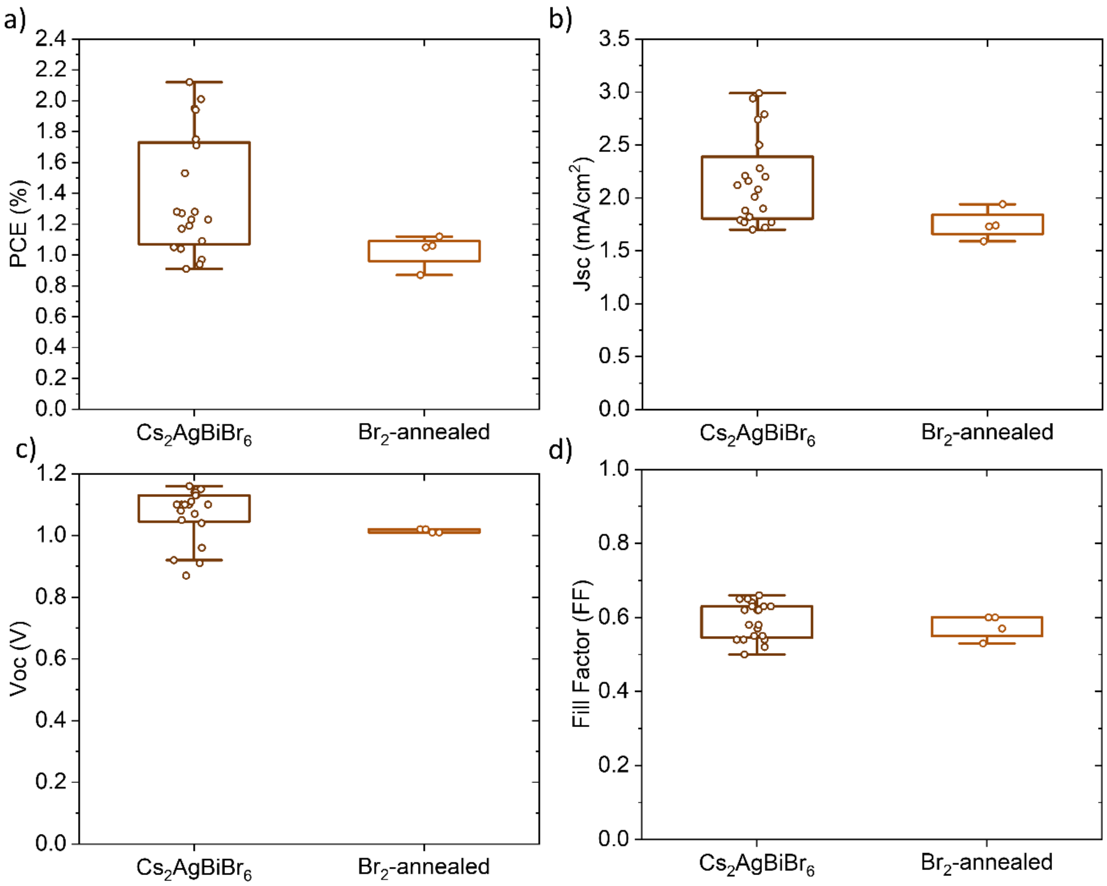

Figure 6.13. (a) Power conversion efficiencies, (b) short-circuit current densities, (c) open-circuit voltages and (d) fill factors for photovoltaic devices made from the reference $Cs_2AgBiBr_6$ perovskite active layer and double perovskites annealed under a bromine vapor environment.

From the aforementioned control experiments, the introduction of bromide species alone does not seem sufficient for the enhancement of double perovskite photovoltaic device efficiency. This hints at the importance of the presence of lithium ions in the additive. Therefore, a control experiment whereby lithium was introduced into the double perovskite as a dopant with, this time, a volatile anion, was devised. Given the volatility of the thiocyanate (SCN^-) counter ion at the thermal annealing temperature of the double perovskite and its proven applicability as a precursor additive in double perovskites in the form of Guanidium thiocyanate (Yang *et al.*),[16] LiSCN was explored as an additive to the double perovskite. Following a method comparable to Method 1, anhydrous LiSCN was synthesized, as reported on the experimental **Chapter 2**, and introduced into the double perovskite precursor solution at concentrations of 1, 3, 5 and 10 mol% (with respect to CsBr content). **Figure 6.14a** shows the resulting X-ray diffraction patterns of double perovskites following introduction of 1-10 mol% LiSCN with respect to CsBr content, where neither the appearance of new phases nor the any remaining LiSCN phases can be observed. However, as observed on the steady-state photoluminescence spectra on **Figure 6.14b**, a significant reduction in photoluminescent intensity can be observed for double perovskite films with a LiSCN additive. This is likely due to the also reduced crystal domain sizes and the appearance of surface aggregates, as observed from SEM images, displayed on **Figure 6.15**.

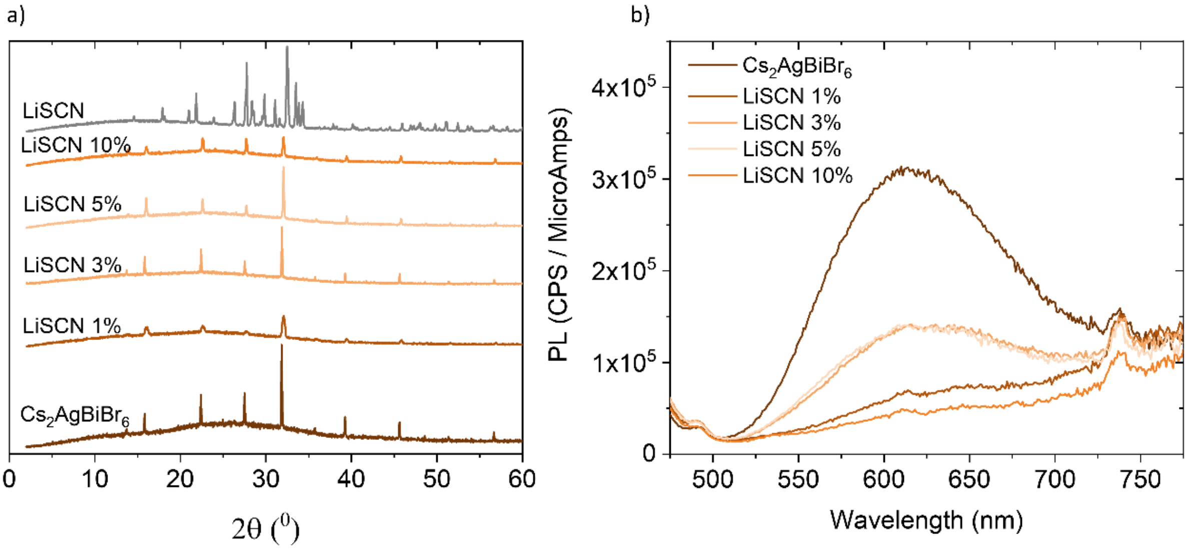

Figure 6.14. (a) X-ray diffraction patterns and (b) steady-state photoluminescence spectra for $Cs_2AgBiBr_6$ reference thin films and films treated with LiSCN additives.

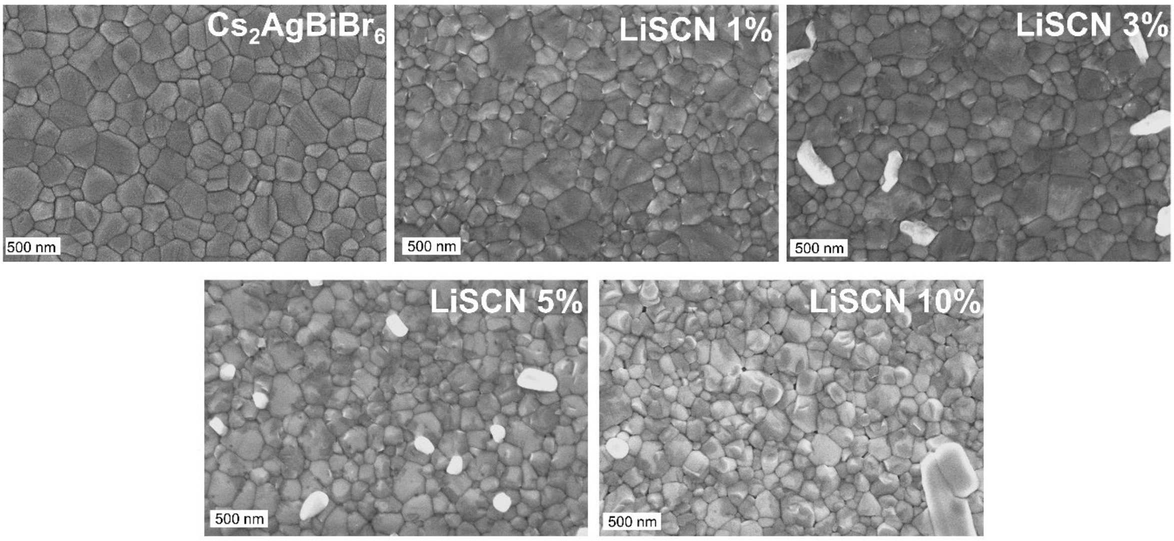

Figure 6.15. SEM images of the reference Cs$_2$AgBiBr$_6$ thin film and films fabricated with LiSCN additives in the double perovskite precursor solution (1-10%, with respect to CsBr).

As a result, no optimum device performing better than the reference could be identified as displayed on the data in the box plots from **Figure 6.16a-d**.

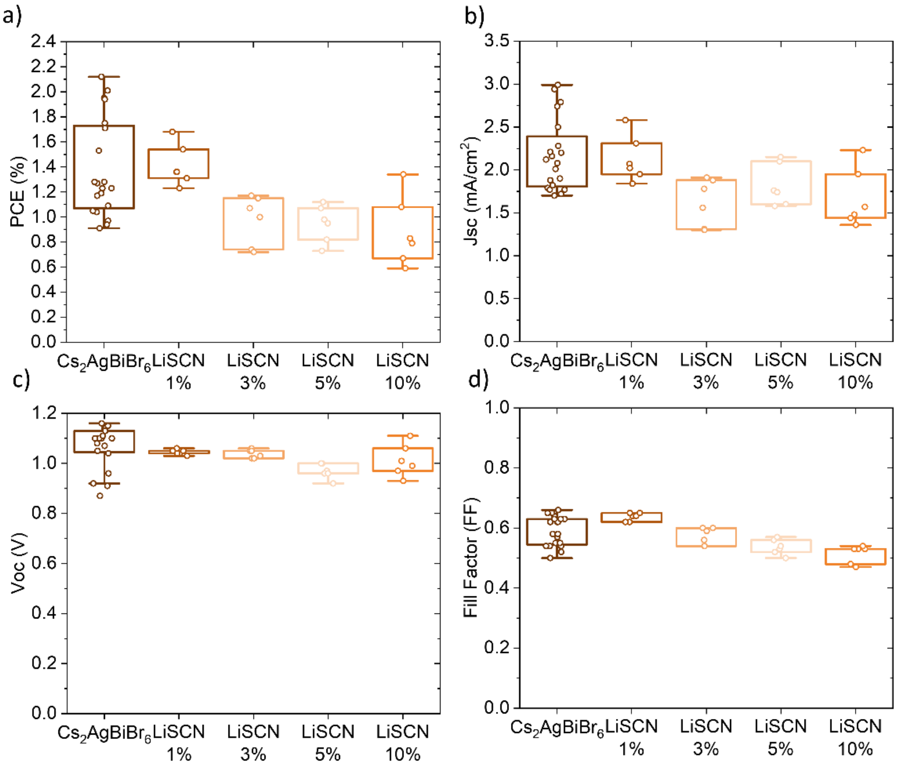

Figure 6.16. (a) Power conversion efficiencies, (b) short-circuit current densities, (c) open-circuit voltages and (d) fill factors for photovoltaic devices made from the reference Cs$_2$AgBiBr$_6$ perovskite active layer and double perovskites treated with a LiSCN additive in molar concentrations of 1-10% with respect to CsBr.

Yang *et al.* have also reported the addition of CsSCN into $Cs_2AgBiBr_6$, where no photovoltaic device performance improvement, and in fact a worsened device performance, could be observed, in comparison to the Guanidium thiocyanate additive.[16] These results further show the importance of the Guanidium cation presence together with the SCN^- counter ion for effective device performance improvement by ameliorating the film quality. Note that the enhanced grain growth and preferential crystallinity obtained using SCN^- in lead-halide perovskites is commonly linked the particular interaction between these species.[17] It is, therefore, plausible to consider that the change in the composition of the perovskites alters this mechanism rendering it inactive for the $Cs_2AgBiBr_6$ double perovskite structure, in the absence of an active cationic species alongside the SCN^-. Similarly, in the present work, the existence of both Li cations and bromide anions as additives is essential for enhancing film qualities and photovoltaic device efficiency. In effect, in order to elucidate the role of LiBr additives/treatments in the double perovskite device performance improvement, further characterization experiments were carried out.

6.3.3 Further spectroscopy characterization experiments

In order to better understand the possible energy level modifications of the LiBr-treated double perovskite, ultraviolet photoelectron spectroscopy (UPS) experiments were carried out to first determine the secondary electron cut-off (**Figure 6.17a**) and the valence band maxima (**Figure 6.17b**), from which the ionization energy with respect to vacuum could be determined.[18,19] (Detailed calculation methods are described on **Chapter 2**).

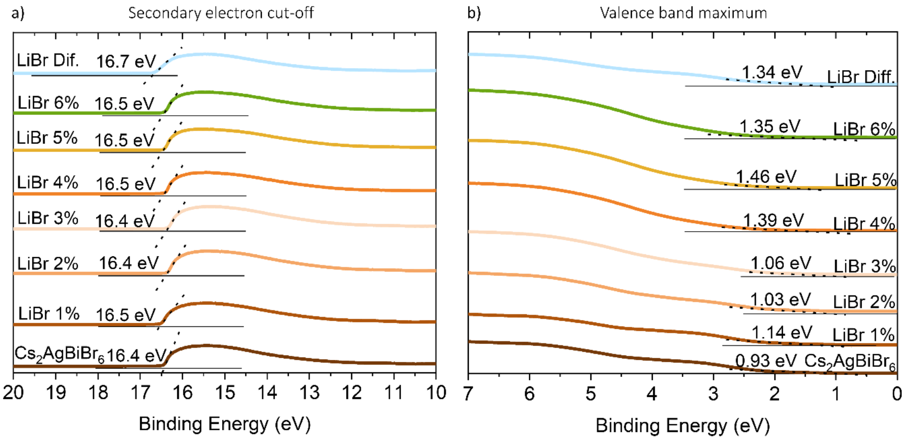

Figure 6.17. Linear fits of the (a) secondary electron cut-off and (b) the valence band maxima for the reference $Cs_2AgBiBr_6$ perovskite and the double perovskite with LiBr as an additive in several amounts as well as with an LiBr diffusion treatment (LiBr Dif.).

Furthermore, from the UV-visible light spectra on **Figure 6.18a**, Tauc plots (**Figure 6.18b**) were derived for an indirect bandgap material,[20] and the band gaps were extracted from linear fits.

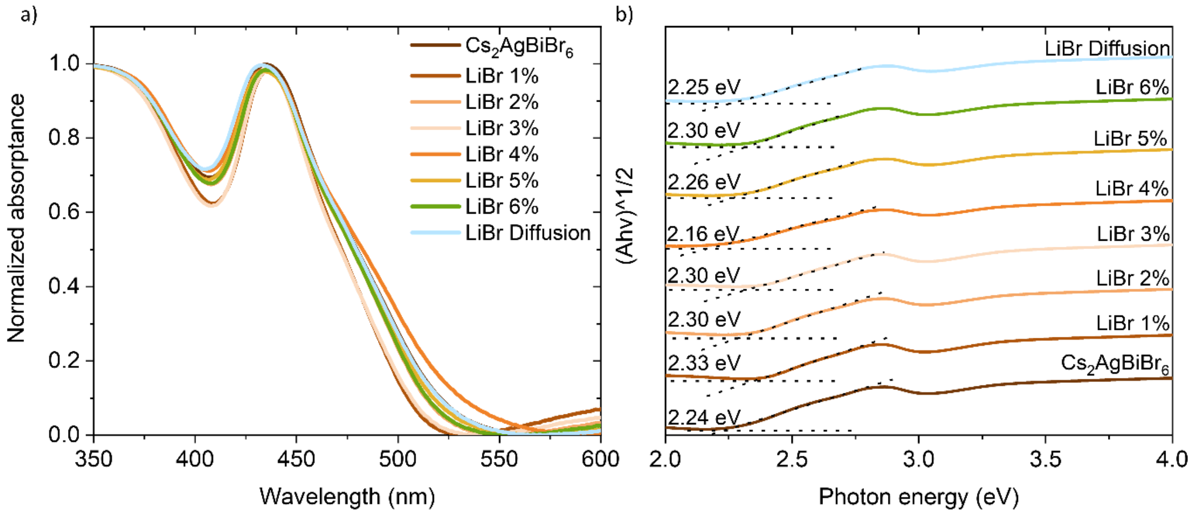

Figure 6.18. (a) Spectral absorptance and corresponding Tauc plots (b) for the $Cs_2AgBiBr_6$ reference thin film and films treated with LiBr via the additive or diffusion method.

With this information in hand, the energy levels could be determined as displayed on **Figure 6.19**, alongside the reported conduction band minima values for FTO, TiO_2 and HOMO and valence band maxima for Spiro and MoO_3 and Au, respectively.[21,22]

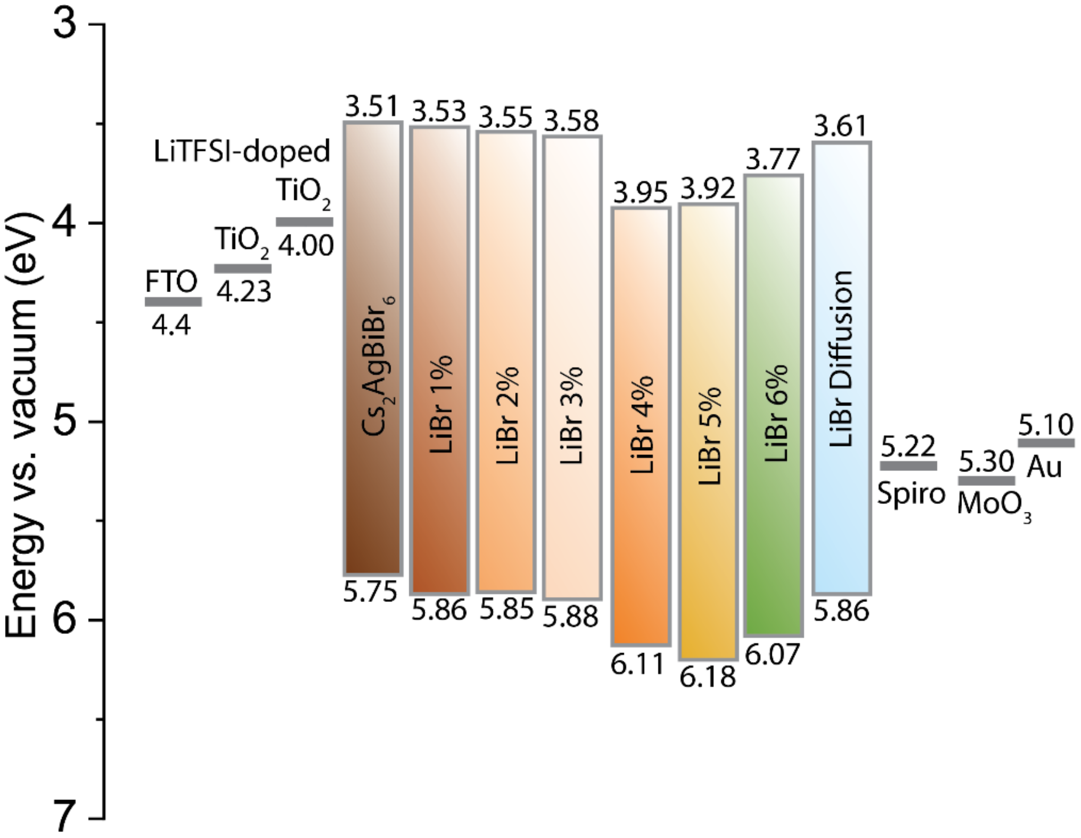

Figure 6.19. Double perovskite calculated energy levels following various LiBr treatments and corresponding energy band alignments with n-i-p device electron and hole collecting layers.

Indeed, one may observe that the LiBr additive treatment in the double perovskite leads to a slight lowering of the conduction band minima and valence band maxima. Given the optimal LiBr additive condition found at 3% LiBr loading, as suggested by photovoltaic data, the continued deepening of valence band maxima in particular appears to have too large of an energy gap for hole extraction, for loadings greater than 4% LiBr; this could account for larger voltage losses (hence, smaller V_{oc} as observed) and the poorer photovoltaic device performances for devices with an LiBr loading greater than 3%. The LiBr diffusion treatment of $Cs_2AgBiBr_6$ does however appear to bring about a more preferential set of energy level modifications, with a 100 meV lowering of the conduction band minimum which could facilitate electron collection by the (doped) TiO_2 electron transport layer and reduce the voltage losses at the interface. Moreover, the 110 meV deepening of the valence band maxima does not seem to be detrimental to hole collection given the observed enhanced photovoltaic device performances. In essence, these energetic parameters could well explain the better-performing nature of the LiBr diffusion devices versus the LiBr additive devices.

Next, angle-dependent X-ray photoelectron spectroscopy (XPS) measurements were carried out to determine the depth profiles of the optimal LiBr additive and LiBr diffusion method samples, in comparison to the $Cs_2AgBiBr_6$ reference. Note that, the lithium 1s XPS signal is not easily detected at such low concentrations and for this reason Li content is not quantified in the depth profiles, which are presented on **Figure 6.20**. Furthermore, a 70° sample tilt angle corresponds to the film's surface whereas a 0° tilt angle corresponds more to the bulk, covering the first 10 nm of the film.

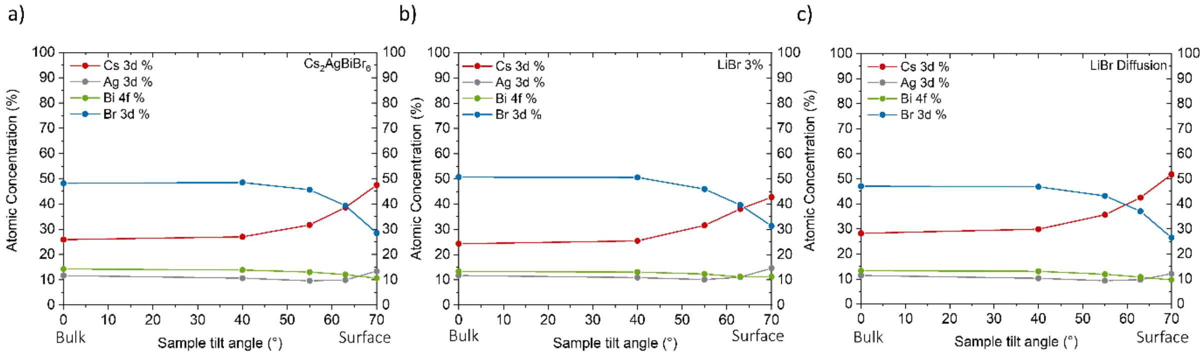

Figure 6.20. Depth-profile X-ray photoelectron spectroscopy of (a) $Cs_2AgBiBr_6$ and the double perovskite with (b) a 3% LiBr additive treatment and (c) an LiBr diffusion treatment, tracking the Cs, Ag, Bi and Br content from the surface to about the first 10 nm of the films.

It is worth noting, as was the case in Chapter 5, that bromide outgassing is a common bottleneck in XPS perovskite measurements, which explains Br atomic concentrations lower than 60% for the double perovskite samples (which therefore leads to overestimated Cs atomic concentration values above 20% as a result).[23–25] Despite this, qualitative observations may still be made in order to track the excess bromide presence brought about by the various LiBr treatments. Namely, Br is evidently increasingly available from the LiBr additive and the LiBr treatment methods on the double perovskite. To better demonstrate this, the ratio of atomic concentrations of bromine to a more consistent element throughout the depth profiles, *i.e.* bismuth, is calculated from the data presented on **Figure 6.20a-c** and shown on **Table 6.7**.

Table 6.7. Angle-dependent XPS Br 3d/Bi4f atomic percent ratios for the $Cs_2AgBiBr_6$ reference sample and a 3% LiBr additive treatment as well as a sample from the LiBr diffusion treatment distributed along the approximately first 10 nm of the sample

	Br 3d/ Bi 4f atomic percent ratios		
Incidence Angle (°)	**$Cs_2AgBiBr_6$**	**LiBr 3%**	**LiBr Diffusion**
0	3.38	3.80	3.54
40	3.50	3.87	3.58
55	3.50	3.73	3.64
63	3.26	3.55	3.44
70 (surface)	2.69	2.78	2.75

From **Table 6.7**, one may observe the larger Br/Bi atomic percent ratios of the LiBr-treated samples in comparison to the $Cs_2AgBiBr_6$ reference, more so for the LiBr 3% addition method than for the LiBr diffusion method. Given that the LiBr diffusion method was more successful at significantly enhancing photovoltaic device performance, it is plausible that the LiBr diffusion method is better-tuned to elegantly distribute the right amount of LiBr to the system, where the diffusion process is slower, allowing for the LiBr to target the correct location in the lattice.

In order to zoom-in further to the chemical environment around the lithium atoms to better understand their role in the double perovskite structure, solid state nuclear magnetic resonance (ssNMR) measurements of the ^7Li chemical environment were taken, by scratching the differently-treated thin double perovskite films and loading the resulting powders into ssNMR rotors. The resulting ^7Li chemical shift signals, alongside the reference signal for LiBr powder are presented on **Figure 6.21**. In order to attempt to magnify the ^7Li signal in the LiBr additive method, a sample with a larger loading of 7.5% LiBr in the double perovskite was also prepared.

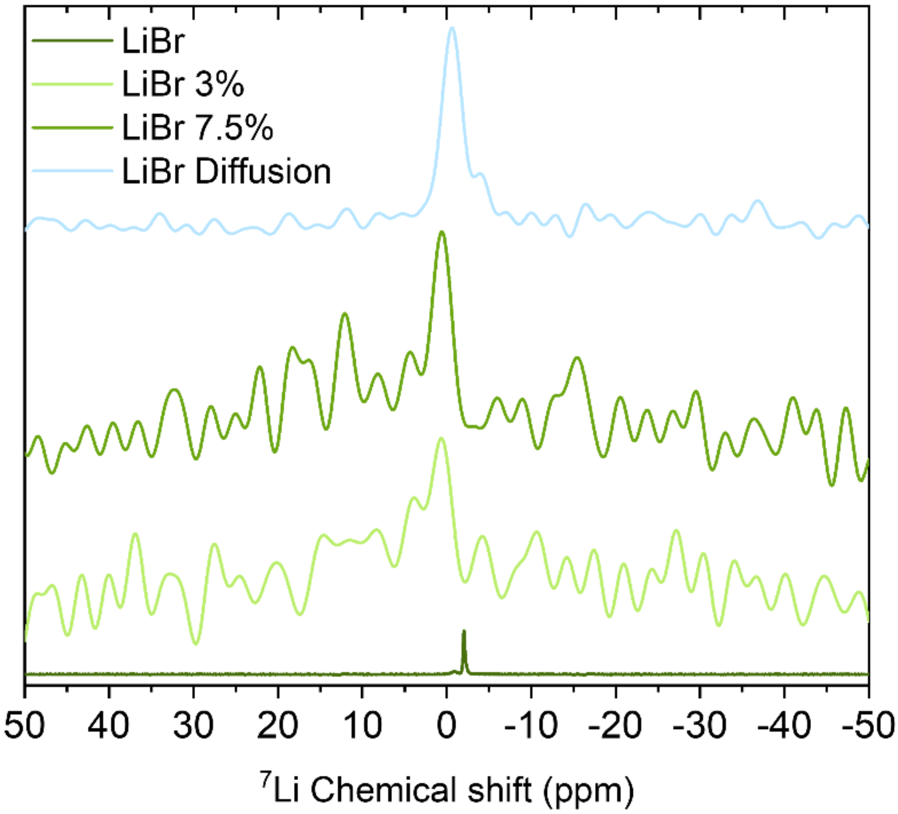

Figure 6.21. ^{7}Li solid state NMR spectra for LiBr, and the $Cs_2AgBiBr_6$ double perovskite samples with a 3% and 7.5% LiBr additives as well as samples submitted to LiBr diffusion treatments.

It first becomes clear that there is no remaining LiBr phase as aggregates in the double perovskite, due to the distinct signal, namely 1.83 ppm for LiBr, -2.07 ppm for the LiBr additive samples and -0.48 ppm for the LiBr diffusion samples. Indeed, the formation of a distinct Li chemical environment could signify, similar to conclusions from new Cs chemical environments in Chapter 5, the of the role of LiBr in the passivation of defects, for instance bromide vacancies in the perovskite, where the lithium would fit into the perovskite interstitials near the healing sites of bromide vacancies. This would also support the enhanced photovoltaic device efficiencies observed from LiBr-treated devices. We note that an excess LiBr loading of 7.5% does not represent any further shift of the ^{7}Li chemical shift signal, indicating a limit to the LiBr activity in the double perovskite. It is suggested that the Li^+ serves to accompany the bromide anions to the bromide vacancy defect sites, while it is itself placed at interstitial positions. The process of bromide vacancy healing proposed for the LiBr diffusion method is demonstrated on **Scheme 6.3**.

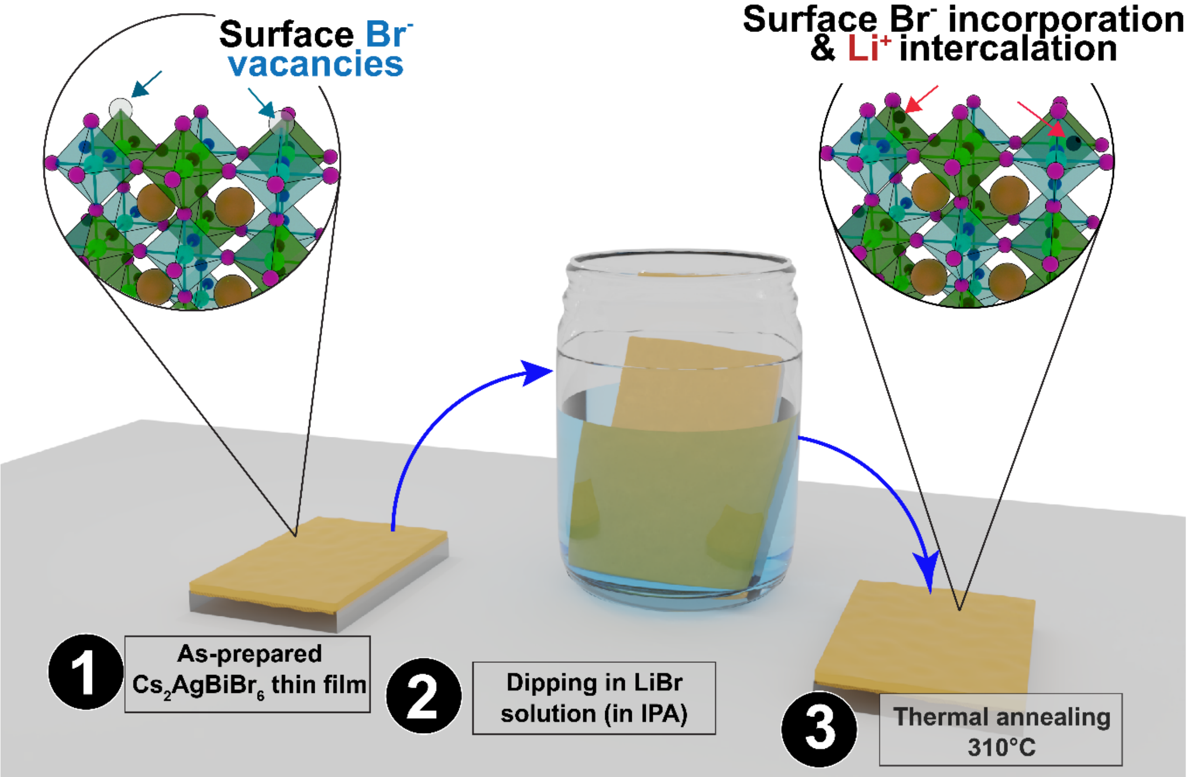
Surface Br⁻ vacancies
Surface Br⁻ incorporation & Li⁺ intercalation
1
As-prepared Cs2AgBiBr6 thin film
2
Dipping in LiBr solution (in IPA)
3
Thermal annealing 310°C

Scheme 6.3. Proposed bromide vacancy healing mechanism via the LiBr diffusion method (Method 2).

6.4 Conclusions

In this Chapter, alternative treatments for the replenishment of bromides into the double perovskite structure of $Cs_2AgBiBr_6$ were presented. LiBr was chosen as the additive of interest, given the hypothesis that a small cation was required to bring in bromide anions into the structure without much affecting the double perovskite phase. Two LiBr addition methods were presented, Method 1 involved direct addition of LiBr into the double perovskite precursor solution whereas Method 2 involved immersing the double perovskite into an LiBr solution for LiBr diffusion. Indeed, XRD measurements demonstrated initial activity of the LiBr in the perovskite structure by introducing a certain degree of strain and lattice shrinking upon LiBr addition. Interestingly, both optimal sets of samples for LiBr addition (3% LiBr) and LiBr diffusion present the same degree of XRD peak shifting and therefore lead to similar degrees of double perovskite lattice shrinking. The LiBr method yielded the best-performing photovoltaic devices with power conversion efficiencies as high as 3.37% in comparison to

2.12% for the champion reference device. This is mainly due to a greatly enhanced perovskite crystal domain size after LiBr post-treatment as observed with the SEM. Furthermore, IMVS measurements have yielded longer charge carrier recombination lifetimes for the LiBr diffusion photovoltaic devices. Control experiments were carried out in order to verify the needs for both Li^+ and Br^- additives, where devices fabricated with methyl ammonium bromide (additive and diffusion), lithium thiocyanate and even bromide vapor annealing of the double perovskite, did not lead to any outperforming devices with respect to the reference. This, in addition to the observation of a distinct Li chemical environment by following the ^7Li chemical shift in the LiBr-treated samples in comparison to pure LiBr shows the chemical activity of LiBr in the double perovskites, where it was proposed that the lithium serves to guide the bromide anions to bromide vacancy sites as it is itself placed at nearby interstitial positions. Moreover, UPS measurements alongside Tauc plot analysis yielded energy levels for the LiBr-treated samples which revealed lower conduction band maxima, thus facilitating electron extraction out of the double perovskite active layer.

6.5 References

[1] M. Keshavarz, E. Debroye, M. Ottesen, C. Martin, H. Zhang, E. Fron, R. Küchler, J. A. Steele, M. Bremholm, J. Van de Vondel, H. I. Wang, M. Bonn, M. B. J. Roeffaers, S. Wiedmann, J. Hofkens, *Adv. Mater.* **2020**, *32*, 2001878.

[2] Z. Zhang, C. Wu, D. Wang, G. Liu, Q. Zhang, W. Luo, X. Qi, X. Guo, Y. Zhang, Y. Lao, B. Qu, L. Xiao, Z. Chen, *Org. Electr.* **2019**, *74*, 204.

[3] J. Li, J. Duan, J. Du, X. Yang, Y. Wang, P. Yang, Y. Duan, Q. Tang, *ACS Appl. Mater. Interfaces* **2020**, *12*, 47408.

[4] H. Wu, Y. Wang, A. Liu, J. Wang, B. J. Kim, Y. Liu, Y. Fang, X. Zhang, G. Boschloo, E. M. J. Johansson, *Adv. Funct. Mater.* **2021**, 2109402.

[5] W. Travis, E. N. K. Glover, H. Bronstein, D. O. Scanlon, R. G. Palgrave, *Chem. Sci.* **2016**, *7*, 4548.

[6] Y. Cai, W. Xie, Y. T. Teng, P. C. Harikesh, B. Ghosh, P. Huck, K. A. Persson, N. Mathews, S. G. Mhaisalkar, M. Sherburne, M. Asta, *Chem. Mater.* **2019**, *31*, 5392.

[7] R. D. Shannon, *Acta Crystallographica Section A* **1976**, *32*, 751.

[8] T. Zhang, Z. Cai, S. Chen, *ACS Appl. Mater. Interfaces* **2020**, *12*, 20680.

[9] H. Lei, D. Hardy, F. Gao, *Adv. Func. Mater.* **2021**, *31*, 2105898.

[10] Z. Zhang, Q. Sun, Y. Lu, F. Lu, X. Mu, S.-H. Wei, M. Sui, **2022**, DOI 10.21203/rs.3.rs-587497/v1.

[11] A. Pockett, G. E. Eperon, T. Peltola, H. J. Snaith, A. Walker, L. M. Peter, P. J. Cameron, *J. Phys. Chem. C* **2015**, *119*, 3456.

[12] Y. Zhao, A. M. Nardes, K. Zhu, *Faraday Discuss.* **2015**, *176*, 301.

[13] N. Guijarro, L. Yao, F. Le Formal, R. A. Wells, Y. Liu, B. P. Darwich, L. Navratilova, H.-H. Cho, J.-H. Yum, K. Sivula, *Angew. Chem. Int. Ed.* **2019**, *58*, 12696.

[14] N. Parikh, S. Narayanan, H. Kumari, D. Prochowicz, A. Kalam, S. Satapathi, S. Akin, M. M. Tavakoli, P. Yadav, *Phys. Status Solidi RRL* **2021**, 2100510.

[15] R. L. Z. Hoye, L. Eyre, F. Wei, F. Brivio, A. Sadhanala, S. Sun, W. Li, K. H. L. Zhang, J. L. MacManus-Driscoll, P. D. Bristowe, R. H. Friend, A. K. Cheetham, F. Deschler, *Adv. Mater. Interfaces* **2018**, *5*, 1800464.

[16] X. Yang, A. Xie, H. Xiang, W. Wang, R. Ran, W. Zhou, Z. Shao, *Appl. Phys. Rev.* **2021**, *8*, 041402.

[17] X. Zhang, G. Wu, W. Fu, M. Qin, W. Yang, J. Yan, Z. Zhang, X. Lu, H. Chen, *Adv. Energy Mater.* **2018**, *8*, 1702498.

[18] B. Philippe, T. J. Jacobsson, J.-P. Correa-Baena, N. K. Jena, A. Banerjee, S. Chakraborty, U. B. Cappel, R. Ahuja, A. Hagfeldt, M. Odelius, H. Rensmo, *J. Phys. Chem. C* **2017**, *121*, 26655.

[19] A. Agresti, A. Pazniak, S. Pescetelli, A. Di Vito, D. Rossi, A. Pecchia, M. Auf der Maur, A. Liedl, R. Larciprete, D. V. Kuznetsov, D. Saranin, A. Di Carlo, *Nat. Mater.* **2019**, *18*, 1228.

[20] J. Tauc, R. Grigorovici, A. Vancu, *Phys.Status Solidi (b)* **1966**, *15*, 627.

[21] Z. Zhou, J. Xu, L. Xiao, J. Chen, Z. Tan, J. Yao, S. Dai, *RSC Adv.* **2016**, *6*, 78585.

[22] J.-H. Li, Y. Li, J.-T. Xu, C. K. Luscombe, *ACS Appl. Mater. Interfaces* **2017**, *9*, 17942.

[23] S. Tan, T. Huang, I. Yavuz, R. Wang, M. H. Weber, Y. Zhao, M. Abdelsamie, M. E. Liao, H.-C. Wang, K. Huynh, K.-H. Wei, J. Xue, F. Babbe, M. S. Goorsky, J.-W. Lee, C. M. Sutter-Fella, Y. Yang, *J. Am. Chem. Soc.* **2021**, *143*, 6781.

[24] Y. Jiang, S.-C. Yang, Q. Jeangros, S. Pisoni, T. Moser, S. Buecheler, A. N. Tiwari, F. Fu, *Joule* **2020**, *4*, 1087.

[25] C. Das, M. Wussler, T. Hellmann, T. Mayer, W. Jaegermann, *Phys. Chem. Chem. Phys.* **2018**, *20*, 17180.

Chapter 7

Overview and Outlook

A closer look at the future of perovskite photovoltaics

This chapter presents an overview of the experimental work carried out within the framework of this doctoral thesis, summarizing the motivation and results behind NDI and BDT molecular incorporation into layered lead-halide perovskites as well. Moreover, the motivation for better understanding lead-free perovskite structures for photovoltaic application purposes is once again presented, and the exciting experimental findings are summarized. An interesting application of lead-free double perovskites as nearly transparent perovskite active layers for building-integrated photovoltaic applications is presented.

With the initial motivation to explore the novel experimental incorporation of functional and optoelectronically-active cations into layered lead-halide perovskites for the hypothesized improvement of structural stability and charge-transporting properties of the perovskite structure, two cationic systems were selected based on their molecular size and previously reported charge transporting capabilities. In this doctoral thesis work, namely, the incorporation of naphthalene diimide (NDI) and benzodithiophene (BDT) molecules into Pb-I-based octahedral layers, as iodide-based cationic salts, was covered, including the challenges of incorporation and resulting optoelectronic properties of the synthesized systems. Namely, for the NDI system, three NDI molecular variants for the cations were tested, the asymmetric NDI ethyl ammonium (NDI-E) and the symmetric NDI diethyl (NDI-diE) and dibutyl (NDI-diB) ammonium iodide salt configurations. While the NDI-diE and -diB systems proved to be unfeasible options for incorporation into layered lead halide perovskites via kinetically-fast and -slow crystallization methods, the NDI-ethyl asymmetric cation system provided evidence of being more versatile towards incorporation into a (not pure) 2D perovskite phase via a slower crystallization method. Indeed, the NDI chromophores tested were likely too large to fit into the lead halide octahedral layers, and for this reason the BDT molecules were instead tested as active layered perovskite cationic spacers. BDT molecular spacers with 2-, 4- and 6- carbon side linker chain lengths were tested, where it was found that the 4-carbon system led to some layered perovskite formation with weak crystallinity whereas the 6-carbon system led to clear and pure 2D perovskite phase formation, whereas no crystallization whatsoever could be observed for the 2-carbon system. Having successfully incorporated the novel BDT cationic system into layered perovskite structures, quasi-layered perovskite systems were then fabricated, in order to harness the structural and optoelectronic property advantages of bulk 3D perovskites. The properties of the fabricated BDT-based quasi layered perovskites were compared to those of analogue well-established phenylethylammonium (PEA)-based quasi layered systems. Given its alternated conjugated structure, the BDT-system brought about enhanced charge transport in the organic layers (already at small loadings), where the resulting photovoltaic devices outperformed those fabricated with the conventional insulating PEA spacers. Moreover, ATR-FTIR measurements suggested the Lewis-base nature of the BDT cation where the electron-rich thiophene groups served as electron donors to iodide vacancy sites, thus passivating defects in the perovskite structure. This, in addition to the large molecular nature of the BDT, led not only to improved photovoltaic device performances but also enhanced device operational stabilities.

Nevertheless, the toxicity of lead-based perovskites remains a serious concern. For this reason, the investigation of lead-free perovskite structures occupies an important part of this thesis work. Namely, this doctoral thesis has focused on further investigating the $Cs_2AgBiBr_6$ lead-free double perovskite structures in particular, given their great potential for photovoltaic applications as a result of their high thermodynamic stability and photoresponse.[1] Nevertheless, reported efficiencies for this perovskite material are well below the calculated Shockley-Queisser limit of 16.4%;[2] this is because several intrinsic defects lead in particular to electron traps within the material while the double perovskite's energy levels are also not well suited to the existing and employed charge collecting layers, meaning work on device optimizations is still to be made.[3,4] Motivated by this challenge, this thesis work first attempted the stoichiometric tuning of $Cs_2AgBiBr_6$ precursors, given reports of suspected intrinsic bromide vacancy defects in the structure,[5–7] by introducing an excess of CsBr into the fabrication precursor solution. Photoluminescence and ^{133}Cs chemical shift solid state NMR measurements revealed hampered non-radiative recombination and the appearance of a distinct Cs chemical environment, which was attributed to the passivation of surface bromide vacancy defects. Moreover, the increased crystal orientation along the (00n) crystal planes was concluded to promote crystal growth as observed by the larger crystal domain sizes with the scanning electron microscope. Overall, this led to a modest average device performance increase mainly as a result of the greater V_{OC} in devices. However, the Cs component of the additive was suspected to be too large of an atom with no particular role. For this reason, LiBr additives in $Cs_2AgBiBr_6$ double perovskites were also explored in this thesis work. Both a precursor solution additive and a LiBr diffusion post-treatment of the double perovskite were attempted. Both methods led to enhanced device performance efficiencies; nonetheless the LiBr diffusion method stood out due to the significantly enhanced photovoltaic device performances after diffusion time and solution concentration optimizations, namely from a power conversion efficiency of 2.12% for the reference device to 3.37% for the LiBr post-treated device. It was observed that LiBr introduction into the bulk of the perovskite structure led to enhanced photoluminescence, showcasing the defect-healing qualities of the LiBr additive. Moreover, for the LiBr diffusion treatment, much greater crystal domain sizes were identified. Energy levels for the resulting LiBr-infused double perovskites were determined, where it was found that more appropriate energy level alignment with the charge collecting layers could be brought about by the LiBr treatment. Moreover, ^{7}Li solid state NMR studies further revealed a distinct Li chemical environment, from that of LiBr powder, once again demonstrating the activity of the Li in accompanying the bromide anions, likely towards the healing of bromide vacancies in the double perovskite structure. Indeed, IMVS measurements reveled much longer charge carrier recombination lifetimes in the LiBr post-treated devices.

Moreover, the aforementioned double perovskite structures have the great property of being nearly optically-transparent, which means that they have prodigious potential in applications such as building-integrated photovoltaics. The photovoltaic device efficiencies presented above are unprecedented for a nearly-transparent all-inorganic active layer of $Cs_2AgBiBr_6$. In this work, optimizations of the gold electrode were carried out where it was found that photovoltaic devices fabricated with nearly-transparent 8 nm gold electrodes yielded results comparable to or even better than those fabricated with 100 nm gold electrodes (**Figure 7.1a**).

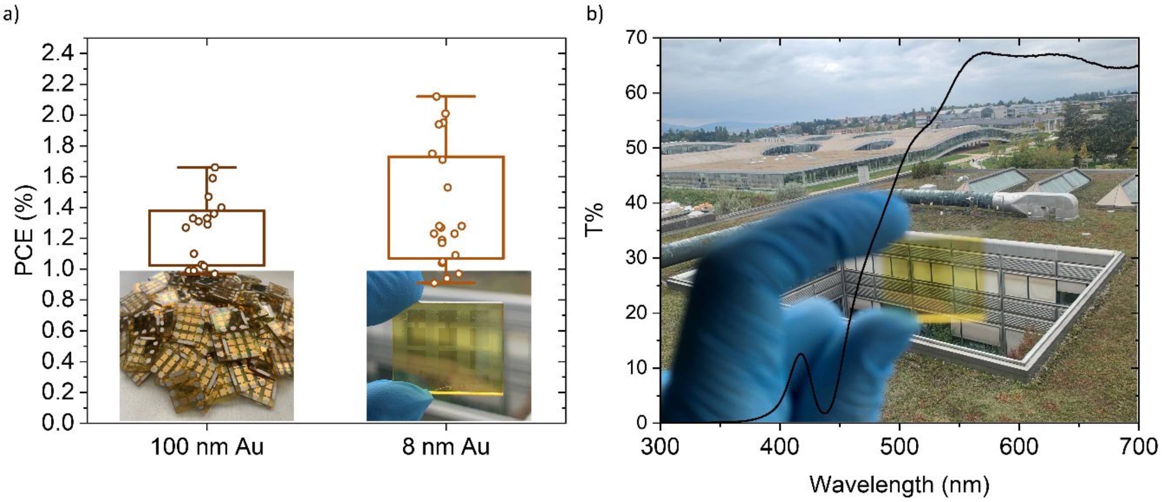

Figure 7.1. (a) Comparison and images of $Cs_2AgBiBr_6$ active layer reference photovoltaic devices with 100 nm and 8 nm Au electrodes (b) optimized device image and transmittance measurements.

Recently, silicon-based transparent solar cells have been reported with a champion efficiency of 7.4% and a 50% transmittance,[8] while the abovementioned double perovskite solar cells are more suitable for high-transparency applications, reaching efficiencies of 3.37% at a nearly 70% transmittance in the upper visible range (**Figure 7.1b**), and which has great potential for further performance improvement. Further comparisons to this and other reported and commercial semi-transparent photovoltaic devices are presented on **Table 7.1**.

Table 7.1. Semi-transparent solar cell technologies

Cell structure	**Approx. median transmittance in the visible 550-700 nm light range(%)***	**PV Efficiency (%)**	**Device area**	**Reference**
Crystalline silicon	50	7.4	1 cm^2	[8]
Copper Indium Gallium Selenide	11	9.78	5 x 5 mm^2	[9]
Organic (polymer)	12	9.40	3.8 mm^2	[10]
Lead-based perovskite with organic cross-linked hole transport layer	45	16.7	16 mm^2	[11]
Commercial (ClearVue) based on micro and nanoparticles / organic polyvinyl butyral interlayer	up to 70	3.3	3.5 x 1.6 m^2	[12]
Lead-free perovskite	67	3.37	0.09 cm^2 (research lab scale)	This doctoral research work

*Extracted from data reported on the respective sources

Moreover, the prospects for (transparent) solar cell technology commercial applications look very promising, where the market for solar energy is remarkably growing from a size of USD 52.5 billion in 2018 to a forecasted USD 223.3 billion in 2026, while there are plenty of available transparent surfaces that could benefit from a photovoltaic functionality.[13]

All in all, this thesis work provided both routes towards stabilization and molecular activity enhancement of layered lead halide perovskites via functional cation incorporation and research on defect mitigation in lead-free layered perovskite photovoltaics, in an effort to bring perovskite photovoltaics closer to a safer, reliable and sustainable future in solar energy harvesting.

References

[1] X. Yang, W. Wang, R. Ran, W. Zhou, Z. Shao, *Energy Fuels* **2020**, *34*, 10513.

[2] E. Greul, M. L. Petrus, A. Binek, P. Docampo, T. Bein, *J. Mater. Chem. A* **2017**, *5*, 19972.

[3] G. Longo, S. Mahesh, L. R. V. Buizza, A. D. Wright, A. J. Ramadan, M. Abdi-Jalebi, P. K. Nayak, L. M. Herz, H. J. Snaith, *ACS Energy Lett.* **2020**, *5*, 2200.

[4] M. T. Sirtl, F. Ebadi, B. T. van Gorkom, P. Ganswindt, R. A. J. Janssen, T. Bein, W. Tress, *Adv.Optical Mater.* **2021**, *9,* 2100202.

[5] F. Lv, T. Zhong, Y. Qin, H. Qin, W. Wang, F. Liu, W. Kong, *Nanomaterials* **2021**, *11*, 1361.

[6] F. Igbari, R. Wang, Z.-K. Wang, X.-J. Ma, Q. Wang, K.-L. Wang, Y. Zhang, L.-S. Liao, Y. Yang, *Nano Lett.* **2019**, *19*, 2066.

[7] T. Li, X. Zhao, D. Yang, M.-H. Du, L. Zhang, *Phys. Rev. Applied* **2018**, *10*, 041001.

[8] K. Lee, N. Kim, K. Kim, H.-D. Um, W. Jin, D. Choi, J. Park, K. J. Park, S. Lee, K. Seo, *Joule* **2020**, *4*, 235.

[9] M. J. Shin, J. H. Jo, A. Cho, J. Gwak, J. H. Yun, K. Kim, S. K. Ahn, J. H. Park, J. Yoo, I. Jeong, B.-H. Choi, J.-S. Cho, *Solar Energy* **2019**, *181*, 276.

[10] Z. Hu, J. Wang, Z. Wang, W. Gao, Q. An, M. Zhang, X. Ma, J. Wang, J. Miao, C. Yang, F. Zhang, *Nano Energy* **2019**, *55*, 424.

[11] J. C. Yu, J. Sun, N. Chandrasekaran, C. J. Dunn, A. S. R. Chesman, J. J. Jasieniak, *Nano Energy* **2020**, *71*, 104635.

[12] "ClearVue's luminescent solar concentrators create clear PV windows," can be found under https://www.pv-magazine-australia.com/2020/04/15/clearvues-luminescent-solar-concentrators-create-clear-pv-windows/.

[13] "Solar Energy Market Size, Trend | Industry Analysis and Forecast - 2026," can be found under https://www.alliedmarketresearch.com/solar-energy-market.

Barbara Primera Darwich

Curriculum Vitae

École Polytechnique Fédérale de Lausanne, Switzerland

EDUCATION

January 2018 – March 2022	**École Polytechnique Fédérale de Lausanne, Switzerland** Ph.D. in Chemistry and Chemical Engineering
2017	**Imperial College, London, UK** M.Sc. Advanced Chemical Engineering with Structured Product Engineering (with distinction).
2014 – 2016	**Columbia University, New York, NY, USA** B.S., Chemical Engineering, Materials Science and Engineering Minor
2011 – 2014	**Rollins College, Winter Park, Florida, USA** B.A., Pre-Engineering.
2012 – 2013	**Jacobs University, Bremen, Germany** Study abroad year.
2011	**International School of Paris, Paris, France** International Baccalaureate (IB), Diploma Programme

ACHIEVEMENTS

2020	**Swiss Study Foundation Member**
2020	**Innosuisse La Forge Prize, EPFL**
2016	**Statoil Scholarship, Imperial College London**.
2014 – 2016	**Dean's List**, Columbia University
2011 – 2013	**President's List**, Rollins College
2013	**The Archibald Granbille Bush Award**, Rollins College
2012	**Chemical Rubber Company Freshman Achievement Award**, Rollins College
2011	**Presidential Scholarship**, Rollins College

COMMUNICATION SKILLS

Spanish: Native
English: Fluent
French: Fluent (C1)
German: Advanced (C1)

INDUSTRIAL EXPERIENCE

June – August 2015	**BASF Agricultural Center, Limburgerhof, Germany** Internship in Crop Protection Crop Protection - Fungicide Formulation: Active ingredient polymeric encapsulation; mechanical mixing/

stirring methods; microscopic observation of suspension and emulsion preparations.

June – August 2014

SCHOTT AG, Landshut, Germany
Internship in Electronic Packaging

Surface Engineering: Galvanic and chemical nickel/gold plating and nickel stripping processes; topography and surface roughness studies with laser scanning microscopy and coating thickness measurement with X-ray fluorescence; quality control.

June – August 2013

Inresa Arzneimittel GmbH, Freiburg, Germany
Internship in the Scientific Department

Recording of product information in compliance with the Standard Operating Procedures; filing of customer inquiries on storage, use and application of pharmaceutical products.

RESEARCH EXPERIENCE

January 2018 – March Present

École Polytechnique Fédérale de Lausanne, Switzerland
Doctoral thesis

Third generation perovskite photovoltaic technology for building-integrated applications. Functionalization of lead-based perovskite to enhance the optoelectronic properties and lifespan under operation. Design and optimization of lead-free perovskites.

2016 – 2017

Song Group, Imperial College, London, UK
Master thesis work

Nanostructured materials for energy storage and conversion; fabrication of microporous polymeric materials into ion-selective membrane separators for rechargeable batteries.

2015 – 2016

Kumar Group, Columbia University, NY, US

Soft materials for renewable energy applications; block copolymer self-assembly in thin films; silicon substrate preparation; solvent-vapor annealing and annealing conditions (solvent composition, vapor pressure, temperature) to control the structure formation of diblock copolyelectrolytes.

2013

Molecular Life Research Center, Jacobs University, Bremen, Germany

Organic CB7 molecule synthesis, NMR analysis, study of CB7 host molecule effects on guest fluorescent dye molecules.

ADDITIONAL EXPERIENCE

2020 – 2021

Master Thesis Supervision of 2 students

(1) Stoichiometry studies of lead-free double perovskites
(2) Interfacial engineering of perovskite photovoltaic devices

At École Polytechnique Fédérale de Lausanne

2018 – 2021

Chemical Engineering Lab teaching assistant

	At École Polytechnique Féderalé de Lausanne
2018 – 2020	**Advanced General Chemistry teaching assistant** At École Polytechnique Féderalé de Lausanne

TECHNICAL SKILLS

PROGRAMMING	Python, Latex, Aspen
SOFTWARE	Origin, Adobe Illustrator, Microsoft Office, AutoCAD, WordPress
MATERIALS' MANUFACTURING & CHARACTERIZATION	Atomic Force & Electron Microscopy, Energy-Dispersive X-Ray Spectroscopy, X-Ray Diffraction Analysis, Deposition by Sputtering and Evaporation, Solution-processing techniques, photovoltaic device characterization, experience on the use of clean-room facilities

SELECTED PUBLICATIONS

- **An open-access database and analysis tool for perovskite solar cells based on the FAIR data principles.** Nat. Energy (2021). DOI: 10.1038/s41560-021-00941-3 (Link)
  T. Jesper Jacobsson , Adam Hultqvist , Alberto García-Fernández, Aman Anand, Amran Al-Ashouri, Anders Hagfeldt, Andrea Crovetto, Antonio Abate, Antonio Gaetano Ricciardulli, Anuja Vijayan, Ashish Kulkarni, Assaf Y. Anderson, Barbara Primera Darwich, … , Zafar Iqbal, Zhiqiang Xie, Eva Unger.

- Benzodithiophene-Based Spacers for Layered and Quasi-Layered Lead Halide Perovskite Solar Cells. ChemSusChem 2021, 14, 3001 – 3009 (Link)
  Barbara Primera Darwich, Nestor Guijarro, Han-Hee Cho, Liang Yao, Luc Monnier, Pascal Schouwink, Mounir Mensi, Jun-Ho Yum, Kevin Sivula.

- **Pseudo-halide anion engineering for α-FAPbI$_3$ perovskite solar cells.** Nature, 2021, 592, 381–385 (Link)
  Jaeki Jeong, Minjin Kim, Jongdeuk Seo, Haizhou Lu, Paramvir Ahlawat, Aditya Mishra, Yingguo Yang, Michael A. Hope, Felix T. Eickemeyer, Maengsuk Kim, Yung Jin Yoon, In Woo Choi, Barbara Primera Darwich, Seung Ju Choi, Yimhyun Jo, Jun Hee Lee, Bright Walker, Shaik M. Zakeeruddin, Lyndon Emsley, Ursula Rothlisberger, Anders Hagfeldt, Dong Suk Kim, Michael Grätzel, Jin Young Kim.

- **A hybrid bulk-heterojunction photoanode for direct solar-to-chemical conversion.** Energy Environ. Sci., 2021, 14, 3141-3151 (Link)
  Liang Yao, Yongpeng Liu, Han-Hee Cho, Meng Xia, Arvindh Sekar, Barbara Primera Darwich, Rebekah A. Wells, Jun-Ho Yum, Dan Ren, Michael Grätzel, Néstor Guijarro and Kevin Sivula.

- **Hydrophilic microporous membranes for selective ion separation and flow-battery energy storage.** Nature Materials 2020, 19, 195 – 202 (Link)
  Rui Tan, Anqi Wang, Richard Malpass-Evans, Rhodri Williams, Evan Wenbo Zhao, Tao Liu, Chunchun Ye, Xiaoqun Zhou, Barbara Primera Darwich, Zhiyu Fan, Lukas Turcani, Edward Jackson , Linjiang Chen, Samantha Y. Chong, Tao Li, Kim E. Jelfs, Andrew I. Cooper, Nigel P. Brandon, Clare P. Grey, Neil B. McKeown and Qilei Song.

- **Lead Halide Perovskite Quantum Dots To Enhance the Power Conversion Efficiency of Organic Solar Cells.** Angew. Chem. 2019, 131, 12826–12834 (Link)
  Néstor Guijarro, LiangYao, Florian Le Formal, Rebekah A. Wells, Yongpeng Liu, Barbara Primera Darwich, Lucie Navratilova, Han-Hee Cho, Jun-Ho Yum, Kevin Sivula

For an updated and complete list of publications, please check GoogleScholar (Barbara Primera Darwich) or follow this link.

CONFERENCES

- POSTER PRESENTATION: **Expanding the functionality of thiophenes in the quest for halide perovskite stabilization**. NanoGe Fall Meeting19 (NFM19) (Link)
  Barbara Primera Darwich, Han-Hee Cho, Nestor Guijarro, Liang Yao, Kevin Sivula, Jun-Ho Yum